NSRO Report No. 1

Solar Physics with the Nobeyama Radioheliograph

Proceedings of Nobeyama Symposium 2004
Kiyosato, Japan, October 26 - 29, 2004

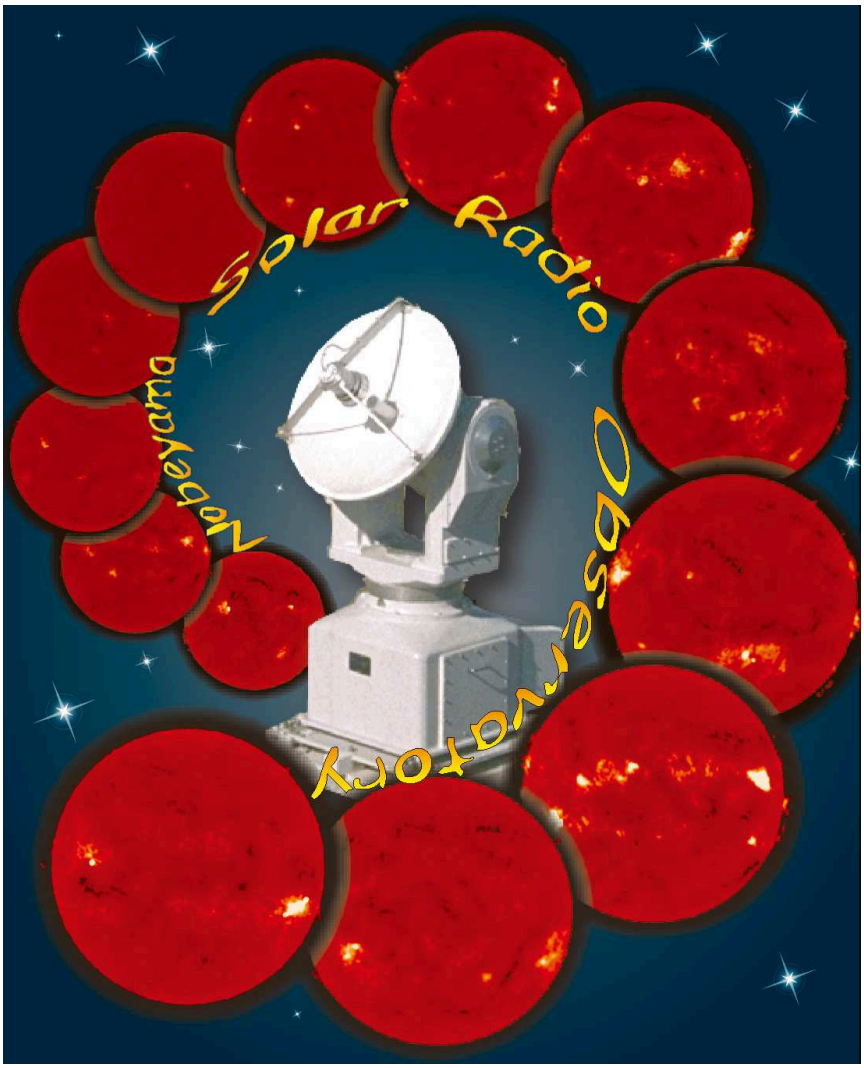

Nobeyama Solar Radio Observatory
December 2006

NSRO Report No. 1

Solar Physics with the Nobeyama Radioheliograph

Proceedings of Nobeyama Symposium 2004
Kiyosato, Japan, October 26 - 29, 2004

Nobeyama Solar Radio Observatory
December 2006

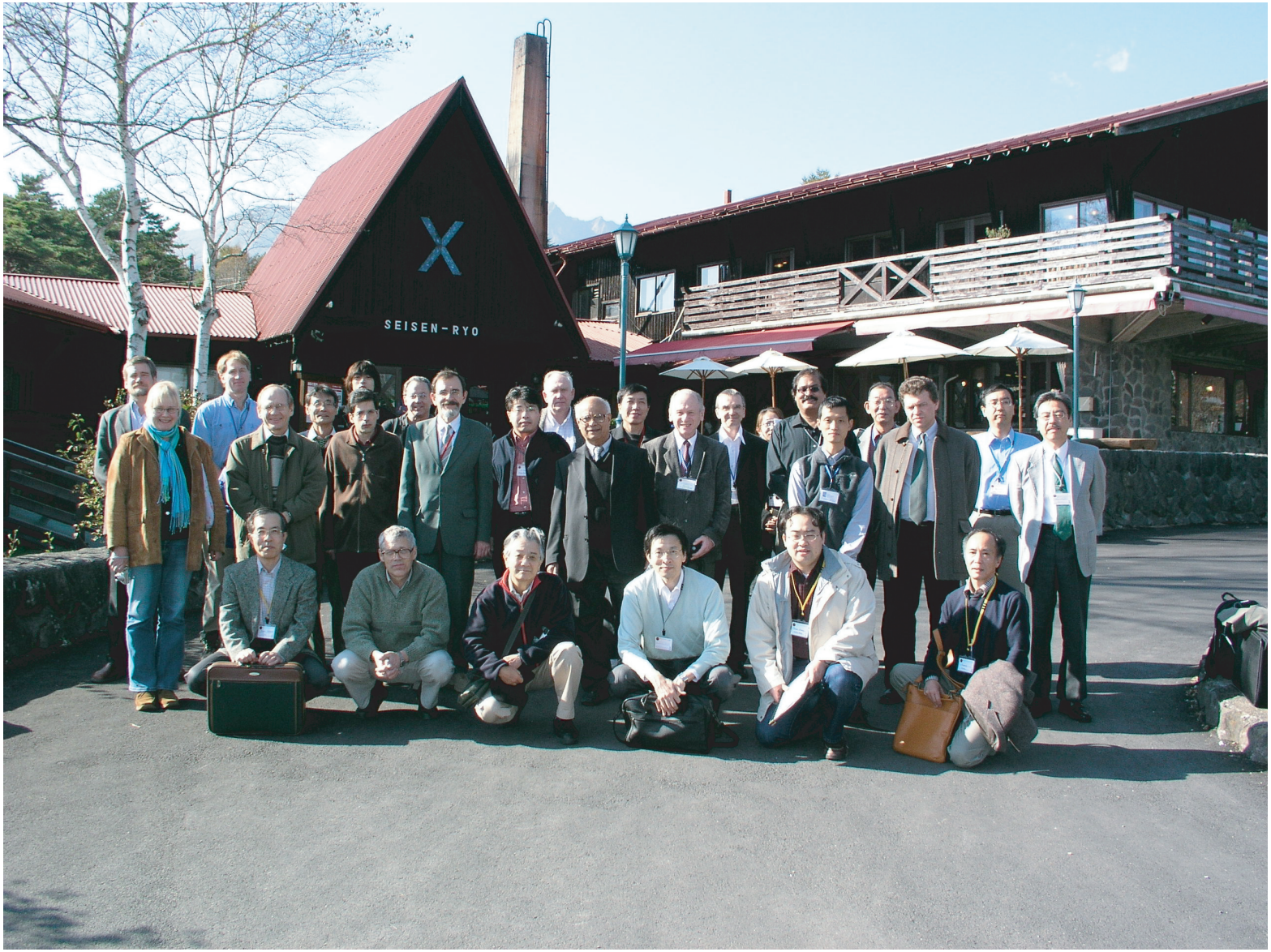
SEISEN-RYO

Contents

Solar Physics with the Nobeyama Radioheliograph – Nobeyama Symposium 2004 –

Kiyoto SHIBASAKI
Nobeyama Solar Radio Observatory, Minamisaku, Nagano, 384-1305, Japan
shibasaki@nro.nao.ac.jp

Abstract

The Nobeyama Radioheliograph (NoRH) has been in operation since 1992 and well covered one solar cycle. Many user groups of NoRH have been formed in the world and we have organized three symposiums related to NoRH in the past.

1. "Symposium on Nobeyama Radioheliograph" November 26-28, 1990 at Nobeyama
2. "New Look at the Sun with Emphasis on Advanced Observations of Coronal Dynamics and Flares" September 6-10, 1993 at Kofu (jointly with *Yohkoh*)
3. "Solar Physics with Radio Observations" October 27-30, 1998 at Kiyosato

We are glad to know that more and more data from NoRH are used and scientific outputs are still increasing. In this symposium, we would like to summarize recent development of solar physics using NoRH and discuss future direction of NoRH.

Key words: Nobeyama Radioheliograph — Plasma — Sun: flares — Sun: corona — Sun: radio

1. Short History of Nobeyama Radioheliograph

The idea of construction of a large radioheliograph was proposed early 1980s by late Professor Haruo Tanaka and solar radio groups in Japan: one at Toyokawa (Research Institute of Atmospherics, Nagoya University) and the other at Nobeyama (Tokyo Astronomical Observatory, University of Tokyo). To realize such a large project, merger of two major solar radio groups was suggested. On the occasion of establishment of National Astronomical Observatory (NAOJ) in 1988, Toyokawa group and Nobeyama group merged together and pushed to construct the Large Radioheliograph at Nobeyama. Finally in 1990, it was financed and the construction work started.

The original plan of the construction period was three years. Due to the delay of financing, solar activity was in the declining phase and the possibility of cooperation with *Yohkoh* satellite during the active period of the Sun was decreased. So, we decided to shorten the construction period to two years. We successfully completed the hardware construction before the end of March 1992 and started test observation in April (Nakajima et al. (1994), Nishio et al. (1994)). Soon after the start of the test observation, we could manage to get the first 17 GHz image of the Sun. Routine observation started late June 1992. The observing frequency of NoRH in the beginning was 17 GHz only. We added 34 GHz receivers and replaced sub-reflectors by frequency selective ones to realize dual-frequency observations in 1995 (Takano et al. 1997). Circular polarization observing capability is limited to 17 GHz.

In 2004, NAOJ joined newly established National Institute of Natural Sciences (NINS, 5 national research institutes including NAOJ). NINS is fully supported by the government but has more freedom compared to the former national institutes which had been directly attached to the Ministry of Science and Education. Nobeyama Solar Radio Observatory benefited from this change. We can invite many scientists from abroad and can attend international meetings more frequently. We hope this change further enhances cooperation between foreign users and Nobeyama Solar Radio Observatory and more data are used to enhance solar physics.

2. Scientific Objectives of NoRH

Main scientific objective of NoRH construction was to understand particle acceleration mechanisms in solar flares. After more than one solar cycle of observations, we still do not understand how high-energy electrons, which emit strong microwave through gyro-synchrotron mechanism, are produced in solar flares.

Geometrical configuration of magnetic loops which favors particle acceleration was found by combining microwave images with hard X-ray and soft X-ray images taken by HXT and SXT telescopes onboard *Yohkoh* respectively (Nishio et al. (1997), Hanaoka (1996)). Interaction regions of small loops and large loops seem to be the location of particle acceleration. NoRH found a clear evidence of high-energy electron injection into a large loop and propagation along the loop (Yokoyama et al. 2002). This is one of the targets of NoRH design. The spatial and temporal resolutions were determined to be able to detect these phenomena. Many oscillatory phenomena were found which may reflect particle acceleration mechanism itself or magnetic loop modulation (e.g. Asai et al. (2001), Nakariakov et al. (2003)). Highly anisotropic pitch angle distribution of accelerated electrons is sug-

gested to explain localized emission around loop top instead of loop foot points where magnetic field is stronger (Melnikov et al. 2002).

Although the main scientific objective of NoRH construction was to understand particle acceleration mechanisms in solar flares, NoRH showed its capability for many other subjects. One is for the study of eruptions. NoRH is a very good detector of prominence eruptions above the solar limb due to very steady operation and to weather insensitive observing wavelength compared to optical observations. It is also important that microwave observation is continuum observation, not line observation. Large Doppler shift due to large line-of-sight velocity does not affect the detectability of eruptive prominences. Statistical studies of prominence eruptions covering several years or one solar cycle were done (Gopalswamy et al. (2003), Shimojo et al. (2006)).

Studies of sunspot oscillations (Gelfreikh et al. (1999), Shibasaki (2001a)), magnetic field in active regions and in the corona and polar brightening studies (Shibasaki 1998) are also very interesting subjects. Studies of solar cycle dependence of these phenomena will contribute to understand global activities of the Sun.

3. A New Solar Flare Model

The current standard model of solar flares is based on magnetic reconnection. Normal solar corona is in low beta state: plasma pressure is negligibly small compared to magnetic pressure. In the low-beta corona, it is believed that free energy is stored in the form of electric current. Sudden dissipation of the current or release of stored energy is a solar flare.

Recent microwave, soft X-ray and EUV imaging observations of solar flares with high-cadence and high spatial resolution show that dense plasma is involved in solar flares from the beginning. Based on these observations, I have been proposing a high-beta model of solar flares, which is very similar to high-beta disruptions in magnetically confined nuclear fusion experiments. (Shibasaki (2001b), Shibasaki (2002)).

When plasma beta value increases in a curved magnetic loop, a localized interchange mode of instability, called ballooning instability is triggered. Energy source of the instability is free thermal energy of plasma due to confinement. Ballooning instability develops where beta value is larger than the critical value and curvature radius is the smallest. Top of coronal loops filled with high-density plasma is the favorable location for ballooning instability. Plasma flows along curved magnetic loops are also good candidate for ballooning instability. The critical value of the plasma beta is order of several percent depending on magnetic field geometry. From the analogy of high-beta disruption in magnetically confined nuclear fusion experiments, we can expect finger-like plasma structure perpendicular to the magnetic field, plasma turbulence, particle acceleration and so on. They are very similar to various solar flare phenomena.

To prove this model, it is necessary to measure plasma beta values in the solar corona. With the use of NoRH circular polarization measurements above the limb, we can measure line-of-sight values of magnetic field strength in the hot and dense plasma in the solar corona. I hope, the high-beta model will explain many puzzling features of solar flares including particle accelerations and more generally activities in the solar atmosphere.

4. Data Use and Future

We adopt open data policy for NoRH data. Immediately after observations, raw data and some processed data are freely available for research, educational and public outreach purposes. Solar flares and prominence eruption events are automatically detected and listed with images and movies on our home page (`http://solar.nro.nao.ac.jp/`). Due to development of the INTERNET and increased capability of image synthesis computers and storage disk space, open data policy resulted in forming large number of international user groups. To further enhance data usage of NoRH, we invited many users to Nobeyama for data analysis and organized international meetings. We hope, this trend of increasing data usage will continue and finally to find clear answer to particle acceleration mechanisms and other solar phenomena in near future.

This symposium is supported by Japan Society for the Promotion of Science as one of International Meeting Series.

References

Asai, A., Shimojo, M., Isobe, H., Morimoto, T., Yokoyama, T., Shibasaki, K., & Nakajima, H. 2001, ApJL, 562, L103

Gelfreikh, G. B., Grechnev, V., Kosugi, T., & Shibasaki, K., 1999, Sol. Phys., 185, 177

Gopalswamy, N., Shimojo, M., Lu, W., Yashiro, S., Shibasaki, K., & Howard, R. A. 2003, ApJ, 386, 562

Hanaoka, Y. 1996, Sol. Phys., 165, 275

Melnikov, V. F., Shibasaki, K., & Reznikova, V. E. 2002, ApJL, 580, L185

Nakajima, H. et al., 1994, Proc. IEEE, 82, 705

Nakariakov, V. M., Melnikov, V. F., & Reznikova, V. E. 2003, A&A, 412, L7

Nishio, M. et al., 1994, Proc. Kofu Symposium, NRO report 360, 19

Nishio, M., Yaji, K., Kosugi, T., Nakajima, H., & Sakurai, T. 1997, ApJ, 489, 976

Shibasaki, K. 1998, ASP Conf. Ser, 140, 387

Shibasaki, K. 2001a, ApJ, 550, 1113

Shibasaki, K. 2001b, ApJ, 557, 326

Shibasaki, K. 2002, ESA SP-506, Proc. 10 th. European Solar Physics Meeting, 749

Shimojo, M., Yokoyama, T., Asai, A., Nakajima, H., & Shibasaki, K. 2006, PASJ, 58, 85

Takano, T. et al., 1997, Coronal Physics from Radio and Space Observations, Proc. CESRA Workshop, Lecture Notes in Physics, Springer, 183

Yokoyama, T., Nakajima, H., Shibasaki, K., Melnikov, V. F., & Stepanov, A. V. 2002, ApJL, 576, L87

Progress in Understanding Radio Emission from Solar Flares: Observations with the Nobeyama Radioheliograph 1999-2004

T. S. Bastian*
National Radio Astronomy Observatory
tbastian@nrao.edu

Abstract

Studies of solar flares based on observations by the Nobeyama Radioheliograph and related instruments such as the Owens Valley Solar Array, the Nançay Radioheliograph, and the Solar Submillimeter Telescope, as well as supporting instruments such as the RHESSI, TRACE, and SOHO missions, are reviewed for the period 1999-2004. Work on the classification of solar radio bursts is briefly discussed. Recent observational work on loop-top radio sources and rapidly propagating emission signatures is summarized and its interpretation in terms of electron anisotropies is described. Possible acceleration processes yielding such anisotropies are also briefly discussed. Recent work on electron acceleration and transport in a relatively dense plasma environment is summarized. Finally, recent work at millimeter and submillimeter wavelengths is described.

Key words: Sun: flares – Sun: radio radiation – Sun: X-rays, gamma rays

1. Introduction

The pursuit of understanding the physics of solar flares is a complex and multi-faceted affair. In order to piece the parts of a puzzle together observations across the electromagnetic spectrum are required, as well as insights and motivation gained through theory and modeling. Access to key pieces of the puzzle are provided by radio spectroscopic and imaging observations, which allow observers to image thermal and nonthermal electron emissions in the flaring source. Centimeter, millimeter, and submillimeter wavelength emissions are particularly important as probes of the most energetic electrons released in a flare. The Nobeyama Radioheliograph (NoRH) has therefore played a central role in extending our understanding of basic processes in solar flares and in uncovering new phenomena that occur during flares.

This review summarizes recent progress in understanding physical processes in solar flares based on radio observations. The emphasis is on observations made by the NoRH and by other radio observatories since the last Nobeyama Symposium in 1998 (Bastian et al. 1999). There have been two major observational developments during this time. First, beginning in May 1998, high resolution imaging in extreme ultraviolet (EUV) wavelengths by the Transition Region and Coronal Explorer (TRACE) became available and has played an important role in joint radio/EUV studies of flares (e.g., White, this proceedings). Second, beginning in February 2002, the Ramaty High Energy Spectroscopic Solar Imager (RHESSI) has provided high resolution spectroscopic imaging of hard X-ray (HXR) emission from flares and microflares (see Hudson, this proceedings). The contributions of both missions are reflected in the work presented in this proceedings.

More than half the papers presented in this proceedings are devoted to aspects of flares and particle acceleration and provide a good sample of progress in these areas. The magnetic evolution of flare-producing active regions is discussed by Pohjolainen and by Hori et al.; properties of energetic electrons in flares is discussed in papers by Nakajima et al., Takasaki et al, and Masuda; electron acceleration and transport processes are discussed by Melnikov and by Tanuma, with fast propagating radio signatures discussed by Shibasaki and by Hori et al.; gyrosynchrotron emission from anisotropic electron distributions are discussed by Fleishman; diagnostics of magnetic fields in flares are discussed by Huang; pulsation events and their interpretation are discussed by Kumio et al., Stepanov et al., and Asai; microflares are discussed by Kundu et al.; spatial and temporal fine structures are discussed by Altyntsev et al.; recent efforts to model microwave emission from flares are described by Nindos.

In the following, I provide a broad overview of several topics touched on in these proceedings and elsewhere in the literature. The overview is necessarily topical in nature but reflects those areas where I believe new phenomena have been uncovered and/or new insights have been gained into the flare phenomenon. I begin with recent work on the classification of radio bursts in §2. In §3 I discuss electron acceleration and transport, including the trap plus precipitation model, electron anisotropies, loop-top electron acceleration, and possible signatures of streaming electrons. In §4 I discuss plasma environments in which flares can occur, and in §5 I summarize recent work on millimeter and submillimeter observations of flares. I conclude in §6.

* The National Radio Astronomy Observatory is a facility of the National Science Foundation operated under cooperative agreement by Associated Universities, Inc.

2. The Spectral Taxonomy of Radio Bursts

It is worth beginning with a reminder of why observations at centimeter wavelengths (cm-λ) are important to studies of the flare phenomenon. It has been known since the 1960s (see, e.g., Kundu 1965 for a review of early work) that cm-λ emission is intimately related to HXR emission and that both serve as powerful tools for characterizing the population of electrons that often carry the bulk of the energy released in a flare. As such, they offer unique diagnostic of magnetic energy release, electron acceleration, and electron transport processes. Yet radio emission occurs over a much broader range than cm-λ. What is the importance of cm-λ emission relative to longer-wavelength (decimeter- and meter- wavelengths)? It has been known for many years (Giudice & Castelli 1975) that radio bursts are composed of multiple spectral components, classified as G, C, and A components according to whether the flux density decreased with frequency, showed a spectral maximum, or increased with frequency, respectively. It was found that pure C components accounted for a little more than half of the events observed (54%), while pure G and composite GC events accounted for 19% and 21% of the total, respectively. Of the remainder, A components accounted for only 1% of the total. Roughly 5% were classified as complex, or type M, for "miscellaneous".

An update to the work by Giudice & Castelli, who studied nine fixed frequencies between 245 MHz and 35 GHz has been performed by Nita et al. (2004), using the Owens Valley Solar Array (OVSA) between 1-18 GHz. While the OVSA study has narrower frequency coverage, it has frequency resolution of a few percent. Nita et al. classified bursts somewhat differently than Giudice & Castelli, designating bursts as type C (cm-λ), type D (cm-λ), or type CD. In contrast to Giudice & Castelli, Nita et al. find that 80% of their sample of 412 OVSA events are pure C, whereas only 5% are pure D and 15% are CD. Of the composite CD events, 12% had peak flux densities < 100 SFU, 19% had peak flux densities between 100-1000 SFU, and 60% had peak flux densities > 1000 SFU. That is, composite events tend to be large events. Interestingly, Castelli et al. (1967) first drew attention to the correlation between large GC (or type "U") events and major proton events as manifested by polar cap absorption events at 30 MHz.

To summarize, a modern classification of dm-λ to cm-λ radio bursts shows that the majority (80%) are pure C type; cm-λ studies of flares therefore provide access to the most common manifestation of radio emission from flares. A critical class of flares are those of type CD or GC that include dm-λ and/or m-λ emission. These tend to be the largest flares and are associated with solar energetic particle events. Type G or D emission has a detailed taxonomy of its own (e.g., radio bursts of type II, III, and IV) but these topics, albeit fascinating, lie outside the scope of this review. However, at the opposite end of the radio spectrum we discuss recent work on high frequency bursts at mm-λ and submm-λ in §6.

3. Electron Injection and Transport

Emissions from energetic electrons at X-ray and radio wavelengths have played a central role in making progress toward an understanding of the flare phenomenon. At cm-λ, energetic electrons emit via the well-understood gyrosynchrotron mechanism whenever and wherever energetic electrons interact with magnetic fields. Observations of gyrosynchrotron emission are therefore ideally suited as a probe of electron acceleration and transport processes in flares. However, effective exploitation of cm-λ emission depends on appropriate instrumentation. As a solar-dedicated imaging instrument operating at 17 and 34 GHz, the NoRH provided an important step in this direction and has made several important contributions to revealing new phenomena relevant to electron acceleration and transport. After summarizing a framework in which many features of HXR and cm-λ observations can be understood, recent developments are described.

3.1. TTP/DP Model

Beginning with Melrose & Brown (1976) the so-called "trap plus precipitation" (TPP) model has enjoyed some success in explaining various features of HXR and cm-λ observations in many flares. The TPP model is based on the idea that coronal magnetic loops serve naturally as magnetic traps. An electron in a uniform magnetic field and with velocity components parallel and perpendicular to the magnetic field vector will follow a helical trajectory with a pitch angle $\alpha = 3Dtan^{-1}(v_\perp/v_\parallel)$. In coronal magnetic loops the magnetic field is stronger at its footpoints than at its looptop and the magnetic field therefore converges as it nears the Sun. Since the first adiabatic invariant $\mu = p_\perp^2/2B \propto v_\perp^2/B$ is conserved, $v_\perp$ increases and $v_\parallel$ decreases as B increases. The pitch angle α therefore increases as an electron propagates toward the chromosphere. One of two things then happens: if the electron propagates close enough to the Sun it penetrates the chromosphere and loses its energy to Coulomb collisions in the high-density environment and is lost from the trap, a process called electron precipitation. Alternatively, if the electron's pitch angle reaches 90° before it suffers significant energy loss due to collisions, it mirrors and remains in the coronal magnetic loop. Let $\alpha_\circ$ represent the initial pitch angle of an electron injected into the loop. The loss cone is defined by the angle $\alpha_{LC} = 3D\sin^{-1}[(B_\circ/B_p)^{1/2}]$, where $B_\circ$ is the magnetic field strength where the electron is injected and B_p is its value at the height where it precipitates from the loop. Electrons with pitch angles $\alpha_\circ < \alpha_{LC}$ are in the loss cone and therefore directly precipitate from the loop whereas electrons with $\alpha_\circ > \alpha_{LC}$ mirror at the foot points and remain trapped in the loop until some physical process scatters them into the loss cone and/or they lose their energy and are thermalized. Several mechanisms cause electrons to scatter into the loss cone. Coulomb collisions between electrons and electrons, and electrons and ions, are omnipresent and establish the maximum lifetime of an electron in the trap. However, other scattering mechanisms – e.g., wave-particle interac-

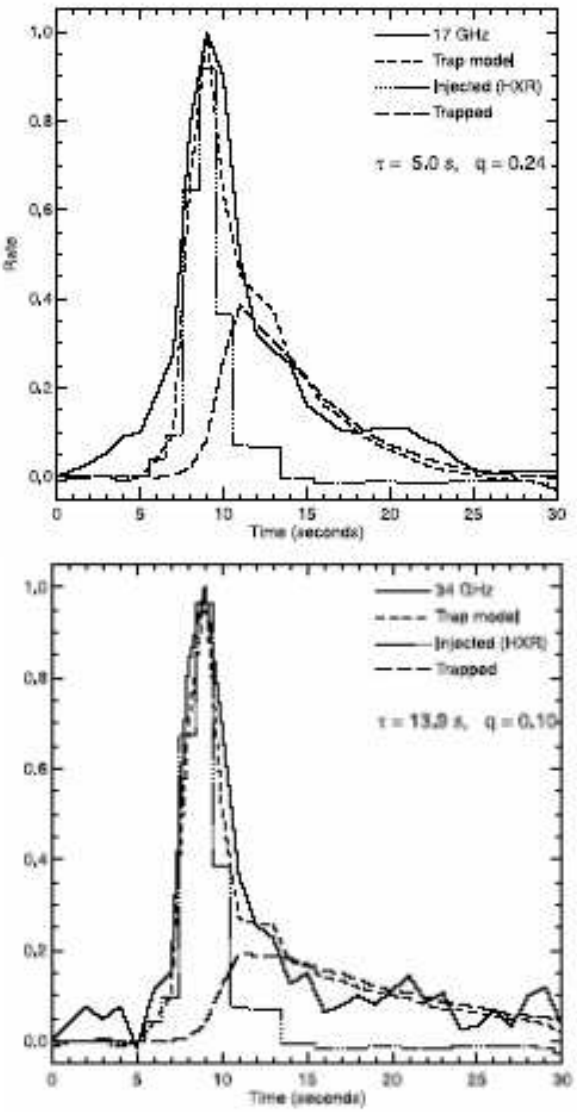

Fig. 1. Observations of the 1998 Jun 13 flare. Light curves are shown for the 17 and 34 GHz emission, and relative count rates for the *Yohkoh* HXT 53-93 keV channel (M2). The HXR profile is used as a proxy for the electron injection rate. The data are compared with a trapping model. The long-dashed curves represent emission from the trapped electrons. After Fig. 7 in Kundu et al. (2001).

tions (Bespalov et al. 1987)– may cause strong- or diffusive pitch-angle scattering on much shorter time scales and therefore dominate electron transport. In the simplest version of the TPP model, however, Coulomb collisions dominate.

Electron injection and transport in the context HXR emission and the TPP model have been studied by numerous authors: e.g., Emslie et al. 1979, MacKinnon et al. 1983, Vilmer et al. 1986, Hulot et al. 1989, Alexander 1990, McClements 1990, Bruggman et al. 1994, Aschwanden et al. 1997, Alexander & Metcalf 2002, to name just a few. For electrons with energies $< 160keV$, the Coulomb collision frequency $\nu_C \propto n_{th}E^{-3/2}$. Since more energetic electrons suffer fewer collisions than less-energetic electrons, they have longer life times in the trap. In this way, the distinctive delay structure of energetic photon emissions in HXR, and in high frequency radio emission at cm-λ, can be understood as well as the relative timing between electronic and ionic emissions (e.g., Hulot et al. 1989, 1992). Moreover, the background density in the trap n_{th} can be inferred by detailed analysis of HXR or radio delays as a function of energy (Aschwanden et al. 1997) or frequency (Lee et al. 2000, Lee & Gary 2000). A recent example of NoRH observations of a simple impulsive flare that shows clear evidence of electron trapping at 17 and 34 GHz is shown in Fig. 1 (from Kundu et al. 2001a).

Aschwanden et al. (1997, 1998a,b) pointed out that for an injection of electrons into the magnetic trap, some fraction will have pitch angles such that they are in the loss cone and they directly precipitate (DP) from the trap. The fraction of injected electrons that directly precipitate from the trap depends on the magnetic mirror ratio $R = 3DB_p/B_\circ$. This modification of the TPP model is referred to as the "trap plus precipitation/direct precipitation" (TPP/DP) model (Fig. 2). The DP component is of great interest because it reflects the energy distribution function of the injected electrons, unmodified by transport effects other than time-of-flight dispersion from the injection site to the precipitation point, assuming no evolution of the injection spectrum during an injection time (Brown et al. 1998). The TPP/DP model represents an interesting deconvolution problem. In many cases, the coronal (thin target) contribution to the HXR emission is negligible and the emission is dominated by thick-target bremsstrahlung emission by electrons precipitating from the magnetic trap. Hence, the HXR emission is dominated by footpoint emission composed of DP electrons and those that have been trapped for a time before precipitating. In other words, HXR emission is generally only sensitive to precipitating electrons. In contrast, microwave emission is sensitive to the entire distribution of electrons (both trapped and DP components). However, the trapped component is expected to dominate the emission at a given frequency because the number density of trapped electrons represents a time-integral of the injection function over a trapping time whereas the DP component is promptly lost from the trap.

Gyrosynchrotron and HXR radiation are thus highly complementary. Unfortunately, this complementarity has been difficult to exploit in practice, primarily because of limitations in available instrumentation. Both spectral regimes require the means to perform time-resolved broadband imaging spectroscopy. While RHESSI indeed has the means to do this, it is not yet possible to do so at radio wavelengths. Instead, observers have often been forced to rely on total flux measurements at fixed frequencies (NoRP, Berne) and/or time-resolved imaging at only one or two frequencies (NoRH), or low-resolution imaging spectroscopy (OVSA). Nevertheless, recent observations have shown that while the TPP or TPP/DP models provide a useful framework for interpreting the observations,

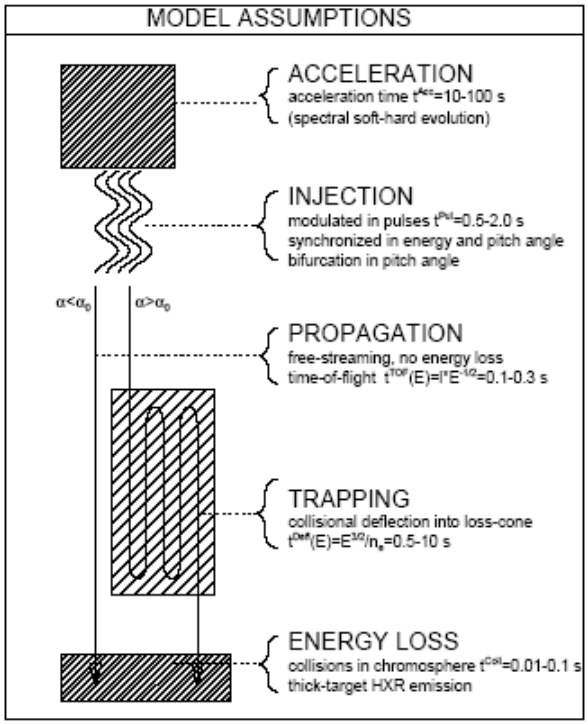

Fig. 2. Schematic of the TPP/DP model where upon injection, those electrons with pitch angles within the loss cone directly precipitate, whereas those electrons with pitch angles outside the loss cone will remain trapped until scattered into the loss cone. From Aschwanden (1998).

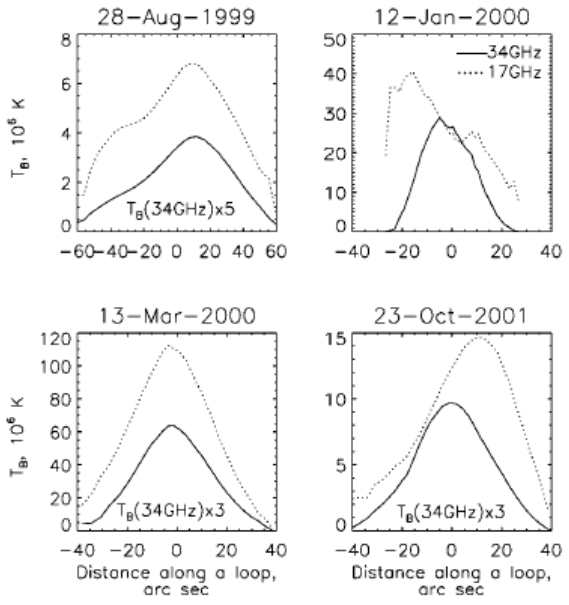

Fig. 3. Examples of loop-top sources. Each panel shows the variation of brightness at 17 and 34 GHz along the length of a flaring loop. From Melnikov et al. (2002).

they are by no means the full story. For the remainder of this section, I touch on examples of recent flare observations that show evidence for strong electron anisotropies and their possible causes, as well as observations that may show evidence for streaming, or beamed, electrons.

3.2. Electron Anisotropy

For an isotropic distribution of energetic electrons in a coronal magnetic loop, the morphology of the gyrosynchrotron source is strongly frequency dependent. Bastian et al. (1998) show that at high frequencies, the source is footpoint-dominated whereas at low frequencies, the source can be optically thick and the maximum brightness is found at the loop top in such cases. An important development in recent years is the identification of "loop top" sources in flares observed at high frequencies by the NoRH. While loop top sources had been suggested long ago (e.g., Marsh & Hurford (1982) and references therein) on the basis of early observations made by the Very Large Array, recent OVSA and NoRH observations have stimulated renewed interest in the loop top sources and their underlying cause or causes.

White et al. present 17 and 34 GHz observations of the M1.6 flare at S23E60 on 1999 May 29. The microwave emission was optically thin and, in the early phase of the flare, originated in the loop footpoints or loop legs. However, as the flare proceeded the source evolved to a complete loop morphology dominated by a loop top source at both 17 and 34 GHz, a morphology that could not be fit by gyrosynchrotron emission from a simple isotropic electron distribution function. Melnikov et al. (2002) present a sample of four flares, each of which shows clear evidence for loop top sources at 17 and 34 GHz (Fig. 3). The authors find that the observed emission is consistent with an anisotropic distribution of energetic electrons near the loop top, the sense of the anisotropy such that the electron distribution is strongly peaked perpendicular to the magnetic field. Melnikov et al. conclude that the anisotropy likely reflects that of the injected electrons and therefore yields insight into the electron acceleration/injection mechanism.

Lee et al. (2000) studied two flares, A and B, that occurred in close succession on 1993 June 3 with NoRH and OVSA. The microwave emission of flare A was significantly greater in intensity and duration than that of flare B. In contrast, the SXR emission from flare A (GOES C2.8) was significantly less than that of flare B (GOES M1). The spectral evolution of flare A suggested that electron energy loss was dominated by Coulomb collisions and that the background density in the magnetic trap was relatively low (5×10^9 cm^{-3}) whereas the background density inferred for flare B was substantially higher (8×10^{10} cm^{-3}). In a second study, Lee & Gary 2000 explored the spectral evolution of the microwave spectrum of flre A in the context of the TPP model under the assumption that the evolution was the result of electron transport effects and was not a function of electron acceleration or injection. Included in the formulation was an anisotropic electron distribution function. Fitting to the (optically thin) total power spectra, Lee & Gary find that the best-fit model indeed required an anisotropic distribution that

was strongly peaked (angular width $\approx 30°$) perpendicular to the magnetic field.

Several lines of observational evidence, based on imaging and spectroscopy of microwave sources, suggest that anisotropic electron populations that are located near the tops of flaring magnetic loops and are strongly peaked perpendicular to the magnetic field. In order to fully characterize the phenomenon, the incidence and circumstances of loop top sources must be determined and their circumstances explored using suitably selected statistical samples. In addition to the imaging domain, the spectral domain can be more fully exploited to explore anisotropic electron distribution functions. Fleishman & Melnikov (2003a,b) have computed gyrosynchrotron emission spectra expected from various anisotropic electron distribution functions and find that the intensity, spectral index, and source polarization are all sensitive to the degree and type of anisotropy. Hence, polarization spectroscopy could be an important tool for probing electron anisotropies in flares.

3.3. Loop-top Acceleration

Important questions follow from the conclusion that anisotropic electron distributions are produced by some flares near the tops of coronal magnetic loops: what physical process or processes produce such distributions and what do they tell us about electron acceleration, injection, and transport? These questions have not yet been answered in detail but preliminary explorations have been made into acceleration mechanisms that may be operative near coronal loop tops that would result in electron distributions that are strongly peaked perpendicular to the magnetic field.

Somov & Kosugi (1997) proposed that collapsing magnetic traps may play a role as a secondary electron acceleration mechanism in flares. In the "standard" flare scenario, magnetic reconnection takes place in a current sheet above flare loops (e.g., Forbes & Priest 2000) in a cusp configuration. Reconnected field lines relax in succession from the cusp-like topology to a more-nearly force-free configuration (Fig. 4). Karlický & Kosugi (2004) modeled this idea numerically, including the effects of Coulomb collisions, and found that electrons could be betatron-accelerated to high energies and that highly anisotropic distribution functions resulted at the loop top. It is worth mentioning that, to overcome energy losses to Coulomb collisions, effective acceleration of electrons via the collapsing magnetic trap model requires the injection of electrons that have already been accelerated to an energy above some threshold energy. Pre-acceleration may plausibly occur in the current sheet via DC electric fields.

Qiu et al. (2004) present OVSA and *Yohkoh* HXT observations of the X-class flare observed on 2001 Apr 6, which is characterized by an impulsive and gradual phase. The gradual phase shows evidence for footpoint separation and continuing thick target HXR emission, implying continuing electron acceleration during the gradual phase. Qiu et al. propose that, in this example, the collapsing trap model is a viable acceleration mechanism.

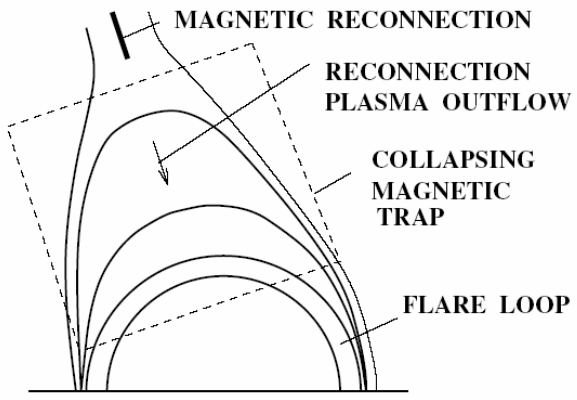

Fig. 4. Schematic of the collapsing magnetic trap. From Karlický & Kosugi (2004).

Aschwanden (2004) explores a similar "dynamic trap" model to account for the apparent synchronization of pulsed particle injection as inferred from time-of-flight measurements of electrons using in HXR observations. Noting that the loss cone would increase as the magnetic field relaxed from a cusp-like to force-free configuration, Aschwanden suggests electrons could be injected into the trap in a largely energy-independent manner.

While a great deal of both observational and theoretical work remains in order to understand the role that anisotropic electrons play in the flare phenomenon, it is interesting to note that magnetic trap models – TPP, TPP/DP, and now, collapsing or dynamic magnetic traps – continue to play a fruitful role.

3.4. Fast Electron Propagation

A scientific goal of the NoRH was to resolve in time electron propagation effects in flares and related phenomena. One such example is that of a collimated ejection of nonthermal electrons in association with a flare and Hα surge, reported by Nakajima & Yokoyama (2002). The collimated jet moved upward with an apparent speed of ≈ 3000 km s^{-1}. A second intriguing example was reported by Yokoyama et al. (2002), who observed the GOES M2.8 flare of 1999 Aug 28. The flare was analyzed in a high cadence imaging mode at 17 and 34 GHz, where 10 images per second were produced. At least two propagating features were measured in the high cadence images. One appeared to propagate at a speed > 6000 km s^{-1} whereas another appeared to propagate at 90000 km s^{-1}; i.e., at $0.3c$.

The authors interpret the rapidly propagating signal in terms of fast electrons streaming from one end of the magnetic loop to the other. A problem raised by this interpretation is that if the speed of the emitting electrons is taken to be that of the propagating gyrosynchrotron emission, the energy of the emitting electrons is only 23 keV. This is far less than the expected energy of electrons responsible for the 17 GHz emission: the authors argue that the magnetic field strength in the source must be of order 200-400 G, implying the energy of the emitting

electrons is of order 1 MeV. The speed of 1 MeV electrons is nearly that of light. The authors suggest the discrepancy might be resolved if the fast electrons are injected into the source with a relatively large pitch angle ($\approx 70°$). The signal with a lower apparent propagation speed may be consistent with the local Alfvén speed or, perhaps, with the propagation of a "turbulent mirror".

4. Dense and Cool Flares

The plasma density in flaring loops has been studied for many years using SXR and EUV observations. These studies have produced density estimates ranging from 10^{10} cm^{-3} to more than 10^{12} cm^{-3} (e.g., Doschek 1990). Aschwanden et al. (1997) have considered radio and SXR diagnostics of the electron number density in flaring loops. In particular, in an analysis of 14 different flares, they compare electron number densities derived from *Yohkoh* SXT observations with those inferred from dm-λ radio bursts and find that the values inferred depend on the time and place the measurement is made. Using type IIIdm and reverse-slope dm-λ radio bursts, densities of 6×10^8 cm^{-3} to 10^{10} cm^{-3} are inferred in the electron acceleration region. The accelerated electron are stopped in the chromosphere, liberating their energy and driving so-called chromospheric evaporation. Again, using dm-λ radio bursts, Aschwanden & Benz find densities of 10^9 cm^{-3} to 5×10^{10} cm^{-3} at the evaporation front, presumably reflecting the pre-flare loop density; they find densities a factor of 3.6 higher (i.e., 4×10^{10} cm^{-3} to 2×10^{11} cm^{-3}) behind the fronts. Finally, the densities inferred for "filled" loops based on SXR measurements is 2×10^{10} to 2.5×10^{11}. Therefore, while large densities are expected following main-phase energy release and the evaporation it produces, pre-flare loop densities do not appear to be large.

Nevertheless, in some cases, even pre-flare loop densities can be significant. Veronig & Brown (2004) report two examples of a new class of HXR source where the corona is so dense that it is collisionally thick to electrons with energies up to 50 keV, with chromospheric evaporation dominated by energy deposition via conduction rather than electron precipitation. Initial loop densities in excess of 10^{11} cm^{-3} are inferred. It is interesting to note that high plasma densities and temperatures can yield a high plasma β. Shibasaki (2001) has recently considered the implications of high-β plasma environments for flaring and has suggested such environments may be unstable to the "ballooning instability".

More recently, Bastian, Fleishman, & Gary (2006) have analyzed an example of a flare observed on 24 Oct 2001 by the NoRH, NoRP, OVSA, TRACE, and *Yohkoh*. This flare is similar to that observed by White et al. (1992), described as an "impulse response" event by Hudson & Ryan (1995). These events are characterized by a steep low-frequency spectral cutoffs indicative of a high ambient density which causes both Razin suppression and free-free absorption below ~ 10 GHz. The event reported by White et al. showed no frequency-dependent delays in the flux maximum, in contrast to expectations based on the TPP or TPP/DP model. The event analyzed by Bastian et al. shows delays that show a frequency dependence that is opposite to that expected for the TPP or TPP/DP model. A detailed analysis of the event resulted in the following scenario: that the radio source initially comprised a cool ($\sim 2 \times 10^5$ K), dense (10^{11} cm^{-3}) plasma permeated by a magnetic field of order 165 G. The radio emission and its spectral shape and evolution result from an injection of fast electrons into the dense ambient plasma. Due to a large magnetic mirror ratio neither electron precipitation, nor thermal conduction, produced significant chromospheric evaporation. Therefore, the density of the flaring loop did not change significantly during the course of the flare. Importantly, however, energy was deposited in the loop via collisions and/or turbulent heating that yielded a significant increase in plasma temperature. The temperature increase led to decreased free-free absorption and could account for the inverse delay structure of the event.

To conclude this section, both radio and HXR techniques have revealed new types of environments in which energy release and electron acceleration appears to occur. The extreme nature of these environments may lead to new insights regarding the energy release mechanism and/or particle acceleration and transport.

5. Submillimeter Emission from Flares

With the advent of the Solar Submillimeter Telescope (SST) at El Leoncito in the Argentine Andes (Kaufmann et al. 2000), and the Köln Observatory for Submillimeter and Millimeter Astronomy (KOSMA) near Zermat, Switzerland (Lüthi et al. 2004), a new spectral window has opened at mm- and submm-λ wavelengths. The SST is a 1.5 m telescope that operates at 212 and 405 GHz while KOSMA is a 3 m telescope that operates at 230 and 345 GHz. Emissions at these frequencies probe relativistic electrons accelerated in flares. It has been known for some time that a different population of energetic electrons may be involved in the production of mm-λ radiation, at least for some flares. Observations with the Berkeley, Maryland, Illinois Array (BIMA) suggested that the electron energy distribution function flattens toward higher energies (e.g., Kundu et al. 1994). For example, Trottet et al. (1998) present HXR and γ-ray spectroscopy of flares wherein the cm-λ/mm-λ emission appears to be associated with electrons with energies of 0.4-0.7 Mev, which have a flatter spectrum than lower energy electrons. Trottet et al. (2002) report the first observations of a flare above 200 GHz. The observations, made jointly with the SST and OVSA, showed an impulsive spike produced by synchrotron emission from relativistic electrons with energies of 10-15 MeV, and an extended phase that was mostly due to thermal free-free emission=2E They show that in this case, too, the 212 GHz impulsive emission appears to be a due to electrons with a rather hard energy spectrum. A number of additional new and intriguing observations have been reported from the SST and KOSMA.

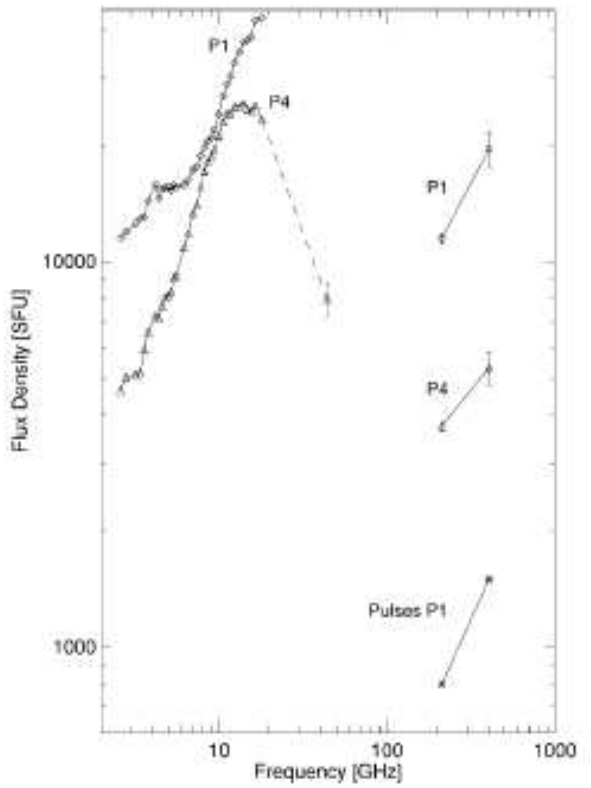

Fig. 5. Spectra of the 2003 Nov 4 flare from cm-λ to submm-λ. Note that while the cm-λ emission appears to be consistent with gyrosynchrotron emission, the submm-λ spectral component is inverted. From Kaufmann et al. (2004).

Kaufmann et al. (2001, 2002) report SST and OVSA observations of the X1.1 on 22 Mar 2000 and the X5.6 flare on 6 Apr 2001. A new and curious feature of the submm-λ emission is the presence of sub-pulses or spikes of radiation, with amplitudes of 5-10% and a recurrence rate of ≈ 50 per minute. Raulin et al. (2003) studied the spike phenomenon in the X5.3 flare of 25 Aug 2001, demonstrating that spikes observed at 212 and 405 GHz are correlated and that the pulse rate is correlated with the overall flux of the event. Raulin et al. suggest that the spikes are intimately related to primary energy release. A second study of the same flare (Raulin et al. 2004) suggests that the energy requirements of the event were extreme, requiring that $\approx 5 \times 10^{36}$ electrons must be accelerated to energies > 20 keV each second in a source with a magnetic field strength > 1 kG!

A second intriguing discovery was reported by Kaufmann et al. (2004) in which the presence of an inverted high frequency spectral component is reported (Fig. 4). In particular, the flare of 4 Nov 2003 displays a spectrum that *increases* between 212 and 405 GHz, in stark contrast to the flat or strongly decreasing spectrum expected for optically thin thermal free-free emission or nonthermal gyrosynchrotron emission, respectively. Using observations from KOSMA and the Berne polarimeters, Lüthi et al. (2004) present an analysis of the flare of the GOES X17.2 flare that occurred on 28 Oct 2003. Here, too, an inverted spectrum is seen from 230 to 345 GHz. The cause of the inverted spectral component is presently unknown. Among the possibilities are emission from optically thick thermal or nonthermal components, positron emission (Lingenfelter & Ramaty 1967), inverse Compton radiation (Kaufmann et al. 1986), or another mechanism.

6. Summary and Conclusions

This brief review has summarized progress on several fronts related to microwave observations of solar flares, with particular emphasis on observations from the NoRH, and joint observations made by the NoRH and HXR instrumentation such as *Yohkoh* and RHESSI, as well as examples of those made jointly with TRACE. Microwave observations are well matched to the majority of solar flares, which produce gyrosynchrotron emission in this wavelength band.

While the TPP and TPP/DP models have provided a useful framework for understanding a number of aspects of both radio and HXR observations of flares, recent work has highlighted the presence of loop-top sources in flares. These are the result of highly anisotropic electron distributions, the distribution being strongly peaked perpendicular to the magnetic field. As a means of explaining such distributions, as well as the energy dependence of HXR pulse timing, dynamic or collapsing trap models have been considered. In addition to perpendicular anisotropies, it is possible that gyrosynchrotron emission from streaming or beamed electron distributions has been observed. It appears that energy release occurs in relatively dense, collisionally thick environments, as discovered by RHESSI. However, NoRH and NoRP observations have shown that energy release in cool and dense environments is also possible. Finally, recent work at submm-λ has revealed the presence of a new spectral component during flares. The origin of this component is presently unknown.

To conclude, while progress on some outstanding problems has been made, new and intriguing observational phenomena have been discovered. Future work requires joint observations across the electromagnetic spectrum as well as further progress in developing next-generation radioheliographs (e.g., the Frequency Agile Solar Radiotelescope) to supplement and to build upon the excellent work done with the NoRH.

References

Aschwanden, M. J. 1998, ApJ 502, 455
Aschwanden, M. J. 2004, ApJ 608, 554
Aschwanden, M., et al. 1997, ApJ 487, 936
Aschwanden, M. J., Schwartz, R. A., & Dennis, B. R. 1998, ApJ 502, 468
Alexander, D. 1990, A&A, 235, 431
Alexander, D., & Metcalf, T. R. 2002, Solar Phys., 210, 323
Bastian, T. S., Gopalswamy, N., & Shibasaki, K. (eds.) 1999, Solar Physics with Radio Observations, NRO Rep. No. 479
Bastian, T. S., Benz, A. O., & Gary, D. E. 1998, ARAA 36, 131

Bastian, T. S., Fleishman, G. F., & Gary, D. E. 2006, ApJ, submitted.
Bespalov, P. A., Zaitsev, V. V., & Stepanov, A. V. 1987, Solar Phys., 114, 127
Bruggmann, G., Vilmer, N., Klein, K.-L., Kane, S. 1994, Solar Phys. 149, 171
Castelli, J. P., Aarons, J., & Michael, G. A. 1967, JGR, 72, 5491
Emslie, A. G., McCaig, M. G., & Brown, J. C. 1979, Solar Phys., 63, 175
Fleishman, G. D., & Melnikov, V. F. 2003, ApJ 587, 823
Fleishman, G. D., & Melnikov, V. F. 2003, ApJ 584, 1071
Giudice, D. A., & Castelli, J. P. 1975, Sol. Phys. 44, 155
Hulot, E., Vilmer, N., & Trottet, G. 1989, A&A, 213, 383
Hulot, E., Vilmer, N., Chupp, E. L., Dennis, B. R., & Kane, S. R. 1992, A&A, 256, 273
Karlický M. & Kosugi, T. 2004, A&A 419, 1159
Kaufmann, P., Correia, E., Costa, J. E. R., Zodi Vaz, A. M. 1986, A&A 157, 11
Kaufmann, P., et al. 2000, in ASP Conf. Ser. 206, High Energy Solar Physics: Anticipating HESSI, ed. R. Ramaty & N. Mandshavidze (San Francisco: ASP), 318
Kaufmann, P., et al. 2001, ApJ 548, L95
Kaufmann, P., et al. 2002, ApJ 574, 1059
Kaufmann, P., et al. 2004, ApJ 603, L121
Kundu, M. R. 1965, Solar Radio Astronomy (New York: Interscience Publication)
i, K., & Sakurai, T. 2000, ApJ 545, 1084
133, 467
Kundu, M. R., White, S. M., Shibasaki, K., Sakurai, T., & Grechnev, V. V. 2001, ApJ 547, 1090
Lee, J., & Gary, D. E. 2000, ApJ 543, 457
Lee, J., Gary, D. E., & Shibasaki, K. 2000, ApJ 531, 1109
Lee, J., Gary, D. E., Qiu, J., & Gallagher, P. T. 2002, ApJ 572, 609
Lee, J., Bong, S.-C., & Hong, S. Y. 2003, JKAS, 36, 63
Lüthi, T., Lüdi, A., & Magun, A. 2004, A&A, 420, 361
Lingenfelter, R. E., & Ramaty, R. 1967, P&SS, 15, 1303
Marsh, K. A., & Hurford, G. J. 1982, ARAA, 20 497
McClements, K. G. 1990, A&A, 230, 213
Melrose, D. B., & Brown, J. C. 1976, MNRAS 176, 15
akajima, H., & Yokoyama, T. 2002, ApJ 570, L41
Nita, G. M., Gary, D. E., & Lee, J. 2004, ApJ 605, 528
Qiu, J., Lee, J., & Gary, D. E. 2004, ApJ 603, 335
Raulin, J.-P., et al. 2004, ApJ 592, 580
Raulin, J.-P., et al. 2004, Solar Phys. 223, 181
Shibasaki, K. 2001, ApJ, 557, 326
Somov, B., & Kosugi, T. 1997, ApJ 485, 859
Trottet, G., Chupp, E. L., Marschhaeuser, H., Pick, M., Soru-Escaut, I., Rieger, E., & Dunphy, P. P. 1994, A&A, 288, 647
Trottet, G., et al. 1998, A&A, 334, 1099
Trottet, G., et al. 2000, A&A, 356, 1067
Trottet, G., Raulin, J.-P., Kaufmann, P., Siarkowski, M., Klein, K.-L., & Gary, D. E. 2002, A&A, 381, 694
Veronig, A. M., & Brown, J. C. 2004, ApJ 603, L117
Vilmer, N., Trottet, G., & MacKinnon, A. L. 1986, A&A 156, 64
White, S. M., Kundu, M. R., Bastian, T. S., Gary, D. E., Gurford, G. J., Kucera, T., & Bieging, J. H. 1992, ApJ 284, 656
White, S. M., Kundu, M. R., Garaimov, V. I., Yokoyama, T., & Sato, J. 2002, ApJ 576, 505
White, S. M., Krucker, S., Shibasaki, K., Yokoyama, T., Shimojo, M., & Kundu, M. R. 2003, ApJ 595, L111
Yokoyama, T., Nakajima, H., Shibasaki, K., Melnikov, V. F., & Stepanov, A. V. 2002, ApJ 576, L87

Electron Acceleration and Transport in Microwave Flaring Loops

Victor F. Melnikov
Radiophysical Research Institute (NIRFI), Nizhny Novgorod 603950, Russia
meln@nirfi.sci-nnov.ru

Abstract

Nobeyama Radioheliograph has high spatial and temporal resolution at two frequencies where a nonthermal radio source is often optically thin. Such capabilities provide us with unique opportunity to get constraints on properties of mildly relativistic electrons accelerated and propagating in flaring magnetic loops. In this paper we review recent studies of Nobeyama observations concerning 1) spatial distribution of microwave brightness and spectral slope along flaring loops; 2) peculiarities of their temporal dynamics in different parts of a loop; 3) consequences of the obtained findings on spatial, spectral and pitch-angle distributions of high energy electrons.

Key words: the Sun: flares, microwave emission—particle acceleration and transport

1. Introduction

Spatial distribution of nonthermal emission along a single flare loop can bring us important information on the particle acceleration and transport. Studies of the microwave spatial distribution began in 80s using the WSRT and VLA facilities. The discovery of two kinds of microwave sources, single compact loop-top sources and double sources with their peaks located close to the conjugate magnetic footpoints (Marsh & Hurford 1980; Kundu et al. 1982; Kawabata et al. 1982; Nakajima 1983), stimulated the development of theoretical simulations of gyrosynchrotron brightness distribution along model magnetic loops (see Alissandrakis & Preka-Papadema (1984); Klein & Trottet (1984); Bastian, Benz & Gary (1998)). Later the similar studies were carried out using the Nobeyama Radioheliograph (NoRH) observations at single frequency 17 GHz (Hanaoka 1996; Nishio et al. 1997; Hanaoka 1999). They showed the existence of the double and triple radio sources associated with the footpoints of large and smaller flaring loops.

In recent years the new NoRH facilities have allowed to obtain images of solar flares at two high frequencies, 17 and 34 GHz, simultaneously with high angular ($5'' - 10''$) and temporal (0.1 s) resolution. These frequencies are remarkably higher than the usually observed spectral peak frequency, f_{peak} =5-10 GHz (Nita, Gary & Lee 2004), at which the optical thickness of gyrosynchrotron emission $\tau \approx 1$. This gives a chance to study the brightness distribution having the information on microwave spectrum slope, and, therefore, on the optical thickness in different parts of a flaring loop. Such high capabilities provide us with unique opportunity to get constraints on properties of mildly relativistic electrons accelerated and propagating in flaring magnetic loops.

Already the first reports on these two frequency observations (Melnikov et al 2001; Nindos et al 2001) gave quite unexpected results showing that at least in some events the bright looptop source is optically thin. This fact is in evident disagreement with the simulated brightness distribution of optically thin microwave emission along inhomogeneous magnetic loop. Several new studies were published during last years developing further understanding of the problem (Kundu et al. 2001; Melnikov, Shibasaki & Reznikova 2002a; Melnikov et al. 2002b; White et al. 2002; Lee et al. 2002; Lee et al. 2003; Karlicky & Kosugi 2004; Su & Huang 2004; Melnikov et al. 2005). Of special interest are new results concerning the spatial distribution and dynamics of the microwave spectral slope along flaring loops (Yokoyama et al. 2002; Melnikov et al. 2002b; Fleishman & Melnikov 2003; Zhou, Su & Huang 2005).

This paper is restricted to properties of single well resolved loop-like microwave sources. We review mainly our recent studies of Nobeyama observations concerning 1) spatial distribution of microwave brightness and spectral slope along flaring loops; 2) peculiarities of their temporal dynamics in different parts of a loop; 3) consequences of the obtained findings on spatial, spectral and pitch-angle distributions of high energy electrons. We show that detailed comparative analysis of the microwave brightness distribution along single magnetic loops using the new NoRH observations and model simulations gives us some new important constraints on the acceleration/injection mechanisms and kinetics of mildly relativistic electrons in solar flares.

2. Brightness distribution along extended flaring loops

The existence of the double and triple radio sources associated with the footpoints of flaring loops, as well as asymmetric sources, shown by Hanaoka (1996); Nishio et al. (1997); Hanaoka (1999), agrees well with the existing theoretical models of radio emission (Alissandrakis & Preka-Papadema 1984; Klein & Trottet 1984; Bastian, Benz & Gary 1998). The obvious reason of such the location is strong dependence of gyrosynchrotron intensity on

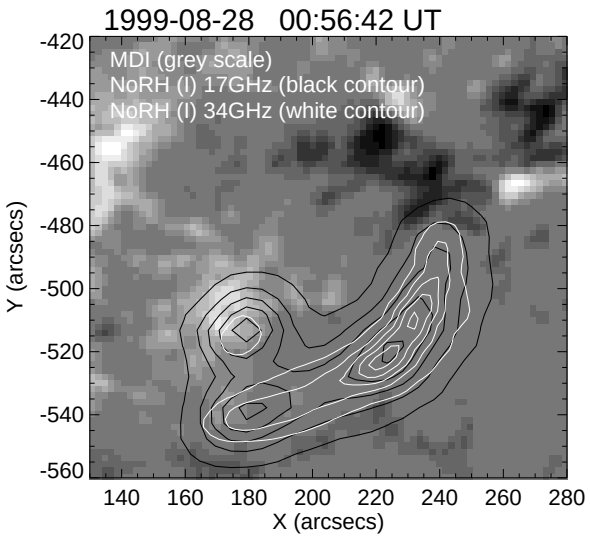

Fig. 1. SOHO/MDI photospheric magnetograms (gray scale) overlaid by contours of radio images at 0.1, 0.3, 0.5, 0.7 and 0.9 levels of the maximum brightness temperature (black for 17 GHz and white for 34 GHz). Magnetograms were obtained near the time of radio burst and were rotated to the moment of radio images.

magnetic field strength. On the other hand, the location of the brightness peak of optically thin microwave emission in the looptop is a challenge to our understanding of processes in flaring loops. In the next sections we will consider this problem in detail.

2.1. Spatial profiles of microwave brightness

For the detailed study of the spatial properties of microwave emission from a flare loop we selected only flares, which are characterized by the presence of well resolved extended single microwave sources and relatively simple time profiles both at 17 and 34 GHz. We have chosen the flares occured on 1999 August 28, 2000 January 12, March 13, 2001 October 23 and 2002 August 24. Their sizes (25-90 arc sec) exceed considerably the beam size of the Nobeyama Radioheliograph (NoRH) ($\Delta\varphi \sim 5''$ and $\sim 10''$ at 34 GHz and 17 GHz, respectively). The 1st, 3d and 4th flares occurred on the solar disk, the 2nd and 5th near the East and West limbs, respectively. The projections of the radio sources on the disk display a well developed loop-like structure at both frequencies. The limb source has an elliptic shape. Their peak brightness temperature varies from source to source from $7.0 \cdot 10^6$ K up to $1.2 \cdot 10^8$ K at 17 GHz and from $8.0 \cdot 10^5$ K up to $2.5 \cdot 10^7$ K at 34 GHz. The bursts show quite simple time profiles at 17 and 34 GHz with the duration of the main peaks in the range $\Delta T_{0.5} = 20 - 110$ s.

All the radio sources are optically thin at least at 34 GHz. Indeed, as analysis shows, the flux density spectral slope in the range 17-34 GHz is negative during the impulsive phase of the microwave bursts.

For the analysis of the microwave source structure we also used NoRH polarization maps as well as magnetographic data from SOHO/MDI. An example of overplotted NoRH and MDI maps is displayed on Fig.1. A loop like microwave source with the brightness maximum in its center is seen at 34 GHz map (white contours). Our analysis of MDI data has shown that the central part of the source is not associated with photospheric sunspots under the loop top. At the same time the MDI maps display the magnetic field enhancements of opposite polarities near two ends of the loop-like structures (supposed to be the indications of the loop footpoints).

The spatial profiles of the brightness along the loop-like radio sources at the peak time for each event are shown in the Fig.2. We can clearly see the brightness maxima to be located close to the central part of the sources. This is especially well pronounced for the highest frequency, 34 GHz, where the sources must be optically thin.

Note that the similar brightness distributions at the peak time of three limb flares observed with NoRH were obtained by Kundu et al. (2001). This proves that such kind of the brightness distribution for extended flaring loops is quite common and, therefore, should be studied in detail.

2.2. Time delays of the emission from different parts of a loop-like microwave source

In Fig.3a,b we show the flux time profiles from the regions corresponding to different parts of the loop source for the event on March 13, 2000: the loop-top (black contour in Fig.4b,c) and the north-east footpoint (white dashed-dotted contour at the same plots). Time profiles of the emission from the second footpoint are not shown here since their behavior is very similar. The size of the regions used for the flux calculations is 10" × 10".

It is well seen that the burst of emission from the loop top is delayed against the burst from the footpoint source by several seconds. This delay is more pronounced at 34 GHz than at 17 GHz. Furthermore, it is clearly seen that the time profiles of emission from the loop top are wider and their decay is slower than those from the region near the footpoint. We did not find any noticeable delay between time profiles at both frequencies from the conjugate footpoints.

The similar delays and differences in the characteristic decay time are observed for all the events from our sample (see, for instance, Fig.10 for the event of 28 Aug 1999). Note that the flux peaks from the footpoint sources are coincident in time with the flux peaks of hard X-ray emission (compare Fig.10 and Fig.11 where the vertical line indicates the moment of the hard X-ray emission peak, 00:56:42 UT).

2.3. Time delays of microwave emission at different frequencies

A comparison of the microwave time profiles of emission at the frequencies 17 and 34 GHz from the same parts of a loop-like radio source is shown on Fig.3c,d and Fig.10. One can clearly see that, for the main peak of the bursts, the emission at higher frequency, 34 GHz, is delayed against that at 17 GHz. This is well pronounced

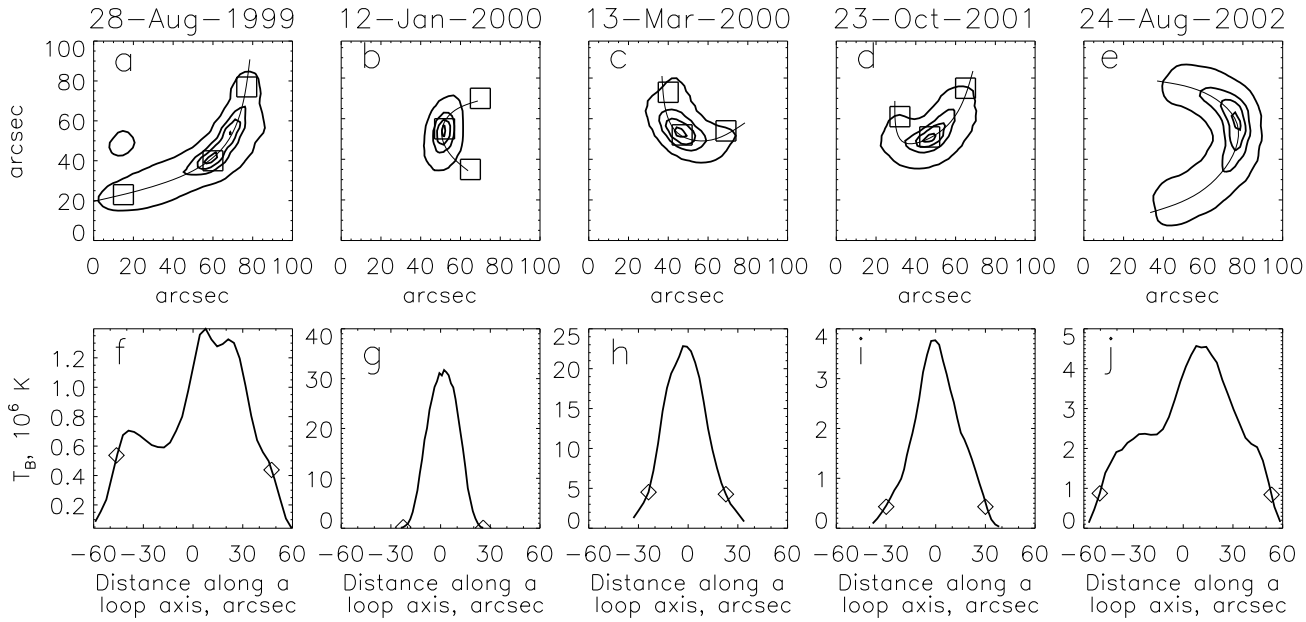

Fig. 2. *Top panel*: 34 GHz contour images of the sources at the moment of the bursts peaks (except e, this image is for the rise phase) for five events under study. Contours show 0.1, 0.5, 0.75 and 0.95 levels of the maximum brightness temperature. Thin curve shows the visible flaring loop axis. Three boxes of the size $10'' \times 10''$, two near footpoints and one near the loop-top show the areas which the flux time profiles were calculated from. *Bottom panel*: spatial distributions of radio brightness temperature at 34 GHz along a visible flaring loop axes shown on top panel for each event by thin curve. Zero position on the x-axes of bottom panel corresponds to the middle of the loop axis, calculated as a half of the axis length. Negative values corresponds to left footpoint on fig. a, c, d and lower footpoint on fig. b, e.

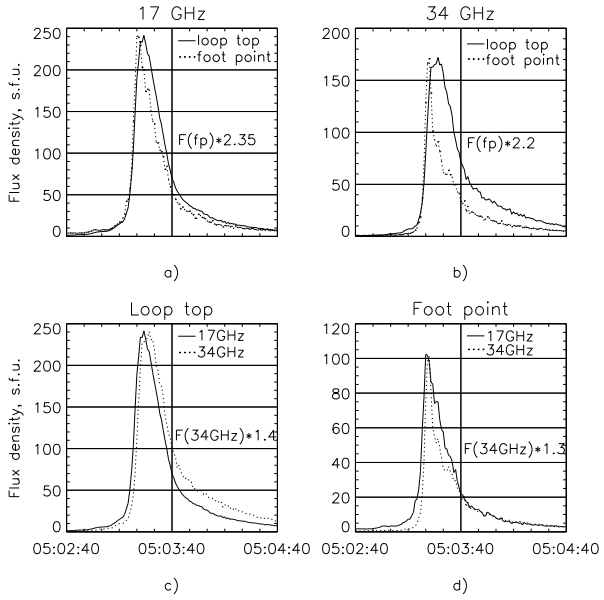

Fig. 3. NoRH time profiles of the flux densities from the 10"x10" boxes located at the loop top and the left footpoint (see Fig.4) of the flare 2000 March 13.

for the loop-top part of the sources. However there are no such delays for the footpoint parts. The footpoint emission at both frequencies reaches its maximum almost simultaneously with the peak of the corresponding hard X-ray burst (see Fig.10, 11).

2.4. Redistribution of microwave brightness along flaring loops

Further analysis of the microwave brightness distribution along the five well resolved flaring loops shows that it does not remain constant during a single peak of a burst (Melnikov et al. 2002b). In almost all the analyzed events there is the same tendency (see, for example, Fig.4). In the beginning of a burst there is always a time interval when brightness peaks (or one peak) are situated near the footpoints of a loop (both or only one). And close to the burst maximum or on the decay phase, an area near the looptop becomes most bright. A similar dynamics of brightness distribution was observed and studied in detail by White et al. (2002) in the event 1999 May 29.

To show this tendency more quantitatively, in Fig. 5 we compare the time profiles of fluxes and their ratios from the 10"x10" boxes, located near the left footpoint (a), right footpoint (c) and in the loop top (b) of the flaring loop in the event 2000 March 13. The location of the boxes are shown on Fig. 2(c). The *dotted* and *solid* lines correspond to the 17 and 34 GHz emission, respectively. The flux densities ratio F_{LT}/F_{FP} from the loop-top and

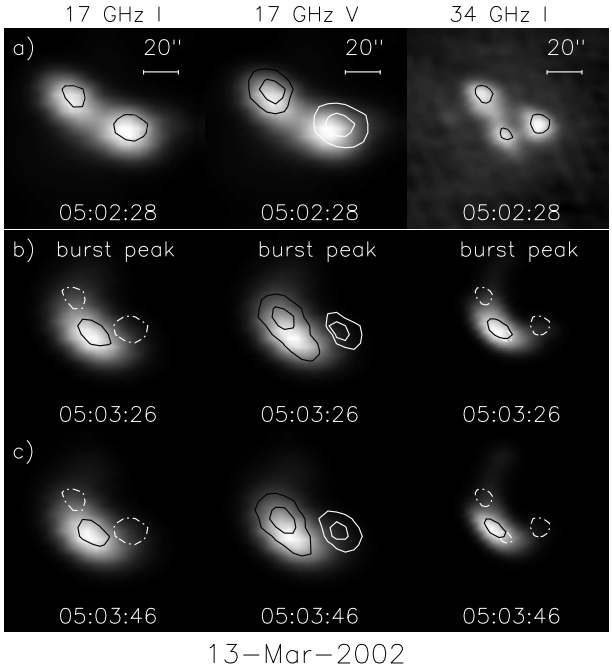

Fig. 4. NoRH images at the rise and peak phases of the flare 2000 March 13. Left and right panels: intensity at 17 and 34 GHz with the contours at the level 95% of the maximum at the current time (black solid line) and at the moment 05:02:28 UT (white dashed-dotted line). Middle panel: polarization V with the contours at the levels 40% and 80% of the maximum, black for positive V, and white for negative V.

the footpoint regions is calculated for the left footpoint (d) and for the right one (e). It is well seen that the ratios increase during the burst, especially fast on the early decay phase where maximum values of ratios reach 4-5.

Quite different evolution of the brightness distribution is realized during the limb event 2002 August 24. During the main peak of the burst, on its rising phase from 00:59:00, the southern footpoint of the loop becomes most bright at 34 GHz and remains the brightest part of the loop till the maximum at 01:00:30. At the peak time the brightness temperature reaches extremely high value at 34 GHz: $T_{Bmax} \approx 250$ MK. In Fig. 6a, b we can also see two other brightness peaks: one near the opposite (nothern) footpoint and one near the looptop. But they are much weaker. Only on the decay phase the looptop becomes relatively brighter then the footpoint sources which almost disappear to the moment of the valley before the second peak on the time profile (Fig. 6c, d). During the decay the brightness temperature in the southern footpoint source decreases by 5 times, and in the looptop only by 20%.

It is worth to note that during the main peak, when the total flux changes by 20-30 times, the visible size of the microwave flaring loop has almost not changed. It means that the emission flux changes entirely due to changes in number of mildly relativistic electrons in the loop but not in the area or volume of the source. More or less similar situation was observed for other flares from our set.

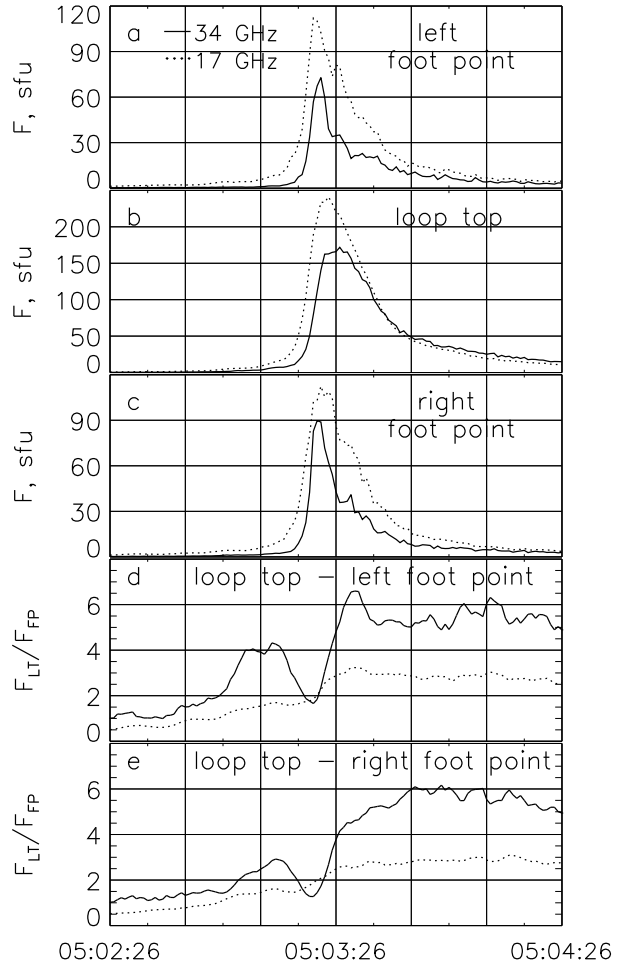

Fig. 5. NoRH time profiles of the flux densities from the 10"x10" boxes, located at the left footpoint (a), right footpoint (c) and in the loop top (b) of the flare 2000 March 13. The flux densities ratio F_{LT}/F_{FP} from the loop-top and the footpoint regions is calculated for the left footpoint (d) and for the right one (e).

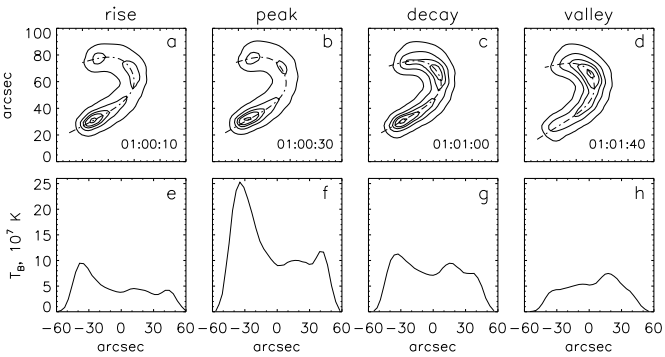

Fig. 6. Evolution of the brightness distribution during the limb event 2002 August 24.

2.5. *Comparison with the existing model predictions*

The most interesting feature of all the flares is that the peak of a microwave brightness distribution is located near the loop top at the burst maxima (except 2002 August 24).

This fact disagrees with the well known model simulations by Alissandrakis & Preka-Papadema (1984), and Klein & Trottet (1984) that predict the brightness peaks of optically thin emission to be near the footpoints of extended loops with a nonuniform magnetic field. The increase of the brightness temperature occurs because of the strong dependence of gyrosynchrotron intensity, I_f, on the magnetic field strength, B, that is expected to be larger near the feet of an extended loop. For example, if the electron power law spectral index $\delta = 4$, then according to Dulk (1985)

$$I_f \propto NB^{3.4}(\sin\theta)^{2.2}, \quad (1)$$

where N is the number of nonthermal electrons, θ is the viewing angle (angle between the magnetic vector and line of sight). It follows from the model by Alissandrakis & Preka-Papadema (1984) that even if an observer looks at a loop from above, the ratio of brightness temperatures in the loop top, I_{fLT}, and at the peak near footpoints, I_{fFP}, is equal to $I_{fLT}/I_{fFP} \simeq 0.5$ for the magnetic field difference $B_{LT}/B_{FP} = 1/2$. Note that the brightness peak near a footpoint is localized above the layers of strong chromospheric absorption, in the region where the view-angle $\theta \ll 90^\circ$, but is still not too small.

The striking fact is that the brightness peak at the looptop may be also observed for limb flares. For a limb loop which plane is almost perpendicular to the line of sight, $\theta = 80 - 90^\circ$, like for the events 2000 January 12 and 2002 August 24 from our set, the ratio is expected to be much lower for the same difference in magnetic strength: $I_{fLT}/I_{fFP} \sim 0.1 - 0.2$. As can be seen in Fig.2 (and also from the analysis of the limb events by Kundu et al. (2001); White et al. (2002)) the observable ratios at the highest frequency 34 GHz are just opposite: $I_{fLT}/I_{fFP} \sim 3 - 20$.

In the frame of the existing models such a strong increase of the brightness near the loop top is not possible to explain with usual assumptions on physical conditions in a flaring loop.

The possibility to have a hump in brightness near the loop top due to the effect of optically thick emission (Preka-Papadema & Alissandrakis 1992; Bastian, Benz & Gary 1998) is ruled out in our case since for all the events under study the frequency spectral index between 17 and 34 GHz is negative and, therefore, the microwave emission from the loops is optically thin at least at 34 GHz.

For loops near the solar disk center where the viewing angle θ is small near the footpoints the following two assumptions can make the loop top brighter than the footpoints. The first is constant magnetic field along the flaring loops (see Petrosian 1982 and Eq.(1)). The second is considerable transverse pitch-angle anisotropy of emitting electrons (Fleishman & Melnikov 2003; Fleishman 2005). The first assumption is problematic since the constancy of magnetic field strength along a loop suggests no trapping effect in contrast with our observations of well pronounced time delays (see sections 2.2- 2.3) in the analyzed events. The second assumption looks very probable. It is supported by observations of the spectral steepening toward footpoints that is also may be a consequence of the anisotropy (see section 3), as well as by the model simulations of electron distributions in flaring loops (see sections 2.6, 2.7).

For loops close to the limb with their plane almost perpendicular to the line of sight, the effects of both mentioned assumptions are too small to explain the observable ratios I_{fLT}/I_{fFP} and the shape of spatial profile along a loop (Kundu et al. 2001; White et al. 2002; Fleishman & Melnikov 2003).

2.6. Distribution of high energy electrons along a flaring loop.

We have to notice that the existing model simulations were made for the homogeneous distribution of energetic electrons along a loop. This assumption may strongly deviate from the reality. Indeed, the existence of delays (section 2.3) between the higher and lower frequency and hard X-ray intensity time profiles is an evident indication of electron trapping in microwave sources (Melnikov 1994; Melnikov & Magun 1998). The delays (section 2.2) between microwave emissions from the looptop and footpoints as well as longer decay of the emission from the looptop are a strong evidence of the trapping and accumulation of high energy electrons in the upper part of flaring loops.

A strong relative enhancement of energetic electron density near the looptop can eliminate the contradiction between the observations and the model predictions (Melnikov, Shibasaki & Reznikova 2002a). Under this assumption we can easily derive the magnitude of the electron number density enhancement from Eq.(1) and the observed ratios I_{fLT}/I_{fFP} mentioned in Section 2.5. The corresponding difference in the number densities in the loop top and footpoints falls in the range $N_{LT}/N_{FP} \sim 10 - 100$.

To illustrate this idea, Fig.7 displays three types of normalized spatial distributions along a loop. On the left hand the number density (dashed line) and column number density (solid line) electron distributions, and magnetic field distribution (dotted line) are shown. These types of electron spatial distributions are obtained in the collisionless case when the first adiabatic invariant constancy along a magnetic field line with nonuniform strength $B(s)$ is fulfilled: $[1-\mu^2(s)]/B(s) = const$, and the corresponding electron pitch-angle distributions in the loop center are taken to be (a) beam-like $\phi(\mu) = exp[-(1-\mu^2)/\mu_\parallel^2]$, with the beam width along magnetic field $\mu_\parallel = 0.3$, (b) isotropic (with taking into account the loss cone), and (c) pancake-like $\phi(\mu) = exp[-\mu^2/\mu_\perp^2]$, with the beam width transverse to magnetic field $\mu_\perp = 0.4$, where $\mu = cos\alpha_0$, α_0 - pitch-angle in the loop center.

The corresponding gyrosynchrotron intensity distributions along the model loop in optically thin regime (at 34 GHz) are shown on the right-hand panels of Fig. 7. The emission is calculated using the exact formalism (Ramaty 1969; Fleishman & Melnikov 2003). It is sup-

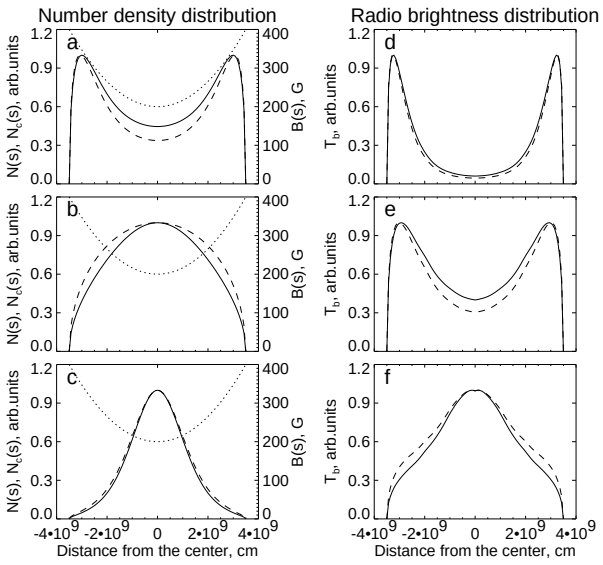

Fig. 7. Normalized spatial distributions along a loop (Melnikov et al. 2002a). Left column: number density (dashed line) and column number density (solid line) for the beam-like (a), loss-cone (b), and pancake (c) electron pitch-angle distributions; magnetic field distribution is shown by dotted line. Right column: corresponding gyrosynchrotron intensity in optically thin regime (at 34 GHz).

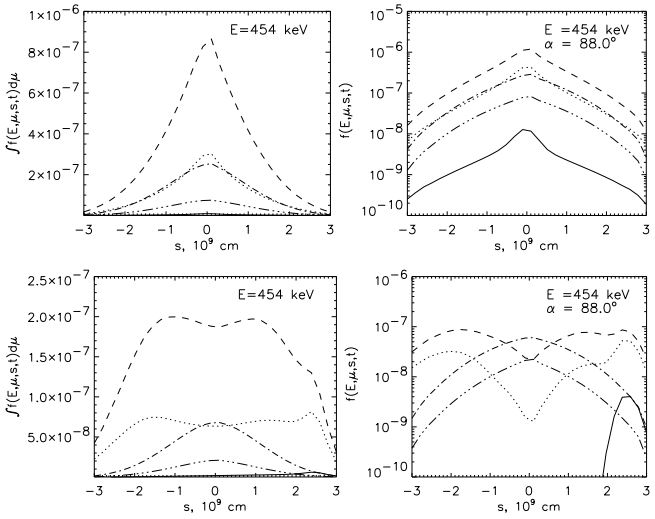

Fig. 8. Results of the model simulations using the Fokker-Planck equation (Gorbikov & Melnikov 2005). The distribution functions for the rising phase of injection are shown by solid ($t = 0.2$ s), dotted ($t = 1.7$ s) and dashed ($t = 3.25$ s) lines, and for the decay phase by dot-dashed ($t = 7.1$ s) and dot-dot-dot-dashed ($t = 10$ s) lines. Top panel represents the time evolution for Model 1 (the maximum of injection function is located in the center of the trap, $s = 0$), and bottom panel for Model 2 (the maximum of injection function is located near the foot, $s = 2.4 \times 10^9$ cm). On the left: the electron distribution function is integrated over all μ and displayed in linear scale. On the right: the distribution function is shown only for electrons with pitch-angle $\alpha = 88^o$.

posed that electrons have a power law energy dependence: $g(E) = g_0 E^{-\delta}$; the model loop is located close to the limb and the viewing angle $\theta = 80^o$. Two strong peaks of radio emission are observed for the beam-like and even for the loss-cone distribution, while the well defined peak of the number density exists in the loop center (see Fig.7a-d,b-e). Only in the case of the pancake distribution we can get a pronounced radio brightness peak at the center of a limb loop (Fig.7c-f). A degree of brightness concentration to the loop center (the ratio I_{fLT}/I_{fFP}) can vary in wide range depending on the parameter $\mu_\perp$ of the Gaussian distribution function.

2.7. Dynamics of electron spatial distribution

To understand the origin of peculiarities of microwave brightness distribution and its dynamics along different flaring loops we do modeling of the time evolution of electron spatial distribution along a magnetic loop by solving the non-stationary Fokker-Planck equation under different assumptions on the physical conditions in the loop and for different positions of the injection site (loop top, loop foot).

We consider the non-stationary Fokker-Planck equation in the form (Hamilton et al. 1990), which takes into account Coulomb collisions and magnetic mirroring:

$$\frac{\partial f}{\partial t} = -c\beta\mu\frac{\partial f}{\partial s} + c\beta\frac{dlnB}{ds}\frac{\partial}{\partial \mu}\left[\frac{1-\mu^2}{2}f\right]$$

$$+\frac{c}{\lambda_0}\frac{\partial}{\partial E}\left(\frac{f}{\beta}\right) + \frac{c}{\lambda_0\beta^3\gamma^2}\frac{\partial}{\partial\mu}\left[\left(1-\mu^2\right)\frac{\partial f}{\partial\mu}\right] + S, \qquad (2)$$

where $f = f(E, \mu, s, t)$ is electron distribution function of kinetic energy $E = \gamma - 1$ (in units of mc^2), pitch-angle cosine $\mu = cos\ \alpha$, distance from the flaring loop center s, and time t, $S = S(E, \mu, s, t)$ is injection rate, $\beta = v/c$, v and c are electron velocity and speed of light, $\gamma = 1/\sqrt{1-\beta^2}$ is Lorentz factor, $B = B(s)$ is magnetic field distribution along the loop, $\lambda_0 = 10^{24}/n(s)ln\Lambda$, $n(s)$ is plasma density distribution, $ln\Lambda$ is Coulomb logarithm. We conducted our numerical calculations for two cases using the method developed by Gorbikov & Melnikov (2005). In the first case (Model 1) the source of high energy electrons is located in the magnetic trap center $s = 0$, and in the second one (Model 2) near a trap foot $s = 2.4 \times 10^9$ cm. In both models the trap (loop) is symmetrical and its half-length is 3×10^9 cm and magnetic mirror ratio $B_{max}/B_{min} = 5$. Plasma density is homogeneous along the loop with $n(s) = 2.5 \times 10^{10}$ cm^{-3}. The injection function $S(E, \mu, s, t)$ is supposed to be a product of functions dependent only on one variable (energy E, cosine of pitch-angle μ, position s, and time t):

$$S(E, \mu, s, t) = S_1(E)S_2(\mu)S_3(s)S_4(t), \qquad (3)$$

where the energy dependence is a power law $S_1(E) = (E/E_{min})^{-\delta}$, $E_{min} = 30$ keV, with spectral index $\delta = 5$; pitch-angle distribution is isotropic $S_2(\mu) = 1$; time dependence is Gaussian $S_4(t) = exp[-(t - t_m)^2/t_0^2]$, $t_m = 2.5$ s, $t_0 = 1.4$ s; spatial distribution is also Gaussian. For Model 1: $S_3(s) = exp(-s^2/s_0^2)$, and for Model 2: $S_3(s) = exp[-(s - s_1)^2/s_0^2]$, where $s_0 = 3 \times 10^8$ cm, $s_1 = 2.4 \times 10^9$ cm.

The results of the model simulations are presented in Fig. 8 where one can see the time evolution of electron number density along the loop for electrons with energy $E = 454$ kev.

It follows from Fig. 8 that for the case of Model 1 the shape of the spatial distribution does not change much with time. During all the injection phases the distribution remains similar, with the peak located at the looptop. The simulation also reveals strong perpendicular anisotropy of the electron pitch-angle distribution in the loop. The degree of electron concentration near the looptop is strong enough to produce a peak of the microwave brightness distribution (compare with Fig. 7).

In the case of Model 2, the shape of the spatial distribution changes with time dramatically forming a sequence of distributions from double-peak in the beginning to single peak on the decay phase. The comparison with Fig. 7 shows that such distributions should produce two well pronounced radio brightness peaks near the footpoints in the beginning and maximum phases of a burst, and the brightness peak at the loop top in the decay phase of the burst.

2.8. Constraints on the particle acceleration/injection and kinetics

The findings considered above put some constraints on the particle acceleration/injection and kinetics of high energy electrons in flaring magnetic loops.

It follows from our analysis that the looptop peak of the electron distribution on the maximum phase of a burst may be produced if the injection region is located near the loop top. The injected pitch-angle distribution should be isotropic or anisotropic of the pancake type. Such kind of injection is considered in some acceleration/injection models (Somov and Kosugi (1997); Fletcher (1999); Petrosian et al. (2002)). Recently Jakimiec (2002), Somov & Bogachev (2003) and Karlicky & Kosugi (2004) developed models which consider a magnetic trap collapsing after reconnection and providing conditions for the betatron acceleration of electrons transverse to magnetic field lines. On the other hand, there are models suggesting the DC-electric field acceleration along the axes of a twisted loop or the stochastic MHD-turbulent cascade acceleration, in which the acceleration occurs along the magnetic field lines (see for a review Miller et al. (1997), Aschwanden (2002)). Our simulations show that this type of injection can not produce microwave brightness peak in the looptop during the main phase of injection. However, we can not exclude the chance of the looptop source formation due to pitch-angle scattering and accumulation of trapped electrons in the top part of a loop on the decay phase.

The results of sections 2.6 and 2.7 show that microwave brightness peaks near the footpoints of a loop is easy to get if the injection region is located near one of the footpoints. This conclusion is quite general, simulations reveal that it works for any pitch-angle distribution of injected electrons. It means that the acceleration mechanism itself is not very important, the main thing here is the position of the acceleration/injection region. We can conclude that in cases when microwave flaring loops show brightness maxima near footpoints (like for the event 24 August 2002 or the events observed by Hanaoka (1996); Nishio et al. (1997); Hanaoka (1999)), the acceleration may take place in the loop leg close to a footpoint. We have to note, however, that this explanation is not unique. The footpoint brightenings could be observed even if the acceleration takes place in the looptop. But in this case the injection should occur preferably along the loop axes ("beam-like" injection). To distinguish between the two possibilities we have to involve some other observational properties of the microwave flaring loop. For this some further detailed investigations are needed. A more rigid set of constraints can be obtained from a study of spatial/spectral dynamics of microwave/HXR-emissions.

3. Spectral properties of the microwave emission in flaring loops

Spectral features of mildly relativistic electrons accelerated in solar flaring loops can be studied using observations of their optically thin gyrosynchrotron microwave emission which spectrum can usually be described by the power law:

$$F_\nu \propto \nu^\alpha, \tag{4}$$

where F_ν and ν are the flux density and frequency, respectively.

One of the important findings related to this topic is the dynamic flattening of the frequency spectrum during the rise and decay phases of impulsive bursts in the cm-mm wavelengths (Melnikov & Magun 1998). In the majority of events such the spectral flattening on the decay phase of bursts is accompanied by the simultaneous spectral softening of the corresponding hard X-ray emission (Melnikov & Silva 2000). This striking difference in the spectral behavior was interpreted as the natural consequence of the non-stationary "trap+precipitation" model, which takes into account the energy spectrum hardening of trapped electrons due to Coulomb collisions as well as the difference between the spectral evolutions of injected/directly precipitated and trapped electrons. On the other hand, Lee & Gary (2000) have shown that the evolution of the pitch-angle distribution of non-thermal electrons in a flaring loop can play an important role in the interpretation of the microwave spectral flattening.

Till recently studies of the spectral evolution of optically thin microwave emission of solar flares were carried out for the full Sun observations without any spatial resolution. One has got only the spectral relationships averaged over a whole source. Consequently, the physical models of a radio source were quite simplified. They considered the electron energy spectral evolution in a flare loop as a whole not taking into account possible inhomogeneity of both magnetic field and plasma density along the loop. Evidently, a study of microwave spectral evolution in different parts of a flare loop on the base of observations with a good spatial resolution may provide us by new, additional information. This information may help us to de-

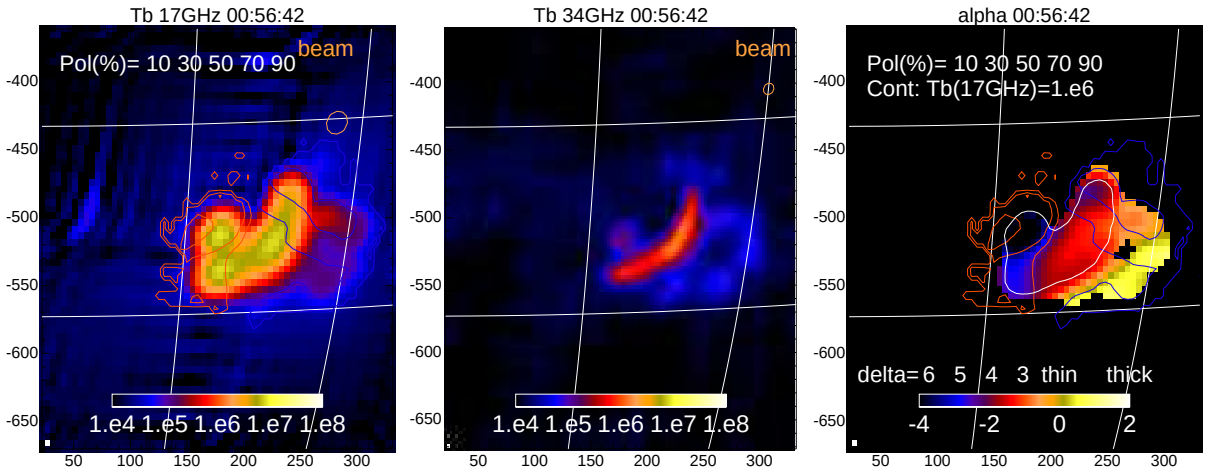

Fig. 9. Intensity and spectral slope distributions along the extended flaring loop in the event 28 August 1999 (Yokoyama et al. 2002). Left and middle panels: Microwave intensity (brightness temperature) map at 17 and 34 GHz obtained by NoRH in unit of Kelvin (color bar for the levels). Red and blue contours on the left panel indicate the polarization degree at levels of 10, 30, 50, 70, and 90 %. Beam size at half level of the peak intensity is shown as a brown circle at the right upper corner. Right panel: Map of microwave spectral slope α. The levels for each color are shown in the color bar, which is indexed below the bar with the values of α and is indexed above the bar with the power-law index of the electron distribution function δ derived by the Dulk's (1985) model. White contour indicates the level of the intensity of $T_{\rm b}$ =1 MK at 17 GHz. Blue and red contours are the same as those in the left panel.

velop a more appropriate physical model of a radio source and get better understanding of particle acceleration and transport in flare loops.

3.1. Spectral slope distribution along flaring loops

Nobeyama Radioheliograph provides us with observations at two high frequencies 17 and 34 GHz. So it gives unique possibility to study spectral slope's dynamics and its spatial distribution along flaring loops.

The parameter α described as

$$\alpha = \frac{ln(F_{34}/F_{17})}{ln(34/17)} \qquad (5)$$

characterizes the spectral slope between 17 and 34 GHz. For some extent this parameter can serve as an approximation to the frequency spectral index. This approximation is quite reasonable when the spectral peak of the emission is located at frequencies $f < 17$ GHz, which is the case for the events we discuss here. Note that due to the difference of the beam sizes at 17 and 34 GHz, the corresponding intensities F_{34} and F_{17} must be calculated after the adjustment of images at 17 and 34 GHz to the same antenna beam size. This is achieved by the convolution of the 17 GHz image with the 34 GHz beam and vice versa.

The very first study of the microwave spectral distribution along the extended flaring loop in the event 28 August 1999 (Yokoyama et al. 2002) has revealed very interesting regularity. The value of the radio spectral index is considerably higher (by approximately 1) in the footpoints than in the looptop. It is valid all the time during the main emission peak. This can be clearly seen in Fig.9 where distributions of intensity (left and middle panels) and spectral slope α (right panel) along the loop are shown. The color map of α and the color bar clearly indicate the increase of α near the footpoints of the loop. This regularity has been confirmed further in detailed studies of other extended flaring loops characterized by negative spectral slope between 17 and 34 GHz (Melnikov et al. 2002b; Zhou, Su & Huang 2005). New works by Takasaki et al (2005) and Kiyohara et al (2005) were also presented at Nobeyama Symposium 2004.

3.2. Microwave spectral evolution

A study of the microwave spectral evolution in different parts of five well-resolved loop-like radio sources (flares on 28 Aug 1999, 12 January 2000, 11 and 13 Mar 2000, 23 Oct 2001) were undertaken in the work by Melnikov et al. (2002b). For the analysis of these flares, hard X-ray data detected with the Yohkoh/HXT and the BATSE/CGRO hard X-ray spectrometers as well as magnetographic data from SOHO/MDI were also used. The frequency spectrum slope in the range 17-34 GHz during the impulsive phase of the bursts was negative throughout the sources extension. The common features found for all the events are as follows. The temporal evolution of α for different parts of a loop-like source, where it is optically thin (negative α), shows the very common behavior: a gradual increase of its value in the rise and decay phases of the bursts (for illustration see Fig. 10). This "soft-hard-harder" behavior of the microwave emission is associated with the "soft-hard-soft" behavior of the corresponding hard X-ray emission (Fig. 11). Such opposite evolution of the spectral slopes of the microwave and hard X-ray emissions on the decay phase is similar to the spectral evolutions of these emissions integrated over a whole source (Melnikov & Silva 2000).

Along with this it was found that the temporal increase of α (flattening of the microwave spectrum) during the

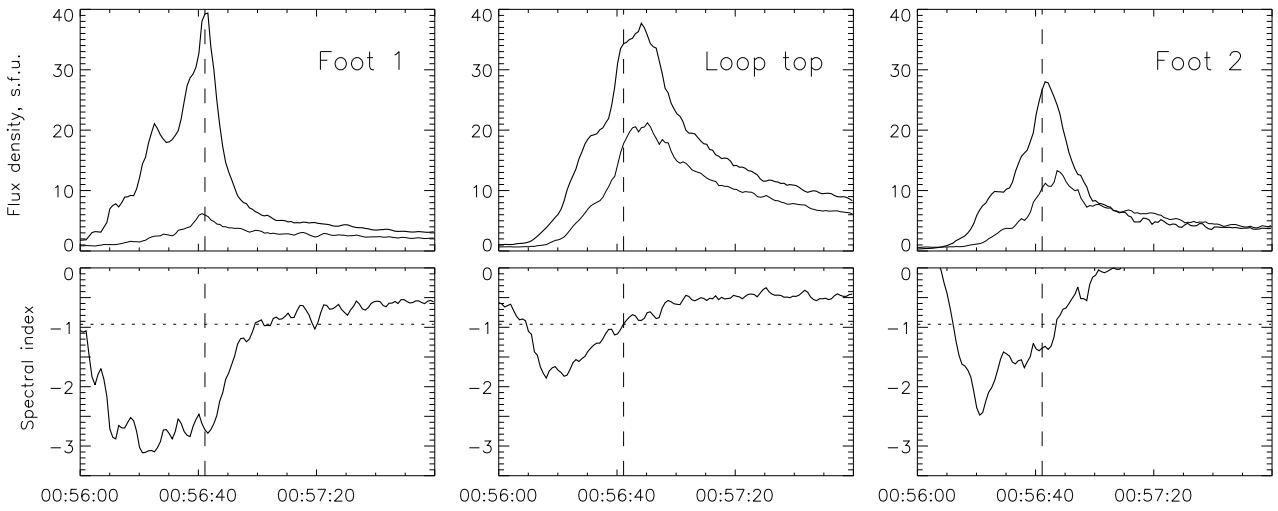

Fig. 10. Top panel: NoRH time profiles of the flux densities from the $20'' \times 20''$ boxes located at the loop top (middle panel) and the footpoints (left and right panels) of the flare 1999 August 28. Bottom panel: the corresponding time profiles of the spectral index calculated with equation (5). Vertical line indicates the moment of the hard X-ray emission peak, 00:56:42 UT.

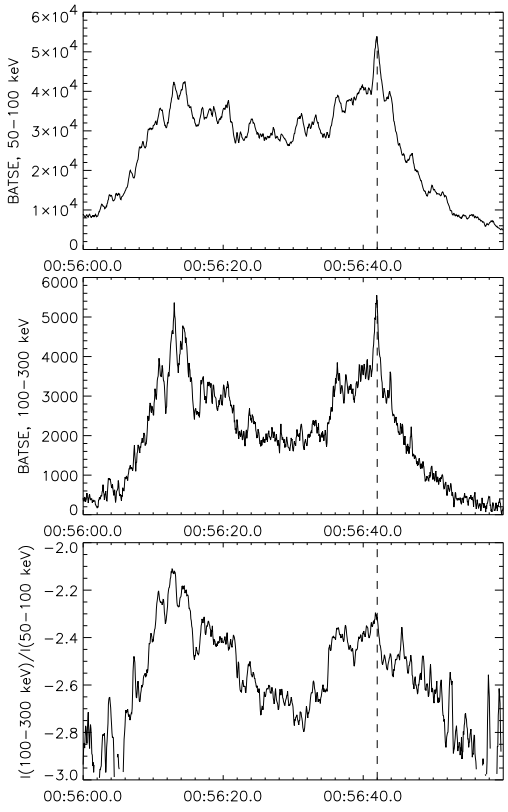

Fig. 11. Temporal profiles of hard X-ray emission during the event of 1999 August 28. Top and middle panels: Total fluxes at energy intervals $E_1 = 50-100$ keV and $E_2 = 100-300$ keV. Bottom panel: Flux ratio $I(E_2)/I(E_1)$ time profile corresponding the spectral index γ_x time profile of the hard X-ray spectrum $I(E) \propto E^{-\gamma_x}$. Vertical line indicates the moment of the emission peak at 00:56:42 UT.

decay phase goes remarkably faster in the regions close to the footpoints than near the loop top. In the event 28 August 1999 (see Fig.10), the index α changes from -2.7 to -1.0 and from -1.3 to -0.2 for the left and right loop footpoints, respectively, whereas from -1.0 to -0.6 for the looptop during the interval of 20 s after HXR-peak.

3.3. Possible physical reasons of the spectral properties

We see four possible reasons for the observed difference in spectral slopes between the looptop and footpoints regions.

The first one is associated with a perpendicular anisotropy of the electron pitch-angle distribution. Due to stronger directivity of gyrosynchrotron emission at higher frequencies the anisotropic distribution provides systematically steeper frequency spectra at quasi-parallel directions than at quasi-transverse directions (Fleishman & Melnikov 2003). This reason may well work for disk flares since for them the foot-point source is observed at a quasi-parallel direction, while the loop-top source in quasi-transverse. In the left bottom panel of Fig. 12 one can see that in the optically thin regime, at $f > f_{peak}$, the spectral index considerably (by 0.5 to 1) increases with the degree of anisotropy (change of the loss-cone angle θ_c from 0 to $\pi/2$), while it is almost constant in the case of quasi-transverse propagation (the right bottom panel).

Note that the effect of the anisotropy is expected to be less pronounced for limb flaring loops (though this depends on a specific difference between the electron pitch-angle distributions in the looptop and footpoints). Meanwhile, sometimes one observes the same spectral slope distribution also for limb flares (Melnikov et al. 2005). The following effects are free of this limitation.

The second reason is the influence of magnetic field strength on the frequency spectral slope around a fixed frequency. An increase of spectral index at lower harmonics is a general feature of gyrosynchrotron emission from a power law electron energy distribution in the case

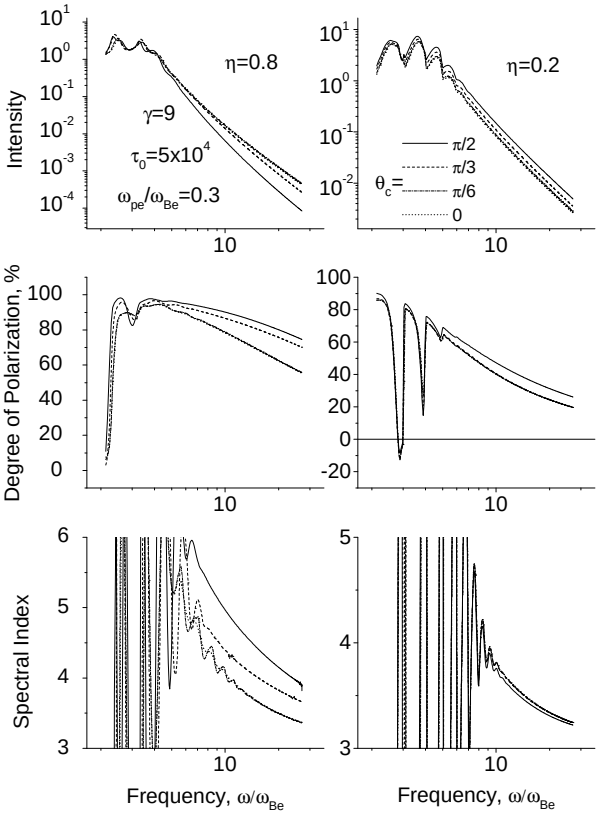

Fig. 12. The gyrosynchrotron radiation intensity, degree of polarization and spectral index vs frequency for various loss–cone angles θ_c in sin-N pitch-angle distribution (Fleishman & Melnikov 2003). The decrease of intensity and increase of spectral index with θ_c are clearly seen for the quasi-parallel propagation ($\eta = 0.8$). The increase of spectral index at lower harmonics is also well pronounced.

of low density plasma $\omega_{pe} < \omega_{Be}$. The increase from the relativistic limit ($\alpha_{rel} = (\delta - 1)/2$) that is realized at harmonic number $\omega/\omega_{Be} \geq 100$ may reach 0.5-1 as can be seen on bottom left and right panels in Fig.12. In a footpoint the magnetic field strength is expected to be higher than in the loop top. Therefore, the corresponding emission at a given frequency is generated at a lower harmonics and with a steeper spectrum.

Another effect that may greatly influence the spectral slope at frequencies $f > f_{peak}$ is Razin suppression (Razin 1960). Due to this effect the spectral index α may be considerably (by 0.5-2) smaller than even α_{rel} if the parameter ω_{pe}/ω_{Be} in the source is sufficiently high (Fleishman & Melnikov 2003). Since this parameter has to be larger in the looptop than near footpoints due to weaker magnetic field strength, we expect a spectral flattening in the looptop. A detailed diagnostics of flare plasma shows that this effect may be the main one at least for some flares (Melnikov et al. 2005). In Fig.13 one can clearly see that due to enhanced Razin suppression in the top part of the flaring loop the spectral peak shifts to higher frequencies and the spectral slope at $f > f_{peak}$ becomes flatter than in the source near a footpoint.

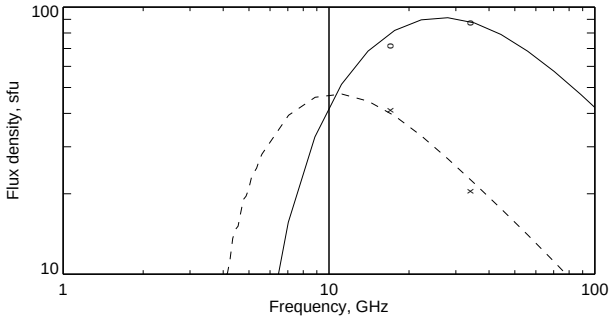

Fig. 13. Comparison of observed fluxes at 17 and 34 GHz from the loop top (circles) and footpoint (crosses) sources with 10" × 10" area and the corresponding microwave spectra calculated for these sources (Melnikov et al. 2005). The plasma density is assumed constant along the loop, $n_0 = 8 \times 10^{10}$ cm^{-3}, the magnetic field is 100 G and 200 G in the loop top and footpoint sources, respectively.

The fourth possible reason is a difference in energy spectrum slopes of electrons propagating in the looptop and footpoints regions. It is expected that the population of emitting electrons consists of two parts: trapped and directly precipitating into footpoints. The first part gives its contribution into microwave emission mainly in the looptop region while the second part in the footpoint regions. The energy spectrum of trapped electrons is supposed to be harder than of precipitating ones due to long lasting Coulomb interactions with the background plasma. Therefore, the frequency spectral slope of emission from the footpoints should be steeper. This idea may be exploited as an explanation of a better fit between electron spectra derived from microwaves and hard X-ray spectra coming from footpoints than from the looptop (see, for example, Kiyohara et al (2005)). However, it has to be checked by careful modeling with an use of the Fokker-Planck equation.

The observed temporal flattening of the microwave spectrum in its optically thin part is another interesting property. The flattening occurs throughout the loop-like source (from the loop top to the footpoints) in parallel with simultaneous softening of hard X-ray spectrum during the decay phase of bursts. Together with observed time delays at higher frequencies, these properties indicate on a different spectral behavior of low energy electrons generating hard X-ray emission and mildly relativistic electrons trapped in flaring loops and generating the microwave emission. The most probable explanation of this is that the hard X-ray emission is generated by directly precipitating electrons, and the microwaves mostly by trapped ones whose energy spectral evolution is defined by transport effects like Coulomb collisions (or wave-particle interactions) (Melnikov & Silva 2000). New properties of temporal behavior which may correct the explanation are the differences in the dynamics of flux and spectral slope of emissions coming from the top and footpoint parts of a flaring loop. They include: 1) slower intensity decay and time delays of microwave emission from the loop top part compared to the footpoint part; 2) faster

spectral flattening of emission from the footpoint part.

These spatial-temporal peculiarities, together with spatial dependence of the spectral slope, may be adjusted to each other if one takes into account the magnetic field inhomogeneity in a flaring loop. The physical reason for that is the following. The gyrosynchrotron emission at a given frequency from the loop top is generated at higher harmonics of gyrofrequency due to the lower magnetic field compared to the footpoint region. In its turn the emission at higher harmonics is generated by more energetic electrons that have a remarkably longer life time in the trap. The longer lifetime of these electrons explains naturally a) the slower intensity decay, b) the delays of emission and more gradual spectral flattening of emission from the loop top compared to the footpoints. Moreover, as it was mentioned earlier, the emission at higher harmonics also is expected to have flatter frequency spectrum that fits well with the observed flattening in the looptop.

Right now we can not exclude that some of the spatial-temporal properties of the frequency spectrum are caused by an acceleration mechanism itself. Before making firm conclusions all of them need to be carefully checked using self-consistent theoretical modeling and additional independent information on magnetic field strength, plasma density and electron energy spectrum in specific flaring loop.

4. Conclusion

Recent Nobeyama Radioheliograph observations reveal a set of new important spatial-spectral-temporal properties of microwave flaring loops. Among them are 1) the fact that the brightness distribution along flaring loops may have the maximum in the looptop even in the case of optically thin emission; 2) change of the initial distribution with brightness maxima near footpoints to the distribution with the looptop brightness maximum on the decay phase of a burst; 3) the existence of delays between the time profiles of emission from the loop top and footpoints; time delays at higher frequency; 4) the steepening of the microwave frequency spectrum along a loop from the top to its footpoints; 5) temporal flattening of the spectrum on the rise and decay phases of bursts; the faster flattening near footpoints than in the looptop on the decay phase.

Consideration of possible reasons explaining these properties reveal an importance of such effects as: 1) trapping and accumulation of accelerated electrons in the upper part of flaring loops, 2) transverse anisotropy of the electron pitch-angle distribution and its influence on the microwave intensity and spectral slope, 3) scattering of energetic electrons leading to a redistribution of electrons in a flaring loop and hardening of their energy spectrum, 4) Razin suppression and its influence on the microwave frequency spectrum, 5) dependence of the frequency spectrum slope on the magnetic field strength in a source. We should also emphasize an importance of the position of an acceleration/injection site inside a flaring loop. It greatly influences upon many observable spatial characteristics of microwave flaring loops.

So far we have not got sufficient information about the main effects which mostly responsible for the observed properties. We believe that relative significance of the listed effects may be determined only under complex, multi-wavelength and detailed case-studies of some specific flares.

All together the discussed findings put important new constraints on the particle acceleration/injection mechanisms and the kinetics of high energy electrons in flaring magnetic loops. We hope that future Nobeyama Radioheliograph observations will give us new excellent keys for solving problems of solar flare physics.

Acknowledgments

The work was partly supported by the RFBR grants No.04-02-39029, 04-02-16753. V.M. thanks the National Astronomical Observatory of Japan for the support of his visit to NRO. Author is also grateful to Drs. K.Shibasaki, V.Reznikova and S.Gorbikov for fruitful discussions, and to Drs. H.Nakajima and Y.Hanaoka for providing the corrected microwave data on the event of 2002, August 24 for use in this publication.

References

Alissandrakis, C.E., and Preka-Papadema, P. 1984, A&A, 139, 507
Aschwanden, M.J. 2002, Space Science Reviews, 101, 1
Bastian, T.S., Benz, A.O, & Gary, D.E. 1998, ARAA, 36, 131
Dulk, G. A. 1985, Ann. Rev. Astron. Astrophys., 23, 169
Fleishman, G. D., & Melnikov, V. F. 2003, ApJ, 587, 823
Fleishman, G. D., 2005 (this Proceedings)
Fletcher, L. 1999, ESA SP-448, 2, 693
Gorbikov G.D. & Melnikov V.F., 2005, *Mathematical Modeling* (in press)
Hamilton R.J., Lu E.T. & Petrosian V. 1990 ApJ, 354, 726
Hanaoka, Y. 1996, Sol. Phys., 165, 275
Hanaoka, Y. 1999, PASJ, 51, 483
Jakimiec, J. 2002, Proc. 10th European Solar Physics Meeting, Solar Variability: From Core to Outer Frontiers, Prague, Czech Republic, 645
Karlicky, M. & Kosugi, T. 2004, A&A, 419, 1159
Kawabata, K, et al. 1982, in "Proc. Hinotori Symp. on Solar Flares", eds. ... (Tokyo: ISAS), 168
Kiyohara, J., Takasaki, H., Narukage, N, Masuda, S., Nakajima, H., Yokoyama, T. 2005 (this Proceedings)
Klein, K.-L., and Trottet, G. 1984, A&A, 141, 67
Kundu, M., Schmall, E.J., & Velusamy, T. 1982, ApJ, 253, 963
Kundu, M.R., Nindos, A., White, S.M., and Grechnev, V.V. 2001, ApJ, 557, 880
Lee, J., and Gary, D.E. 2000, ApJ, 543, 457
Lee, J., Gary, D.E., Qiu, J., Gallacher, P.T. 2002, ApJ, 572, 609
Lee, J.W., Bong, S.C, & Yun, H.S. 2003, JKAS, 36, S63
Marsh, K.A., and Hurford, G.J. 1980, ApJ, 240, L111
Melnikov, V. F. 1994, Radiophys. & Quant.Electr., 37(7), 557
Melnikov, V.F., and Magun, A. 1998, Sol. Phys.., 178, 153
Melnikov, V.F., and Silva, A.V.R. 2000, ASP Conf. series, 206, 371, 475

Melnikov, V.F., Shibasaki, K., Yokoyama, T., Nakajima, H., and Reznikova, V.E. 2001, Abstracts of the CESRA workshop, July 2-6, 2001, Munich, Germany
Melnikov V.F., Shibasaki K. & Reznikova V.E. 2002a, ApJ, 580, L185
Melnikov, V.F., Yokoyama, T., Shibasaki, K., and Reznikova, V.E. 2002b, ESA SP-506, 339
Melnikov V.F., Reznikova V.E., Shibasaki K. & Nakariakov V.M., 2005, A&A, 439, 727
Miller, J.A., Cargill, P.J., Emsly, A.G. et al. 1997, GRL 102, No.A7, 14, 631
Nakajima, H. 1983, Sol. Phys., 86, 427
Nindos, A., Kundu, M. and White, S. 2001, Abstracts of the CESRA workshop, July 2-6, 2001, Munich, Germany
Nishio, M., Yaji, K., Kosugi, T., Nakajima, H., and Sakurai, T. 1997, ApJ, 489, 976
Nita, G. M., Gary, D. E., Lee, J. W. 2004, ApJ, 605, 528
Petrosian, V. 1982, ApJ, 255, L85
Petrosian, V., Donaghy, T. Q., & McTierman, J. M. 2002, ApJ, 569, 459
Preka-Papadema, P., and Alissandrakis, C.E. 1992, A&A, 257, 307
Ramaty, R. 1969, AJ, 158, 753
Razin, V.A. 1960, Izv. VUZov Radiofizika, 3, 921
Somov B.V.& Bogachev S.A. 2003, Astronomy Letters, 29, 621
Somov, B.V., and Kosugi, T. 1997, ApJ, 485, 859
Su, Y.N. & Huang, G.L., 2004, Sol. Phys., 219, 159
White, S., Kundu M., Garaimov V., Yokoyama, T., & Sato J. 2002, ApJ, 576, 505
Yokoyama, T. , Nakajima, H., Shibasaki, K., Melnikov, V.F., & Stepanov, A.V. 2002, ApJ, 576, L87
Zhou, A.H. Su, Y.N. & Huang, G.L. 2005, Sol. Phys., 226, 327

MHD-Oscillations of Coronal Loops and Diagnostics of Flare Plasma

A.V.Stepanov[1], K.Shibasaki[2], Yu.G. Kopylova[1], and Yu.T.Tsap[3]

[1]*Pulkovo Observatory, St.Petersburg, Russia*
[2]*National Astronomical Observatory, Nobeyama, Japan*
[3]*Crimean Astrophysical Observatory, Nauchny, Crimea, Ukraine*

Abstract. Effects of ballooning and radial oscillations of coronal magnetic loops on the modulations of microwave and X-ray emission from flare loops are considered. The damping mechanisms of loop MHD-modes are analyzed. The method for diagnostics of flare plasma parameters using peculiarities of the microwave and X-ray pulsations is proposed. The diagnostic method was applied for two solar flares: on May 8, 1998 and August 28, 1999 observed with the Nobeyama Radioheliograph.

1. INTRODUCTION

Solar and stellar flares reveal quite often quasi-periodic modulations in optical, X-ray, and radio emission. More than 30 years ago Rosenberg (1970) proposed to associate the short-period (~1 s) pulsations of type IV solar radio bursts with the magneto-hydrodynamic (MHD) oscillations of coronal loops. Coronal magnetic loops are fundamental structures of coronae of the Sun and late type stars (Bray et al 1991; Benz et al 1998; Schrjiver et al 1999). Subsequently, Rosenberg's idea was developed by many authors (see the reviews by Aschwanden (1987, 2003)), but no convincing evidence for the validity of this approach has been found until recently. In the late 1990s, ultraviolet observations from the TRACE satellite with a high spatial resolution revealed oscillations of coronal loops in active regions (Aschwanden et al 1999), which provided a strong impetus for the rapid development of a new promising direction of research called "coronal seismology". Such a great interest is largely explained by the possibility of a further improvement in the methods for diagnosing of plasma and magnetic fields in the region of flare energy release (see, e.g. Zaitsev and Stepanov 1982,1989; Nakariakov et al 1999; Kopylova et al 2002).

It is well known that the radial fast magneto-acoustic (FMA) oscillations of coronal loops can lead to the second (0.5-5 s) oscillations of emission from solar flares (Rosenberg 1970; Zaitsev and Stepanov 1982; Kopylova et al 2002). Oscillations with a period P = 10-30 s are attributed usually to Alfven or kink modes (Zaitsev and Stepanov 1989; Qin et al 1996; Nakariakov et al 1999). At the same time, if the plasma parameter $\beta = 8\pi\kappa_B nT/B^2$ in a loop is not too small the ballooning mode can be responsible for ten-second modulation (Kopylova and Stepanov 2002). An indications on the ballooning disturbances in solar flare loops are suggested by microwave observations with the Nobeyama Radioheliograph (Shibasaki 1998), Yohkoh data (The Yohkoh HXT Image Catalogue 1998) as well as by physical models (Sakai 1982; Shibasaki 2001).

The radial and ballooning oscillations look very similar in properties, because they cause a periodic variation of the magnetic field, gas pressure, and the loop cross section. Therefore, fast sausage and ballooning mode are very important in the context of prominent modulation of flare emission. Moreover they must be strongly damped. Their Q-factor cannot be too high ($Q \leq$ 10-30) in agreement with the observational data obtained in various wavelength ranges (e.g., Asai et al. 2001). In this case the Q-factor of the FMA oscillations in flare loops is determined by electron thermal conduction (Zaitsev and Stepanov 1982). In several cases, however, ion viscosity plays a more significant role in the dissipation of these modes (Kopylova et al 2002). Consequently, the damping mechanisms for the modes under consideration should be studied additionally.

In this talk, based on the technique proposed by Zaitsev and Stepanov (1982), we determine the flare plasma parameters from the pulsation characteristics of nonthermal gyrosynchrotron and

X-ray emission. This technique is widely used to diagnose the plasma of both solar (see e.g. Qin et al 1996) and stellar (Mullan et al 1992; Mathioudacis et al 2003) flares.

In Section 2 the physical properties of the ballooning and radial modes are analyzed and the peculiarities of dispersion relations are discussed. In Section 3, we consider the damping mechanisms for the FMA oscillations of coronal magnetic loops. In Section 4 the modulation of nonthermal gyrosynchrotron emission by FMA oscillations is considered and the method for diagnosing the flare plasma using microwave and X-ray pulsation is suggested. Section 5 is devoted to the application of the proposed method.

2. BALLOONING AND RADIAL OSCILLATIONS

Ballooning mode

Two approximations (drift and MHD) can be used to describe the ballooning mode of flute perturbations. The difference between these two approaches is that in the drift approximation, the magnetization currents are disregarded, while in the MHD approximation, the displacement current is ignored by formally assuming it to be equal to zero (Tsap and Kopylova 2004). In ideal MHD, which also remains valid for a magnetized isotropic plasma (Volkov 1964), flute perturbations develop through the imbalance between the forces exerted on a plasma volume. As follows from the linearized MHD equations, the expression for the second variation of the potential energy of a system with a sharp boundary can be represented as (Meyer et al 1977):

$$\delta W = \delta W_i + \delta W_e + \oint_S \frac{\langle p \rangle}{R} \xi_n^2 dS$$

where the subscripts correspond to the change in energy inside (i) and outside (e) the magnetic configuration, while the last term describes the effects of the centrifugal force $<p>/R$, $<p> = p_e + p_i$ is the gas pressure difference, and ξ_n is the transverse displacement. It is easy to show that in the solar corona, where the radius of curvature of magnetic field lines $R >> r$ (r is the small loop radius), the curvature effects in the first two terms on the right-hand side of this equation may be disregarded; i.e. it describes the well-studied oscillations of the magnetic flux tube. If, however, the radius of curvature R is small enough and if the gas pressure difference inside and outside the loop is large, then the surface integral can play a significant role. In particular, this integral is responsible for the generation of ballooning oscillations and flute instability. We particularly emphasize that the above equation is valid only for conservative systems; i.e. it describes only the non-emitting modes. Thus, by the ballooning oscillations of coronal loops, we mean the FMA modes slightly modified by the centrifugal force (the perturbations are elongated along the magnetic field) that do not generate MHD waves in the surrounding medium. Their period, as that for the corresponding modes of the magnetic flux tube (Nakariakov et al 2003), is determined by the longitudinal loop scale. The estimates obtained in ideal MHD using the method of normal modes also provide evidence for the analogy between the flute and FMA modes. As applied to the Earth's magnetosphere, Burdo et al (2000) used the system of linear differential equations of ideal MHD in curvilinear coordinates to show that the dispersion relations for magneto-acoustic and ballooning oscillations at small values of β and the gas pressure gradient are almost identical. This suggests that the modes under consideration are similar in physical properties; in particular, the same dissipative processes must govern their damping.

Let us consider small deviations of plasma tongue having the scale $L_1 = L/N$, where $L \approx \pi R$, N is the number of plasma tongues. Small oscillation domain in the contrast of the domain of ballooning instability corresponds to the real part of the frequency: $\omega^2 > 0$. Oscillations

occur as the result of acting of two forces: the force dealing with gas pressure gradient and magnetic field line curvature $F_c \sim p/R$, and the back-ward force due to the magnetic field tension $F_t \sim B^2/R$.

The dispersion relation for the ballooning mode can be represented as (Mikhailovskii 1971):

$$\omega^2 - k_{\|}^2 c_A^2 = -\frac{p}{R\rho l} \qquad l = \begin{cases} a, & a >> \lambda_\perp \\ \lambda_\perp, & a << \lambda_\perp \end{cases} \tag{1}$$

Here $c_A = B/\sqrt{4\pi\rho}$ is Alfven velocity, $a = n\left(\partial n/\partial x\right)^{-1}$ is the typical scale of plasma density inhomogeneity across the magnetic field, $\lambda_\perp$ is the transverse scale of plasma tongue. Since the loop foot points are frozen in the photosphere, the relation $k_{||} = N\pi/L$ holds for the longitudinal component of the wave vector, where N is the number of oscillating regions that fit into the loop length L. Using Eq.(1) we determine the period of the ballooning oscillations

$$P_1 = \frac{L}{c_A}\sqrt{\frac{1}{N^2 - L\beta/(2\pi l)}} \tag{2}$$

Under typical solar flare loop condition $L \sim 10^{10}$ cm, $l \sim 10^8 - 10^9$ cm, and plasma beta $\beta \le 0.1$, we have $L\beta/(2\pi l) \le 1$. Hence the Eq. (2) for pulsation period can rewrite as

$$P_1 \approx \frac{L}{c_A N} \tag{3}$$

Radial mode

If no curved magnetic field the ballooning disturbances do not exist. In this case as the first approximation the eigen-oscillations of a coronal magnetic loop (magnetic flux tube) can be investigated using the homogeneous plasma cylinder with radius r and the length L with fixed ends. The magnetic field ***B*** is directed along the cylinder axis. Let us suppose that plasma inside the loop has density ρ_i, the temperature T_i, and the magnetic field B_i. The outside plasma parameters are ρ_e, T_e and B_e. Dispersion equation for eigen-oscillations of plasma cylinder with the frequency ω and parallel and perpendicular to the axis components of the wave vector $k_{||}$ and $k_\perp$ can be written as (Meerson et al 1978; Roberts et al 1983)

$$\frac{J_m'(\kappa_i r)}{J_m(\kappa_i r)} = \alpha \frac{H_m^{(1)'}(\kappa_e r)}{H_m^{(1)}(\kappa_e r)}. \tag{4}$$

Here $\kappa^2 = \dfrac{\omega^4}{\omega^2(c_s^2 + c_A^2) - k_{\|}^2 c_s^2 c_A^2} - k_{\|}^2, \alpha = \dfrac{\kappa_i \rho_i}{\kappa_e \rho_e}\dfrac{\omega^2 - k_{\|}^2 c_{Ai}^2}{\omega^2 - k_{\|}^2 c_{Ae}^2},$

c_s is the sound velocity, J_m and $H_m^{(1)}$ are the Bessel and Hankel functions of the first kind, $k_{//} = s\pi/L$, s = 1,2,3,… In the case of slender ($r/L << 1$) and dense ($\rho_e/\rho_i << 1$) cylinder in the axial symmetrical case (m = 0) from Eq. (4) we obtain the period of fast magneto-acoustic (sausage) oscillations, which is most effective in the context of modulation of the emission:

$$P_2 = 2\pi/\omega_2 = \tilde{r}/\sqrt{c_{si}^2 + c_{Ai}^2}, \quad \tilde{r} = 2\pi r/\eta_j, \tag{5}$$

where η_j = 2.4, 5.52, 8.65 correspond to zeros of the Bessel function $J_0(\eta)$.

3. DAMPING OF FMA OSCILLATIONS

Loop radial oscillations undergo acoustic damping caused by the emission of waves into the surrounding medium. The acoustic damping rate is (Meerson et al 1978)

$$\gamma_a = \frac{\pi}{2}\omega_2\left(\frac{\rho_e}{\rho_i} - \frac{k_{||}^{\ 2}}{k_{\perp}^{\ 2}}\right) \tag{6}$$

Here $k_\perp = \eta_j / r$. There is no damping for $\rho_e/\rho_i < k_{||}^2/ k_\perp^2 \approx r^2/L^2$, e.g. for comparatively thick loop. In this case we have total internal reflection and plasma cylinder becomes an ideal resonator. Moreover, as it follows from observations, the density of the matter inside flare loops is two to three orders of magnitude higher than its density outside (Doshek 1994). So, there is a jump of impedance for FMA waves. As a result, the acoustic damping of the FMA oscillations of coronal loops becomes insignificant and dissipative processes inside the loop play main role.

Under solar flare condition the most important damping mechanisms for FMA modes are the electron thermal conductivity and ion viscosity (Stepanov et al 2004):

$$\gamma_c = \frac{1}{3}\frac{M}{m}\frac{\omega^2}{\nu_{ei}}\beta^2\cos^2\theta\sin^2\theta\,, \tag{7}$$

$$\gamma_v = \frac{1}{12}\sqrt{\frac{M}{2m}}\frac{\omega^2}{\nu_{ei}}\beta\sin^2\theta \tag{8}$$

Here, m and M are the electron and ion masses, respectively, $\theta = \arctan(k_\perp/k_{||})$ is the angle between the magnetic field **B** and the wave vector **k**, $\omega_{Bi} \approx 9.6 \times 10^3 B$ is the ion gyrofrequency.
Effective frequency of electron-ion collisions is

$$\nu_{ei} = \frac{5.5n}{T^{3/2}}\ln\left(10^4\frac{T^{2/3}}{n^{1/3}}\right) \approx 60\frac{n}{T^{3/2}} \tag{9}$$

The study of radial (sausage) mode damping of magnetic loops in the case of $k_{||} = 0$ were performed by Kopylova et al (2002). It has been shown that the most important damping effect is ion viscosity. But for ballooning oscillations ($k_{||} \neq 0$), the result can be different because as it follows from Eqs.(7) and (8), the damping rate depends strongly on the angle θ. To decide which process is more important we compare the decrements:

$$\frac{\gamma_v}{\gamma_c} \approx \frac{4\times10^{-3}}{\beta\cos^2\theta} \tag{10}$$

For typical value of $\beta \approx 0.1$ from Eq. (10) we find that ion viscosity less important comparing the electron thermal conductivity if $\theta < 80^\circ$. As it was mentioned in Sec.2 Eqs. (7) and (8) can be used for ballooning mode also.

4. MODULATION OF GYROSYNCHROTRON EMISSION AND FLARE PLASMA DIAGNOSTICS

Both sausage and ballooning oscillations supply deep modulation of gyrosynchrotron emission of energetic electrons in a loop. Indeed, these oscillations cause changes in the magnetic field strength, and in the scale sizes of the emitting region. We will apply our diagnostics method to the flare events observed by NoRH at 17 and 34 GHz for which the optically thin gyrosynchrotron emission of non-thermal electrons is responsible.

The flux of optically thin gyrosynchrotron emission (Dulk and Marsh 1982)

$$F = \zeta \Omega d \ \propto B^{\xi} \qquad \xi = 0.9\delta - 1.22 \tag{11}$$

Here ζ is emissivity, Ω is source solid angle, d is the source depth, δ is the spectral index of energetic power-law electrons. We took into account also that due to the conservation of the magnetic flux $d \sim B^{-1/2}$, and $\Omega \sim B^{-1/2}$. Using Eq. (10) we can write the modulation depth as

$$\Delta = (F_{\max} - F_{\min})/F_{\max} = 2\xi \frac{\delta B}{B} \tag{12}$$

Here δB is the deviation of loop magnetic field during oscillations. In accordance with Eqs. (7) and (10) the Q-factor for $\theta < 80^{\circ}$ is determined by the electron thermal conductivity

$$Q = \frac{\omega}{\gamma_c} \approx \frac{2 m_e}{m_i} \frac{P \nu_{ei}}{\beta^2 \sin^2 2\theta} . \tag{13}$$

Oscillations can excite due to the rapid enhancement of the gas pressure inside a loop $\delta p \approx n \kappa_B T$ at the impulsive phase of solar flare. Hence we can get the following relation:

$$\beta \approx 2 \frac{\delta B}{B} = \frac{\Delta}{\xi} = \varepsilon , \tag{14}$$

From the formulas for periods (3) and (5), Q-factor (13) and modulation depth (14) we find the expressions for determination of temperature, density, and magnetic field of the flare loop using observation data on the pulsations of microwave emission (Table 1)

Table 1

Ballooning oscillations	Sausage oscillations
$T = 2.42 \times 10^{-8} \dfrac{L^2 \varepsilon_1}{N^2 P_1^2}$	$T = 1.2 \times 10^{-8} \dfrac{\bar{r}^2 \varepsilon_2}{P_2^2 \chi}$
$n = 5.76 \times 10^{-11} \dfrac{Q_1 L^3 \varepsilon_1^{7/2} \sin^2 2\theta}{N^3 P_1^4}$	$n = 2 \times 10^{-11} \dfrac{Q_2 \bar{r}^3 \varepsilon_2^{7/2}}{P_2^4 \chi^{3/2}} \sin^2 2\theta$
$B = 6.79 \times 10^{-17} \dfrac{Q_1^{1/2} L^{5/2} \varepsilon_1^{7/4} \sin 2\theta}{N^{5/2} P_1^3}$	$B = 2.9 \times 10^{-17} \dfrac{Q_2^{1/2} \bar{r}^{5/2} \varepsilon_2^{7/4}}{P_2^3 \chi^{5/4}} \sin 2\theta$

Here $\chi = 10\varepsilon_2 / 3 + 2$, temperature T in Kelvin degrees, density n in cm^{-3}, and magnetic field B in G.

5. APPLICATION OF DIAGNOSTIC METHOD

Let us consider as examples the effects of coronal loop oscillations on the radiation of solar flares on May 8,1998 and August 28,1999.

Single loop flare on May 8,1998

This M3.1 X-ray class event occurred in the active region NOAA 8210 with coordinates S15 W82 in the time interval 01:49-02:17 UT. Time profiles of impulsive phase of the burst in hard X-ray and radio emission is shown in Fig.1a. One can see that there is no evident time delay between

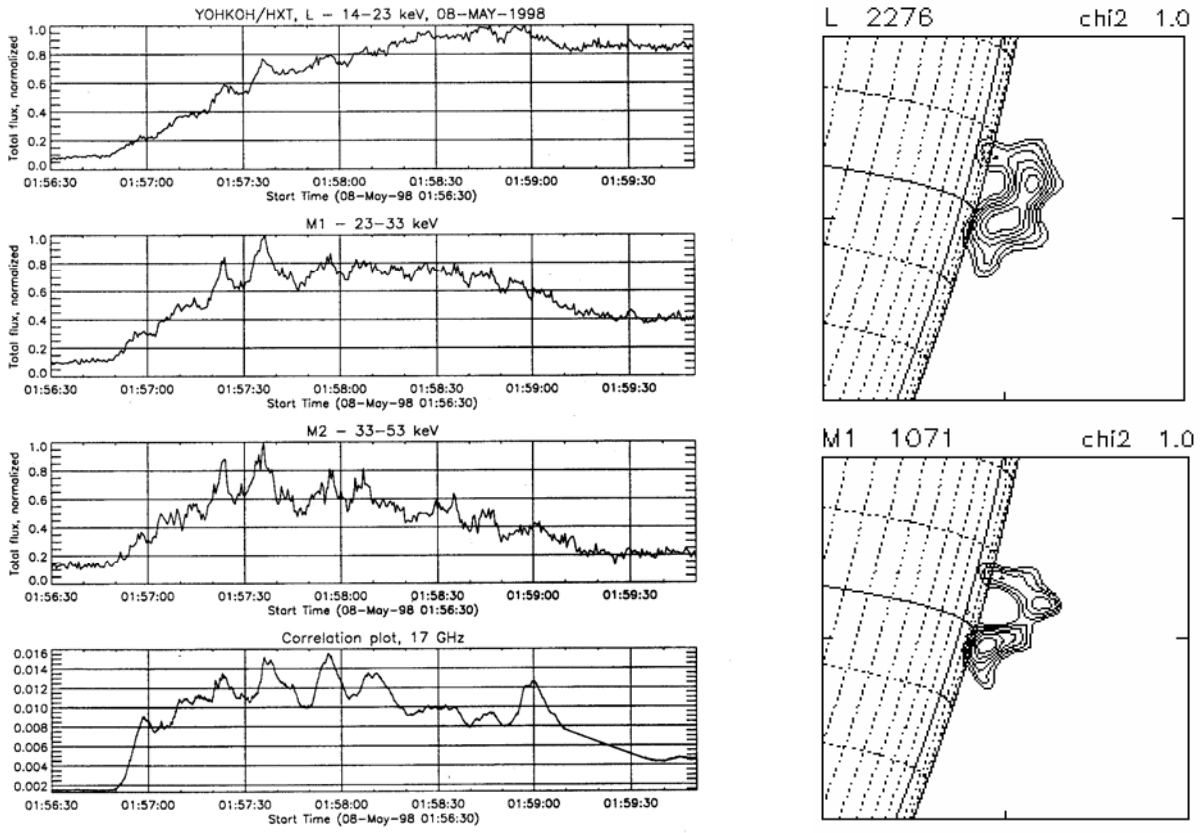

Fig. 1. (a) Time profiles for X-ray fluxes from the solar flare of May 8, 1998 in channels L (14–23 keV), M1 (23–33 keV), and M2 (33–53 keV) obtained onboard the Yohkoh satellite, and time profile of 17 GHz burst obtained with the Nobeyama Radioheliograph. (b) Images of hard X-ray source in channels L and M_1.

hard X-ray and 17 GHz pulses. Fig.1b shows that in L and M_1 channels the source has a "tongue-shape" form, which is typical for ballooning disturbances. Pulsations at microwaves and in hard X-rays can be connected with oscillations of plasma tongues. From Fig.1b it follows that four tongues ($N = 4$) are in the loop with the length $L \approx 8\times10^9$ cm. One can estimate $\mathrm{tg}\,\theta = k_\perp / k_\parallel \approx 2.25$, e.g. $\theta \approx 66^\circ$. Fourier analysis of the time profile of the impulsive phase of the flare (Fig.1a) gives the typical period $P_1 \approx 16$ s. Modulation depth of optically thin gyrosynchrotron emission is $\Delta \approx 0.3$, and pulsation quality $Q \approx 25$. Based on thick target X-ray model it is possible to estimate the spectral index of power-law electrons $\delta = 4.5$ and from Eqs. (12) and (14) the plasma beta

$\beta = \Delta / \xi \approx 0.11$. Using Table 1 we determine the temperature $T \approx 3.8 \times 10^7$ K, density $n \approx 4.3 \times 10^{10}$ cm^{-3}, and magnetic field $B \approx 230$ G in the flare loop.

Flare burst on August 28,1999

The impulsive phase of this M2.8 X-ray class solar flare was observed in the time interval 00:55-00:58 UT in the active region NOAA 8674 with coordinates S25 W11 (Yokoyama et al 2002).

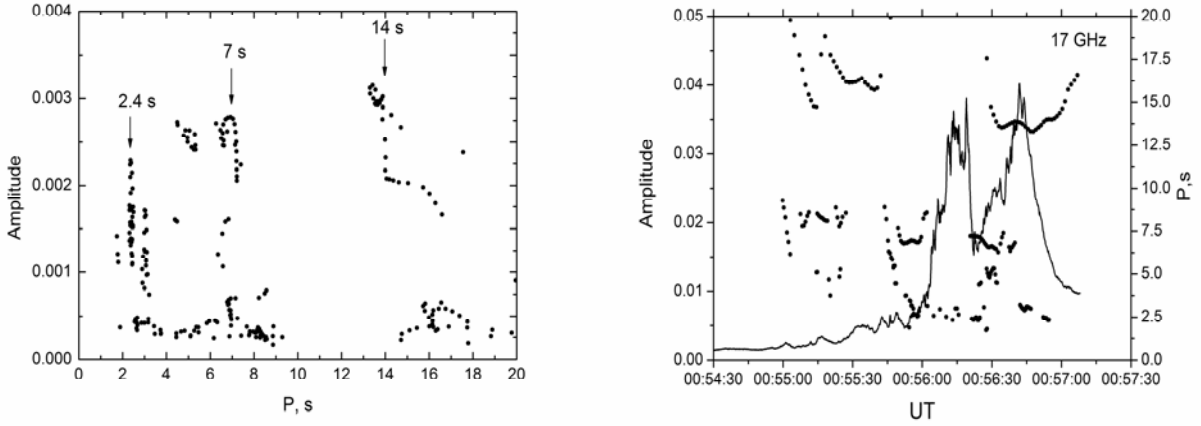

Fig. 2. (a) Dynamic spectrum of oscillations in 17 GHz flux constructed by means of a wavelet analysis for the solar flare of August 28, 1999. (b) Time profile for the emission obtained with the Nobeyama Radioheliograph, and the time variations of the oscillation period.

NoRH observations have shown that flare consists of two main sources (Yokoyama et al 2002). First compact (≤ 10") source was located near the sunspot, and the second one – a large (≥ 70") coronal loop, was just above the compact source. Time profile of radio flare reveals quasi-periodic pulsations (Fig.2). As it follows from Fig.2a the maximal amplitudes correspond to the three main branches of pulsations with the periods of about 14 s, 7 s, and 2.4 s. The following scenario can be suggested to the event of August 28,1999. The process of flare energy release can be accompanied by the coalescence of two neighboring loops through the development of ballooning instability in the compact loop. Indeed as it seen from Fig. 2b the oscillations with the period ≈ 14 s, which can be identify with the ballooning mode, has a time gap (00:55:45−00:56:30 UT) that coincides with the onset of propagation of the energetic electron front along the extended loop (Yokoyama et al. 2002). It would be natural to attribute this feature to a rise in the gas pressure and to the violation of oscillation conditions in the compact loop, which led to the development of ballooning instability and the injection of hot plasma and energetic particles into the extended loop. As soon as the compact loop was liberated from the excess pressure, the oscillations of plasma tongues resumed (Fig. 2b). We consider the 7 s oscillations as the second harmonic of the ballooning oscillations. Since the oscillations with the period ≈ 2.4 s emerged only after injection the plasma and energetic particles into the large loop (Fig. 2b), fast sausage radial mode is most likely responsible for this oscillations. The process of loop-loop interaction in this flare looks very similar to the Hanaoka events (Hanaoka 1999).

Period of ballooning oscillations for the fundamental mode ($N = 1$) of compact loop is $P_1 = L/c_A$, where $L \approx \pi \times 10" \approx 2 \times 10^9$ cm. With the extended loop radius $r \approx 3 \times 10^8$ cm for the main radial oscillation mode we have $\tilde{r} = 2.6r \approx 7.8 \times 10^8$ cm. From the observation data we find for both modes the *Q*-factors, $Q_1 = 10$, $Q_2 = 15$, the modulation depth $\Delta_1 = 0.4$, $\Delta_2 = 0.1$, and

power-law spectral indexes $\delta_1 = 5.5$, $\delta_2 = 4.0$ (Yokoyama et al 2002). Taking for example $\theta = 45^\circ$ for compact source and $\theta = 75^\circ$ for extended one from Table 1 we obtain the following plasma parameters for the extended and compact flaring loops correspondingly (Table 2).

Table 2.

Parameter	Extended loop	Compact loop
T , K	2.5×10^7	5.2×10^7
n , cm^{-3}	1.0×10^{10}	4.8×10^{10}
B , G	150	280
β	0.04	0.11

The plasma density and temperature for the flares under consideration can be estimated independently from GOES soft X-ray data (Stepanov et al 2004). For both flares the plasma temperature were estimated as $T \approx 1.5\times10^7$ K, and emission measure $n^2V \approx 10^{49}$ cm^{-3}. Taking the loop volume $V = \pi r^2 L$ for the events of May 8, 1998 and August 28, 1999 GOES data gives the plasma density 4×10^{10} cm^{-3} and 5×10^{10} cm^{-3} respectively, which do not contradict to microwave and hard X-ray diagnostics.

We have shown that proposed diagnostics method based on observations of modulation of solar flare emission and on the physical model of pulsation of flare magnetic loops is quite powerful one. This method opens new possibilities not only for determination of flare plasma parameters but also for understanding of flare physics, for example, the physics of loop-loop interaction.

A.V.S. thanks the Nobeyama Radio Observatory for hospitality. This work was partially supported by RFBR grant No 03-02-17218 and RFBR-GFEN No 04-02-39029.

References

Aschwanden M.J.: 1987, Solar Phys. 111, 113.
Aschwanden M.J., Fletcher L., Schrijver C.J. et al. 1999, ApJ. 520, 880.
Aschwanden M.J.: 2003, NATO Advances Research Workshop, NATO Sci.Ser.II, p.22
Benz, A., Conway J., Güdel M.: 1998, A&A, **331**,596
Bray R J et al 1991 *Plasma Loops in the Solar Corona*.(Cambridge Univ.Press.)
Burdo O.S., Tcheremnykh O.K., Verkhoglyadova O.P.: 2000, Izvestiya RAN, Ser. Phys. **64**, 1896
Doschek G.A.:1994, Proc Kofu Symposium NRO No 360 (eds.Enome S., Hirayama T.), 173.
Dulk G.A., and Marsh K.A.:1982, ApJ. 259, 350.
Hanaoka Y.: 1999, Proc. Nobeyama Symposium NRO No 479, (eds. Bastian T., Gopalswamy N., Shibasaki K.), , 229
Kopylova Yu.G., Stepanov A.V., and Tsap Yu.T.: 2002, Astron.Lett. 28, 783
Kopylova Yu.G., Stepanov A.V.: 2002, Izv. Glavn. Astron. Obs., 216, 555
Mathioudakis M. Seiradakis J.H., Williams D.R. et al.: 2003.A&A, 403, 1101
Meerson B.I., Sasorov P.V., Stepanov A.V.: 1978, Solar Phys. 58, 165
Meyer F., Schmidt H.U., Weiss N.O.: 1977, Mon.Not.R.Astron.Soc. 179, 741
Mikhailovskii A.B.: 1974, Theory of Plasma Instabilities (NY:Consultants Bureau)
Mullan D.J., Herr R.B., Bhattacharyya S.:1992, ApJ, 391, 256
Nakariakov V.M., Ofman L., Deluca E.E. et al. 1999, Science, **285,** 862
Nakariakov V.M., Melnikov V.F., Reznikova V.E. 2003, A&A, **412**, L7
Nobeyama Radioheliograph Catalog of Events, No 3, NRO, Japan, 2002.
Rosenberg H.:1970 A&A, 9, 165.

Sakai J.-I.: 1982, ApJ, 263,970
Shibasaki K. 1998, Proc. Nobeyama Symposium NRO No 479 (eds. Bastian T., Gopalswamy N., Shibasaki K) ,. 419.
Shibasaki K.:2001, ApJ, 557,326
Schrjiver,C.J., Title, A.M., Berger, T.E., Fletcher, L. Hurlburt, N.E.: 1999, Solar Phys.187,261
Stepanov A.V., Kopylova Yu.G., Tsap Yu.T., Shibasaki K. et al: 2004, Astron.Lett. 30, 480
The Yohkoh HXT Image Catalogue, NRO, Japan, 1998.
Tsap Yu.T. and Kopylova Yu.G.: 2004, Kinemat. Fiz. Neb. Tel, 3, 210
Volkov T.F.: 1964, Voprosy Teorii Plazmy, 4 (ed.Leontovich M.) 3
Yokoyama T., Nakajima H., Shibasaki K. et al.:2002, ApJ. 576, L87.
Zaitsev V.V. and Stepanov A.V.: 1982, Sov.Astron.Lett. 8, 132.
Zaitsev V.V. and Stepanov A.V.: 1989, Sov.Astron. Lett., 15, 66

Flare Associated Oscillations Observed with NoRH

Ayumi Asai
Nobeyama Solar Radio Observatory, Minamisaku, Nagano, 384-1305, Nagano, Japan
asai@nro.nao.ac.jp

Abstract

We present an examination of the multi-wavelength observation of a C7.9 flare which occurred on 1998 November 10. This is an imaging observation of the quasi-periodic pulsations (QPPs) obtained with *Yohkoh*/HXT and Nobeyama Radioheliograph (NoRH). We found that the Alfvén transit time along the flare loop was almost equal to the period of the QPP. We therefore suggest that variations of macroscopic magnetic structures, such as oscillations of coronal loops, affect the efficiency of particle injection/acceleration. We also report other QPP events observed with NoRH, and review some works on these flare-associated oscillations.

Key words: Sun: activity — Sun: flares — Sun: corona — Sun : radio — Sun: X-rays, gammarays

1. Introduction

Associated with solar flares, we often observe nonthermal emissions from high-energy electrons during the impulsive phases. The light curves in such hard X-rays (HXRs) and in microwaves show short-lived bursts with durations between 10 s and 10 min (Dulk et al. 1985). These bursts include smaller pulses with shorter duration, and they sometimes show periodicity. A good example of such quasi-periodic pulsations (QPPs) was seen in a flare on 1980 June 7 (Kiplinger et al. 1983; Fig. 1). Nakajima et al. (1983) and Kane et al. (1983) examined the temporal evolution of the HXR and radio spectra and the spatial structure of the flare. They suggest that the QPPs indicate a modulation of the particle injection/acceleration rate. These authors and the followers suggest that the period is comparable to the Alfvén transit time scale.

Asai et al. (2001) examined the QPP using the high resolution HXR and microwave images observed in a solar flare which occurred on 1998 November 10 in NOAA Active Region 8375 (C7.9 on the GOES scale). The flare was observed by *Yohkoh* (Ogawara et al. 1991) and the Nobeyama radio observatory, and clearly showed quasi-periodic behavior in the HXR and microwave time profiles. In the paper we compare the period of the QPP with typical time-scales of flare loops. Then, we discuss the effect of the magnetic structure on the particle injection/acceleration rate. The main parts of the work was already published by Asai et al. (2001) and Grechnev et al. (2003).

We also report the works on flare associated QPPs observed with Nobeyama Radioheliograph (NoRH). These QPP observation can contribute to a new field in the solar physics, called "coronal seismology". Coronal seismology is an efficient new tool that uses standing MHD waves and oscillations as a tool to explore the physical parameters of the solar corona. Therefore, we review these works on the flare-associated oscillations.

2. 1998 November 10 Flare

2.1. Observations

The solar flare occurred in NOAA 8375 (N19, W78) at 00:10 UT, 1998 November 10. Microwave images of the flare were taken with NoRH (Nakajima et al. 1994). The temporal and the spatial resolutions of the NoRH data are 1.0 s and 12″ (6″) for 17 GHz (34 GHz), respectively. The Nobeyama Radio Polarimeter (NoRP; Torii et al. 1979; Shibasaki et al. 1979; Nakajima et al. 1985) measured the total flux of the flare at 1, 2, 3.75, 9.4, 17, 34 and 80 GHz with a temporal resolution of 0.1 s. The HXR images were obtained with the hard X-ray telescope (HXT; Kosugi et al. 1991) aboard *Yohkoh*, with a spatial and temporal resolution of about 5″ and 0.5 s, respectively. The soft X-ray (SXR) images were also obtained with the *Yohkoh* soft X-ray telescope (SXT; Tsuneta et al. 1991). We used full resolution images in the Partial Frame Image mode with a spatial resolution of about 2.″5. We also used magnetogram obtained with the Michelson Doppler Interferometer (MDI; Scherrer et al. 1995) aboard the Solar and Heliospheric Observatory (*SOHO*; Domingo et al. 1995).

Figure 2 shows light curves in the microwave, SXR, and HXR. The top solid line is that of NoRH 17 GHz, the second dotted line is the GOES 1.0 - 8.0 Å channel, the bottom solid line is the HXT M1 band (23 - 33 keV). We can see four bursts in them, and the duration of each burst is a few tens of seconds. The fine spikes in the second burst clearly show the QPPs in both microwaves and HXRs. In this paper we investigate the quasi-periodic nature of the second burst.

2.2. Periodic Pulsation

The flare shows a double source in the microwave data. Figure 3 shows the images of NoRH/17 GHz (*grey contours*), the HXT/M1 band (*black contours*), and SXT at the second burst. We refer to the northern and brighter microwave source as the source "A" and the other one as

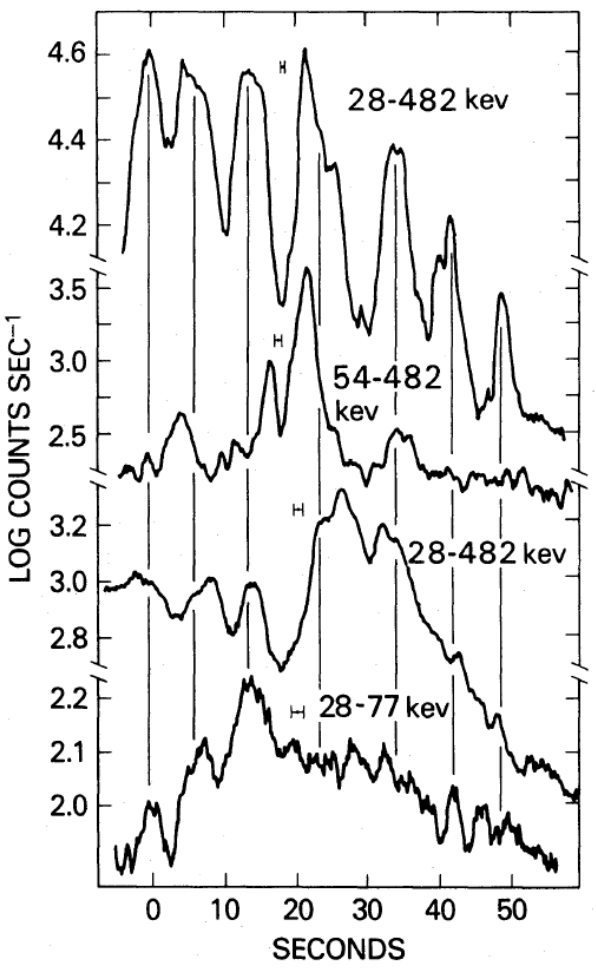

Fig. 1. The impulsive phases of the 1980 June 7 flare (Kiplinger et al. 1983).

source "B". Although the flare shows double sources in microwave, only source "A" showed the QPP, while the source "B" did not (the right panel of Fig. 4). The period calculated from the autocorrelation function of the time profiles was 6.6 s. On the other hand, in the HXR data only one source is seen near source "B", which is the "NON-oscillating" microwave source. The background soft X-ray image (*gray scale*) of Figure 3 shows a small bright kernel at the same region at source "B". We can also see a faint loop which connects the bright kernel and the radio source "A".

The left panel of Figure 4 presents the HXR and microwave time profiles for the second burst, from 00:14:20 UT to 00:14:40 UT. The QPPs are clearly seen. We also calculated the period of the QPPs in HXRs (M1 and M2 bands), and found that the period (6 s) was almost the same as those in NoRP. Analyzing the microwave spectrum using the NoRP data, we confirmed that the emission of QPP originated from optically-thin gyrosynchrotron emission from nonthermal electrons.

To clarify the relation between the microwave QPP at source "A" and the HXR QPP, we investigated in more detail the relationship of the light curves. We calculated the correlation between the time profiles of 17 GHz and the M1 band as a function of the time lag between them. The maximum correlation was found for a delay of the microwave pulsation with a time of 0.6 - 1.0 s. We suggest that the acceleration site lies near the HXR source, and that the delay time between microwaves and HXRss is explained by the flight duration of nonthermal electrons between both the sources. The projected length of the SXR faint loop is about 5.0×10^4 km. Therefore, if we assume that the velocity of the accelerated electrons is about 1.0×10^5 km s^{-1} ($\sim$ 30 % of the speed of light), then the time delay is comparable to the flight duration of the electrons between both the sources. Hence, it is reasonable to suggest that the acceleration site is located near source "B" and the HXR source, and that the microwave source "A" is generated by the traveled electrons along the faint loop. As the reason why source "B" did not show QPP, we suggest that the emission mechanism of source "B" differs from that of source "A". From the spectrum, we concluded the dominant emission mechanism of source "B" is thermal Bremsstrahlung.

3. Physical Parameters and Time Scales

Next, we derive some physical parameters of this flare site to discuss the typical timescales of the flare. Temperature, density, size, and magnetic field strength of the flare loop are needed for the estimation.

In the 1998 November 10 flare the length l and width w of the flare loop were derived from the size of flare kernel seen in the SXT images, and they are about 16,000 and 6,000 km, respectively. The temperature T and the volume emission measure EM are derived from the SXT images, by using the filter ratio method (Hara et al. 1992). The average temperature is calculated to be 9.4 MK. Moreover, assuming the volume V from the size of the flare kernel, we derived the number density n in the top of the flare loop of about 4.5×10^{10} (cm^{-3}). To measure the magnetic field strength of this region is so difficult because; (1) we can not measure the magnetic field strength of the corona directly, (2) we can not obtain the actual magnetic field strength even in the photosphere at the flare region since it is located near the north-west limb. Therefore, we roughly estimated it by calculating the potential field of the flare region based on a magnetogram on November 6 obtained with *SOHO*/MDI. The field strength on the apex of the flare loop B is estimated to be about 300 G by using the potential field extrapolation (Sakurai 1982).

As a result, the acoustic c_s and the Alfvén c_A velocities are estimated as about 360 and 3,100 km s^{-1}), respectively. Then, the acoustic transit time "along" the flare loop is $\tau_{sl} = l/c_s \approx 44$ s, and the acoustic transit time "across" the flare loop becomes $\tau_{sw} = l/c_s \approx 17$ s. Moreover, the Alfvén transit time "along" the flare loop is $\tau_{Al} = l/c_A \approx 5.1$ s, and the Alfvén transit time "across" the flare loop is $\tau_{Aw} = w/c_A \approx 1.9$ s. The values of our estimations are summarized in Table 1. Although the Alfvén transit time is sensitive to the magnetic field strength estimated above, the transit time along the flare loop (τ_{Al})

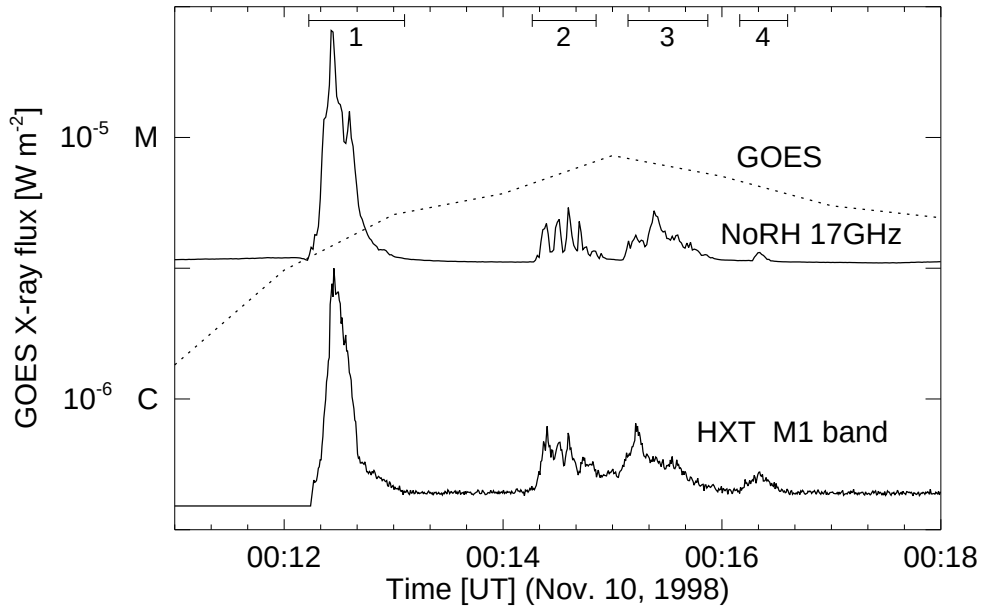

Fig. 2. Temporal evolution of the 1998 November 10 flare. From top to bottom: radio correlation plot observed at 17 GHz with NoRH; soft X-ray flux in the GOES 1.0 - 8.0 Å channel (*dotted line*); hard X-ray count rate measured in the M1 band (23 - 33 keV) of *Yohkoh*/HXT. Four bursts are identified by the numbered top bars.

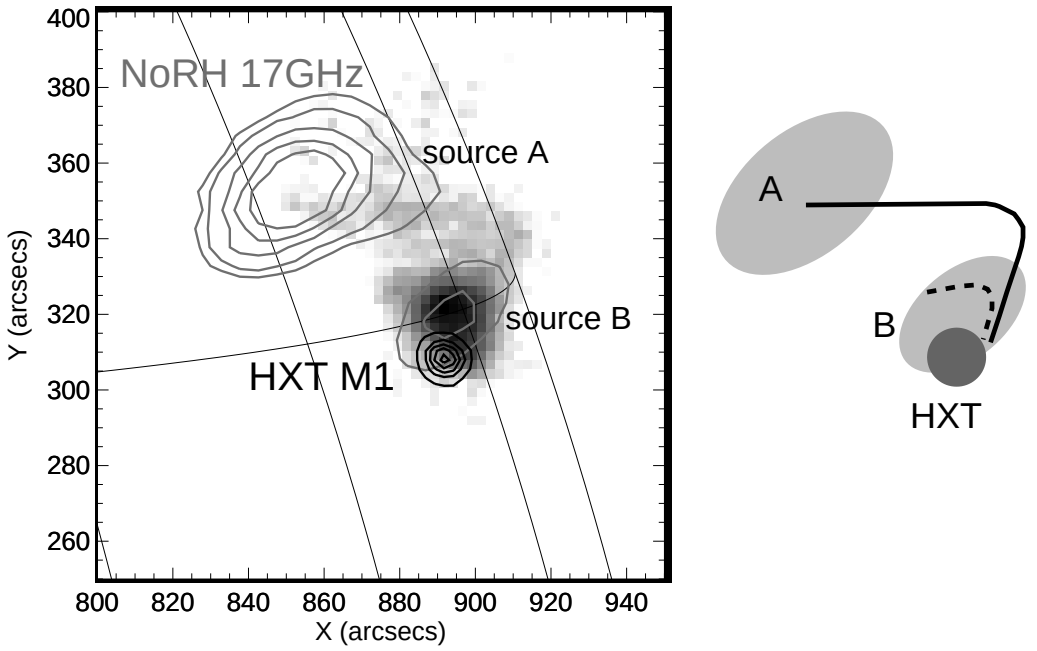

Fig. 3. Left: Coaligned images of the flare in *Yohkoh*SXT (background image), NoRH (17 GHz; *gray contour*) image, and HXT (M1 band) image (*black contour*). Right: a cartoon of this region. The NoRH sources, the HXT source, and SXT faint loop are displayed in light gray, dark gray, and black solid line, respectively. There probably are flare loops (black broken line; see section 3) in microwave source "B" (Asai et al. 2001).

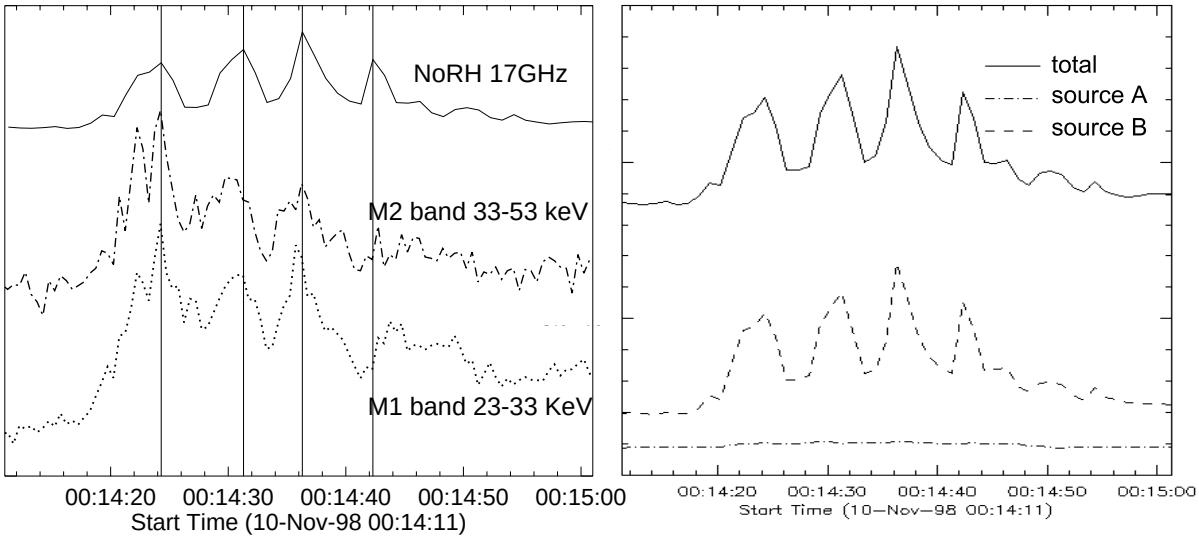

Fig. 4. Left: Light curves of the second burst. From top to bottom: radio brightness temperature observed at 17 GHz by NoRH (*solid line*); hard X-ray count rate measured in the M2 band (33 - 53 keV) (*dash dot line*) and M1 band (23 - 33 keV) (*dotted line*) of *Yohkoh*/HXT. The vertical lines show the peak times of the microwave emission. Right: Light curves of microwave brightness temperature for each emission source.

is the most similar to the observational period of the QPP (6.6 s) in microwave and HXRs.

Recently, S. Kamio (in private communication) statistically (4 events in total) examined these QPPs observed with NoRH. They also derived the physical parameters such as temperature, density, magnetic field strength, and so on, as we did. They found that in most case, the Alfvén transit time is the closest to the observed periods of the QPPs. However, there are few events which showed clear QPPs, and there are quite ambiguity on the estimation of the time scales.

4. Oscillation Mode

Now, let us move on the next topic. We found that the QPP period is comparable to the Alfvén transit time scale along the flare loop. From this, we suggest that QPPs are probably occurred by MHD fast mode oscillation. So, we review recent works about the oscillations, and examine which mode is the most reasonable to the observed QPP period.

4.1. Kink mode oscillation

Recently, the observations with the *Transition Region and Coronal Explorer* (*TRACE*; Handy et al. 1999) satellite have shown coronal loop oscillations that was induced by a flare (Nakariakov et al. 1999). The flare loops are shivering because of the disturbance of the flare. and the oscillations are well explained with kink-mode (Aschwanden et al. 1999) whose oscillation period is equal to the Alfvén transit time "along" the oscillating loops (τ_{Al}). The period of observed oscillation is about 300 s. Moreover, Miyagoshi et al. (2004) performed three-dimensional MHD simulations of the coronal loop oscillation and found that the period of the loop oscillation is also explaind with τ_{Al}.

We apply the kink-mode to the case of the 1998 November 10 flare. As we already mentioned, the observed QPP period are the most similar to the transit time along the flare loop (τ_{Al}). Therefore, the kink mode oscillation is the most reliable to explane the QPPs of the flare. However, we have to note that the oscillating loops observed with *TRACE* are much longer and have much weaker magnetic field at their apexes than the QPPs observed with NoRH. It is doubtful whether it is really possible for the flare loops to oscillate clearly and regularly in such circumstances.

4.2. Sausage mode oscillation

In meric and deci-metric ranges, we can see clear oscillation patterns in their light curves (e.g. McLean & Sheridan 1973). Figure 5 shows an example of the oscillation. Such oscillations with periods of between 0.01 and 1000 sec are sometimes observed associated with solar flares. These oscillations are well explained with the MHD sausage mode.

Nakariakov et al. (2003) reported a QPP event observed with NoRH in the 2000 January 12 event. Although the flare did not show clear QPP in the light curve, they divided the fluctuating component from the smooth component by using Fourier analyses. They also derived other physical parameters on this flare, and then, the fluctuation showed QPP with the period of about 15 second. They discussed which mode corresponds to the oscillation period, by using the physical parameters, and reported that the grobal sausage mode and the second harmonic mode are the most probable.

Table 1. Physical values of flare loop

Parameter		Value	
volume (V)		4.0×10^{27}	cm^3
length (l)		1.6×10^{9}	cm
width (w)		$\sim 6.0\times10^{8}$	cm
temperature (T)		9.4×10^{6}	K
number density (n)		4.5×10^{10}	cm^{-3}
magnetic field (B)		~ 300	G
acoustic velocity (c_s)		3.6×10^{2}	km s^{-1}
Alfvén velocity (c_A)		3.1×10^{3}	km s^{-1}
acoustic transit time	along the loop (τ_{sl})	44	s
	across the loop (τ_{sw})	17	s
Alfvén transit time	along the loop (τ_{Al})	5.1	s
	across the loop (τ_{Aw})	1.9	s

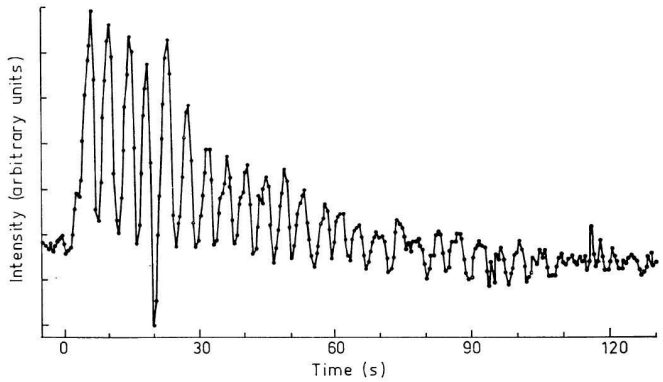

Fig. 5. Regular pulses associated with a solar radio outbursts which occurred on 1972 May 16 at a constant frequency of 230 MHz obtained with the Culgoora radio spectrograph. (McLean and Sheridan 1973).

Nakariakov et al. (2003) and Aschwanden et al. (2004) also mentioned on the QPP of the 1998 November 10 flare, and suggested that the sausage mode can explain the oscillation. However, the sausage mode must be higher harmonics, such as 3 or more. We have not answered the question why only the special harmonics number were dominant for the flare.

Although we have only 4 clear QPP events observed with NoRH, we can probably find much more QPP events, by using their method.

5. Loop Oscillation & Particle Acceleration

Finally, we discuss about the relation between the QPP and particle acceleration. The QPP periods probably show that they are generated by the MHD fast mode oscillation (kink mode and/or sausage mode). Does the oscillation of the coronal loop relate with the particle acceleration/injection?

Tajima, Brunel, & Sakai (1982) showed by numerical simulation that stored magnetic energy is explosively transformed to particle acceleration. They also suggest that the current loop coalescence instability induces the QPPs. Moreover, Tajima et al. (1987) showed that the period of the QPP is equal to the Alfvén transit time "across" the current loop (τ_{Aw}). Although these works were mainly based on the total flux, and the detailed spatial configuration of the flare that shows QPP is still unknown, their work connects the flare loop oscillation and the QPP.

Tsuneta & Naito (1998) propose that nonthermal electrons can efficiently be accelerated by a first order Fermi process at the fast shock located below the reconnection X-point. They suggest that the accelerated electrons are trapped between the two slow shocks, and that the energy injection depends on the length of the fast shock which is pinched by these slow shocks. If the reconnected (flare) loop that is located under the fast shock is oscillating, that the length of the fast shock probably varies with the loop oscillation, synchronously. Hence, we propose, under the hypothesis of the acceleration model proposed by Tsuneta & Naito (1998), that the origin of the QPP in microwaves and HXRs is the modulation of the acceleration/injection of nonthermal electrons. Moreover, we propose that the modulation is produced by the variations of macroscopic magnetic structures, for example, oscillations of coronal loops.

6. Summary & Conclusions

We investigated the impulsive phase of the flare whose time evolution showed a clear QPP in microwaves and HXRs. We found the periods of the QPP, and we estimated some typical time scales of the flare loop from the observational data. We found that the Alfvén transit time along the flare loop was close to the QPP periods in most cases.

Both the kink mode and sausage mode have possibilities to explane the oscillation. Although it is not fixed yet, if we can fix it, the QPPs can become a very useful measure for the coronal seismology. Loop oscillation probably modulates the efficiency of particle acceleration, so we should know how it works, as future works.

References

Asai, A., Shimojo, M., Isobe, H., Morimoto, T., Yokoyama, T., Shibasaki, K., Nakajima, H. 2001, ApJL, 562, L103

Aschwanden, M. J., Fletcher, L., Schrijver, C. J., Alexander, D. 1999, ApJ, 520, 880

Aschwanden, M. J., Nakariakov, V. M., Melnikov, V. F. 2004, ApJ, 600, 458

Domingo, V., Fleck, B., Poland, A. I. 1995, Sol. Phys., 162, 1

Dulk, G. A., McLean, D. J., Nelson, G. J. 1985, in Solar Radiophysics: Studies of emission from the sun at metre wavelengths, eds. McLean D. J. & Labrum N. R. (Cambridge: Cambridge University Press), 53

Grechnev, V. V.; White, S. M.; Kundu, M. R. 2003, ApJ, 588, 1163

Handy, B. N., et al. 1999, Sol. Phys., 187, 229

Hara, H., Tsuneta, S., Lemen, J. R., Acton, L. W., McTiernan, J. M. 1992, PASJ, 44, 135

Kane, S. R., Kai, K., Kosugi, T., Enome, S., Landecker, P. B., McKenzie, D. L. 1983, ApJ, 271, 376

Kiplinger, A. L., Dennis, B. R., Frost, K. J., Orwig, L. E. 1983, ApJ, 273, 783

Kosugi, T., et al. 1991, Sol. Phys., 136, 17

McLean, D. J., and Sheridan, K. V. 1973, Sol. Phys., 32, 485

Miyagoshi, T., Yokoyama, T., Shimojo, M. 2004, PASJ, 56, 207

Nakajima, H., Kosugi, T., Kai, K., Enome, S. 1983, Nature, 305, 292

Nakajima, H., et al. 1985, PASJ, 37, 163

Nakajima, H., et al. 1994, Proc. of the IEEE, 82, 705

Nakariakov, V. M., Ofman, L., DeLuca, E. E., Roberts, B., Davila, J. M. 1999, Science, 285, 862

Nakariakov, V. M., Melnikov, V. F., Reznikova, V. E. 2003, aap, 412, L7

Ogawara, Y., Takano, T., Kato, T., Kosugi, T., Tsuneta, S., Watanabe, T., Kondo, I., & Uchida, Y. 1991, Sol. Phys., 136, 10

Sakurai, T. 1982, Sol. Phys., 76, 301

Scherrer, P. H., et al. 1995, Sol. Phys., 162, 129

Shibasaki, K., Ishiguro, M., Enome, S. 1979, in Proc. of the Res. Inst. of Atmospherics, Nagoya Univ., 26, 117

Tajima, T., Brunel, F., and Sakai, J. 1982, ApJ, 258, L45

Tajima, T., Sakai, J., Nakajima, H., Kosugi, T., Brunel, F., Kundu, M. R. 1987, ApJ, 321, 1031

Torii, C., Tsukiji, Y., Kobayashi, S., Yoshimi, N., Tanaka, H., Enome, S. 1979, in Proc. of the Res. Inst. of Atmospherics, Nagoya Univ., 26, 129

Tsuneta, S., et al. 1991, Sol. Phys., 136, 37

Tsuneta, S., and Naito, T. 1998, ApJ, 495, L67

Flare Physics with the Nobeyama Radioheliograph and RHESSI

A. Nindos
Section of Astrogeophysics, Physics Department, University of Ioannina, Ioannina GR-45110, Greece
anindos@cc.uoi.gr

Abstract

In this article I review the present status of knowledge in areas of special interest for further study using solar flare observations at microwaves from the Nobeyama Radioheliograph and hard X-ray (HXR) observations from RHESSI. The most direct tracers of the electrons accelerated in a flare are the microwave and HXR emissions they produce. The combined microwave and hard X-ray data provide powerful diagnostics of the physical conditions in flaring regions and particularly the magnetic field configuration of the flare and the properties of the energetic electrons. I point out that in order to tackle better the fundamental problem of particle acceleration in solar flares, detailed comparison of the spatial and spectral data with models is needed.

Key words: Sun:corona, Sun:flares, Sun:radio radiation, Sun:X-rays

1. Introduction

A solar flare is a sudden brightening in the solar atmosphere. Typically, radiation is obsreved across virtually the entire electromagnetic spectrum and all atmospheric layers are affected. It is widely believed that the energy for a flare is stored magnetically in the corona prior to the event. The key elements of a typical flare are accelerated particles, the "evaporation" of large masses of high density plasma into coronal magnetic loops and (frequently but not always) magnetic eruptions. The acceleration process yields electrons with energies much higher than the mean energy of the thermal plasma. The most direct tracers of these electrons are the hard X-ray (HXR) and microwave emission they produce.

The launch of the Reuven Ramaty High Energy Solar Spectroscopic Imager (RHESSI) on February 5, 2002 opened up a new era in high-energy solar flare physics due its unique capabilities: it observes flares over a broad range, 3 keV to 17 MeV, i. e. from thermal X-rays to gamma-rays (Lin et al. 2002). Its new approach is to combine for the first time in HXRs high-resolution imaging with high-resolution spectroscopy. Combining RHESSI data with microwave data provides a powerful tool for further progress in flare physics. Among the various radio instruments, the Nobeyama Radioheliograph (NoRH) is the only one which is solar dedicated and provides high spatial resolution images at two frequencies (17 and 34 GHz) with subsecond time resolution for flare events (Nakajima et al. 1994).

The purpose of this article is not to give an exhaustive treatment of flare microwave and HXR emissions. There is already a number of reviews that cover all aspects of microwave flare emission (Kundu & Vlahos 1982; Alissandrakis 1986; Bastian, Benz, & Gary 1998) and HXR emission (Sakao 1994; Hudson & Ryan 1995; Aschwanden 2002). Also a review about the complementarity of microwave and HXR emission has been published by Gary (2000). Here, I will only try to give a comprehensive account of our present knowledge in areas of special interest for further study using combined NoRH and RHESSI data. To this end, I will try to convince the reader that detailed modeling is required in order to exploit the wealth of information provided by the NoRH and RHESSI data.

2. Morphology of HXR and Microwave Emissions

2.1. HXR Sources

Both HXR and microwave flare emissions come from energetic electrons. However, the emission mechanisms at these wavelength ranges are radically different. The HXRs come from bremsstrahlung and there are two general classes of models for the HXR emission from solar flares (e.g. see Hudson, Canfield, & Kane 1978; Tandberg-Hanssen & Emslie 1988; Raulin et al. 1999). In the "thin target" model, the nonthermal electrons are very effectively trapped in the corona and produce HXRs via bremsstrahlung on the ambient coronal ions: in that case the HXR photon spectral index γ is related to the electron energy spectral index δ_x by $\delta_{x,thin} = \gamma - 0.5$. In the "thick target" model, the nonthermal electrons are trapped in closed magnetic loops, where the ambient density is sufficiently low that collisions are ineffective in changing the electron energies. In this case the bulk of the HXRs are produced via bremsstrahlung when the nonthermal electrons strike the dense chromospheric material at the footpoints of the coronal loop, and

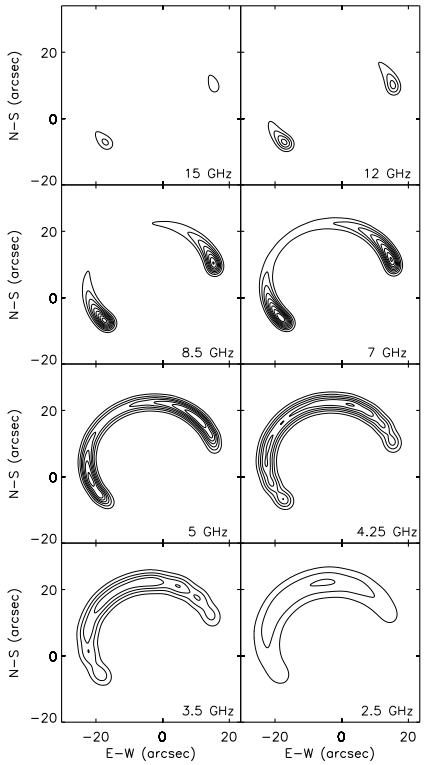

Fig. 1. Gyrosynchrotron model loop calculations at several frequencies. The model is a magnetic loop located at heliographic longitude 50° and latitude 50° north and with a 45° orientation with respect to the local north. The footpoint magnetic field strength is 700 G. The heights above the solar surface of the two lines of force that form the loop are 22″ and 9.5″. The distance between the footpoints is 36″ and the loop transverse dimension is 10″. The energy spectral index of the energetic electrons is 3 and their density is 6×10^6 cm^{-3}. The low- and high-energy cutoffs of the nonthermal electrons are 10 and 500 keV, respectively.

$\delta_{x,thick} = \gamma + 1.5$.

Using Yohkoh's Hard X-ray Telescope (HXT) Sakao (1994) has established that the dominant HXR morphology is the double source, although single compact sources or multiple components are also seen. Of the double sources for which magnetograms are available, the two sources lie on opposite sides of the magnetic neutral line. The study of simultaneous soft X-ray, H_α,and HXR images (e.g. Kosugi et al. 1992; Sakao et al. 1992) shows that the double HXR sources are located at the footpoints of flaring loops (to clarify the description, by the term "loop" I mean a collection of adjacent magnetic field lines sharing a common morphology and adjacent footpoints. Thus, a "single loop" does not mean a single field line; since magnetic field lines have no thickness, there must be infinitely many field lines in a loop of finite volume, and the field lines within the loop may have unresolved structure). Note also that the magnetically weaker footpoint is brighter in HXRs than is the magnetically stronger footpoint (Sakao 1994; Kundu et al. 1995). The above observational picture indicates that impulsive phase HXR emission is dominated by thick-target bremsstrahlung emission by nonthermal electrons. A further argument supporting the thick-target interpetation is that quantitative agreement between microwave and HXR emission during the rise phase of impulsive flares, including the numbers of electrons required (Gary 1985; Lu & Petrosian 1989; Chiuderi-Drago et al. 1998), is only possible if nonthermal thick-target radiation dominates the HXR emission.

2.2. Microwave Sources

On the other hand, the microwaves originate from the gyrosynchrotron mechanism as the energetic electrons spiral along magnetic fields in the corona. The morphology of the microwave flare emission depends on the magnetic field configuration (i.e. the geometry of the flaring region and its location on the disk) and the properties of the nonthermal electrons. In order to show how the magnetic field affects the microwave emission, in fig. 1 I present models of gyrosynchrotron loop emission for typical magnetic field and energetic electron parameters at several frequencies (similar models have been developed by Preka-Papadema & Alissandrakis 1992; Bastian, Benz, & Gary 1998). At high frequencies the emission is compact and optically thin and comes from the footpoints of the loop, and most strongly from the high-field end of the loop. At lower frequencies, the radio emission becomes optically thick and there is a tendency for more extended sources, indicating emission from the entire loop. This picture is consistent with the properties of gyrosynchrotron mechanism: the magnetic field is much stronger near the footpoints, which favors

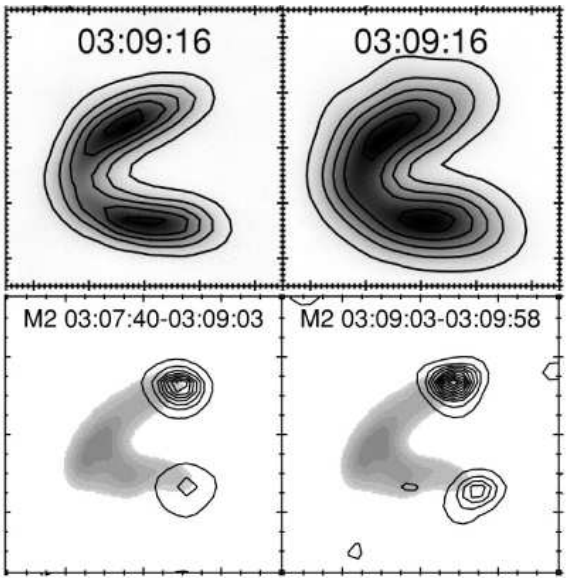

Fig. 2. Images of a flare in radio and X-rays during the impulsive phase. The top row shows radio images at 34 (left panel) and 17 (right panel) GHz total intensity with contours at 10%, 30%,...,90% of the maximum overlaid on gray-scale images of the 17 GHz total intensity. The bottom row shows Yohkoh HXT M2 channel HXR images overlaid on the gray-scale representation of the SXT image of the period 03:11:00-03:11-54 UT (from White et al. 2002).

the higher frequencies. A decrease of the frequency of observation has approximately the same effect as an increase of the magnetic field. Thus when the frequency of observation decreases, we expect to have emission not only from the footpoints but also from a significant part of the loop. Note that in fig. 1, the centroid of the radio emission moves progressively down toward the footpoints at higher frequencies. This effect has been oberved in Owens Valley Solar Array (OVSA) data studied by Wang et al. (1995; 1996). In addition to the role of magnetic field strength in radio emission, there is a strong dependence on magnetic field direction, with the emission coming most strongly from regions where the magnetic field is perpendicular to the line of sight.

As for the nonthermal electrons, Bastian, Benz, & Gary (1998) have pointed out that a magnetic loop acts as a dispersive element: at a fixed frequency higher energy electrons emit at the loop top (weak magnetic field) and lower energy electrons emit at the footpoints (strong magnetic field). This is due to the dependence of mean energy E of the gyrosynchrotron-emitting electrons on the magnetic field strength B and the spectral index of the electron distribution function δ ($E \propto B^{-(0.5+0.085\delta)}$). Furthermore, changing the parameters of the nonthermal electrons the microwave emission is affected as follows. Changing the number density has little effect in the optically thick limit but in the optically thin limit has the same effect as increasing the magnetic field. As for the electron energy cutoffs, imposing an upper limit to the electron energies present in the distribution has a strong suppression effect on radiation at high frequencies which requires very energetic electrons if the magnetic field is not strong. Increasing the low-energy cutoff has little effect on the high-frequency emission since the low-energy electrons do not radiate significantly at high frequencies, but it increases the mean energy of the electrons radiating the optically thick emission and makes it brighter.

Here a word of caution is needed: in the model of fig. 1, I have assumed that the microwave-emitting electrons have uniform density and isotropic pitch angle distribution. This is a zero-order approximation but it is justified by the fact that e.g. in a loss-cone distribution, the electrons missing are those with small pitch angles whose gyroacceleration and hence emissivity is smallest. Most of the emission is produced by the larger pitch angles, so using an isotropic distribution should not affect the results significantly. Furthermore such models with isotropic density and pitch angle distributions are able to reproduce the properties of the microwave emission of some flares *at the peak of the event*: one compares the radio observations with gyrosynchrotron model loop calculations. The best-fit model should satisfy two criteria: (1) the projection of the model loop shape on the plane of the sky should be consistent with the appearance of the flaring loop; and (2) the resulting model radio emission should reproduce both the observed fluxes and structures at the peak of the event. We have been able to derive a self-consistent model for the magnetic field and the properties of the nonthermal electrons for two events. The first was observed at 5 and 15 GHz with the VLA and additional spectral data were provided by the OVSA (Nindos et al. 2000) and the second was observed with the NoRH at 17 and 34 GHz with spectral data from the Nobeyama Polarimeter (Kundu, Nindos, & Grechnev 2004). However, there are certainly flares whose microwave emission can be interpreted only if one considers an anisotropic population of nonthermal electrons. One particular class of such flares is the events which are optically thin but their maximum

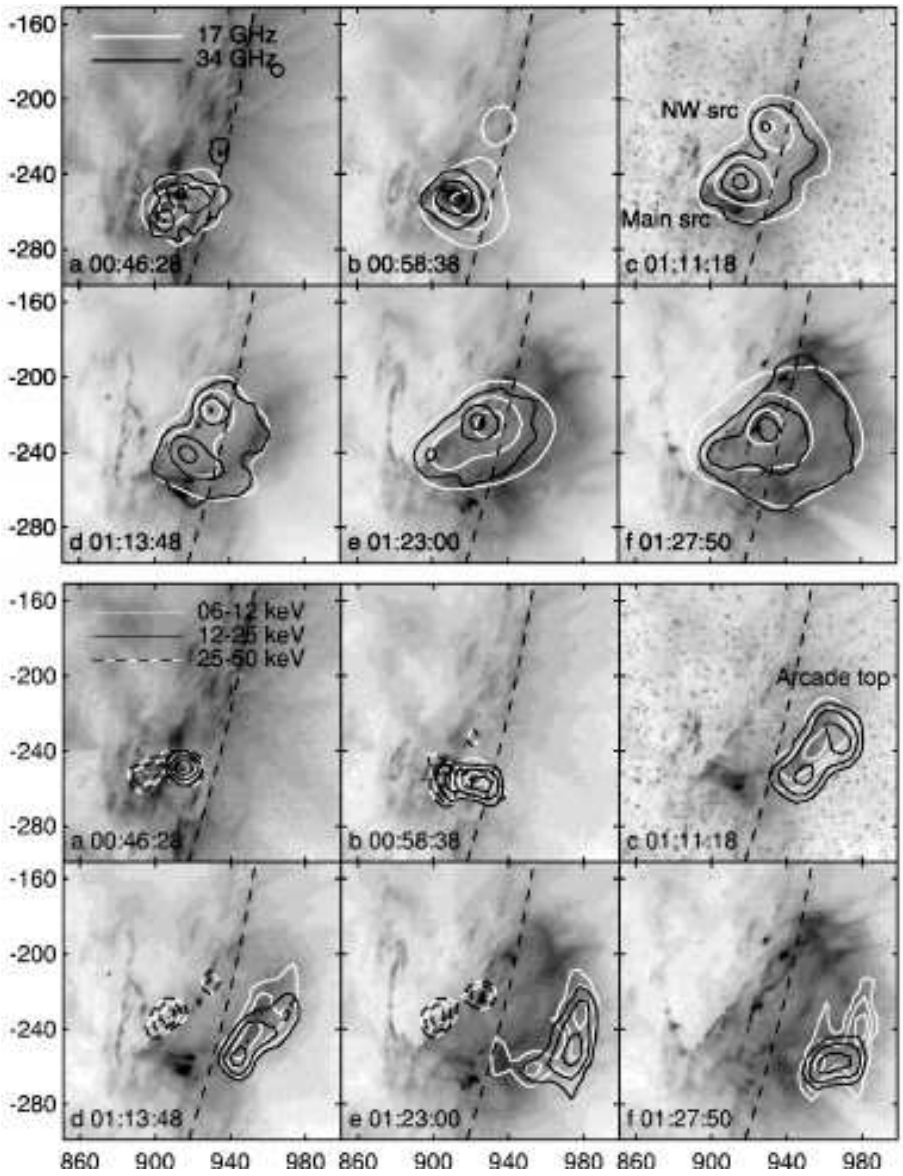

Fig. 3. A flare observed by NoRH and RHESSI. In the two top rows, a sequence of overlays of 17 (white contours) and 34 (black contours) GHz images on TRACE 195 Å Fe XII images (inverted color table) during the flare's main phase. Contour levels are at 10%, 40%, and 80% of the maximum in each image. The two bottom rows show sequence of overlays of RHESSI HXR images overlaid on the TRACE images appearing in the two top rows. 6-12 keV images are shown in white contours, 12-25 keV images in black contours, and 25-50 keV images in dashed contours. Contour levels are at 10%, 40%, and 80% of the maximum in each image (from Kundu et al. 2004).

microwave emission comes from the loop-top (see section 4.1).

2.3. Overall View

From a practical point of view, the analysis presented in sections 2.1 and 2.2 indicates that HXR images and single-frequency radio images may look quite different, and the appearance of the radio images will change depending on frequency. An example, obtained from the study by White et al. (2002), is given in fig. 2: the microwave emission at 17 and 34 GHz covers the whole loop as it is demarcated by the soft X-ray image while the HXR sources are located at the footpoints of the loop.

Simultaneous morphological studies of flares in HXRs, soft X-rays, and microwaves, together with photospheric magnetograms have provided valuable information about the flare configuration over the years. The first such high-resolution observations were published by Alissandrakis, Schadee, & Kundu (1988). Here I do not attempt to cite all relevant literature; the interested reader may refer to the review by Bastian, Benz, & Gary (1998). I only mention the articles by Nishio et al. (1997) and Hanaoka (1996; 1997; 1999) who analyzed NoRH data. Nishio et al. (1997)

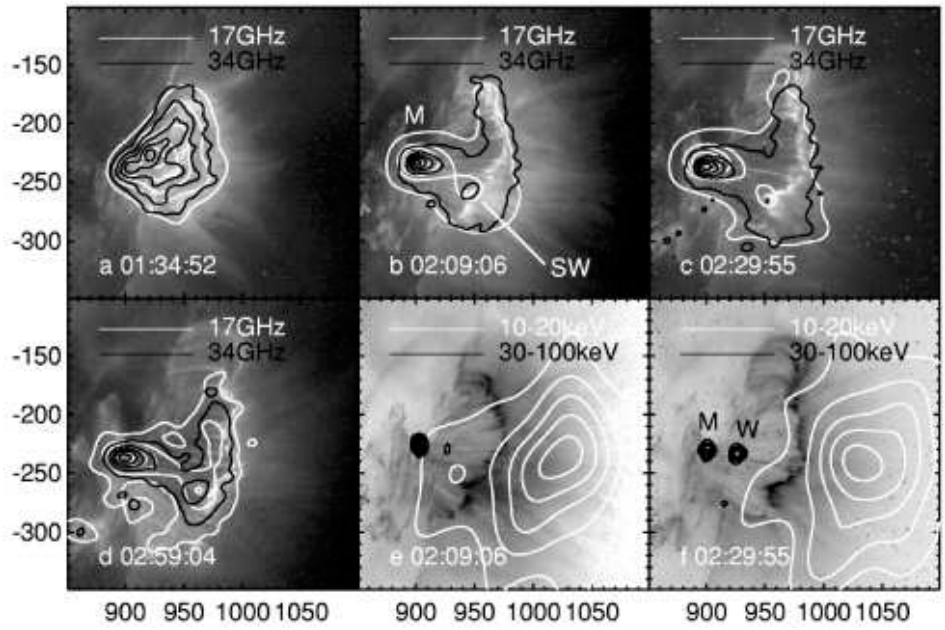

Fig. 4. Evolution of the radio and HXR sources later in the flare presented in fig. 3. The first four images show a sequence of overlays of 17 (white contours) and 34 (black contours) GHz images on TRACE 195 Å Fe XII images during the extended phase of the flare when the loop system is expanding above the west limb. The upper four contour levels are at 30%, 50%, 70%, and 90% of the maximum in each image, while the lowest contours are at 10%, 4%, 2%, and 1%, respectively. The last two images show contours of the RHESSI 10-20 keV (white) and 30-100 keV (black) emission overlaid on TRACE 195 Å Fe XII images (from Kundu et al. 2004).

found that most of the flares they studied involved at least two coronal loops: one loop is compact while the other is larger. Both loops have 17 GHz emission while HXRs are emitted preferentially by the more compact of the two loops. Similarly, soft X-ray emission is brighter in the compact loop. Hanaoka also studied the double-loop configuration flares and found that the compact loop is associated with the emergence of a parasitic magnetic polarity within the active region. These studies indicate that interacting loops of different sizes may give rise to a significant number of flares. Furthermore, configurations involving more complex loop systems also exist (e.g. see the early VLA observations analyzed by Kundu et al. 1982).

2.4. NoRH-RHESSI Observations of a Complex Event

As an example of a complex flare configuration, in figures 3 and 4, I present NoRH and RHESSI observations of an X1 flare analyzed by Kundu et al. (2004). Of course a detailed description of the event cannot be given here due to its complexity; the interested reader is referred to the article by Kundu et al. (2004). The main flare starts after 01:08 UT and the microwave emission consists of several components (see fig. 3). The strong components appearing in panels (c)-(d) have clear HXR counterparts from 01:13 UT onward. The energy distribution in the impulsive phase inferred for the radio-emitting electrons is quite similar to that inferred for the HXR-emitting electrons. After the main phase of the flare, the morphology of the radio sources has changed significantly (see fig. 4). Kundu et al. (2004) identified around 01:38 UT at least four regions showing different temporal behavior. Note that even after the main phase of the flare, the sources M and SW of fig. 4 are nonthermal. The combined radio and HXR data for this event reveal a remarkable diversity of energy release and nonthermal acceleration sites.

3. Electron Dynamics

3.1. Trapping and Precipitation

Most of the morphological studies of the HXR and microwave emission have focused on images obtained at the peak of the event. As we discussed in §2, such studies may provide important diagnostics of the magnetic field and the properties of the nonthermal electrons. But concerning the acceleration process, they merely imply that the HXRs come from the "precipitating component" of the accelerated population while microwaves come from the "trapped component": at the simplest level the acceleration of electrons is regarded as a process that injects the electrons onto magnetic field lines at a time dependent rate. There is always a critical pitch angle, the loss-cone angle α_0, such that electrons with smaller pitch angles are not reflected by the magnetic field as they approach the footpoints. Some

fraction of the electrons are injected with pitch angles lying in the loss-cone and precipitate on their first appoach to the footpoint. The remaining fraction is injected with pitch angles outside the loss-cone and remain trapped in the corona unless pitch angle scattering takes place.

In order to refine the above picture, detailed timing studies are required. In a series of papers, Aschwanden and colleagues (Aschwanden, Schwartz, & Alt 1995; Aschwanden et al. 1996a; 1996b; 1996c) have performed timing studies of HXR data in the energy range of 25-200 keV and demonstrated that the energy-dependent time delays of fast time structures (on time scales less than a few seconds) are consistent with time-of-flight differences, while the smoothly varying HXR flux shows delays of opposite sign that are consistent with electron collisional deflection times. This behavior of the HXR timing has been interpreted (e.g. Aschwanden 1998) in the framework of the "trap-plus-precipitation/direct precipitation" model (TPP/DP): electrons with initially small pitch angle ($\alpha \leq \alpha_0$) precipitate directly to the HXR emission site while electrons with initially large pitch angles ($\alpha \geq \alpha_0$) are temporarily trapped and precipitate after the collisional deflection time.

The identification of direct precipitation in microwaves has begun only recently (Kundu et al. 2001a; Lee et al. 2002). Kundu et al. (2001a) compared the radio time profiles of two simple spiky bursts observed with NoRH at 17 and 34 GHz with a trap model derived using the Yohkoh HXT 53-93 keV time profile. Each microwave time profile was modeled as the sum of a component identical to the hard X-ray time profile (the injection function) and a trapped component derived by intergrating over the injection function convolved with an exponential kernel function. The equation for the radio flux due to the trapped population alone is an integral over the trapped particle energy distribution convolved with the synchrotron emissivity. Furthermore the microwave emission from the directly precipitating electrons will not have the same emissivity as the trapped electrons since, by definition, the precipitating electrons have a different pitch angle distribution.

The above statements certainly constrain future modeling efforts of the time profile of microwave emission. Ideally, one wants to model both the observed radio flux and structures as a function of time (note that the models presented by Nindos et al. 2000 and Kundu, Nindos, & Grechnev 2004 deal with radio observations at the peak of the event only). In general, one *cannot* use the HXR time profile as an injection function for the radio-emitting electrons, let alone the radio flux profile itself which requires an integration over energy convolved with the synchrotron emissivity.

The current status of modeling the time profile of microwave emission exploits the information provided by radio spectra. When the emission is optically thin, the microwave spectrum is a direct measure of the electron energy distribution and can be used as a tool for exploring electron evolution in phase space (Petrosian 1981; Dulk & Marsh 1982). In general an observed radiation spectrum represents a combination of acceleration and the transport effect, which cannot, in general, be separated. However, in the case where the transport process is dominated by Coulomb collisions, we may possibly separate one from the other, as the involved physics is well known. Lee & Gary (2000) selected an event for which they were sure that was dominated by Coulomb collisions. They identified their event as dominated by Coulomb collisions from the observed spectral flattening and microwave morphology in comparison with magnetic field. Lee & Gary (2000) were able to explain the temporal evolution of the microwave spectrum of their event if Coulomb collisions act on an initial narrow pitch angle distribution. Of course, it is fair to say that many events show evidence of more extreme pitch angle diffusion than can be provided by Coulomb collisions.

3.2. Microwaves and HXRs Come from the Same Population Of Electrons?

The discussion in §3.1 suggests that microwave emission and HXR emission have different properties and therefore do not necessarily come from the same population of electrons. However, it is often said that both emissions come from the same population of electrons. It has long been assumed that, because the time profiles of HXR and microwave emission are so similar (Kundu 1961) and because of the tight correlation between peak fluxes in the two emissions (e.g. Kosugi, Dennis, & Kai 1988), the "same" electrons are responsible for the two emissions. Of course, the ultimate proof whether radio-emitting and hard X-ray-emitting electrons are energized by the same acceleration process, requires a demonstration that they have the same energy spectrum and a consistent timing in both wavelength ranges. Here, I give some qualifications on this issue.

First of all, even spatially unresolved observations sometimes show that the time of maximum flux at microwaves lags behind the time of HXR maximum flux by 1-3 sec (Crannell et al. 1978). Also microwave emission usually decays more slowly than the HXR emission. Usually the observed microwave delays are interpreted in the framework of efficient trapping: under Coulomb collisions, high-energy electrons live longer than low-energy electrons. Therefore the energetic electrons producing microwaves remain in the flaring loop longer and the microwaves they produce peak later than the HXRs which come from lower energy electrons. Bastian, Benz, & Gary (1998) refined these results by analyzing flares observed simultaneously by NoRH at 17 GHz and the BATSE instrument on board the Compton Gamma Ray Observatory (CGRO). Using spatially unresolved data, the relative HXR/microwave timing agreed with earlier studies. When the timing comparisons were made using the spatially resolved 17 GHz images, they found that the microwave delay varied significantly within the source with footpoint microwave emission showing the minimum delay with respect to HXRs and loop-top emission showing the largest delays. Such variation of delays within a flaring loop are due to energy-dependent effects (at a given frequency the microwave loop-top emission comes from electrons

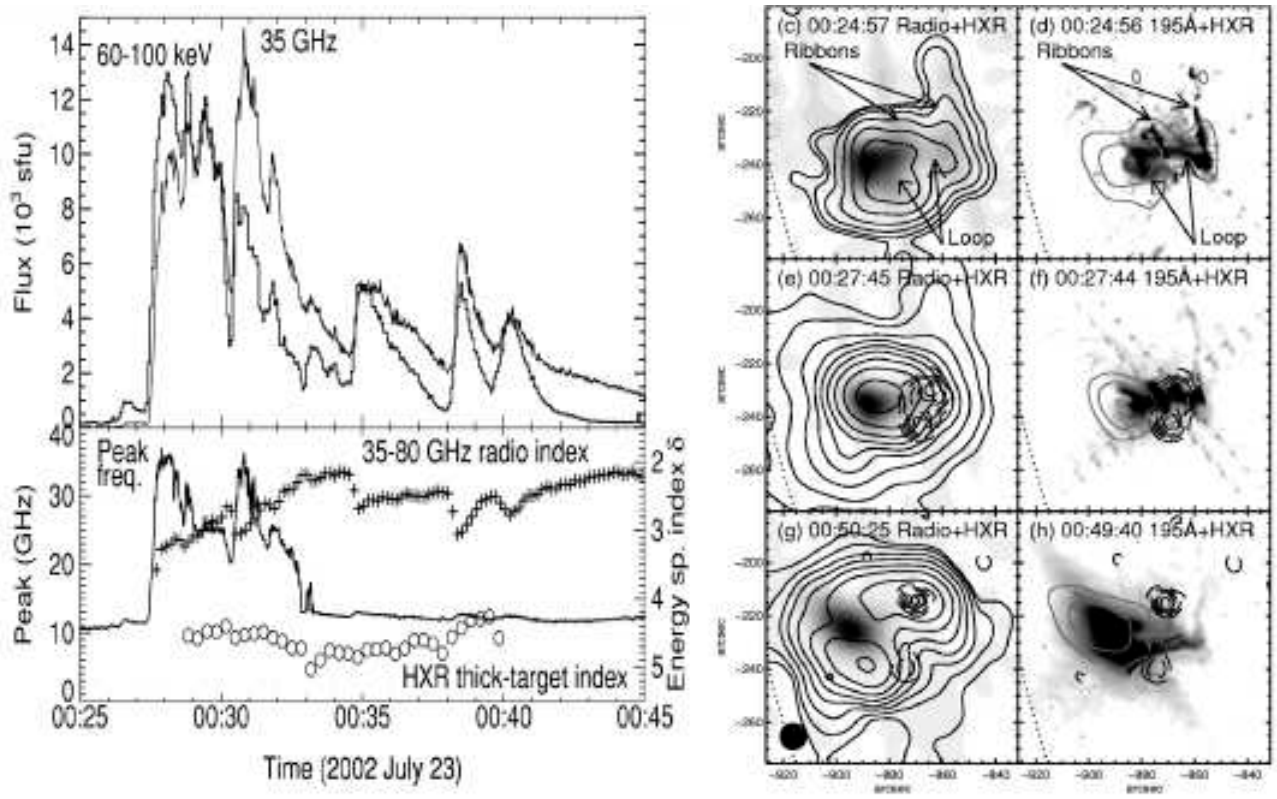

Fig. 5. Left panel, top: comparison of the RHESSI 60-100 keV HXR light curve and the NoRP 35 GHz light curve. Left panel bottom: time evolution of the radio spectral peak frequency (solid curve) and the radio spectral index from 35 to 80 GHz converted to an electron energy spectral index (plus signs). For comparison, the thick target electron energy spectral index from the RHESSI 100-400 keV spectrum is also shown (circles). Right panel: Images of the flare at X-ray, EUV, and radio-λ. The left frames show the RHESSI gray-scale image of 12-20 keV overlaid with 17 GHz contours (solid curves) and 100-150 keV HXR contours. The right frames show a 195 Å image of the same region overlaid with solid gray contours for the 12-20 keV HXRs and dashed black contours for the 100-150 HXR (from White et al. 2003).

with higher energies than those giving footpoint emission).

Furthermore, discrepancies between the electron spectral indexes inferred from microwave and HXR data during the impulsive burst phase have been reported occasionally (e.g. Kundu et al. 1994; Raulin et al. 1999). Silva, Wang, & Gary (2000) studied the statistical properties of 27 flares and found that in 75% of the bursts, the inferred index of the electron energy distribution of the microwave-emitting electrons, δ_r, is harder than that of the lower energy HXR-emitting electrons, δ_x, on average by 0.5-2.0. This implies that there is a breakup in the energy spectra of the electrons. The difference between δ_r and δ_x may be explained either by two different electron populations being accelerated in different sites with distinct physical conditions or in the framework of the "trap-plus-precipitation" model. This model predicts a hardening of the spectra of the trapped electrons because of the losses of lower energy electrons by energy-dependent Coulomb collisions (Trottet & Vilmer 1984). In this case, the microwaves produced by the electrons in the trap reflect this hardening while the HXR spectra produced by the precipitated electrons preserve the original injection spectrum, which is softer.

3.2.1. Microwave and HXR Imaging of High-energy Electrons

RHESSI offers us the opportunity, for the first time, to image HXRs produced by electrons at photon energies above 100 keV. Therefore using simultaneous NoRH and RHESSI observations we can compare the emissions from electrons in the same energy range at two different wavelength regimes. The first such comparison was published by White et al. (2003) (see fig. 5). Note that the gyrosynchrotron mechanism is very efficient and allows us to detect electrons with energies of hundreds of keV even in small flares. On the other hand, flares in which HXRs above 100 keV can be imaged do not happen so often, because the steeply falling power-law spectra do not yield sufficient photons at high energies for image formation.

Fig. 5 (right panel) shows the structure of the radio and HXR sources (the maximum 17 GHz brightness temperature exceeds 10^9 K!). The left panel of fig. 5 indicates that the radio and HXR time profiles are so similar, that one cannot argue that radio emission comes from a long-lived population of trapped electrons while the HXRs come from directly

precipitating electrons as it occurs in other events. The radio and HXR-emitting electrons should have a common origin. Fig. 5 also shows that the peak frequency of the radio spectrum reaches values as high as over 35 GHz. The energy spectral index derived from the 35-80 GHz spectra is $\delta_r \approx 1.6 - 1.8$ which does not agree with the value derived from the 40-400 keV HXRs, which is $\delta_x \approx 4.5$. White et al. (2003) were forced to conclude that a single population of electrons with a power law index of 4.5-5 above 100 keV produces the emission at 17 and 34 GHz if one assumes that the 35-80 GHz spectral index does not reflect the true optically thin value. Both radio and HXR data require extreme densities of electrons to be accelerated in the energy release: over 10^{10} cm^{-3} above 20 keV! Clearly, a systematic search in the RHESSI database is required in order to check whether or not similar events with sufficient photons at such high energies exist. If they do exist, comparing the resulting HXR images with NoRH data will be interesting.

4. Anisotropies/Deviations From the Classical Picture

The discussion in §2, assumed that the microwave-emitting electrons have uniform density and isotropic pitch angle distribution. However, there is ample evidence, both at microwaves and HXRs/gamma-rays, that in some flares the energetic electrons are distributed anisotropically. First of all, there is the prominent directivity of gamma-ray flares (McTiernan & Petrosian 1991) produced by relativistic electrons. Furthermore, Lee & Gary (2000) found that anisotropic pitch-angle distribution (including anisotropic injection) is required for explaining the spectral evolution of a flare at microwaves (see §3). Fleishman & Melnikov (2003a, 2003b) have studied both the optically thin and optically thick gyrosynchrotron emission produced by energetic electrons with anisotropic pitch angle distributions. They found that the properties of the emitted radiation (intensity, optically thin spectral index, degree of polarization) depend sensitively on the type and degree of electron anisotropy. Lately, significant attention has been paid to optically thin loop-top microwave sources as evidence for electron anisotropies.

4.1. Optically Thin Microwave Loop-top Sources

Kundu et al. (2001b) analyzed three limb flares observed with the NoRH at 17 and 34 GHz. The flare geometry was simple with one well-defined flaring loop in each event. The 17 and 34 GHz emissions were optically thin and peaked close to the loop tops. As has been shown by many studies (e.g. Alissandrakis & Preka-Papadema 1984, Preka-Papadema & Alissandrakis 1992, Bastian, Benz, & Gary 1998, Nindos et al. 2000) an optically thin loop in which the magnetic field declines from the footpoint to the loop top will generally be brightest at the footpoints of the loop if the density and pitch angle distribution of the nonthermal electrons are uniform. The angle between the magnetic field and the line of sight also plays an important role, but for the events studied by Kundu et al. (2001b) this angle is expected to be large everywhere along the loop since the flares took place close to the limb. Kundu et al. (2001b) were forced to invoke a magnetic field with constant strength along the loop in order to partly reconcile the observations with gyrosynchrotron loop models like the one presented in §2. This is consistent with studies of nonflaring loops in the EUV and soft X-rays that show little change in the apparent thickness of loops from footpoint to loop top (Klimchuk 2000; Watko & Klimchuk 2000).

A magnetic configuration with little magnetic field variation along the loop creates obvious problems in the trapping of the radio-emitting electrons. Melnikov, Shibasaki, & Reznikova (2002) suggest that the loop top sources in optically thin events are due to the highly inhomogeneous distribution of the energetic electrons along the flaring loop: accelerated electrons are concentrated in the upper part of the loop. This interpetation is supported from timing studies employed by Melnikov et al. (2002): (1) The loop-top emission is delayed by several seconds with respect to the footpoint emission and this delay is more pronounced at 34 than at 17 GHz; (2) the time profile of the loop top emission is wider and its decay slower than those of the footpoint emission; (3) on the other hand, there is almost no delay between the emissions from the regions close to the footpoints. Melnikov, Shibasaki, & Reznikova (2002) considered the question whether the anisotropic distribution of electrons along the loop is due to the acceleration/injection process or due to transport effects. Their simulations seem to support the idea that the high concentration of electrons at the loop top is due to transeverse pitch angle anisotropy of the injected electrons. But they also point out that transport effects (enhanced pitch angle scattering and energy losses near the footpoints due to either higher plasma density in the lower part of the loop or enhanced level of whistler turbulence) can yield a similar morphology. If the transport effects dominate one may expect that at the beginning of the flare the regions closer to the footpoints will be brighter than the loop top. Of course the combination of both acceleration/injection and transport mechanisms is also possible.

Overall, the NoRH data imply that the existence of flares with highly anisotropic distribution of energetic electrons is undeniable. However, we do not know how often such events occur. A statistical study of the properties of the optically thin limb flares observed by the NoRH may shed some light on this question. Note however, that the results of such study may show ambiguites due to the fact that NoRH is not able to resolve the total intensity structures of some flares (e.g. see Kundu et al. 2001a).

4.2. HXR Coronal Sources

The existence of impulsive HXR coronal sources located above the soft X-ray flaring loop is one of the most spectacular discoveries of the Yohkoh mission. This phenomenon is refered to as the "Masuda flare" (Masuda 1994; Masuda et al. 1995) and has attracted significant attention. The Masuda source occurs during the impulsive phase of a flare but appears to be unusual, in that surveys (Aschwanden 2002) only revealed a handful of such events among Yohkoh's many flares. Since the Masuda events have been observed in limb flares we are confident that the coronal HXR brightening is not due to projection effects. The production of HXRs by bremsstrahlung is proportional to the product of the densities of the ambient thermal electrons and the nonthermal electrons. In order to have a coronal source other than by projection effects, one of these densities must peak at the location of the coronal source. In the case of the Masuda flares, there is no plasma density enhancement at the location of the HXR coronal source; therefore it seems to require trapping of the nonthermal electrons there, possibly due to a combination of large pitch angles for the nonthermal electrons and a strong gradient in magnetic field strength from the top of the loop to the bottom in order for magnetic mirroring to be effective (Fletcher & Martens 1998; Metcalf & Alexander 1999).

Masuda et al. (1995) interpreted their discovery as evidence of magnetic reconnection above the soft X-ray flaring loop. The interpretation was done in terms of the so-called "standard reconnection model" (Carmichael-Sturrock-Hirayama-Kopp-Pneuman model, CSHKP) involving a fast-mode MHD shock terminating the reconnection outflow. The HXR coronal source could arise in particle acceleration either at the shock itself via the Fermi mechanism, with trapping by the paired slow-mode shock structures present in the standard reconnection model (Tsuneta & Naito 1998). Alternatively, a stochastic acceleration model (e.g. Jakimiec et al. 1998) could also explain the presence of energy conversion above the loop top.

The Masuda above-the-loop-top sources is not the only kind of coronal HXR sources detected by the Yohkoh HXT. Tomczak (2001) studied 14 behind-the-limb flares with occulted footpoints. This is the best selection criterion if one wants to detect coronal HXR sources without the presence of strong footpoint sources which can disturb the observational features of the coronal source during the process of image reconstruction. In addition to the Masuda sources, Tomczak (2001) found HXR coronal sources cospatial with bright loop-top kernels seen in soft X-ray images. Furthermore, Hudson et al. (2001) found a moving source from an over-the-limb flare. The HXR source emerged from behind the limb as a compact structure identifiable with a microwave source and moved outwards at about 10^3 km/sec.

4.3. RHESSI Observations of HXR Coronal Sources

RHESSI with its superior sensitivity and dynamic range is a suitable instrument for the study of coronal HXR sources. Indeed several coronal sources have been detected since its launch (Jiang et al. 2004). They may appear at different phases of the flare event. According to Jiang et al. (2004), in most cases, their spectrum can be fitted with either a thermal or a power-law model. In the impulsive phase, the spectra seem to fit the power-law model better while in the decay phase the loop top sources are thermal. Balciunaite, Krucker, & Lin (2004) have observed 6 behind-the-limb flares with occulted or partially occulted footpoints and have been able to detect Masuda type above-the-loop-top HXR sources.

Veronig & Brown (2004) studied two flares with HXR emission coming mainly from the loop top and only weak footpoint emission. Both are gradual events with very steep spectra and high coronal column densities This class of HXR sources should not be confused with Masuda sources and are interpreted as "coronal thick-target flares" by Veronig & Brown (2004): the corona is collisionally thick and the energy is released due to collisions in the corona before the electrons reach the footpoints. The implied coronal density of the thermal plasma is about 2×10^{11} cm^{-3}. Both events have been observed within the Nobeyama time zone and it would be interesting to check the radio data against the RHESSI data.

One of the objectives of the RHESSI mission is to check flare reconnection models. Therefore it is not surprising that attention has been paid to the motions of coronal HXR sources: in four events, Sui & Holman (2003) and Sui, Holman, & Dennis (2004) studied the dynamics of the coronal HXR source with respect to the flaring loop and found evidence for the formation and development of a current sheet between the loop top and the coronal source.

Using suitable NoRH and RHESSI data, it will be interesting to study the relation of the mechanism producing coronal HXRs with respect to the process which yields microwave flaring loop emission.

5. Conclusions and Future Work

Two central goals of flare observations are to determine the magnetic field configuration of the flare and the characteristics of the electron population, how it evolves with time and how it relates to the injected population. Achieving progress in these areas is necessary in order to tackle better the fundamental problems of energy release and particle acceleration in solar flares.

Systematic morphological studies using data from the NoRH and RHESSI can give us important information about

the possible configurations that may give rise to energy release and particle acceleration. Using spectral data we need to determine whether the electron energy spectra derived from HXRs are consistent with those derived from microwaves; and if not what causes the discrepancy. Furthermore, in order to obtain quantitative information about the magnetic field and the nonthermal electrons in the flaring region, detailed comparison of the spatial and spectral structure of the observations with models is needed integrating all observational information available. The current gyrosynchrotron loop models are static and do not account for anisotropies of the electron population. Meaningful progress can be made only if we diagnose the anisotropies better: currently we do not know whether the anisotropies are due to acceleration and injection or due to transport effects.

Overall, we need to develop more sophisticated models to account for even the grossest of characteristics of some flares. The NoRH has been, and always will be, a valuable source of data that should be used in such projects. With the future development of the Frequency Agile Solar Radiotelescope imaging spectroscopy in radio will be achieved, resulting to even greater progress in high-energy flare physics.

Acknowledgements

I would like to thank the organizers of the "Nobeyama Symposium 2004" for their invitation and financial support. Prof. C.E. Alissandrakis and Dr. S.M. White are thanked for several fruitful discussions.

References

Alissandrakis C.E. 1986, Sol. Phys. 104, 207
Alissandrakis C.E., Preka-Papadema P. 1984, A&A, 139, 507
Alissandrakis C.E., Schadee, A., Kundu M.R. 1988, A&A, 195, 290
Aschwanden M.J. 1998, ApJ, 502, 455
Aschwanden M.J. 2002, Space Sci. Rev., 101, 1
Aschwanden M.J, Schwartz R.A., Alt D.M. 1995, ApJ, 464, 974
Aschwanden M.J, Hudson H.S., Kosugi T., Schwartz R.A. 1996a, ApJ, 464, 985
Aschwanden M.J, Kosugi T., Hudson H.S., Wills M.J., Schwartz R.A. 1996b, ApJ, 470, 1198
Aschwanden M.J, Wills M.J., Hudson H.S., Kosugi T., Schwartz R.A. 1996c, ApJ, 468, 398
Balciunaite P., Krucker S., Lin R.P. 2004, AGU-SH13A, 1131
Bastian T.S., Benz A.O., Gary D.E. 1998, ARA&A, 36, 131
Chiuderi-Drago F., Alissandrakis C.E., Bentley R.D., Philips A.T. 1998, Sol. Phys., 182, 459
Crannell C.J., Frost K.J., Saba J.L., Matzler C., Okhi K. 1978, ApJ, 223, 620
Dulk G.A., Marsh K.A. 1982, ApJ, 259, 350
Fleishman G.D., Melnikov V.F. 2003a, ApJ, 584, 1071
Fleishman G.D., Melnikov V.F. 2003b, ApJ, 587, 823
Fletcher L., Martens P.C.H. 1998, ApJ, 505, 418
Gary D.E. 1985, ApJ, 297, 799
Gary D.E. 2000, in "High Energy Solar Physics -Anticipating HESSI", ed R. Ramaty, N. Mandzhavidze (ASP Conf. Ser. 206), p. 297
Hanaoka, Y. 1996, Sol. Phys., 165, 275
Hanaoka, Y. 1997, Sol. Phys., 173, 319
Hanaoka, Y. 1999, PASJ, 51, 483
Hudson H.S., Ryan J. 1995, ARA&A, 33, 239
Hudson H.S., Canfield R.C., Kane S.R. 1978, Sol. Phys., 60, 137
Hudson H.S., Kosugi T., Nitta N.V., Shimojo M. 2001, ApJ, 561, L211
Jakimiec J., Tomczak M., Falewicz R., Phillips K.J.H., Fludra A. 1998, A&A, 334, 1112
Jiang Y.W., Liu S.M., Liu W., Petrosian V. 2004, BAAS, 204, 9805
Klimchuk J.A. 2000, Sol. Phys., 193, 53
Kosugi T., Dennis B.R., Kai K. 1988, ApJ, 324, 1118
Kosugi T., et al. 1992, PASJ, 44, 45
Kundu M.R. 1961, J. Geophys. Res., 60, 4308
Kundu M.R., Vlahos L. 1982, Space Sci. Rev., 32, 405
Kundu M.R., Schmahl E.J., Velusamy T., Vlahos L. 1982, A&A, 108, 188
Kundu M.R., White S.M., Gopalswamy N., Lim J. 1994, ApJ (Suppl.), 90, 599
Kundu M.R., Nitta N., White S.M., Shibasaki K., Enome S., Sakao T., Kosugi T., Sakurai T. 1995, ApJ, 454, 522
Kundu, M.R., White S.M., Shibasaki K., Sakurai T., Grechnev V.V. 2001a, ApJ, 547, 1090
Kundu, M.R., Nindos, A., White S.M., Grechnev V.V. 2001b, ApJ, 557, 880
Kundu, M.R., Nindos, A., Grechnev V.V. 2004, A&A, 420, 351
Kundu M.R., Garaimov V.I., White S.M., Krucker S. 2004, ApJ, 1052
Lee J., Gary D.E. 2000, ApJ, 543, 457
Lee J., Gary D.E., Qiu J., Gallagher P.T. 2002, ApJ, 572, 609
Lin R.P., et al. 2002, Sol. Phys. 210, 3
Lu E., Petrosian V. 1989, ApJ, 338, 1122
Masuda S. 1994, PhD thesis, Univ. of Tokyo
Masuda S., Kosugi T., Hara H., Sakao T., Shibata K., Tsuneta S. 1995, PASJ, 47, 677
Melnikov V.F., Shibasaki K., Reznikova V.E. 2002, ApJ, 580, L185
Melnikov V.F., Reznikova V.E., Yokoyama T., Shibasaki K. 2002, in "Solar variability: from core to outer frontiers. The 10th European Solar Physics Meeting, 9 - 14 September 2002", ed A. Wilson (ESA SP-506, Noordwijk), p. 339
McTiernan J.M., Petrosian V. 1991, ApJ, 379, 381
Metcalf T.R., Alexander A. 1999, ApJ, 522, 1108
Nakajima H., et al. 1994, Proc. IEEE, 82, 705
Nindos A., White S.M., Kundu M.R., Gary D.E. 2000, ApJ, 533, 1053
Nishio M., Yaji K., Kosugi T., Nakajima H., Sakurai T. 1997, ApJ, 489, 976
Petrosian V. 1981, ApJ, 251, 727
Preka-Papadema P., Alissandrakis C.E. 1992, A&A, 257, 307
Raulin J.-P., White S.M., Kundu M.R., Silva A.V.R., Shibasaki K. 1999, ApJ, 522, 547
Sakao T. 1994, PhD thesis, Univ. of Tokyo
Sakao T., et al. 1992, PASJ, 44, L83
Silva A.V.R., Wang H., Gary D.E. 2000, ApJ, 545, 1116
Sui L., Holman G.D. 2003, ApJ, 596, L251
Sui L., Holman G.D., Dennis B.R. 2004, ApJ, 612, 546

Tandberg-Hanssen E., Emslie A.G. 1988, The Physics of Solar Flares, (Cambridge Univ. Press, Cambridge)
Tomczak M. 2001, A&A, 366, 294
Trottet G., Vilmer N. 1984, Adv. Space Res., 4(2-3), 153
Tsuneta S., Naito T. 1998, ApJ, 495, L67
Veronig A.M., Brown J.C. 2004, ApJ, 603, L117
Wang H., Gary D.E., Zirin H., Schwartz R.A., Sakao T., Kosugi T., Shibata K. 1995, ApJ, 453, 505
Wang H., Gary D.E., Zirin H., Nitta N., Schwartz R.A., Kosugi T. 1996, ApJ, 456, 403
Watko J.A., Klimchuk J.A. 2000, Sol. Phys., 193, 77
White S.M., Kundu M.R., Garaimov V.I., Yokoyama T., Sato J. 2002, ApJ, 576, 505
White S.M., Krucker S., Shibasaki K., Yokoyama T., Shimojo M., Kundu M.R. 2003, ApJ, 595, L111

Radio Emission from Anisotropic Electron Distributions

Gregory D. Fleishman
National Radio Astronomy Observatory, Charlottesville, VA 22903 USA
gfleishm@nrao.edu

Abstract

The effect of pitch-angle anisotropy of fast electrons on generation of nonthermal radio emission is studied. Incoherent gyrosynchrotron radiation is shown to depend strongly on the anisotropy. In particular, the spectral index of gyrosynchrotron radiation increases up to a factor of 3-4 compared with the isotropic case. The degree of polarization (X-mode) increases for loss-cone distributions, while decreases for beam-like distributions. Ample evidence of the pitch-angle anisotropy effect on (1) spatial distribution of the radio brightness, (2) spatially resolved light curves of the intensity and polarization, (3) spectral hardness of microwave bursts, is found by exploring observations performed with Nobeyama Radioheliograph and Owens Valley Solar Array. Above some threshold in the angular gradient, the electron cyclotron maser instability (coherent gyrosynchrotron emission) can develop, provided that standard gyrosynchrotron emission is accompanied by a lower-frequency intense coherent emission. The coherent emission is studied in detail for a realistic distribution of fast electrons over the energy and pitch-angle. In agreement with observations of narrowband radio spikes, it is found that (1) hard (power-law) distributions over energy are preferable to produce the coherent emission, (2) the threshold of the instability corresponds to quite an anisotropic electron distribution, thus, the pitch-angle anisotropy derived from the properties of the continuum gyrosynchrotron radiation will not necessarily give rise to coherent emission (either enhanced isotropization implied by quasilnear saturation of the instability).

Key words: acceleration of particles—instabilities—radiation mechanisms:non-thermal—Sun:flares—Sun:radio radiation

1. Introduction

Observations of solar radio bursts with Nobeyama Radioheliograph (NoRH) revealed unambiguously the presence of anisotropic pitch-angle distributions of fast electrons accelerated in flares and accumulated in the radio sources. In particular, the existence of the microwave loop-top brightness peak of optically thin gyrosynchrotron (GS) emission (Melnikov et al. 2001; Kundu et al. 2001) has been interpreted as tracer of a strong concentration of mildly relativistic electrons trapped and accumulated in the top of a flaring loop (Melnikov et al. 2002a), which is an evidence of the transverse anisotropy of radiating electrons. Then, Lee & Gary (2000) studied the evolution of the radio spectrum of 1993 Jun 3 flare observed with Owens Valley Solar Array (OVSA) and found important indication of the anisotropic injection of fast electrons into the radio source and their consequent isotropisation due to angular scattering. The importance of the pitch-angle anisotropy for the modern radio data interpretation has been widely discussed during this Nobeyama Symposium (Altyntsev 2005; Bastian 2005; Gary 2005; Melnikov 2005). This paper discusses the effect of the pitch-angle anisotropy on generation of GS radiation (both incoherent and coherent).

A detailed study (stimulated by the mentioned findings) of incoherent GS emission produced by anisotropic pitch-angle distributions of the loss-cone and beam-like types is given in recent papers (Fleishman & Melnikov 2003a; Fleishman & Melnikov 2003b). Accordingly, we outline only briefly why the anisotropy has actually a strong effect on GS emission.

The effect of anisotropy on the optically thin emission is primarily related to the energy-dependent directivity of the GS radiation. Indeed, most of the synchrotron radiation by a single ultrarelativistic electron is emitted within a narrow cone

$$\vartheta \sim \gamma_e^{-1} = mc^2/E \qquad (1)$$

along the particle velocity, where γ_e is the Lorentz-factor of the electron, m, E are the mass and energy of the electron, c is the speed of light, so $\vartheta \ll 1$ if $\gamma_e \gg 1$. On the other hand, for semirelativistic and mildly relativistic electrons responsible for the GS emission, the directivity is not quite as strong, so the anisotropy (if present) can significantly change the radiation spectrum when the transition from moderately relativistic to highly relativistic regime occurs. Typical energies of fast electrons producing solar microwave continuum bursts (which are commonly believed to be produced by GS mechanism, e.g., Bastian et al. 1998) range from hundreds keV to a few MeV. Thus, the pitch-angle anisotropy of fast electrons in solar flares is particularly important for generation of microwave continuum radio emission, as well as for driving instabilities, which can result in coherent radio emissions.

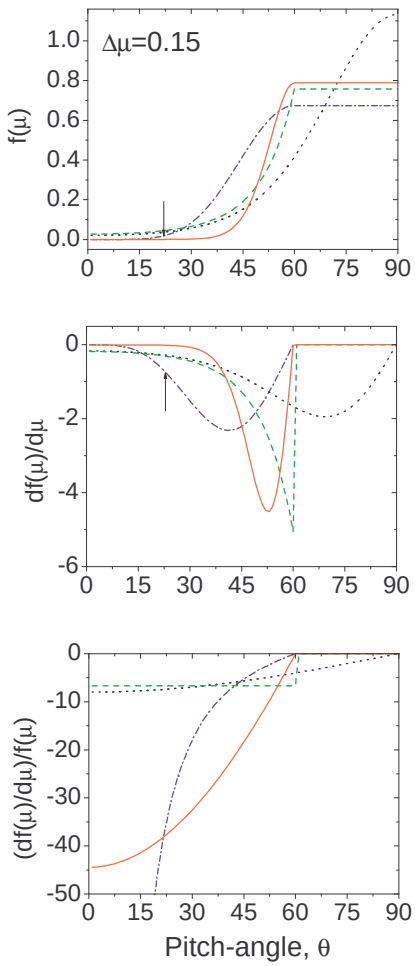

Fig. 1. Top: Angular distribution functions: gaussian (Fleishman & Yastrebov 1994a), dotted line; sin-N loss-cone (Aschwanden 1990) for $N = 6$, dash-dotted line; exponential loss-cone (5) for $\Delta\mu = 0.15$, dashed line; and gaussian loss-cone (6) for $\Delta\mu = 0.15$, solid line. The distributions are plotted for $\mu_0 = \cos\theta_c = 60^o$, all of them are normalized to unity. Middle: The derivatives of the angular distributions over μ. Bottom: the ratios of the derivatives to the distribution functions.

2. Angular Distribution Function

As a first approximation we consider a (simplified) factorized distribution function of fast electrons

$$f(\mathbf{p}) = \frac{N_e}{2\pi} f_1(p) f_2(\mu). \qquad (2)$$

The distribution function (2) is normalized by d^3p

$$\int f(\mathbf{p}) p^2 dp d\mu d\varphi = N_e, \qquad (3)$$

where N_e is the number density of fast electrons, $\mu = cos\theta$, θ is the pitch-angle, φ is the azimuth angle, the specific distributions $f_1(p)$ and $f_2(p)$ are normalized as follows:

$$\int f_1(p) p^2 dp = 1, \qquad \int_{-1}^{1} f_2(\mu) d\mu = 1. \qquad (4)$$

We assumed the distribution function over the momentum modulus to be a kind of power-law, while we consider a few different forms for the pitch-angle distribution to study the sensitivity of the GS properties to the shape of the angular distribution.

In addition to the gaussian and sin-N functions (explored by Fleishman & Melnikov 2003b), we use also the exponential loss-cone function

$$f_2(\mu) \propto \begin{cases} \exp\left(-\frac{\mu-\cos\theta_c}{\Delta\mu}\right), & \mu > \cos\theta_c, \\ 1, & -\cos\theta_c < \mu < \cos\theta_c \\ \exp\left(\frac{\mu+\cos\theta_c}{\Delta\mu}\right), & \mu < -\cos\theta_c, \end{cases} \qquad (5)$$

and the gaussian loss-cone function

$$f_2(\mu) \propto \begin{cases} \exp\left(-\left(\frac{\mu-\cos\theta_c}{\Delta\mu}\right)^2\right), & \mu > \cos\theta_c, \\ 1, & -\cos\theta_c < \mu < \cos\theta_c \\ \exp\left(-\left(\frac{\mu+\cos\theta_c}{\Delta\mu}\right)^2\right), & \mu < -\cos\theta_c. \end{cases} \qquad (6)$$

Let us consider these angular distributions (presented in figure 1) in more detail, having in mind that along with modification of incoherent GS emission the anisotropy can give rise to some instabilities (which depends on relative value of the angular gradient), in particular, to electron cyclotron maser (ECM) emission at the low gyroharmonics. The gaussian angular distribution provides rapid decrease of the number of electrons toward the direction of the magnetic field, and affect the GS substantially (Fleishman & Melnikov 2003b).

However, this distribution is not favorable to drive the instabilities (Fleishman & Yastrebov 1994a, 1994b), because the instability related to the gaussian angular distribution is rather weak being only slightly above the threshold. The efficiency of the instability is set up by relative importance of negative derivative of the distribution function over the momentum modulus and positive contribution related to angular gradient, which can be quantitatively described by the ratio of the angular gradient of the pitch-angle distribution to the angular distribution function itself. Although the angular derivative in figure 1 is not small, the peak value occurs at those angles where the angular distribution function is large, the ratio of these values is, therefore, small everywhere, figure 1 bottom. Thus, the gaussian pitch-angle distribution can be stable against instabilities for rather broad range of parameters.

Sin-N angular distribution (Aschwanden 1990) has very different properties. While this function looks rather smooth (it is continuous function together with its first derivative) and, thus, attractive for the use in theoretical calculations, it cannot be considered as a good approximation for the angular distribution since this function has a very deep intrinsic problem. Indeed, if we compare the behavior of the function and its first derivative, we discover that the derivative decreases (with the decrease of the pitch-angle) much more slowly than the function itself. Particularly, the arrows in figure 1 indicate the region where the derivative is of order of unity, while the

function is much less than unity. Note, that the ratio diverges as the pitch-angle decreases. Thus, sin-N function describes the case of highly unstable electron distribution, which gives rise to ECM instability operating significantly above the respective threshold for any parameters of this function. As a result, the instability exists for almost any shape of the momentum distribution of fast electrons, and its efficiency has extremely weak dependence on the electron spectral index. Such highly unstable distribution function can hardly be built up under reasonable assumptions about fast electron acceleration and transport.

This artificial property has already produced a few unexpected and poorly understood results. In particular, the detailed numerical calculations of the ECM quasilinear saturation (Aschwanden 1990) did not ensure the entire maser saturation even after 50 growth times: the peak value of the growth rate was reduced by less than one order of magnitude for this time. The reason for this surprising behavior is rather slow angular diffusion in the range of small pitch-angles, where the distribution function is small but the angular gradient is sufficiently large to provide the instability and then support it for quite a long time. The quasilinear relaxation occurs differently if the instability operates closer to its threshold (Fleishman & Arzner 2000).

Exponential loss-cone function (5) is free from such kind of problem. From the theoretical point of view it has only one disadvantage – discontinuity of its first derivative at $\theta = \theta_c$. Alternatively, a similar loss-cone distribution but with faster, gaussian, decrease of the number of electrons in the loss-cone (6) is also attractive from the theoretical point of view, since it is a function continuous together with its first derivative.

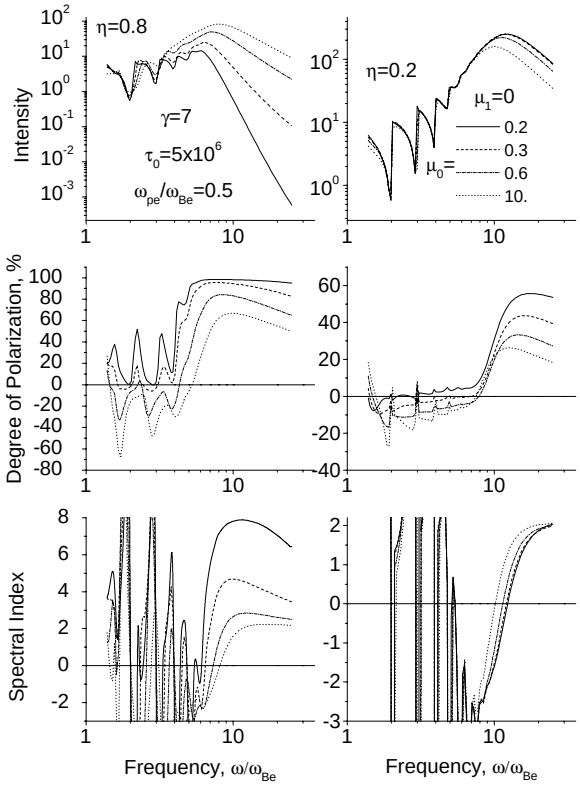

Fig. 2. GS radiation intensity, degree of polarization, and spectral index vs. frequency for various μ_0 in the Gaussian pitch-angle distribution $f_2 \propto \exp\left[-(\mu-\mu_1)^2/\mu_0^2\right]$ of the loss–cone type, $\mu_1 = 0$

3. Incoherent Gyrosynchrotron Emission

The study of the GS emission produced by anisotropic pitch-angle distributions requires exact calculation of the corresponding emission and absorption coefficients (Fleishman & Melnikov 2003b). This is especially important for the directions along which a relatively small amount of particles is moving, so adding up the contributions from numerous electrons moving at unfavorable directions should be done correctly. Figure 2 presents an example of intensity, degree of polarization and spectral index of GS radiation produced by a gaussian angular distribution vs frequency as the degree of the anisotropy (angular gradient) changes (Fleishman & Melnikov 2003b).

The effect of the anisotropy on the properties of GS emission depends evidently on the viewing angle between the directions of wave propagation and the magnetic field. For the quasitransverse (QT) case, $\eta = 0.2$ ($\vartheta = 78^\circ$), right column, the effect of the pitch-angle anisotropy on the spectral index (bottom panel) is rather weak, while the intensity and degree of polarization increase with anisotropy increases. However, the anisotropy has exceedingly large effect on GS radiation produced at a quasiparralel (QP) direction, $\eta = 0.8$ ($\vartheta = 37^\circ$), left column. Indeed, the radiation intensity changes by orders of magnitude compared with the isotropic case. Respectively, the difference in the spectral index in the optically thin frequency range is up to a factor of four (left panel, bottom). Remarkable change of polarization occurs as well: the degree of polarization increases in the optically thin region and can approach 100% for sufficiently high anisotropy. Furthermore, the sense of polarization can correspond to X-mode in the optically thick region contrary to the isotropic case.

Complementary, figure 3 shows the intensity, degree of polarization, and spectral index of GS emission observed at four different viewing angles from the gaussian (6) and exponential (5) loss-cone distributions (all other conditions are the same). GS emission is evidently very sensitive to the type of the angular distribution of fast electrons. The difference between these two distributions are seen most prominently in the spectral index plots: although the spectral index can be as large as 6 for the gaussian loss-cone distribution, it does not exceed 3 for the exponential loss-cone distribution.

Thus, this high sensitivity of the results to the type of the angular distribution can, in principle, be used to obtain important constraints on the pitch-angle distributions present during solar flares. We emphasize, that along

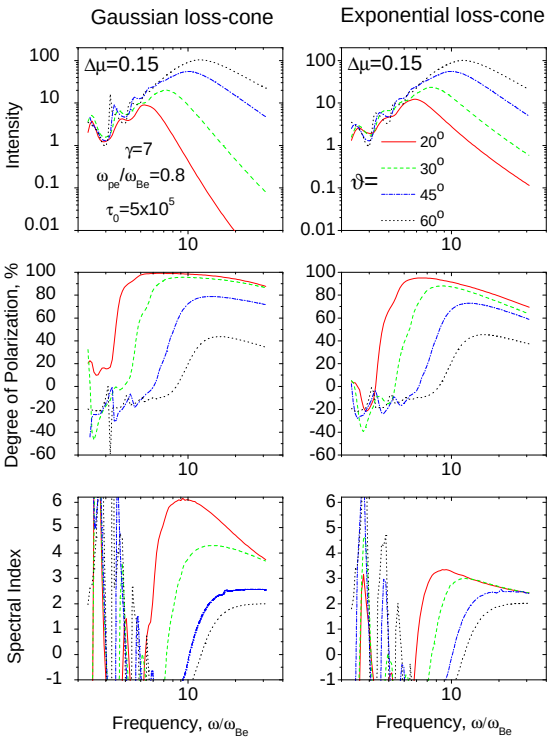

Fig. 3. GS radiation produced by fast electrons with a power-law distribution (with the index $\gamma = 7$) over momentum modulus and gaussian (6) (left) or exponential (5) (right) loss-cone functions. The total intensity, polarization and local spectral index are shown in the plot.

with strong effect on radiation intensity and spectral index, the anisotropy influences the degree of polarization, which also might be applied for quantitative diagnostics of the pitch-angle distribution.

Finally, we have to mention strong effect of pitch-angle anisotropy on the low-frequency "harmonic" structure of GS radiation (Fleishman & Melnikov 2003a). However, detection of this structure in the typical non-homogeneous sources requires high-resolution imaging spectroscopy, which is unavailable yet.

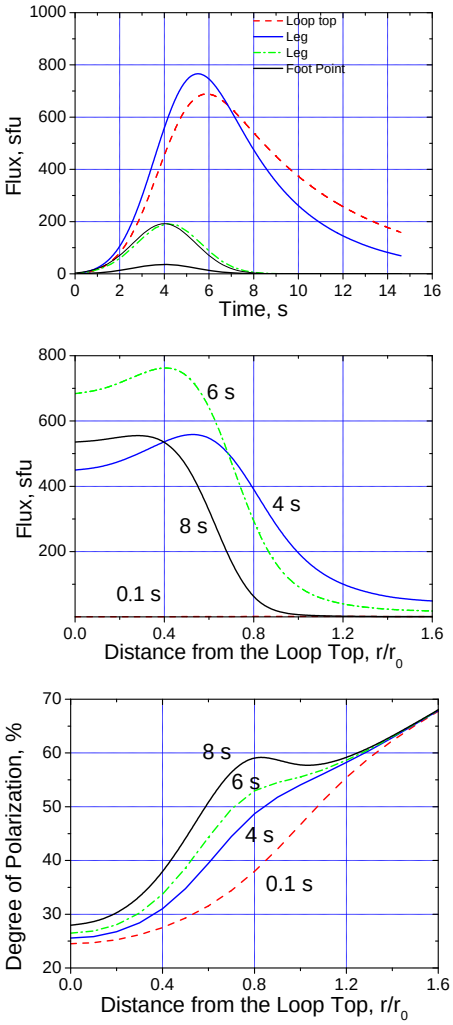

Fig. 4. Example of light curves of the microwave emission from a few positions along the loop for the case of isotropic injection function and angular-dependent life-time of fast electrons (top). The thin line represents the injection profile. Corresponding distributions (at a few time frames) of radio brightness (middle) and degree of polarization (bottom) along the magnetic trap.

4. Anisotropy Build up in the Magnetic Loops

The importance of transport effects (Kennel & Petscheck 1966; Melrose & Brown 1976) for generation of nonthermal emissions during solar flares has been recognized long ago, in particular, the magnetic mirroring was argued to be a key process to account for the loop-top brightness peak of the optically thin GS emission (Melnikov et al. 2002a). This finding implies that the anisotropy can actually be built up due to transport effects even if the injection of fast electrons occurs isotropically (although this does not deny the possibility of anisotropic injection of fast electrons).

Typical treatment of the electron trapping at the magnetic loops frequently explores the idea of empty loss-cone due to particle precipitation and losses at the dense footpoints in the weak diffusion limit. Although this idea brings an apparent advantage of the simplicity, it has also an important disadvantage of the discontinuity of the distribution function over the pitch-angle resulting in steep angular gradient, which affects strongly the calculation of the absorption coefficients.

To avoid the problems with the discontinuity and account for magnetic mirroring, energy losses and weak angular diffusion, we put forward a new model solution of the transport equation:

$$f(E,\mu,s,t) = \int_{-\infty}^{t} \exp\left(-\frac{t-t'}{\tau(E,\mu,s)}\right) g(E,\mu,s,t')dt' \quad (7)$$

where $g(E,\mu,s,t')$ and $f(E,\mu,s,t)$ are the injection and distribution functions of the fast electrons at the radio source vs energy E, the cosine of pitch angle μ, position along the loop s, and time t . Here the phenomenological life-time parameter τ can depend on the energy, position,

and *pitch-angle*.

For the weak diffusion regime we adopt that the life time τ display more or less fast decrease inside the loss-cone (when μ approaches the unity). This ensures smooth behavior of the distribution function, although the angular gradients can still be large for a favorable combination of parameters, and the net anisotropy can grow with time. Examples of the model radio brightness distributions at the subsequent times as a radio burst develops, and the spatially resolved light curves (at an optically thin frequency) in the context of anisotropic transport are shown in figure 4. To reveal the net effect of the angular-dependent transport, figure 4 assumes the life time of the electrons to depend on the pitch-angle of the electron only. It might be noted that the radio brightness peak moves towards the loop-top as the burst develops in agreement with observations (Melnikov et al. 2002a). Complementary, the emission from different locations along the loop displays systematic delay increasing from the foot-points to the loop-top, which has also been widely observed with NoRH data (Melnikov et al. 2002b; Melnikov 2005; Bastian 2005).

The dependence of the degree of polarization on time and its spatial distribution are highly affected by the pitch-angle anisotropy. Indeed, with isotropic injection, magnetic mirroring, and weak angular diffusion adopted in figure 4, the anisotropy increases with time progressively, which gives rise to the increase of the degree of polarization with time in the legs and top of the loop. At the foot-points ($r/r_0 > 1.4$), however, the angular distribution repeats the injected distribution since the life time of the electrons at the foot-points is too small to build up noticeable pitch-angle anisotropy.

5. Observational Evidence of Anisotropic Pitch-Angle Distribution in Flares

Besides already discussed spatial distributions of the radio brightness and spatially localized light curves, behavior of the degree of polarization typical for anisotropic pitch-angle distributions is frequently observed with NoRH. An example of the localized light curve (from one pixel of the magnetic loop leg) and corresponding time profile of the degree of polarization for the flare observed on 28-May-1993 is shown in figure 5. Remarkably, the absolute value of the degree of polarization keeps growing during the main peak of the burst, which is indicative for the increase of the anisotropy probably due to particle losses through the loss-cone, since other parameters affecting the polarization (magnetic field and the viewing angle) cannot change much at the localized region of the loop. The increase of the degree of polarization is followed by its decrease at a later stage of the burst. Interestingly, this turning point in the degree of polarization plot occurs at the same time as the break in the light curve where rapid decay of the radiation intensity slows down noticeably. This indicates that the losses due to precipitation into the loss-cone (which provides the anisotropisation of the electron distribution) are giving way to another decay

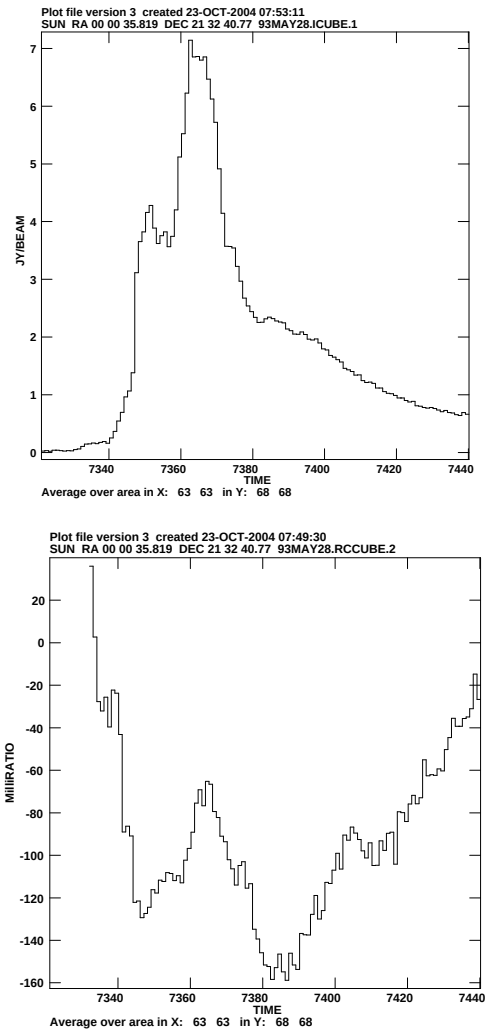

Fig. 5. A localized light curve (top) and and degree of polarization (bottom) for the 28-May-1993 event as observed at 17 GHz with NoRH (courtesy by T.S.Bastian).

process, probably, to Coulomb losses of already accumulated fast electrons. The Coulomb losses result it harder electron spectra, which generate GS radiation with weaker polarization.

A prominent spectral signature of the pitch-angle anisotropy has been found from the detailed analysis of two-component radio bursts composed of a high-frequency GS component and lower-frequency coherent component (Fleishman et al. 2003) observed with OVSA. Indeed, the microwave sources (accompanying the coherent dm spiky emission) observed at QP viewing angles to the magnetic field, figure 6, displays remarkably softer spectra at the optically thin region, than all other events on average, which can only be understood within the effect of loss-cone angular anisotropy on the GS spectrum. Moreover, all of the microwave bursts were highly polarized in the optically thin range (Fleishman et al. 2003), which is most probably related to the pitch-angle anisotropy of the loss-cone type (see figures 2, 3).

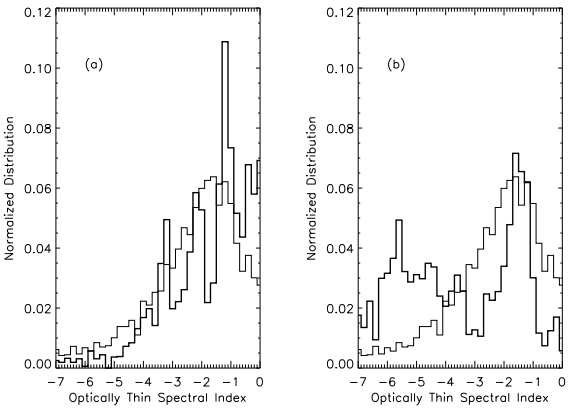

Fig. 6. The histograms of the high-frequency microwave spectral indices (Fleishman et al. 2003) for all bursts recorded by OVSA during 2001 (thin line), superimposed on the corresponding histogram for spike-producing microwave bursts observed at QT viewing angle (left) and QP viewing angle (right), thick lines. Strong excess of the steep spectra is observed in the QP case.

The difference in the spectral indices for these two classes of spike-producing microwave bursts (QT and QP) is as high as 3-4, which implies some important constraints on the shape of the angular distribution function. For example, the exponential decrease of the number of electrons in the loss-cone (5) turns to be too slow to provide the observed difference of 3-4 in spectral indices of optically thin GS emission at QP and QT directions (figure 3, right column). However, the gaussian loss-cone distribution (6) can evidently provide the required difference in the optically thin spectral indices (figure 3, left column). One can also note, that the gaussian loss-cone distribution provides stronger degree of polarization in the optically thin range than the exponential loss-cone distribution.

6. Electron Cyclotron Maser Emission

It is clear and has been well-known for a long time, that the pitch-angle anisotropy can drive instabilities, in particular, ECM instability. In essence, ECM emission is a coherent GS emission arising around lowest harmonics of the gyrofrequency when the absorption coefficient changes the sign and turns to be the amplification coefficient.

The theory of ECM emission in the solar corona has been extensively developed for the recent years (see Fleishman (2004a) for more detailed discussion and references). Big efforts have been made to consider the linear stage of the instability to specify the fastest growing wave-mode as a function of the plasma parameter $Y = \omega_{pe}/\omega_{Be}$, where ω_{pe} is the electron plasma frequency and ω_{Be} is the electron gyrofrequency.

Then, a particular attention has been paid to the role of absorption by the background coronal plasma in either emission source or along the ray path (in the harmonic gyrolayers) (Sharma et al. 1982; Sharma & Vlahos 1984). The absorption in gyrolayers was found to represent a severe problem for the ECM emission to escape the corona (Sharma & Vlahos 1984), since the optical depth of the second gyrolayer calculated with the maxwellian background distribution is typically much larger than unity. However, estimates of nonlinear absorption (when the background distribution is modified by the incident powerful radiation) (Huang 1987) and particle-in-cell simulations (McKeen et al. 1990) show that even fundamental ECM emission has a chance to escape. Nevertheless, it remains unclear if the nonlinear absorption actually happens in solar conditions or not (and, accordingly, which harmonics can really escape the source to the observer).

Nonlinear stage of the ECM instability has also been studied. *One-dimensional* particle-in-cell simulations (Pritchett 1986) were found to agree well with a simplified analytical approach (Wu et al. 1981). The one-dimensional quasilinear saturation of the instability gives rise to a plateau formation in the distribution function of fast electrons over the transverse (to the magnetic field) velocity, providing, therefore, an absolute stabilization of the electron distribution. This means, that only the wave-mode with the largest growth rate can be amplified substantially, while weaker growing wave-modes remain practically unamplified.

The quasilinear relaxation is well known to occur rather differently for the *two-dimensional* case (Akhiezer et al. 1974) relevant to the ECM emission. Indeed, the relaxation due to the dominant mode affects the electron distribution in such a way that the new (modified) distribution is stable against this particular wave-mode. However, this new state is not necessarily stable against generation of other wave-modes, i.e., it is not absolutely stable distribution. Thus, other wave-modes can well continue to grow until they start to affect the electron distribution in their turn.

Two-dimensional fully relativistic numerical calculations of the ECM quasilinear relaxation (Aschwanden 1990) revealed many important properties of the relaxation process against the fastest growing mode. However, the initial sin-N distribution function adopted for the calculations has artificially large angular gradient in the range of pitch-angles practically free from fast electrons as has been already discussed in figure 1. Quasilinear relaxation has further been studied numerically for a particular set of the involved parameters when the lower-hybrid wave-mode has the largest growth rate (Fleishman & Arzner 2000). The electron distribution was shown to remain clearly anisotropic after the relaxation against the lower-hybrid waves. The new anisotropic distribution is, however, stable against the lower-hybrid waves, although unstable against the electromagnetic wave-modes in agreement with the general results of the plasma physics (Akhiezer et al. 1974). In addition, the time profile of the generated wave energy density was found to resemble the observed spike time profiles (Güdel & Benz 1990). Nevertheless, the ECM saturation process has not been studied in detail yet, thus, additional studies of the quasilinear relaxation against electromagnetic wave-modes are necessary.

The role of coronal inhomogeneities both in ECM source and at the ray path was analyzed. Effect of MHD-waves on the longitudinal transparency window (Robinson 1991a) and on the efficiency of the mode conversion (Robinson 1991b) was studied. Then, ECM line formation in a source with random inhomogeneities was found to produce either spectral broadening or splitting of the initial peak depending on the strength of the inhomogeneity (Fleishman 2004b). Mutual action of regular coronal non-uniformity and random local inhomogeneities was considered for a beam-like electron distributions (Vlasov et al. 2002).

In the previous section we concluded that the gaussian loss-cone function (6) is a good candidate for the electron pitch-angle distribution in the main source of continuum GS emission in the spike-producing events. Let us consider here the main properties of ECM emission produced by fast electrons with this angular distribution and power-law distribution over momentum modulus to be compared with the observed properties of the radio spikes appeared at the main phase of the burst. The results presented below are obtained numerically from fully relativistic calculations of the exact expressions of the GS absorption coefficient.

6.1. Basic parameters.

The growth rate value depends on many parameters, therefore, we first selected a set of basic parameters and then varied each of them successively. This approach allows to discuss properly what effect is produced by each particular parameter.

For our calculations we selected two basic values of the plasma frequency to gyrofrequency ratio, $Y = \omega_{pe}/\omega_{Be} =$ 1, 1.3. When $Y = 1$, the most rapid growth of the extraordinary waves occurs at the second harmonics, $s = \omega/\omega_{Be} \approx 2$ and of the ordinary waves at the fundamental, $s \approx 1$, while for $Y = 1.3$ the growth of O1 waves becomes ineffective, and it is giving way to O2 waves.

The angular distribution (6) depends on two parameters: loss-cone angle θ_c and the width of the distribution $\Delta\mu$. We selected $\theta_c = 60^o$ and $\Delta\mu = 0.15$. The later value allows the instability to operate in the moderately-above-threshold regime. For the basic distribution of fast electrons over momentum we selected the following parameters typical for flares: $p_0/mc = 0.2$ ($E_{kin} \approx 10\ keV$), $p_{br}/mc = 3$ ($E_{kin} \approx 1.1\ MeV$) and $\gamma = 6$. It is assumed that at $p > p_{br}$ the power-law distribution is giving way to exponential cut-off.

6.2. Effect of plasma density.

The effect of plasma density on the growth rates at the lowest harmonics of the gyrofrequency was repeatedly studied for various electron distributions (Sharma et al. 1982; Sharma & Vlahos 1984; Li 1986; Winglee & Dulk 1986; Aschwanden 1990; Fleishman & Yastrebov 1994a; Fleishman & Yastrebov 1994b; Ledenev 1998; Stupp 2000; Fleishman 2004a). It has been established that for small $Y < 0.2-0.4$ the fundamental extraordinary waves (X1) have the largest growth rates. Then, for larger

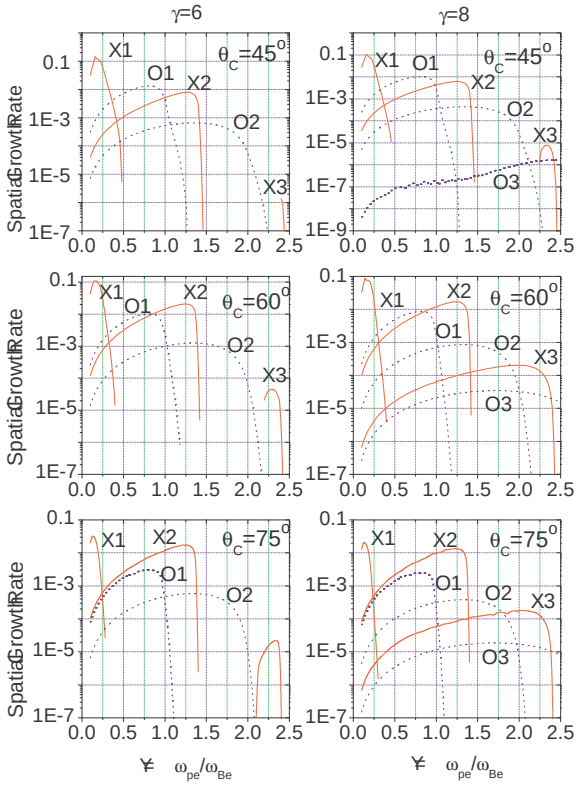

Fig. 7. Dimensionless spatial growth rates (normalized by $\frac{\pi\omega_{Be}}{2c}\frac{N_e}{N}$) for three first harmonics of the gyrofrequency for various parameters: $\gamma = 6$ (left column), $\gamma = 8$ (right column); $\theta_c = 45^o$ (top), $\theta_c = 60^o$ (middle), $\theta_c = 75^o$ (bottom). Set of basic parameters is used: $\Delta\mu = 0.15$, $p_0/mc = 0.2$, $p_{br}/mc = 3$.

Y, the amplification of X1 waves becomes inefficient and other waves become dominant (O1, X2, ...). Our calculations agree well with this standard picture (since it is largely related to kinematic restrictions).

The dependence of the growth rates on Y (for the adopted power-law momentum distribution and gaussian loss-cone angular distribution) in the limits $0.1 < Y < 2.5$ is given in figure 7. The growth rate of each harmonics decreases rapidly when the cut-off frequency of corresponding wave-mode exceeds the respective multiple of gyrofrequency (i.e., when $Y > 1$ for O1 waves, $Y > \sqrt{2}$ for X2 waves, $Y > 2$ for O2 waves etc). The absolute peak of the growth rate at a particular harmonics of the extraordinary waves is noticeably larger than of ordinary waves at the same harmonics. The absolute peak value decreases as the harmonic number increases.

The range of Y variation where a wave-mode is the fastest growing mode depends on parameters of the fast electron distribution. In particular, for small loss-cone angle value (top), the growth rates of O1 waves are larger than of X2 waves for $Y < 1$. However, the difference between them decreases as θ_c increases (middle) and X2 waves grow faster than O1 waves for large θ_c (bottom) in agreement with the finding by Winglee & Dulk (1986). Respectively, O1 mode grows faster than X2 mode if $Y < 1$ for $\theta_c = 45^o$, if $Y < 0.85$ for $\theta_c = 60^o$, and never for $\theta_c = 75^o$.

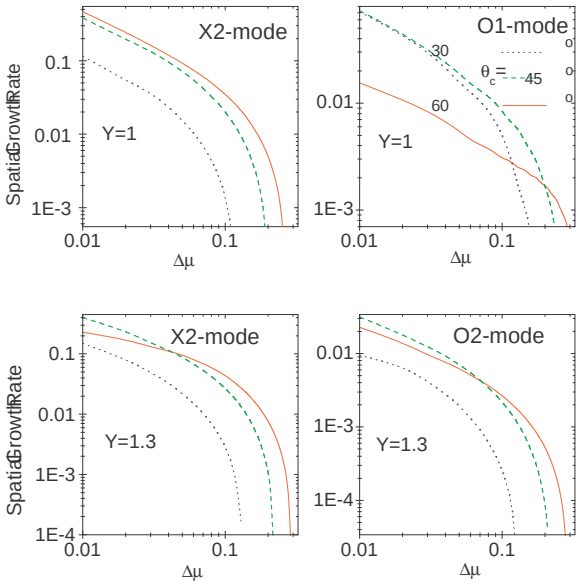

Fig. 8. Spatial growth rates for X2-, O1-, and O2- modes vs width of the loss-cone distribution $\Delta\mu$ for the basic set of parameters and three θ_c values.

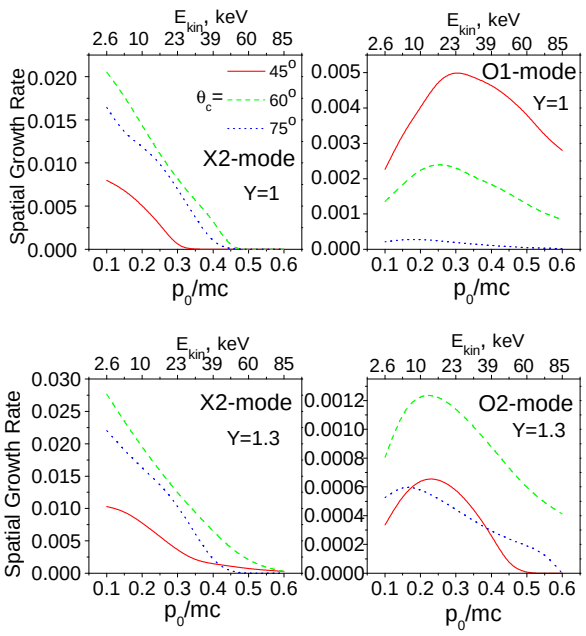

Fig. 9. Spatial growth rates for X2-, O1-, and O2- modes vs minimal momentum of fast electrons p_0 for the basic set of parameters and three θ_c values.

Then, for $Y > \sqrt{2}$ the O2 mode is the dominant, and for $Y > 1.8$ the X3 mode may dominate (if it is unstable for a particular set of parameters).

We note an interesting feature specific for our electron distribution: the amplification of the third harmonics of both extraordinary and ordinary waves is ineffective for hard electron spectra (e.g., $\gamma = 6$, left column) for most of the Y range, while it is effective for softer spectra (e.g., $\gamma = 8$, right column). The reason for the instability suppression for the hard spectrum is the destructive contribution of (true absorption by) high-energy electrons. For softer electron distributions the role of high-energy electrons is less important allowing the instability at the third harmonics. Note that for the gaussian angular distribution used in (Fleishman & Yastrebov 1994a, 1994b), the instability suppression by high-energy tail of power-law distribution is important even at the fundamental and second harmonics, since the gaussian distribution provides weaker angular gradients than considered here gaussian loss-cone distribution (6).

6.3. Effect of angular distribution.

The dependences of the maximized (over the emission frequency and angle) spatial growth rates on θ_c displays bell-shaped curves for any mode. The most effective amplification of O1 waves occurs around $\theta_c \approx 45^o$, while around $\theta_c \approx 60^o$ for O2 waves and even higher values for X2 waves. No qualitative difference is seen for various electron spectral indices γ.

Of particular importance is the dependence on the width of the distribution $\Delta\mu$, figure 8. Evidently, all the growth rates increase as $\Delta\mu$ decreases because this corresponds to stronger angular gradients, and, thus, to stronger instability. However, the growth rates decrease as $\Delta\mu$ increases first gradually and then rapidly. This rapid decrease occurs when the instability approaches its threshold provided by negative contribution of the momentum term ($\partial f/\partial p = -\gamma f$) in the expression for the GS absorption coefficient. When $\Delta\mu$ exceeds $0.1-0.3$ (depending on other parameters) the instability disappears. We emphasize that this happens when the pitch-angle distribution of fast electrons remains clearly anisotropic. Thus, such anisotropic distributions can generate standard GS emission without coherent ECM emission.

The detailed shape of the curves depends on other parameters, like Y and θ_c. For X2 and O2 waves, large θ_c values are preferable, while for O1 waves – lower θ_c values. However, for all considered cases, $\theta_c = 60^o$ has the largest threshold $\Delta\mu$ value.

6.4. Effect of distribution over momentum.

The growth rates of all considered wave-modes display rather weak dependence on p_{br} for the selected set of basic parameters, so we do not present the corresponding plots. We should note, however, that this property of the ECM emission is model-dependent and valid if the instability operates noticeably above the threshold. If the instability is very close to its threshold, the behavior of the momentum distribution in the high-energy range may be important. In particular, this is the case of gaussian pitch-angle distribution (Fleishman & Yastrebov 1994a, 1994b).

The dependence of the growth rates on the minimal momentum p_0 is shown in figure 9. Shape of the curves is clearly different for various harmonics and wave-modes. X2 waves display decreasing curves with increasing p_0,

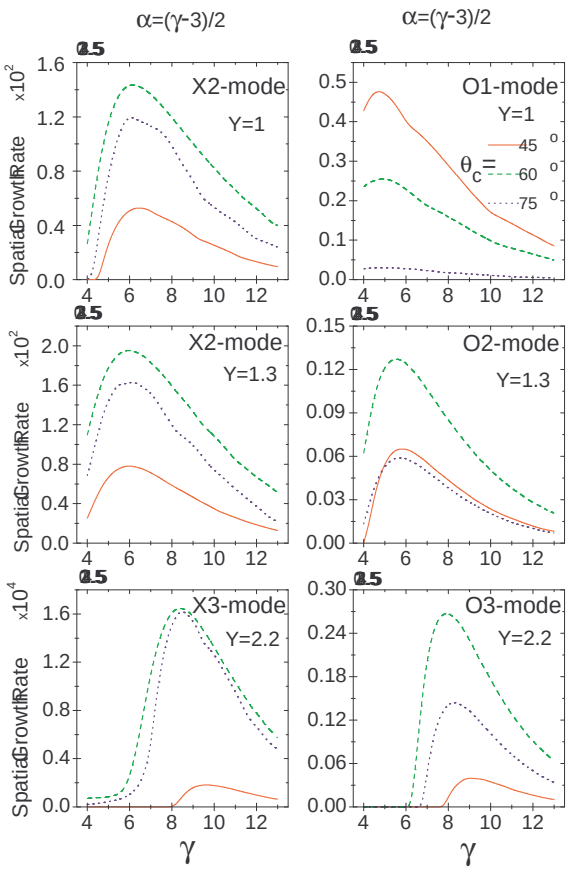

Fig. 10. Spatial growth rates for X2-, X3-, O1-, O2-, and O3- modes vs spectral index of fast electron distribution γ for the basic set of parameters and three θ_c values.

thus, low-energy electrons are preferable to produce these waves. Wide loss-cones ($\theta_c = 60^o$, 75^o) provide larger growth rates than narrower loss-cone ($\theta_c = 45^o$).

Ordinary waves are generated most effectively if the low-energy cut-off is about 20 keV for O2-mode and about 10 keV for O2 mode, although the corresponding peaks are rather broad. Narrow loss-cone ($\theta_c = 45^o$) is the most efficient to produce O1 waves and wider one ($\theta_c = 60^o$) is preferable to produce O2 waves. The wide loss-cone of $\theta_c = 75^o$ is less effective for the both harmonics of the ordinary waves.

Considering together the plots in figure 9, we can conclude that different fractions of fast electrons are responsible for generation of these different wave-modes. Thus, quasilinear relaxation against one (the dominant) mode should not necessarily provide saturation of all other wave-modes in agreement with numerical quasilinear simulations (Fleishman & Arzner 2000).

The dependences of the growth rates on the electron spectral index γ are of particular importance, since they can be compared with observations of accompanying continuum (microwave and HXR) emissions. All the curves shown in figure 10 are bell-shaped; peak of each curve corresponds to a favorable γ value specific for each wave-mode. The decrease of the growth rates for harder spectra (smaller γ) is provided by negative contribution of high-energy electrons at large harmonics. The decrease for softer spectra (larger γ) is related to the increase of the instability threshold that is proportional to γ for the power-law momentum distribution of the electrons.

The favorable γ value depends on the harmonic number and type of the wave. X2 waves have the peak around $\gamma = 6$ (which corresponds to the synchrotron spectrum with the index 1.5) for a broad range of the involved parameters. A bit lower values are favorable for O2 waves. However, O1 waves display the peak at rather small values $\gamma = 4 - 5$.

It is remarkable that the favorable γ values for the third harmonics are significantly larger than for the fundamental and second harmonics: it is about 8 (synchrotron spectral index 2.5) for O3 waves and even larger for X3 waves. Such a different behavior of the curves for the different waves can in principle be used to specify the contribution of various harmonics to the spike radiation.

7. Discussion

We conclude the pitch-angle anisotropy to affect significantly the radio emission from solar flares. First of all, we should mention the strong effect of the anisotropy on the intensity and spectral index of the emission in the optically thin region, which relates primarily to the energy-dependent directivity (1) of the synchrotron radiation by a single electron.

Currently, it is discovered with the NoRH data that microwave emission from the foot-point parts of extended flaring loops displays systematically softer spectra ($\Delta\alpha \sim$ 1-1.5 in the domain 17 GHz to 34 GHz) than from the loop-top part (Yokoyama et al. 2002; Melnikov 2005). Evidently, the pitch-angle anisotropy can make an important contribution to the observed spectral index variations. Indeed, if we take into account the convergence of the magnetic field lines towards the foot-points, we should expect a more anisotropic electron distribution (due to a larger loss-cone) in the foot-point source than in the loop-top source. Furthermore, for the disc flares the foot-point source is observed at a QP direction, while the loop-top source is observed at a QT direction, which results in *systematically* softer spectra of GS radiation from the foot points compared with the loop-top. Thus, the pitch-angle anisotropy probably plays a key role in the observed variations of the spectral index of the microwave radiation along the loop. Moreover, the pitch-angle anisotropy has strong effect on polarization properties of GS emission, which is widely observed with NoRH.

Coherent GS emission (ECM) is also highly relevant for understanding the current radio observations. The available data about the radio spikes are pretty consistent with the idea that the source of spike cluster is a loop filled by fast electrons and relatively tenuous background plasma (Fleishman et al. 2003). The trapped fast electrons (with a power-law energy spectrum and a loss-cone angular distribution) produce continuum GS emission through the

entire loop, while each single spike is generated in a *local* source inside this loop by ECM mechanism when some favorable conditions are fulfilled. Most probably, the local source is formed when the local anisotropy is increased compared with the averaged one to produce ECM emission (Fleishman & Melnikov 1998). The assumed fluctuations of the pitch-angle distribution of fast electrons can be produced by the magnetic turbulence (Fleishman & Melnikov 1998; Barta & Karlicky 2001). Accordingly, if the averaged angular distribution is stable against ECM generation, the number of spikes in an event should increase as the intensity of the magnetic turbulence increases (and other equal conditions). Complementary, the closer the averaged angular distribution to the instability threshold, the larger the amount of the local sources (and, respectively, the number of spikes) might be formed by the same magnetic turbulence.

The scale of a single spike source is estimated (indirectly) as $\sim 200\ km$ (Benz 1985); a wave should experience many e-folding amplifications over this length to produce observable spike with large brightness temperature, so this requirement reads $\kappa \gg 5 \cdot 10^{-8} cm^{-1}$, where κ is the spatial amplification coefficient. We conclude (from the numbers in figure 7) that the required amplification can easily be provided for the fundamental and second harmonics of both X- and O- modes. Moreover, the amplification of X3 mode is also possible if fast particles are numerous enough, $N_e/N \gtrsim 10^{-2}$, while the amplification of O3 mode is less probable.

The dependence of the growth rate on the fast electron distribution is of primary importance since it can be compared with the observations. Indeed, the decrease of the growth rates with the γ increase corresponds to smaller efficiency of the ECM emission for softer spectra of fast electrons. The correlation of this type is actually observed when spectra of microwave or HXR emission simultaneous to spike bursts are analyzed: the harder the fast electron spectrum the stronger the averaged spike flux (Fleishman et al. 2003). The range of microwave spectral indices is typically $\alpha = 1 - 4$. Thus, we can conclude that most of the spikes are generated at a harmonics not larger than second. ECM emission at the third harmonics (see Figure 10) is the most efficient if $\gamma \approx 8$ ($\alpha \approx 2.5$), therefore, the softer microwave spectra should be preferable for the third harmonics generation in the range $\alpha < 2.5$, which has not been observed for spikes yet.

Then, the dependences on the angular gradient value ($\Delta\mu$) display clearly that the instability disappears (as $\Delta\mu$ increases) when the pitch-angle distribution still remains highly anisotropic ($\Delta\mu = 0.2 - 0.3$). Accordingly, the overall distribution of fast electrons accumulated at the loop may be rather anisotropic for a long time providing noticeably softer GS spectra (for a QP viewing angle) than the isotropic distribution, which is observed indeed (Fleishman et al. 2003).

Acknowledgments

The National Radio Astronomy Observatory is a facility of the National Science Foundation operated under cooperative agreement by Associated Universities, Inc. This work was supported in part by NSF grant AST-0307670 and NASA grant NAG5-11875 to New Jersey Institute of Technology, and by the Russian Foundation for Basic Research, grants No.02-02-39005, 03-02-17218.

References

Akhiezer, A.I., Akhiezer, I.A., Polovin, R.V., Sitenko, A.G., & Stepanov, K.N. Plasma Electrodynamics, (Ed. - A.I.Akhiezer), Moscow, Nauka 1974 (Pergamon, Oxford, 1975)
Altyntsev, A.T. 2005, Proc. of Nobeyama Symposium
Aschwanden, M.J. 1990, A&AS, 85, 1141
Aschwanden, M.J., & Güdel, M. 1992 ApJ, 401, 736
Barta, M., & Karlicky, M. 2001, A&A, 379, 1045
Bastian, T.S. 2005, Proc. of Nobeyama Symposium
Bastian, T.S., Benz, A.O, & Gary, D.E. 1998, ARAA, 36, 131
Benz, A.O. 1985, Sol. Phys., 96, 357
Fleishman, G.D. 2004a, Astron. Zh., 81, 72 (transl.: Astron. Repts., 48, 65)
Fleishman, G.D. 2004b, ApJ, 601, 559
Fleishman, G.D., & Arzner, K. 2000, A&A, 358, 776
Fleishman, G.D., Gary, D.E., & Nita, G.M. 2003, ApJ, 593, 571
Fleishman, G.D., & Melnikov, V.F. 1998, Physics - Uspekhi, 41, 1157
Fleishman, G.D., & Melnikov, V.F. 2003a, ApJ, 584, 1071
Fleishman, G.D., & Melnikov, V.F. 2003b, ApJ, 587, 823
Fleishman, G.D., & Yastrebov, S.G. 1994a, Sol. Phys., 153, 389
Fleishman, G.D., & Yastrebov, S.G. 1994b, Astron. Zhurn., 71, 531
Gary, D.E. 2005, Proc. of Nobeyama Symposium
Güdel, M., & Benz, A.O. 1990, A&A, 231, 202
Huang, G.-L. 1987, Sol. Phys., 114, 363
Kennel, C.F., & Petscheck, H.E. 1966, J. Geophys. Res., 71, 1
Kundu, M.R., Nindos, A., White, S.M., & Grechnev, V.V. 2001, ApJ, 557, 880
Lee, J., & Gary, D.E. 2000, ApJ, 543, 457
Ledenev, V.G. 1998, Sol. Phys., 179, 405
Li, H.W. 1986, Sol. Phys., 104, 131
McKeen, M.E., Winglee, R.R., & Dulk, G.A. 1990 in Proc. of 3th Workshop Max'91 Solar Flares (Eds. R.R.Winglee & A.L.Kiplinger), Colorado, Boulder, p.29
Melnikov, V.F. 2005, Proc. of Nobeyama Symposium
Melnikov, V.F., Shibasaki, K., Nakajima, H., Yokoyama, T. & Reznikova, V.E. 2001, CESRA Workshop (München, 2-6 July 2001)
Melnikov, V.F., Shibasaki, K., & Reznikova, V.E. 2002a, ApJL, 580, L185
Melnikov, V.F., Reznikova, V.E., Yokoyama, T., and Shibasaki, K. 2002b, in: Proc. of the SPM-10 "Solar Variability: From Core to Outer Frontiers", Prague (ESA SP-506, December 2002), ed. A.Wilson, p.p.339-342
Melrose, D.B., & Brown, J.C. 1976, MNRAS, 176, 15
Pritchett, P.L. 1986, Phys. Fluids, 29, 2919
Robinson, P.A. 1991a, Sol. Phys., 134, 299
Robinson, P.A. 1991b, Sol. Phys., 136, 343

Sharma, R.R., & Vlahos, L. 1984, ApJ, 280, 405
Sharma, R.R., Vlahos, L., & Papadopoulos, K. 1982, A&A, 112, 377
Stupp, A. 2000, MNRAS, 311, 251
Vlasov, V.G., Kuznetsov, A.A., & Altyntsev, A.T. 2002, A&A, 382, 361
Winglee, R.R., & Dulk, G.A. 1986, Sol. Phys., 104, 93
Wu, C.S, Tsai, S.T., Xu, M.J., & Shen, J.W. 1981, ApJ, 248, 384
Yokoyama, T., Nakajima, H., Shibasaki, K., Melnikov, V.F., & Stepanov, A.V. 2002, ApJL, 576, L87

Radio diagnosis of coronal magnetic field, non-thermal electrons, and fine structures associated with microwave bursts

Huang Guangli *
Purple Mountain Observatory, Chinese Academy of Science, Nanjing, China
glhuang@pmo.ac.cn

Abstract

Key words: magnetic field — non-thermal electrons — magnetic reconnection — microwave bursts

1. Introduction

It is necessary to solve two key problems before any models of solar flares or coronal mass ejections (CMEs) are well compared with solar observations (Forbes, 2004).

1. How to measure coronal magnetic field and to get the favor magnetic configuration in corona, where flares and CMEs are triggered by magnetic reconnections.

2. How to determine the exact time and location of magnetic reconnections if the scale of current sheets are much smaller than the spatial resolution of present solar telescopes.

It is well known that radio observations under different radiation mechanisms may provide a unique diagnosis of coronal magnetic field and the non-thermal electrons. Some techniques for radio measurements of the magnetic fields in both chromosphere and corona were reviewed by Kundu (1990), such as the measurement of polarization at millimeter bands for estimating the magnetic field in the active regions of chromosphere, the properties of gyroresonance radiation in microwaves for estimating the magnetic field in corona above the active regions, and a direct measurement of the coronal magnetic field using cyclotron line emission. The author of this paper will pay attention only to the radio diagnosis of coronal magnetic field and non-thermal electrons associated with microwave bursts, which means the radiation mechanism in this case is dominated by the non-thermal gyro-synchrotron emissions and relevant absorptions.

On the other hand, the fine structures (FS) at decimeter and centimeter bands have been intensively studied with observations of the radio dynamic spectra in recent solar circles. It is believed that these FS may be considered as the radio signatures of magnetic reconnections and particle acceleration. For example, the start frequencies of type *III* bursts are emitted at the level in corona where non-thermal electrons are accelerated. The radio millisecond spikes may be more closed to the acceleration site than type *III* bursts (Benz et al., 1982). Especially, the bidirectional frequency drifts caused by the electron beams accelerated from reconnection site in two opposite directions may show the level of reconnection site in corona at the reversal frequencies (Robison et al. 2000; Xie et al. 2000; Huang et al. 1998, 2004a). Moreover, type *II* or *IV* bursts and relevant FS (such as zebra strips) are closely associated with shock waves and CMEs (Mclean, 1985), their start frequencies correspond to the level in corona where the speed of CMEs is larger than the local Alfvén speed.

The time and frequency resolutions become as high as possible in some recent solar radio spectrographs for observing the FS. But it is difficult to locate the compact sources of these FS in solar disk for understanding their relationship with the other solar resolvable observations. Before some new radio telescopes with high spatial, temporal, and frequency resolutions (such as FASR) are completed in near future, it is considerable to use the radio data with spatial resolutions, such as the Nobeyama Radio Heliograph (NoRH) and etc, together with the data of radio spectrographs for the researches on the radio diagnosis of coronal magnetic field, non-thermal electrons, and fine structures associated with microwave bursts. Some recent works are reviewed in this paper.

2. Diagnosis of coronal magnetic field and non-thermal electrons

2.1. Approximations used by Dulk & Marsh

Dulk & Marsh (1982) managed to simplify generally the complicated expressions for gyro-synchrotron emissions (Krüger, 1979) in a series of exponential forms that can be related to observations, but that the magnetic field, the density of non-thermal electrons, and the propagation angle are given in an implicit, and thus not practical form. Based on the approximation used in Dulk & Marsh (1982), the explicit expressions of the coronal magnetic field and the line-of-sight number of non-thermal electrons versus brightness temperature, frequency, turnover frequency, and spectral index were proposed by Zhou & Karlický (1994) and Huang & Zhou (1999) for solar microwave bursts with non-thermal gyro-synchrotron radiation mechanism.

$$B = \left[\frac{c^2}{k_B T_{b\nu} A_1}\nu_p^{1.3+0.98\delta}\nu^{-0.78-0.9\delta}\right]^{\frac{1}{0.52+0.08\delta}} \quad (1)$$

* The author would like to thank the SOC of Nobeyama Symposium, 2004 for the review paper in the Proceedings. This study is supported by the NFSC projects No.10333030 and 10273025, and "973" program with No.G2000078403.

$$A_1 = 4.24\times10^{14+0.3\delta}(\sin\theta)^{0.34+0.07\delta}\times$$
$$\times(2.8\times10^6)^{2.52+0.08\delta} \quad (2)$$

$$NL = T_{b\nu}\Big(\frac{k_B\nu^2}{c^2}\Big)A_2^{-1}B^{-1} \quad (3)$$

$$A_2 = 3.3\times10^{-24-0.52\delta}(\sin\theta)^{-0.43+0.65\delta}\Big(\frac{\nu}{\nu_B}\Big)^{1.22-0.9\delta} \quad (4)$$

Here, B is the magnetic field strength. c is the velocity of light in vacuum. k_B is the Boltzmann constant. $T_{b\nu}$ and S_ν are respectively the brightness temperature and the radio flux at a given frequency ν in the optical thin part of the microwave spectra. ν_p is the peak or the turnover frequency. ν_B is the electron gyro-frequency. θ refers to the angle between wave vector and magnetic field. δ is the energetic spectral index of non-thermal electrons with a single power law distribution, and $\delta = (1.22-\gamma)/0.9$, γ is the radiation spectral index (Dulk & Marsh, 1982).

However, the propagation angle θ is still remained as a free or unmeasurable parameter in these expressions. Hence, the coronal magnetic field and the density of non-thermal electrons can not be calculated self-consistently using Eqs.(1)-(4). One method was proposed by Huang & Nakajima (2002) to solve the propagational angle with the polarization degree r_c (Dulk, 1985), together with brightness temperature, frequency, turnover frequency, and spectral index.

$$r_c = 1.26\times10^{0.035\delta}10^{-0.071\cos\theta}\Big(\frac{\nu}{\nu_B}\Big)^{-0.782+0.545\cos\theta} \quad (5)$$

which is rewritten as an equation of x ($x=\sin\theta$):

$$x^2 + \left(\frac{c_2+c_3\log_{10}x}{c_4+c_5\log_{10}x}\right)^2 = 1 \quad (6)$$

All of the coefficient in Eq. (6) are measurable and defined in Huang & Nakajima (2002). After the angle is solved from Eq. (6), the 2-dimensional distribution of the coronal magnetic field strength is calculated self-consistently in one event on Nov. 28, 1998 observed by NoRH. Fig.1 shows the contours (100-600 Gauss) of the calculated magnetic field strength overlaid on the brightness temperature of NoRH at 17 GHz in different times of the microwave burst. In fact, two components of magnetic field parallel and perpendicular to the wave vector are obtained in these calculations with the solved propagational angles.

Another way to solve the angle was obtained by Huang (2004b) with the expression of the turnover frequency in Dulk (1985).

$$\nu_p \approx 2.72\times10^{3+0.27\delta}(\sin\theta)^{0.41+0.03\delta}(NL)^{0.32-0.03\delta}$$
$$\times B^{0.68+0.03\delta} \quad (7)$$

the logarithm of Eqs.(1), (3) and (7) will lead to three linear equations of B, NL, and θ, which are readily solved to get three explicit expressions of B, NL, and θ versus ν, $T_{b\nu}$, δ, and ν_p as shown in Eqs.(8)-(10) (Huang, 2004b):

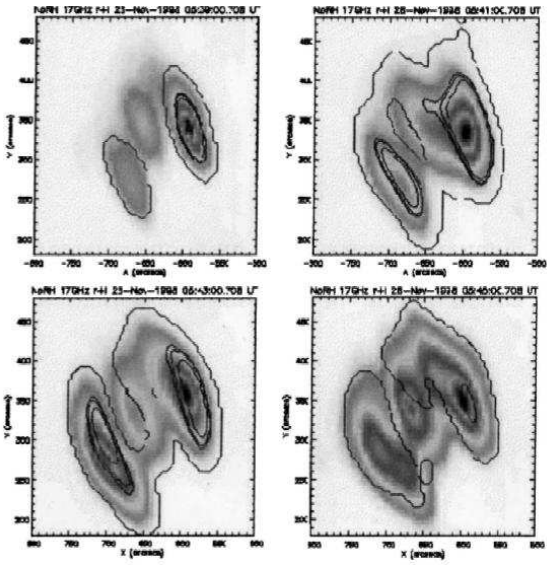

Fig. 1. The contours (100-600 Gauss) of the calculated magnetic field strength overlaid on the brightness temperature of NoRH at 17 GHz in different times of a microwave burst on Nov. 28, 1998.

$$\sin\theta = 10^{f_{11}(\delta)}T_{b\nu}^{f_{12}(\delta)}\nu^{f_{13}(\delta)}\nu_p^{f_{14}(\delta}) \quad (8)$$

$$NL = 10^{f_{21}(\delta)}T_{b\nu}^{f_{22}(\delta)}\nu^{f_{23}(\delta)}\nu_p^{f_{24}(\delta}) \quad (9)$$

$$B = 10^{f_{31}(\delta)}T_{b\nu}^{f_{32}(\delta)}\nu^{f_{33}(\delta)}\nu_p^{f_{34}(\delta}) \quad (10)$$

All of these coefficients are defined as the functions of δ (Huang, 2004b). The general calculations from Eqs.(8)-(10) for the relationship of B versus ν, $T_{b\nu}$, δ, and ν_p are displayed in Fig.2. When $\delta < 3.5$, B is monotonously increasing with ν and $T_{b\nu}$ respectively, and decreasing with ν_p. When $3.5 \le \delta < 6.0$, B is monotonously decreasing with ν and $T_{b\nu}$ respectively, and increasing with ν_p. When $\delta \ge 6.0$, B is again monotonously increasing with ν and $T_{b\nu}$ respectively, and decreasing with ν_p. Hence, B is a non-monotonic function of δ for given ν, ν_p, and $T_{b\nu}$.

On the other hand, the relationship of the line-of-sight number of non-thermal electrons with ν_p, ν, and $T_{b\nu}$ respectively does not change with different values of δ. NL is always monotonously increasing with ν and T_b respectively, and decreasing with ν_p. Hence, NL is a monotonic function of δ, and NL always increases with increasing the value of δ for a given ν, ν_p, and $T_{b\nu}$.

2.2. Ramaty and Takakura's model

It is emphasized that the approximations used by Dulk & Marsh (1982) are only available for $2 < \delta < 7$, $10 < s < 100$ (s is harmonic number), low energy cutoff equals $10keV$, $\theta \sim 20^\circ - 80^\circ$, ν_p defined as the frequency at the optical depth $\tau \approx 1$, and the emission of X-mode. Also, these approximations can be used only for a simple and isolated source without significant changes of the magnetic field, the angle and etc, along the line-of-sight within the emission region.

The more strict model of non-thermal gyro-synchrotron

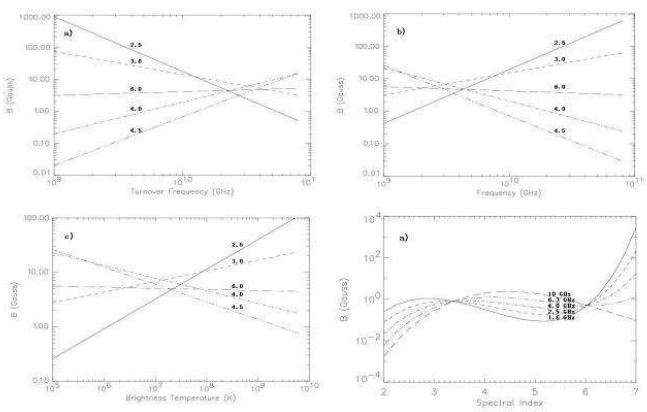

Fig. 2. The calculated magnetic field B versus a. ν_p with ($\nu = 10^{11} Hz$ and $T_{b\nu} = 10^6 K$, b. ν with $T_{b\nu} = 10^6 K$ and $\nu_p = 10^9 Hz$, and c. $T_{b\nu}$ with $\nu = 2.0 \times and 10^9 Hz$, $\nu_p = 10^9 Hz$. The value of δ is selected as 2.5 with solid line, 3.0 with short--dashed line, 4.0 with dot-dashed line, 4.5 with dot-dot-dot–dashed line, and 6.0 with long-dashed line, respectively. The panel d. for the calculated magnetic field B versus the spectral index with $\nu = 10^{10} Hz$, $T_{b\nu} = 10^6 K$, and different values of ν_p from 1.6 GHz to 10.0 GHz.

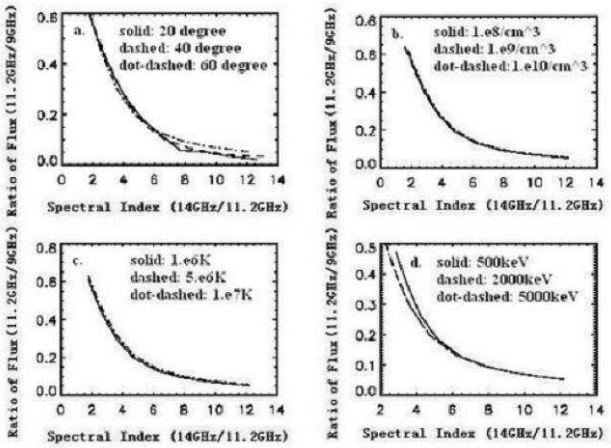

Fig. 3. The effects of different p_{max}, N, T, and θ on the graph of the ratio of flux at 11.2 GHz and 9 GHz versus γ calculated from the ratio of flux at 14 GHz and 11.2 GHz. a. $\theta = 20, 40, 60°$, $N = 10^9 cm^{-3}$, $T = 5 \times 10^6 K$, $E_{max} = 5MeV$, b. $N = 10^8, 10^9, 10^{10} cm^{-3}$, $\theta = 60°$, $T = 5 \times 10^6 K$, $E_{max} = 5MeV$, c. $T = 10^6, 5 \times 10^6, 10^7 K$, $\theta = 60°$, $N = 10^9 cm^{-3}$, $E_{max} = 5MeV$, d. $E_{max} = 0.5MeV, 2MeV, 5MeV$, $\theta = 60°$, $N = 10^9 cm^{-3}$, $T = 5 \times 10^6 K$. Some parameters are fixed, such as B_0=800 Gauss, δ =2-7, $E_{min} = 10keV$ in all panels.

radiations with a single power-law distribution ($F(E) = AE^{-\delta}$) are derived by Ramaty (1969) and Takakura et al. (1970), in which the thermal cyclotron resonant absorption and a dipole magnetic field are considered. The Razin effect and self-absorption may be neglected at higher frequencies or optical-thin part.

$$T_{b\nu_\mp} = \frac{A\pi e^2 cd}{3k_B}(2.8 \times 10^6 B_0)^{1/3} F_{\nu_\mp}, \quad (11)$$

$$F_{\nu_\mp} = \int \eta_{\nu_\mp} s^{-2/3} \exp^{-\sum_{s+1}^{6} \tau_{js}} ds \quad (12)$$

$$\eta_{\nu_\mp} = \frac{1}{2|\cos\theta|} \sum_{n=s+1} \int_{p_{min}}^{p_{max}} (a \pm b)^2 \frac{(\sqrt{1+p^2}-1)^{-\delta}}{1+p^2} dp \quad (13)$$

$$\tau_{js} = \frac{\pi e^2}{m_0 c}(\frac{k_B T}{m_0 c^2})^{s-1} \frac{s^{2s}}{2^s s!} dN\nu(\sin\theta)^{2(s-1)} \times n_\pm \quad (14)$$

$$n_\pm = \frac{(\sin^2\theta + 2s\cos^2\theta \pm \sqrt{\sin^4\theta + 4s^2\cos^2\theta})^2}{\sin^4\theta + 4s^2\cos^2\theta \pm \sin^2\theta\sqrt{\sin^4\theta + 4s^2\cos^2\theta}}. \quad (15)$$

Here, $T_{b\nu_\mp}$, $F_{\nu_\mp}$, and $\eta_{\nu_\mp}$ are respectively brightness temperature, flux, and emissivity at a give frequency ν. The sign of $\mp$ refers to the ordinary or extraordinary modes in the cold plasma dispersion relation. m_0 is the mass of an electron. B_0 is the magnetic field in photosphere. d is the scale of the dipole magnetic field. N and T are respectively the density and the temperature of the ambient plasma. p_{min} and p_{max} are the momentum in respect to E_{min} (low cutoff energy) and E_{max} (high cutoff energy).

There are more free parameters in Eqs.(11)-(15) than that in the approximations used by Dulk and Marsh (1982), such as A, B_0, p_{min}, p_{max}, N, T, and θ. The effects of θ, N, T, and p_{max} on the calculations are shown by the ratio of flux at 11.2 GHz and 9 GHz versus γ calculated from the ratio of flux at 14 GHz and 11.2 GHz, in which $\theta = 20, 40, 60°$, $N = 10^8, 10^9, 10^{10} cm^{-3}$, $T = 10^6, 5 \times 10^6, 10^7 K$, $E_{max} = 0.5MeV, 2MeV, 5MeV$, respectively from left-top to right-bottom panel (Huang, 2004c). The coefficient A of power-law is just cancelled by the ratio between two frequencies. It is evident that the variation of θ, N, T, and p_{max} with typical values ranged in corona only make small difference in the curves of Fig.3.

When the magnetic field B_0 is 200, 500, and 800 Gauss, the calculated curves are separated evidently in Fig.4. Hence, the local magnetic field is a very sensitive parameter to the calculations (Huang, 2004c).

Moreover, the variation of E_{min} from 10-90 keV also has strong effect on the calculations as shown in Fig.5.

Therefore, some insensitive parameters may be fixed, such as θ, N, T, and p_{max}, but the magnetic field and the low energy cutoff have to be solved together. On the other hand, the low energy cutoff is fixed as 10 keV in the approximations used by Dulk & Marsh (1982). So, the calculations of Eqs.(1)-(10) are still not self-consistent. On the other hand, if the range of low energy cutoff is limited in small values such as 10-30 keV (Huang, 2004c), Eqs.(1)-(10) may be a good approximations of magnetic field and non-thermal density.

A more recent calculations with Eqs.(11)-(15) show the density of non-thermal electrons in loop top source is always larger than that in foot point source in two examples of NoRH (Fig.6), in one of which foot points are much strong than loop top, but in another event, the loop top

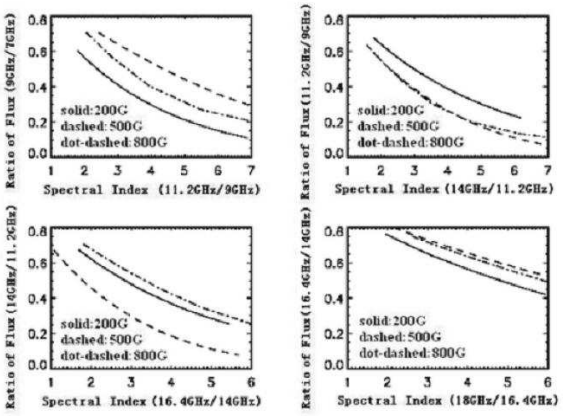

Fig. 4. The magnetic field B_0 is 200 (solid), 500 (dashed), and 800 (dot-dashed) Gauss respectively for different ratio and γ ($(\delta = 5,\ \theta = 60^\circ,\ N = 10^9 cm^{-3},\ T = 5 \times 10^6 K,\ E_{min} = 10keV,\ E_{max} = 5MeV$).

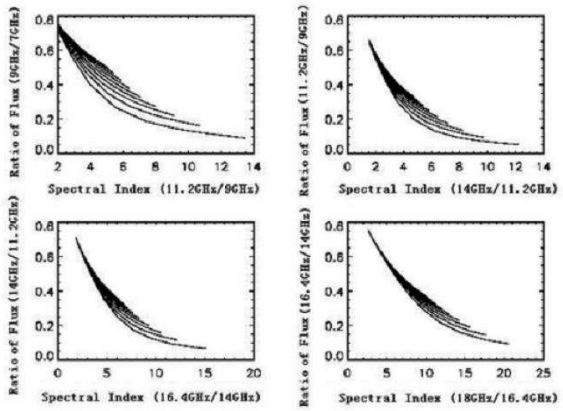

Fig. 5. The magnetic field B_0 is 800 Gauss for different ratio and γ, $E_{min} = 10 - 90keV$, respectively from bottom to top of each panel, $N = 10^9 cm^{-3}$, $T = 5 \times 10^6 K$, $E_{max} = 5MeV$, $\theta = 60^\circ$, $\delta = 2 - 7$.

is much stronger than foot points (Zhou et al., 2004).

3. Diagnosis of the location of radio fine structures

3.1. Millisecond spikes at 2.6-3.8 GHz

Solar radio millisecond spikes are recognized as the solar magnetic activities with the smallest time and space scale, and well associated with HXR elementary bursts, as well as evidence for the coherent plasma emission and particle acceleration with short time scale originated from magnetic reconnections sites or shock fronts. The millisecond spikes are often detected in decimeter bands (Benz, 1986), with time scales of several ten or hundred milliseconds, narrow bandwidth of 2-5 percent, and fast drift rate of several tens to hundreds MHz per second.

It is difficult to locate the sources of spike emissions due to their very compact size (hundreds or even tens km) predicted from the short time scale and narrow bandwidth. Some measurements were reported by Krucker et al. (1995, 1997) with VLA at 333 MHz and YOHKOH/SXT, respectively. A scenario is proposed where the energy is released in or near the spike source, and in which the spikes, the type *III* bursts and the thermal source originate from the same energy release. Another measurement was reported by Altyntsev et al. (1995) with SSRT at 5.7 GHz, the source size is unexpected large (tens arcsec) may be caused by the strong angular scattering at centimeter bands (Bastian, 1994).

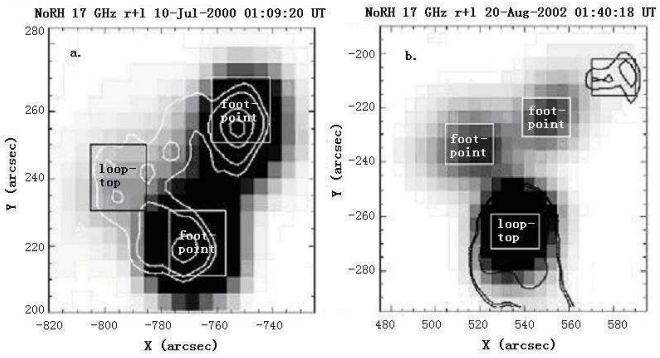

Fig. 6. a. The NoRH image at 17 GHz on July, 10, 2000. b. The NoRH image at 17 GHz on Aug 20, 2002.

One event on Nov.2, 1997 is studied at 2.6-3.8 GHz with high time (8 ms) and frequency (10 MHz) resolutions (Huang, 2004d). Several spikes with lifetime of tens ms and relative bandwidth of 2-3% were superposed on the ambient burst (Fig.7). The most interesting feature of one spike at 03:04:54.6 UT (marked in Fig.7) is a very fast frequency drift (several GHz/s) in bi-direction with reversal frequency at about 3 GHz (Fig.8), which is important to determine the level of magnetic reconnection in corona (Liu et al., 2002).

Figs.9-10 show the NoRH contours at 17 GHz overlaid on YOHKOH/SXT and SOHO/MDI images around the time of spike emissions. The radio source is composed of one extended source is embedded in a large and bright soft X-ray loop system, and a compact source located at one foot-point of a small soft X-ray loop. The magnetic field is simplified as a dipole with multiple positive (white) and negative (black) polarities. The 17 GHz contours are marked by "a" (compact source), and "b, c, d, e, f" (extended source). Fig.11 show the time profiles at these sub-sources, the counterpart of the radio spike at 03:04:54.6 UT only exists in the compact source, with Stocks I, V components and polarization degree in Fig.12. Moreover, the magnetic field in the compact source is larger than that in the extended source, the condition the electron cyclotron maser mechanism for spike emissions is satisfied only in the compact source, i.e., the electron plasma frequency is smaller than the electron gyrofrequency (Huang, 1987).

Even the working frequencies of NoRH is much larger

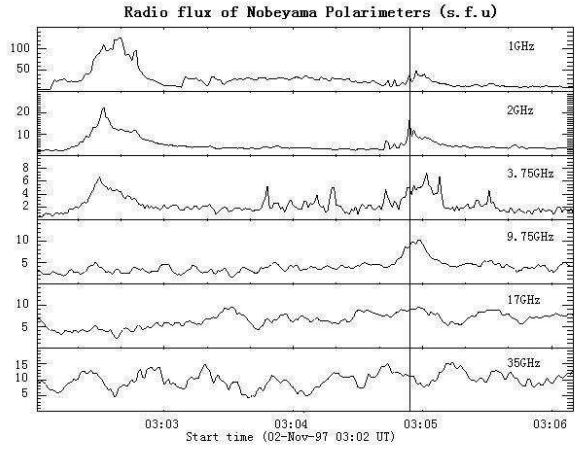

Fig. 7. The time profiles at 1, 2, 3.75, 9.75, 17, and 35 GHz of NoRP on Nov.2, 1997. The line is marked as the selected time of a radio spike.

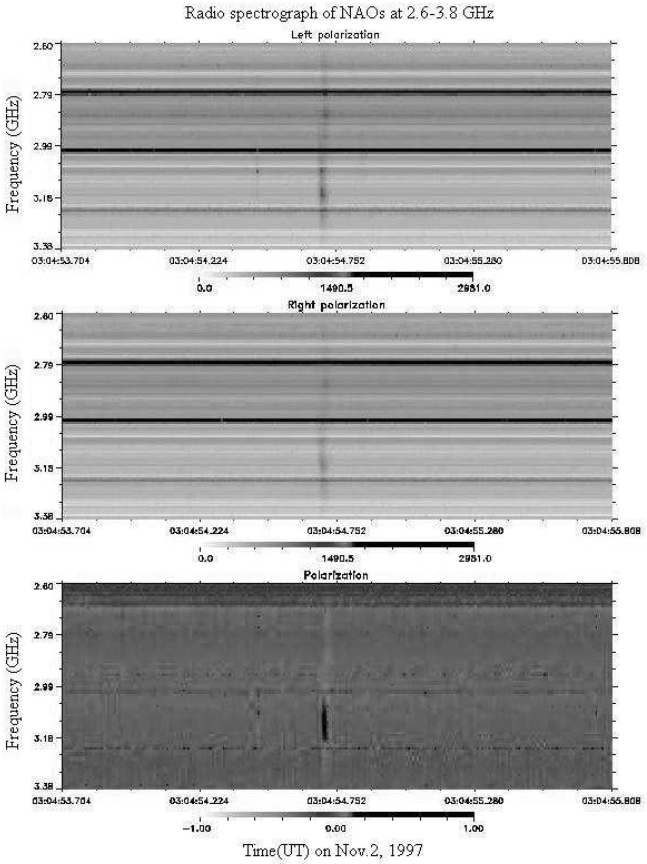

Fig. 8. The 2.6-3.8 dynamic spectrum of a radio spike at 03:04:54.6 UT on Nov.2, 1997.

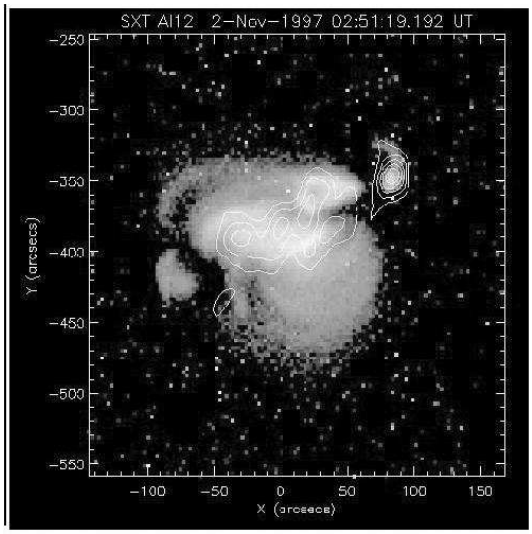

Fig. 9. The contour of the radio source at NORH 17 GHz (03:04:58 UT) overlapped on the YOHKOH/SXT (03:15:04.135 UT) image in AR8100 on Nov. 2, 1997.

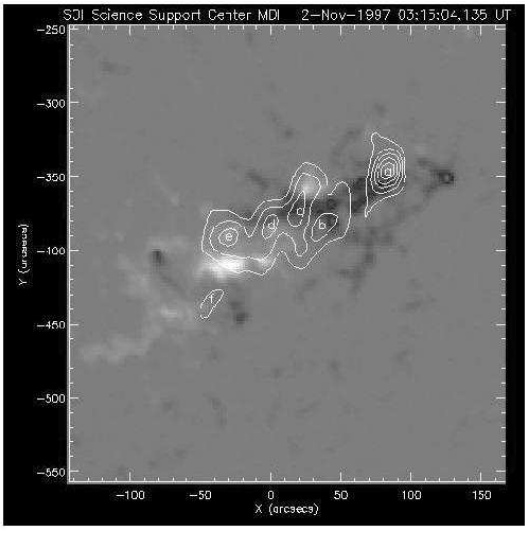

Fig. 10. The contour of the radio source at NoRH 17 GHz (03:04:58 UT) overlapped on SOHO MDI magnetogram at 03:15:04135 UT on Nov. 2, 1997.

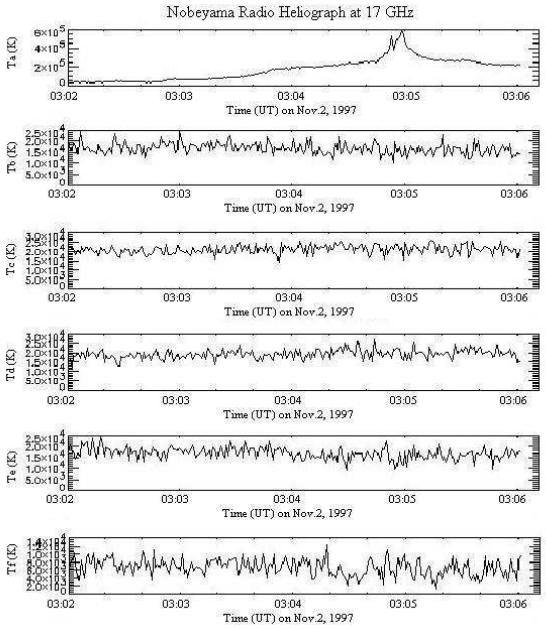

Fig. 11. The time profile of NoRH 17 GHz in the marked positions "a-f" as in Fig.6.

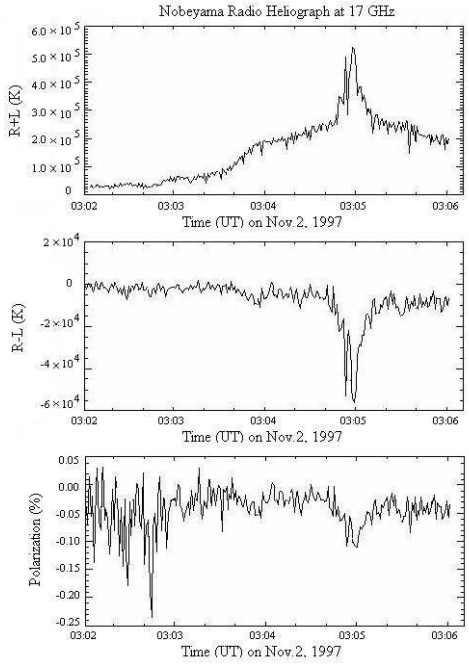

Fig. 12. The I (R+L), V (R-L) components and polarization of NoRH 17 GHZ in the compact source on Nov. 2, 1997.

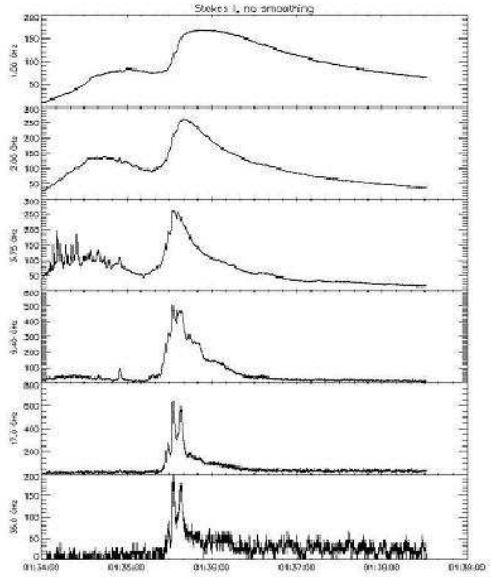

Fig. 13. The time profiles at 1, 2, 3.75, 9.75, 17, and 35 GHz of NoRP on Aug.25, 1999.

than that of the spectrograph, and the counterpart of the spike at 17 GHz is not clear in NoRP data (Fig.7), but it is really visible in NoRH data with high spatial resolution and sensitivity. The physical explanation for this counterpart is that the electron beams for spike emissions at lower frequencies may reach very low corona for 17 GHz emissions.

3.2. Type III-like at 4.5-7.5 GHz

Fig.13 gives another example of rich fine structures (FS) started about one minute prior to the main burst with the maximum emission at 4 GHz for the FS, and 10 GHz for the main burst, respectively. The time profiles at 4.5-7.5 GHz coincide very well with that of hard X-ray (from 25 keV to >300 keV) in both of the main burst and the FS as shown in Fig.14 (Huang et al., 2003).

The dynamic spectrum at 4.5-7.5 GHz in the top panel of Fig.14 show a group of type *III*-like bursts with drifts from lower to higher frequencies, which means that the electron beams move down from higher to lower corona. The burst at the start frequency around 4 GHz should be emitted close to the level of acceleration or reconnection site. The sources of the FS and main burst are located in Fig.15, the double source appeared, and down source (FS) was only strong in the pre-flare phase, after that the up source (main burst) was dominated. The SOHO/MDI contours in Fig.16 shows a typical dipole magnetic field around the main source, which should be contributed by the foot-point emissions. On the other hand, the FS seem to be emitted close to the loop top, which is consistent with the typical flare model. The location of FS is confirmed by the time profiles of different sources. Fig.17 gives the Stocks I and V at 17 GHz of the main and FS sources. It is evident that a strong fluctuations in the pre-

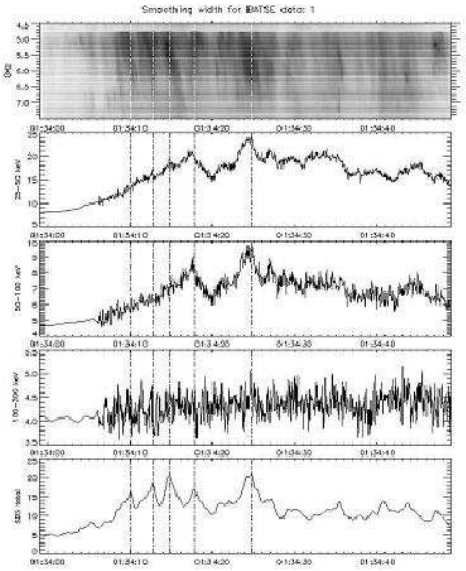

Fig. 14. The comparison between the time profiles of BATSE X-ray (three middle panels for three energy channels) and the spectrum of radio FS at 4.5-7.5 GHz (top panel) as well as the integrated time profile in full band (bottom panel) on Aug 25, 1999.

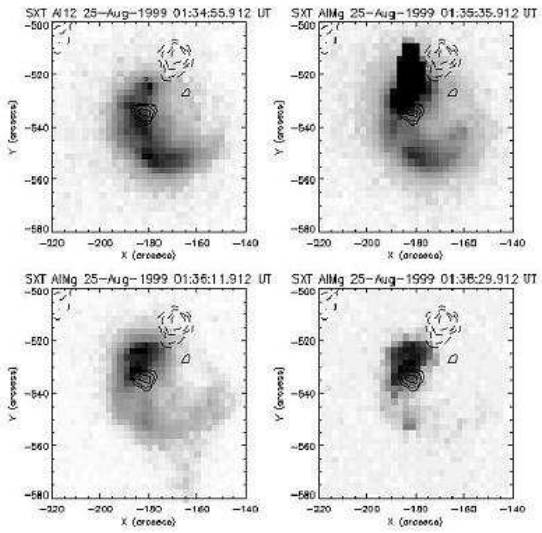

Fig. 16. The contours of SOHO/MDI (solid lines for 200 G, 300 G, and 400 G, dashed lines from -200 G to -1000 G with interval of 200 G) overlaid on YOHKOH/SXT images in the event on Aug 25, 1999.

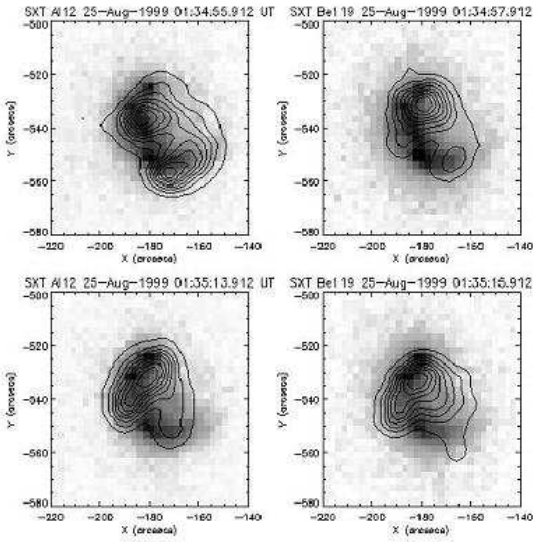

Fig. 15. The contours of R+L at 17 GHz of NoRH (5×10^4-10^6 K) overlaid on YOHKOH/SXT images in the pre-flare and rising phases of the event on Aug 25, 1999.

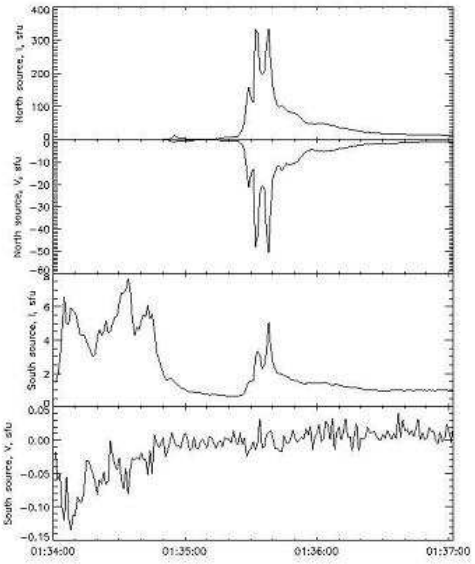

Fig. 17. The time profiles (Stokes I) and polarization (Stokes V) at 17 GHz of NoRH in the main (first and second panels) and FS (third and fourth panels) sources, respectively.

flare phase only happened in the source of FS at 17 GHz, which is consistent with the time profile at 3.75 GHz in Fig.13.

The dynamic spectrum with high time resolution (5 ms) in Fig.18 shows one example of the type *III*-like, which may be considered as a twisted magnetic rope with time

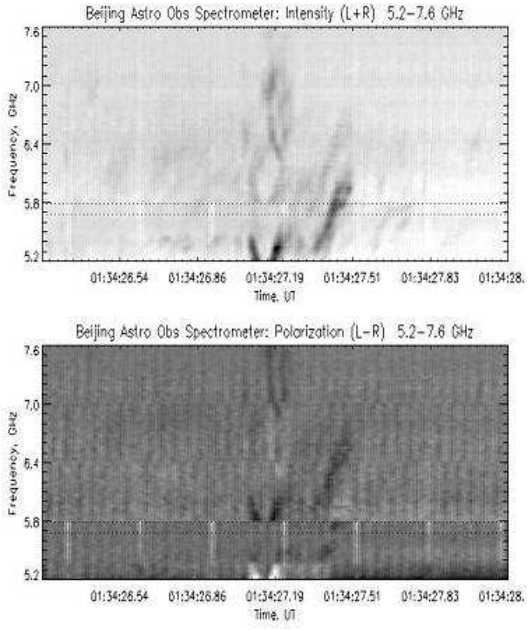

Fig. 18. The dynamic spectrum with time resolution of 5ms for a selected type *III*-like at 5.2-7.6 GHz of NAO on Aug 25, 1999.

interval of 0.3 s and frequency interval of 0.5 GHz, and the phase velocity of a typical Alfvén speed (Huang et al., 2003).

3.3. Microwave type IV and III, and zebra at 2.6-7.6 GHz

In an event on April 21, 2002 with X1.5 flare and very high-speed CME (Huang, 2004e), the time evolution of TRACE images overlaid by NoRH 17 GHz contours (Fig.19). The main radio burst started at higher frequencies as shown in the first panel with a double source at two foot-points as shown in SOHO/MDI magnetograph and 34 GHz contours of NoRH (Fig.20). After that, a radio ejection was detected from foot 1 at 01:49 UT (while foot 2 disappeared), associated with the expanded flare and post-flare loops. The loop-top was extended along the solar limb and well coincident with the EUV loops. The velocity of radio ejection and expanded loops keeps ten km/s until the post-flare phase.

It is emphasized that the polarization sense of the radio ejection at loop-top source (LCP) is opposite to that at foot 1 (RCP) as shown in Fig.21.

Figs.22-23 show the Stokes I and V profiles at 1, 2, 3.75, 9.75, 17 and 35 GHz of NoRP in this event. The maximum time is around 01:25 UT with turnover frequency of about 10 GHz corresponding to the 17 GHz emission from foot 2 source in Figs.19-20. Almost during the same time as the radio ejection started (01:50 UT) from foot 1, a very strong emission at low frequencies (1-2 GHz) appeared with reversal polarization sense from RCP to LCP, which predicted as the coherent emissions by Kundu et al. (2004).

The coherent emissions are analyzed with dynamic

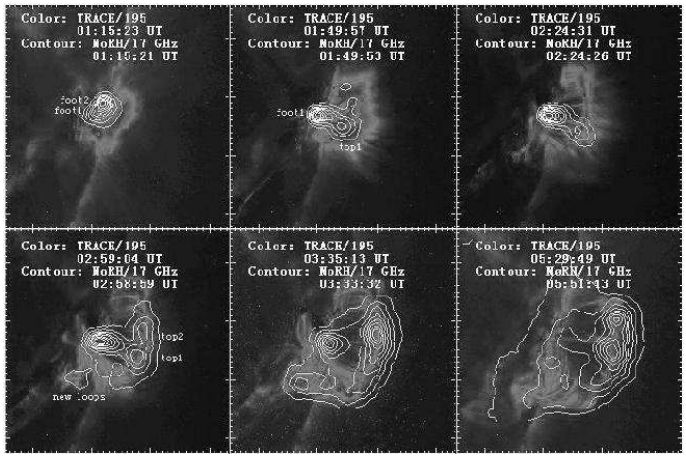

Fig. 19. The TRACE images overlaid by 17 GHz contours of NoRH at different phase of the event

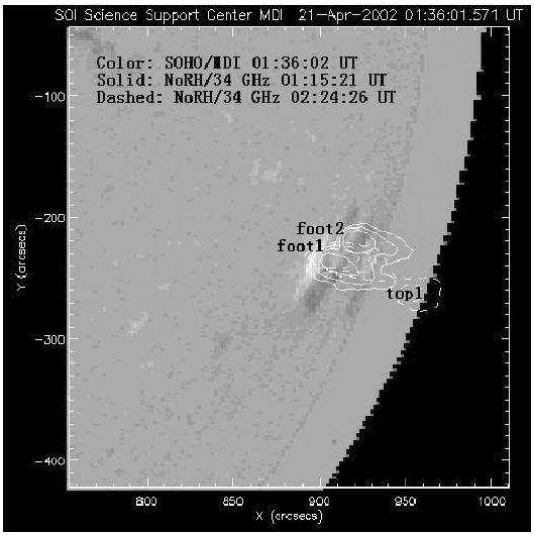

Fig. 20. The SOHO/MDI magnetograph overlaid by 34 GHz contours at 01:15:21 (solid) and 02:24:26 (dashed) UT

spectra of Hiraiso and Chinese Radio Spectrographs. There are a pair of moving type *IV* bursts respectively at 0.2-2 GHz from higher to lower frequencies and at 2.6-3.8 GHz from lower to higher frequencies (Fig.24).

The fine structures with fast frequency drifts evidently exist in the the type *IV* continuums at 0.2-2.0 GHz and 2.6-3.8 GHz. The dynamic spectra at 2.6-3.8 GHz with time resolution of 8 ms (Fig.25) are selected in four time intervals marked in Fig.24. The strong fluctuations at 2.6-3.8 GHz (Figs.22-23) indicate that the type *IV* bursts are not real continuums. A group of quasi-periodic emission clusters are shown in the top panel of Fig.25. There are very slow frequency drift of moving type *IV* (5 MHz/s) and the very fast drift of type *III* (several GHz/s) respectively in second and third panels. The fourth panel shows the multiple zebra strips with middle frequency drift (50 MHz/s). The three components of frequency drifts are

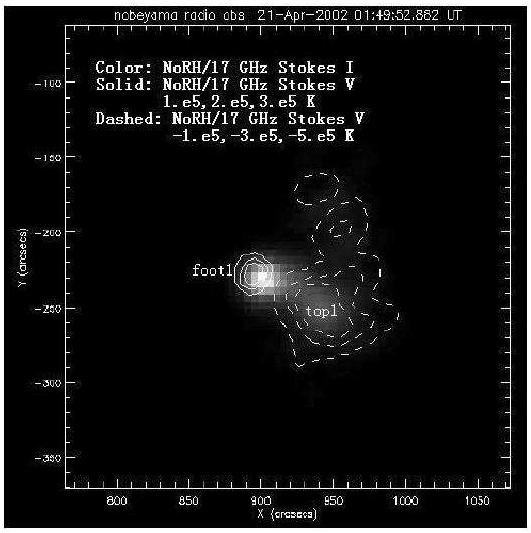

Fig. 21. The contours of Stokes V at 17 GHz are overlaid on Stokes I image at 17 GHz of NoRH (01:49:53 UT)

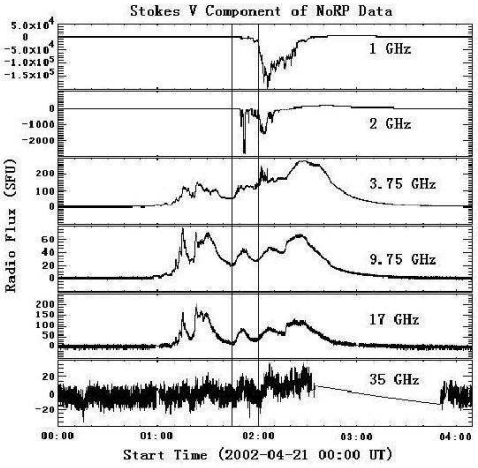

Fig. 23. The Stokes V profiles at 1, 2, 3.75, 9.75, 17 and 35 GHz of NoRP in the event

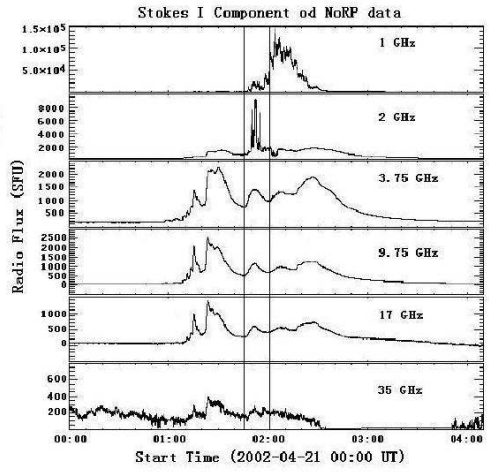

Fig. 22. The Stokes I profiles at 1, 2, 3.75, 9.75, 17 and 35 GHz of NoRP in the event

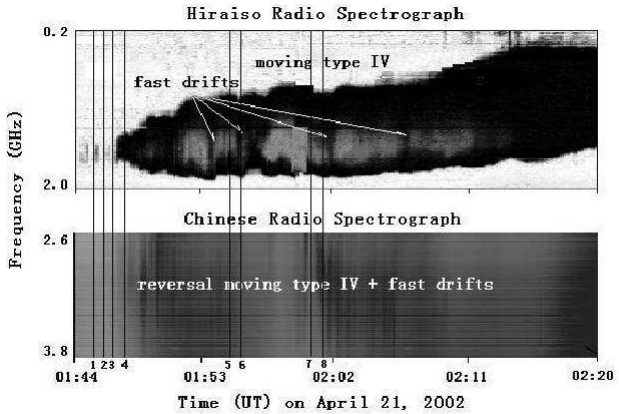

Fig. 24. A pair of moving type *IV* bursts at 0.2-2.0 GHz and 2.6-3.8 GHz

mixed in all panels of Fig.25., which may correspond to different speeds of current sheet or flare loop (tens km/s), shock waves (hundreds km/s), and non-thermal electrons (tens or hundreds keV) associated with magnetic reconnections that took place above the 17 GHz loop-top source in Figs.19-21.

The location of FS sources are also studied in some recent papers for zebra structures at 4.5-7.5 GHz with data of SSRT and Chinese spectrographs (Altyntsev et al., 2004; Melnikov et al., 2004).

4. Summary

The approximations of Dulk & Marsh may be used for diagnosis of coronal magnetic field and non-thermal electrons with non-thermal gyro-synchrotron radiations when

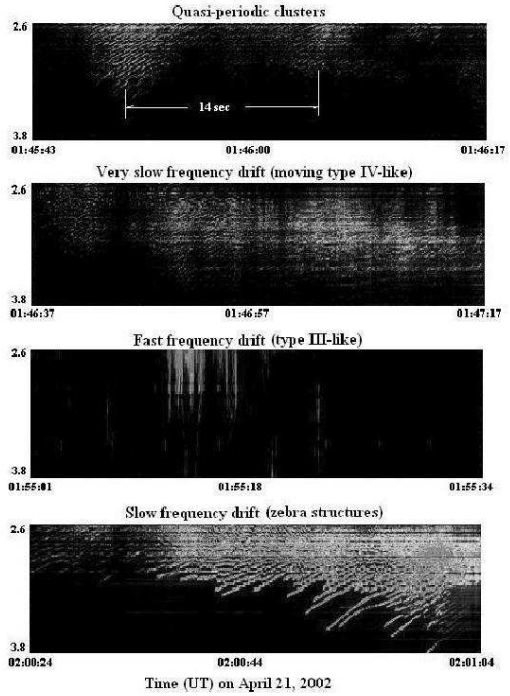

Fig. 25. The quasi-periodic emission clusters and three components of frequency drifts from top to bottom in the dynamic spectra at 2.6-3.8 GHz.

the low energy cutoff is close to 10 keV, as well as the other conditions given in Dulk & Marsh (1982) are satisfied. A series of papers (Zhou et al., 1994; Huang et al., 2000; 2002) are completed for this purpose, some explicit functions of coronal magnetic field and non-thermal electrons are derived from the self-consistent calculations with measurable values of frequency, turnover frequency, flux or brightness temperature, and spectral index.

On the other hand, if the low energy cutoff varies in a broad range (Gan et al., 2002), the coronal magnetic field and low energy cutoff should be calculated simultaneously with more strict model of non-thermal gyro-synchrotron radiations (Ramaty, 1969; Takakura et al., 1970). The other parameters are not sensitive to the calculations, such as the high energy cutoff, propagation angle, the density and temperature of ambient plasma (Huang et al, 2004c). Therefore, the new method will be developed for radio diagnosis coronal magnetic field and non-thermal electrons with non-thermal gyro-synchrotron radiations.

The another topic mentioned in this paper is the location of radio bursts with FS. Especially, the bursts or the FS with frequency drifts, such type *III* bursts and millisecond spikes with very fast drifts caused by particle accelerations, the moving type *IV* bursts with slow drifts caused the moving of flare and post-flare loops, or the middle drifts of the zebra structures caused by shock waves. The location of these bursts or FS may give some direct or indirect signature of magnetic reconnections and particle accelerations. The key point to locate the sources of the radio bursts with FS is how to joint the data of heliographs with high spatial resolution and the data of spectrographs with high temporal and frequency resolutions.

References

Altyntsev, A. T., Grechnev, V. V., Zubkova, G. N., Kardapolova, N. N., Lesovoi, S. V., Rosenraukh, Y. M., and Treskov, T. A., 1995, A&A, 303, 249
Altyntsev, A. T., Kuznetsov, A. A., Meshalkina, N. S., and Yan Yihua, 2004, A&A (accepted)
Bastian, T. S., 1994, ApJ, 426, 774
Benz, A. O., Jaeggi, M., and Zlobec, P., 1982, A&A, 109, 305
Benz, A. O., 1986, Solar Phys., 104, 99
Dulk, G. A., and Marsh, K. A., 1982, ApJ, 259, 350
Dulk, G. A., 1985, ARA&A, 23, 169
Forbes, T. G., 2004, Proceedings of IAU Symposium 226, (invited review)
Gan, W. Q., Li, Y. P., and Zhang, J., 2001, ApJ, 552, 858
Huang, G. L., 1987, Solar Phys., 114, 363
Huang, G. L., Qin, Z. H., Yang, G., Fu, Q. J., and Liu, Y. Y., 1998, ApSS, 259, 317
Huang, G. L., and Zhou, A. H., 1999, New Astron., 4, 591
Huang, G. L., and Nakajima, H. 2002, New Astron., 7, 135
Huang, G. L., Wu, H. A., Grechnev, V. V., Sych, R. A., and Altyntsev, A. T., 2003, Solar Phys., 213, 341
Huang, G. L., 2004a, JGR, 109, 2105
Huang, G. L., 2004b, A&A (accepted)
Huang, G. L., Zhou, A. H., Su, Y. N., and Zhang, J., 2004c, New Astron. (in press)
Huang, G. L., 2004d, ApSS (in press)
Huang, G. L., and Lin, J., Proceedings of IAU Symposium 226 (accepted)
Krüger, A., 1979, Introduction to Solar Radio Astronomy and Radio Physics, Reidel
Krucker, S., Aschwanden, M. J., Bastian, T. S., and Benz, A. O., 1995, A&A, 302, 551
Krucker, S., Benz, A. O., and Aschwanden, M. J., 1997, A&A, 317, 569
Kundu, M. R., 1990, Mem. S.A.It., 61, 431.
Kundu, M. R., Garaimov, V. I., White, S. M., and Krucker, S., 2004, ApJ, 600, 1052
Liu, Y.Y., Fu, Q.J., Qin, Z.H., Huang, G.L., and Wang, M., Science in China (Series A), 45, 114
Mclean, D. J., ed., 1985, Solar Radio Physics, Cambridge Press
Melnikov, V. F. et al., 2004 (to be submitted)
Robinson, P. A., and Benz, A. O., 2000, Solar Phys., 194, 345
Ramaty, R., 1969, ApJ, 158, 753
Takakura, T., and Scalise, E., 1970, Solar Phys., 11, 434
Xie, R. X., Fu, Q. J., Wang, M., and Liu, Y. Y., 2000, Solar Phys., 197, 375
Zhou, A. H., & Karlický, M., 1994, Solar Phys., 153, 441
Zhou, A. H., and Su, Y. N., 2004, Solar Phys. (accepted)

Methods to analyze imaging radio data on solar flares

Victor V. Grechnev *
Institute of Solar-Terrestrial Physics, Lermontov Street 126, Irkutsk 664033, Russia
grechnev@iszf.irk.ru

Abstract

Putting additional constraints on physical conditions based on the observed quantities, microwave imaging data crucially enhance reliability of results and consistency of interpretations. This is why microwave imaging data is a necessary constituent of observational data sets on solar flares, and they are widely used in their analyses. At the same time, to identify essential features and study their behavior, one has to deal with large data sets of hundreds frames. However, this allows a single image, a variance map, that represents overall dynamics of the event. In this review, methods are presented that allow identification of active flare sources in large data cubes and investigation of the detected positions of sources in both Stokes I and V images using analyses of variance maps, combined difference images, and total flux time profiles. By analyzing the similarity of time profiles for different-polarity Stokes V sources, one can reveal magnetic connectivity. Imaging techniques at the NoRH in both the local and remote modes as well as interactive data analysis using IDL are also briefly discussed.

Key words: Sun: radio radiation — Sun: flares — methods: data analysis — techniques: image processing

1. Introduction

Comprehensive data sets in various emissions on an event under investigation put several observational constraints on physical conditions and scenarios considered. Analyzing them, one loses freedom to speculate, but gains confidence in that the estimates obtained from various observations using different methods are reliable, the interpretation is robust, and this everything is consistent with many observational facts. When studying solar flares, one has to analyze both thermal and non-thermal emissions. Whereas thermal emissions (e.g., soft X-rays, extreme ultraviolet) show fine spatial structures of flare regions and their vicinity, non-thermal emissions (primarily hard X-rays) provide information on high-energy particles accelerated in flares. Being responsive to both thermal and non-thermal flare manifestations, microwave imaging data are widely used in analyses of solar flares. Being highly sensitive to magnetic fields, radio observations give a unique method of identifying magnetic configurations and estimating magnetic field strengths in the corona. Well known are facts when it is not possible to disclose all important flare sources without microwave observations (e.g., in cases of strongly asymmetric loops—Kundu et al. 1995). In addition, microwave images have wide dynamic range (> 100 for NoRH and can be still improved using optimal weighting of visibilities, while it was ~ 10 for *Yohkoh*/HXT). All these convince that microwave observations of solar flares are quite necessary, rather than supplementary only.

Typical tasks to be solved in analyses of solar flares are: a) to identify active flare sources, b) to find out their nature and emission mechanisms, and c) to relate their properties with parameters of plasmas and accelerated particles in flaring regions, i.e., to constrain physical conditions based on the observed quantities.

Most microwave imaging data on solar flares have been come during the last decade from the Nobeyama Radioheliograph (NoRH, Nakajima et al. 1994). Besides images, NoRH produces correlation plots, which sample small spatial scales by using combined responses from the longest baselines of the radio interferometer. A researcher who is going to use NoRH imaging data must first produce a set of images ("data cube") from raw data, and then to identify active flare sources.

Known ways to reveal flaring sources involve 1) analyses of "base" (Kundu et al. 1995) or "running" difference images (Delannée et al. 2000), 2) viewing in the movie mode, and 3) analyses of time profiles along several check points of a data cube (Hanaoka et al. 1994). However, all of them are insufficiently efficient and have some other weak points. Therefore, studies of solar flares involve time-consuming, laborious processing and analyzing large sets of images. Here, methods are described, which involve a set of techniques that allow efficient identifying short-term features in imaging data (Grechnev 2003). *The methods were developed primarily for analyses of NoRH data.*

2. Essence

2.1. Choice of the time interval for imaging

NoRH correlation plots can be used for that. Correlation plots can be misleading if the spatial structure is complex, but they show temporal variations of compact features. Then the image set over the whole time interval

* The essence of the methods was developed in NRO, when V. Grechnev was a Foreign Research Fellow of NAOJ

chosen is produced with a required cadence.

2.2. Search for active flaring sources

Robertson (1991) first proposed to use variance imaging in radio astronomy. Then r.m.s. images were used by Tsiropoula, Alissandrakis & Mein (2000), and Nindos et al. (2002) in studies of quasi-periodic oscillations. Variance maps (or r.m.s. images) can be also successfully used to find important flare sources. The variance maps are computed by calculating variance of every spatial point of the data cube along its temporal dimension. The variance map presents the dynamics of the entire event, with the value of each its point showing the temporal variability of the corresponding spatial point. Therefore, variable sources that change their brightness, position, etc. come into view in the variance map—of course, according to the statistical importance of their variability. For reasons of computational efficiency, I calculate the variance (r.m.s.) map σ_{ij}^2 for a data cube x_{ijk} using the expression

$$\sigma_{ij}^2 = 1/N \sum_{k=1}^{N} x_{ijk}^2 - 1/N^2 \left(\sum_{k=1}^{N} x_{ijk} \right)^2$$

where $k = 1, 2, \ldots, N$ is the number of the image "layer" in the data cube. This expression is equivalent to the definition of the variance (see, e.g., Cramér 1946), but does not contain cross terms, which decreases the computational time.

Images to be analyzed using variance maps must be well calibrated and coaligned. The variance map catches such problems of an image set. The effect of random shifts less than the size of a source is a ring-shaped response in the variance map, with "darker" middle and "brighter" strip along the edge. The effect of jumps between few fixed positions well exceeding the size of the source is appearance of false additional sources.

If the considered interval is so long, that the solar rotation becomes important, it should be compensated, or other precautions should be undertaken. Otherwise, there is enough time for significant displacements of quiet sources, and this inevitably results in their artifactitious appearance as strongly variable duplicated sources.

2.3. Time profiles of flaring sources

When active flare sources are identified and selected, I analyze their time profiles separately by integrating pixel values over small areas covering the sources entirely. The total flux time profiles are computed for each source as $S_{[sfu]} = 2k\,(\nu/c)^2 \sum_i T_{Bi}\,\Delta\Omega = 7.22 \times 10^{-11}\ \nu_{[GHz]}^2\ \rho_{[arcsec]}^2 \sum_i T_{Bi[K]}$, with k being Boltzmann constant, c speed of light, $T_{Bi} = (R_i + L_i)/2$ brightness temperature of each pixel (with a linear size of ρ), ν frequency, and $\Delta\Omega$ solid angle corresponding to one pixel of the image.

Next, when prominent features in the time profiles are found, I produce detailed image sets with as short time interval between them as necessary. Then variance maps are used again, and this process can be repeated iteratively, until the whole dynamics of the spatial structure is revealed. The iterations are performed to reveal all important sources and to compute the time profiles for each of them as detailed as the physical task requires.

2.4. Magnetic connectivity

To identify magnetic connectivity, one can use the fact that the gyrosynchrotron emission from a flare loop at 17 GHz usually is conspicuously polarized, and the sign of the polarization must be opposite in conjugate footpoints of a flare loop (if there is no polarization reversal, which can be expected at 17 GHz to be close to the limb). In addition, when one deals with a particular flare loop, then the same electron population is likely responsible for the emissions from both footpoints; hence, their time profiles may be expected to be similar in shape (but not in either flux or brightness temperature values). Hence, one can try to identify magnetic connectivity of the detected regions by comparing various time profiles computed for the Stokes V component in all the regions, and finding those, that match in local peaks and have the opposite polarization (note, however, that it is not always possible). Difference images are also useful here, as produced in the following way. First, some images taken during a peak are averaged. Then another image is composed from frames taken before the peak and/or after it. Finally, the latter image is subtracted from the former one. (This way can be applied to both Stokes V and I images.) The next step is the comparison of time profiles for loop footpoints found.

When events with simple spatial structure are analyzed, this approach is quite straightforward. Moreover, sometimes magnetic connectivity can be revealed even from the analysis of the total intensity time profiles as Hanaoka (1999), Kundu et al. (2001), and Grechnev & Nakajima (2002) did. In more complex cases, the way described can become rather sophisticated; nevertheless, using just this way, Grechnev, Kundu & Nindos (2004) succeeded to follow formation of a post-eruptive arcade in a long-duration eruptive event of February 16, 1999.

2.5. Spectral index

When dealing with radio maps produced by NoRH, one can study data at two operating frequencies of 17 and 34 GHz. Taking into account that these frequencies usually belong to the optically thin high-frequency part of the microwave burst spectrum, note that the flux density of the thermal bremsstrahlung is almost the same at these two frequencies, whereas gyrosynchrotron emission from high-energy electrons has a rather steep spectral slope. These two emission mechanisms are dominant for flaring sources at these frequencies (gyrosynchrotron emission in the impulsive phase and free-free emission in the decay phase). It is easier to identify the emission mechanism for a microwave source if one knows the spectral index of its emission α, which can be calculated from two-frequency data.

One can compute the spectral index as $\alpha = \log(S_L/S_H)/\log(\nu_H/\nu_L)$ with S_ν being flux density measured at the frequency of ν, and subscripts "*F*" and "*H*" denote the higher and lower frequencies. To estimate the spectral index correctly, the difference in the beam sizes at the two frequencies should be compensated. One can do this, following Nobeyama Solar Group, by convolving 17 GHz images with the NoRH beam pattern at 34 GHz, and by convolving 34 GHz images with the NoRH beam pattern at 17 GHz.

2.6. Thermal contribution

Thermal bremsstrahlung in microwaves can be found from soft X-ray data (e.g., *Yohkoh*/SXT, *GOES*): $S_{[sfu]} \approx 3 \times 10^{-45} EM_{[cm^{-3}]} T_{[K]}^{-1/2}$, where EM and T are emission measure and temperature of the observed source. In a similar way, a simulated microwave "image" in optically thin free-free emission can be computed using column EM and T_e distributions inferred from soft X-ray imaging data (e.g., from *Yohkoh*/SXT images—see, e.g., Grechnev et al. 2004b).

3. Examples

This sections demonstrates the capability of the variance method by considering examples of 17 GHz data analyses for two impulsive flare events recorded with NoRH.

3.1. Event of December 22, 1999

An impulsive solar flare of December 22, 1999 occurred in the active region 8807 (N17 E15) during 01:50–02:37 UT with a peak of M1.8 at 02:16 UT according to *GOES*. The spatial and temporal structure of the flare microwave emission was complex. However, the rise phase of the event had rather simple structure, and it is convenient to use it as an example to show what we gain from variance maps.

The image set to be analyzed consists of *167* 17 GHz snapshots produced using *Fujiki program*[1] with an interval of 1 sec. This imaging software provides higher spatial resolution. Figure 1a shows an averaged image of the flare region of $314'' \times 314''$ composed from the whole image set. Several microwave sources can be seen in this image: compact sources 1, 2, and 3 as well as a faint extended feature 4 in the northern (upper) part of the frame. Note that the source 3 is the brightest one here.

The variance map computed from the same set of *167* images is shown in Fig. 1b. One can see here, however, that the most prominent is source 1; source 2 is weaker; and no more bright sources are detectable. To investigate behavior of the sources, we extract three regions in the images using the masks shown in Fig. 1a as dashed contours. The time profiles of the variable parts of the total flux emitted by sources 1, 2, and 3 are shown in Fig. 2 along with the whole total flux computed from the entire frames.

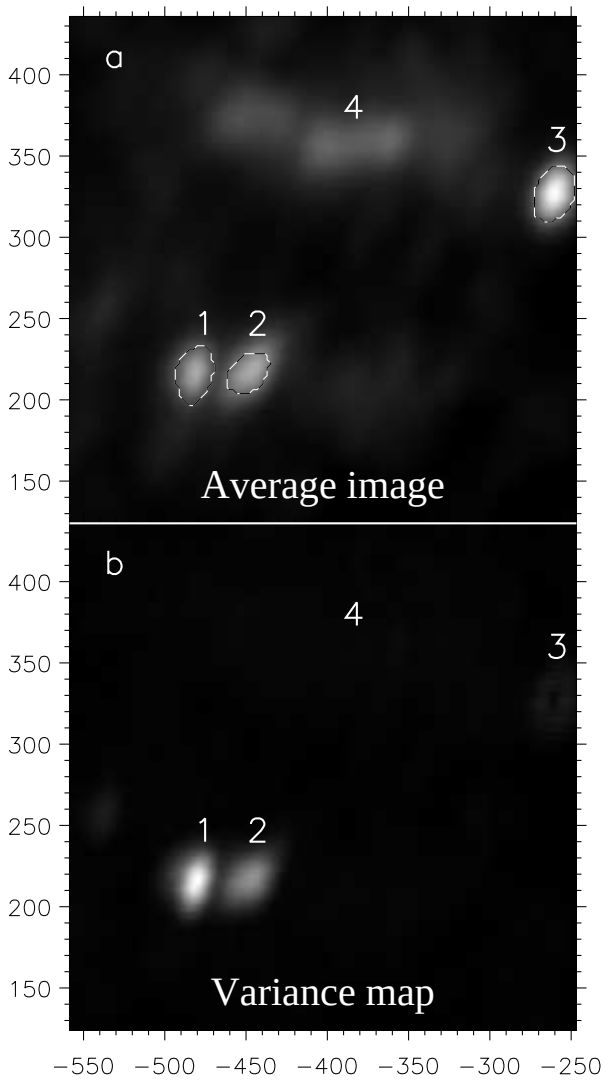

Fig. 1. The initial stage of December 22, 1999 event: **a** the image produced by averaging of all *167* 17 GHz NoRH frames within the analyzed interval; **b** the variance map computed from this set. The masks to select the most prominent sources 1–3 are shown in panel **a** as dashed contours, and time profiles of the sources are shown in Fig. 2. Axes show arc seconds from the solar disk center. Both images are shown non-linearly, at the power of 0.8.

[1] see http://solar.nro.nao.ac.jp/norh/doc/manuale/index.html

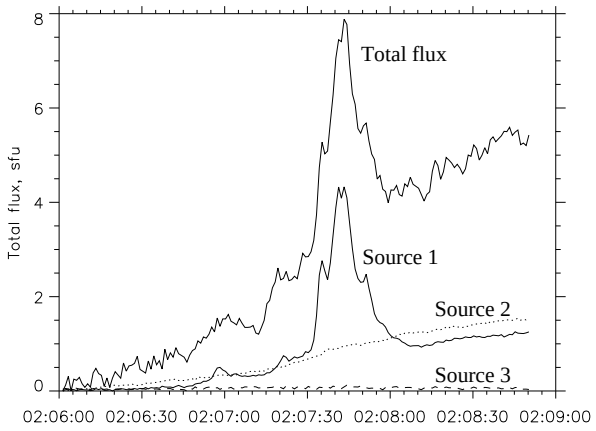

Fig. 2. Total flux time profiles for three sources shown in Fig. 1 along with the whole total flux computed from the entire frames. Minimum values of all time profiles are subtracted.

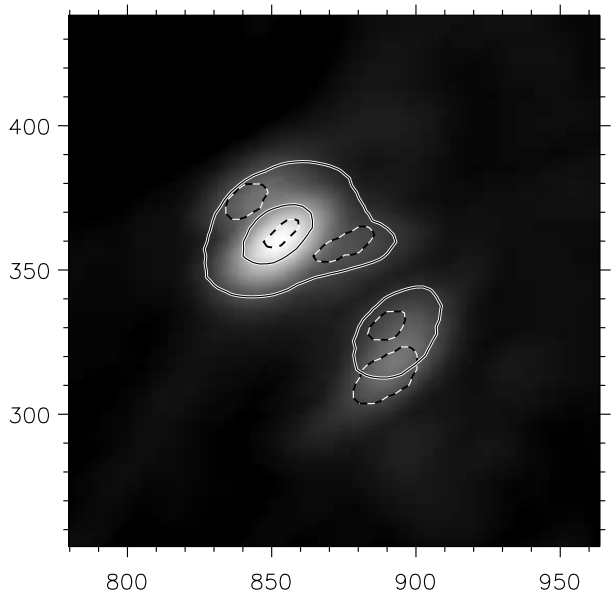

Fig. 3. The variance map computed from *231* NoRH 17 GHz images for November 10, 1998 event. The interval of the computation is from the thick "dash–three dots" line shown in Fig. 8 up to the end of the record. Five active sources (dashed contours) can be revealed from the variance map, while the image at the peak of the second burst (the instant labeled large "C" in Fig. 5) shows two sources only (solid contours at [0.05, 0.5] of the maximum). Axes show arc seconds from the solar disk center.

The situation visible in the variance map essentially differs from the picture shown by the average image. The strongest source 3 is not visible because it is almost unchanged: its brightness temperature is 0.22 MK, and the variations do not exceed 30 000 K. Source 1 is of the highest variability, although in the average image it is weaker than both sources 2 and 3, and we can really see in Fig. 2 that its behavior is the most impulsive. Its brightness temperature reaches 0.7 MK, whereas the brightness temperature of source 2 is $T_B \leq 0.25$ MK. The extended northern brightening (4) with $T_B = 80\,000 \pm 15\,000$ K does not show any detectable variability; hence, it is not detectable in the variance map.

This example shows that the major impulsive processes in early beginning of the flare were associated with source 1, which was likely non-thermal. The similarity of the smoother background of source 1 with the time profile of source 2 suggests their probable connection. However, the strongest, likely gyroresonance, source 3 had no relation to active processes during the event.

3.2. Event of November 10, 1998

More complex spatial and temporal structures are exemplified by the well-known flare event of November 10, 1998, first presented by Asai et al. (2001). The event actually included a train of four bursts, in the second of which pulsations with an extraordinarily high modulation depth were observed. For the first glance, two flare sources were present in 17 GHz images of the event, in particular, in its pulsating part. However, the spatial structure contained more features in the reality.

Figure 3 shows a variance map computed from a 1-sec set of *231* NoRH snapshots observed during the interval to cover three last bursts (from thick "dash–three dots" line in Fig. 5 up to the end of the record). Two prominent microwave sources observed at one of peaks of the pulsating burst are shown on top of the halftone background by solid contours, but careful examination allows detecting five variable regions marked with dashed contours in the figure. Note that the sizes of these regions were selected from reasons of their separation rather than to cover the sources entirely. This is why in Fig. 5 just the average brightness temperatures are shown rather than the total fluxes.

Figure 4 shows 17 GHz images of the event for four times. Dashed contours show **five** active flare sources 1–5 revealed by the variance method. The time profiles of those sources are shown in Fig. 5. In the light curves, we can select some representative moments when some features show up. By subtracting from images corresponding to those moments (solid lines and capital letters) other images, before those features (broken lines and the corresponding small letters), we obtain a picture of microwave sources responsible for those features in the time profiles.

Next, we come back to Fig. 4. Halftone background in *left column* shows *non-subtracted* images, while *right column* shows *subtracted* images. So, we see in right column those sources, which were responsible for the brightenings **B**, **C**, and **D** as well as the long decay **A**.

This event was studied in more detail by Grechnev, White & Kundu (2003).

4. Technical details

I perform all data handling in IDL[2] environment, which is the most common for the solar community. All routines

[2] IDL is the trademark of Research Systems, Inc. http://www.rsinc.com

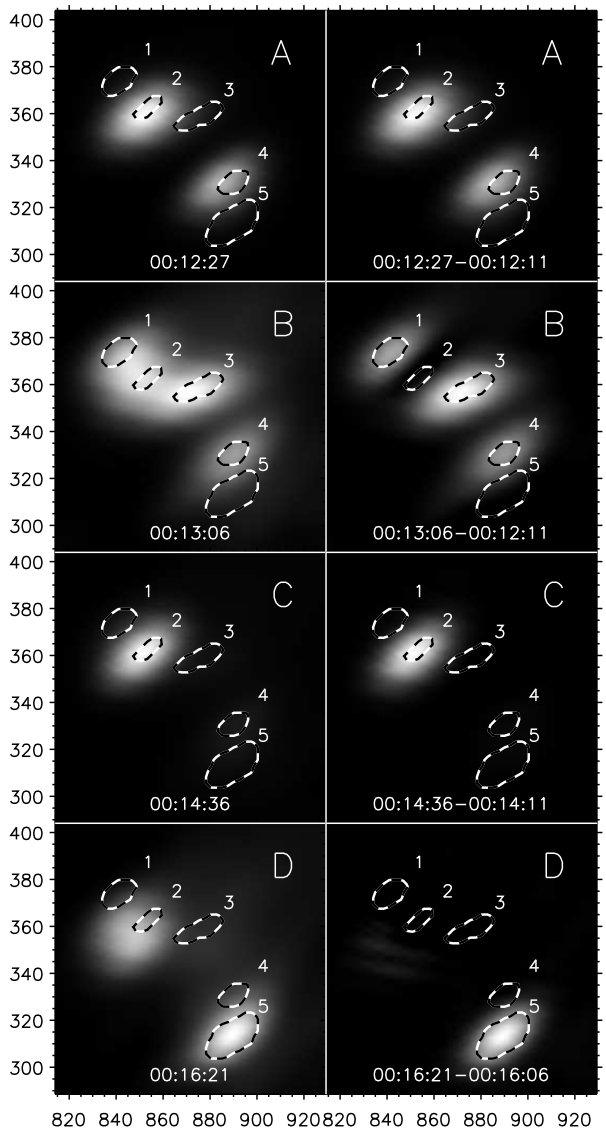

Fig. 4. NoRH 17 GHz images of November 10, 1998 event. Left column shows 17 GHz images observed at some characteristic times labeled with capitals "A"–"D" in Fig. 5. Right column shows *difference* images produced by subtraction from images in the left columns another ones, observed at times labeled with the corresponding small letters "a"–"d" in Fig. 5. Active sources revealed by the variance map are shown by dashed contours. Axes show arc seconds from the solar disk center.

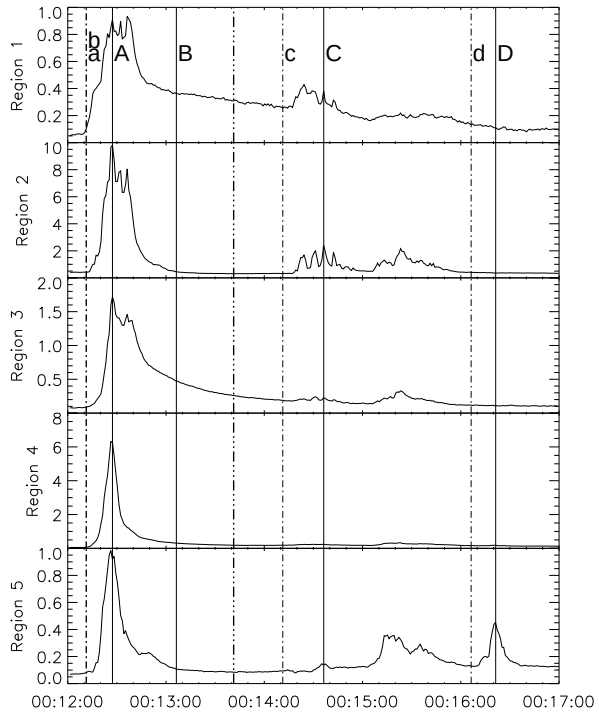

Fig. 5. NoRH 17 GHz time profiles of average brightness temperatures (MK) over the regions labeled 1–7 in Fig. 4

hereinafter refer to IDL.

4.1. Imaging

To produce images from raw NoRH data, I use the routine **norh_synth** developed by T. Yokoyama that provides an interface to fill in parameter files for an imaging software, and starts the running of the program. In my code, I arrange some environment in addition to this routine, and create the parameter file with a unique name formed from the system time. This allows several imaging jobs to be queued simultaneously. This way can be used in both the local mode, in Nobeyama, and the remote mode—elsewhere in the world (using access via secure shell, **ssh**).

4.2. Manipulation with Graphics without Graphical Output

To perform routines that need graphical output (e.g., **MAP_SET** when working with the orthographic projection) *in the remote mode without access to X Windows display*, one can use the **Z** buffer graphics device. I give below a simple example to show how to find heliographic coordinate of the brightest point in a NoRH image using built-in IDL routines.

```
data = readfits(filename, header)
Sz = size(data)
init_device = !d.name
set_plot, 'Z'
device, set_resolution = Sz[[1,2]]
X0=sxpar(header,'crval1')/sxpar(header,'cdelt1')
```

```
Y0=sxpar(header,'crval2')/sxpar(header,'cdelt2')
Centvr=[sxpar(header,'crpix1')–X0, $
    sxpar(header,'crpix2')–Y0]
Radius=sxpar(header,'solr')/sxpar(header,'cdelt1')
map_set, sxpar(header, 'solb'), 0, 0, /ortho, $
    position = [0,0,1,1]
!x.s=[Center[0], Radius] / float(!d.x_size)
!y.s=[Center[1], Radius] / float(!d.y_size)
amax = max(data, imax)
print, convert_coord(imax mod Sz[1], $
    imax/Sz[1], /dev, /to_data)
set_plot, init_device
```

The way to control the **MAP_SET** routine used here was proposed by Stern (1997).

4.3. Analysis and Visualization

To analyze three-dimensional data cubes, I developed IDL routines and functions **varmap**, **timeprof**, **total_flux** and some others, which can be found at the Web site http://ssrt.iszf.irk.ru/idl.

A variance map for the array **x** can be computed using a simple IDL code:

total(x∧2, 3)/N – total(x, 3)∧2/N∧2),

which is performed by my function **varmap**. By calculation of the mean value over a quiet (dark) non-zero region in the variance map, one can find the instrumental sensitivity appropriate for the data cube under consideration. Everything below this level can be simply zeroed.

The variability of major non-thermal flare sources is strong; hence, to detect all features of interest, it is useful to display variance maps non-linearly. At the first step, the histogram-equalized transformation can be used to reveal as much variable regions as possible:

tvscl, hist_equal(image)

This drastically decreases the contrast, and both bright and faint features become visible. Next, I apply a power-law display (for example, with a power of 0.3):

tvscl, (image > 0)∧0.3

or, for bipolar images,

tvscl, (image > 0)∧0.3 – (–image > 0)∧0.3

This operation is performed by my function **magpower**, which is convenient, if the **image** itself is some expression also.

Regular instrumental contributions (e.g. sidelobes of the beam pattern) also show up in the variance map. This allows judging whether a source can be due to an instrumental effect, if it is located in the sidelobe region and resembles variations of the major source responsible for these sidelobes.

4.4. Selection of Sources

Prominent sources can be selected using various ways. If a source is strong and isolated, it can be easily detected in a particular frame, or in an averaged image. If it is not so strong, then a variance map can be used to detect it. To form the mask for a particular source, discrimination above some threshold can help, for example,

s1 gt max(s1)*0.4

produces the mask to embrace the source **s1** by the level of 0.4. To separate merged sources, the morphological erosion operator can be used (the **erode** IDL function). Separation of several sources can be performed using the **label_region** built-in IDL function.

After that, time profiles over the regions found can be computed using the **total_flux** function.

Some remarks about interactive data analyses using IDL can be found at the Web site: http://srg.bao.ac.cn /weihailect/Grechnev/Grechnev01.htm.

5. Concluding Remarks

Studies of microwave data on solar flares involve laborious processing and analyzing large three-dimensional data arrays, which can be expedited using the methods outlined.

I developed the essence of the methods and started to use them when studied the impulsive solar flare of September 17, 1999 (Nakajima & Grechnev 1999; Grechnev & Nakajima 2002). Taking advantages of those methods, we were able to analyze large image cubes and to reveal faint impulsive sources, which turned out to be important in understanding flare processes. Further, using those methods, cursory analyses of some dozens of solar flares have been carried out. Some of studies that were more comprehensive have been already published (Kundu & Grechnev 2001, Kundu et al. 2001; Garaimov & Kundu 2002).

The methods can be also used in investigating variable objects in other images. In particular, the variance method was successfully used by Kundu et al. (2001) to study evolution of photospheric magnetic fields. The methods can be also helpful when multi-frequency radioheliographs, which are currently under development (e.g. FASR), start observing the Sun, and data anticipated will well exceed those we deal with so far.

Acknowledgments. The author thanks A. Uralov, A. Altyntsev, H. Nakajima, M. Kundu, and V. Garaimov for fruitful discussions, examination, and the first usage of the method. This work was partly supported by INTAS under grant No. 00-00543 as well as by the Russian Foundation of Basic Research under grants 03-02-16591, 03-02-16229, 03-07-90054, 02-02-39030-GFEN, and the Ministry of Education and Science under grant NSh-477.2003.2.

References

Asai A., Shimojo M., Isobe H., Morimoto T., Yokoyama T., Shibasaki K., Nakajima H. 2001, ApJL 562, L103.

Crámer H. 1946, Mathematical methods of statistics. Princeton, Princeton University Press.

Delannée C., Delaboudinière J.-P., Lamy P. 2000, A&A 355, 725

Garaimov V.I., Kundu M.R. 2002, Sol. Phys. 207, 355

Grechnev V.V. 2003, Sol. Phys. 213, 103

Grechnev V.V., Nakajima H. 2002, ApJ 566, 539

Grechnev V.V., White S.M., Kundu M.R. 2003, ApJ 588, 1163
Grechnev V.V., Kundu M.R., Nindos A. 2004, A Study of Accelerated Electrons in Solar Flares from Nobeyama, Yohkoh, and Other Observations. Nobeyama Symp. 2004 "Solar Physics with the Nobeyama Radioheliograph", http://solar.nro.nao.ac.jp/meeting/nbym04/index.html; PASJ, 2005, in preparation
Grechnev V.V., Borovik V.N., Bugaenko O.I., Bogachev S.A., Grigorieva I.Y., Kuzin S.V., Lesovoi S.V., Livshits M.A., Pertsov A.A., Rudenko G.V., Slemzin V.A., Stepanov A.I., Shibasaki K., Uralov A.M., Zandanov V.G., Zhitnik I.A. Observations of a posteruptive arcade on October 22, 2001 with CORONAS-F, other spaceborne telescopes, and in microwaves. Nobeyama Symp. 2004 "Solar Physics with the Nobeyama Radioheliograph", http://solar.nro.nao.ac.jp/meeting/nbym04/index.html; 2005, PASJ, in preparation
Hanaoka Y., Kurokawa H., Enome S. et al. 1994, PASJ 46, 205
Hanaoka Y. 1999, PASJ 51, 483
Kundu M.R., Nitta N., White S.M. et al. 1995, ApJ 454, 522
Kundu M., Grechnev V. 2001, Earth, Planets and Space 53(6), 585
Kundu M.R., Grechnev V.V., Garaimov V.I., White S.M. 2001, ApJ 563, 389
Nakajima H., Nishio M., Enome S., Shibasaki K., Takano T., Hanaoka Y., Torii C., Sekiguchi H., Bushimata T., Kawashima S., Shinohara N., Irimajiri Y., Koshiishi H., Kosugi T., Shiomi Y., Sawa M., Kai K. 1994, Proc. IEEE 82(5), 705
Nakajima H., Grechnev V.V. 1999, Proc. Yohkoh 8th Anniversary Symp., Explosive Phenomena in Solar and Space Plasma. Ed. Kosugi, T., Watanabe, T., Shimojo, M. (Sagamihara: ISAS), p119
Nindos A., Alissandrakis C.E., Gelfreikh G.B., Bogod V.M., Gontikakis C. 2002, A&A 386, 658
Robertson J.G. 1991, Australian J. Phys. 44, 729
Stern D. 1997, Private communication
Tsiropoula G., Alissandrakis C.E., Mein P. 2000, A&A 335, 375

Radio Observations of Solar Eruptions

N. Gopalswamy
NASA Goddard Space Flight Center, Greenbelt, MD USA
gopals@fugee.gsfc.nasa.gov

Abstract

Coronal mass ejections (CMEs) are composed of multithermal plasmas, which make them produce different radio signatures at different wavelengths. The prominence core of CMEs are of the lowest temperature and hence optically thick at microwave frequencies and hence are readily observed. The Nobeyama Radioheliograph has exploited this fact and observed a large number of prominence eruptions over most of solar cycle 23 and parts of cycle 22. This paper reviews recent studies on prominence eruptions and their contributions for understanding the CME phenomenon. In particular, the following issues are discussed: (i) the statistical and physical relationship between CMEs and the radio prominence eruptions, and how this relationship manifests as a function of the solar cycle; (ii) The asymmetry of prominence eruptions between northern and southern hemispheres; (iii) the relationship between prominence eruptions and CME cores; (iv) the implications of the cessation of high-latitude PEs before the reversal of the global solar magnetic field, and (v) the implications of the high-latitude PEs and CMEs for the modulation of galactic cosmic rays. Finally, the importance of the Nobeyama Radioheliograph data to future missions such as STEREO and Solar-B are discussed.

Key words: Sun: activity — Sun: flares — Sun: corona — Sun : radio

1. Introduction: Sun in Microwaves

A microwave imager such as the Nobeyama Radioheliograph (NoRH, Nakajima et al., 1994) observes a large number of features on the Sun occurring at various layers of the solar atmosphere: (1) the quiet solar disk at 10,000 K, which is the upper chromospheric layer of the Sun, optically thick in microwaves. (2) Active regions, which appear as small bright patches due to free-free emission from the active region loops and gyroresonance emission from sunspots. The sunspots appear as the strongest features in active regions when there is no flaring. (3) Filaments are cool (∼8000 K) features suspended in the hot corona against a brighter (Tb ∼10,000 K) solar disk and hence appear as dark linear features, somewhat similar to what is seen in Hα. (4) Prominences are the same as filaments observed above the solar limb, but appear bright because the background now is not the solar disk, but the cold sky. The corona itself is optically very thin in microwaves and contributes only a few 100 K to the observed brightness temperature. (5) Sometimes mounds consisting of AR loops (Tb >10,000 K) are seen at the limb. (6) Bright post-eruption loops are observed when active regions erupt. When quiescent filaments erupt, the post-eruption loops take the form of an arcade. The brightness temperature of the post-eruption structures depends on the emission mechanism. Gyrosynchrotron emission from flare loops can exceed 1 MK. (7) On rare occasions, one can also observe dimming (deficit of free-free emission) above the limb (Gopalswamy, 2003). Many of these features can be seen in the 17 GHz microwave image obtained on 2000 February 26 at 23:51:24 UT (see Fig.1). Various features discussed above are marked. This snapshot illustrates the wealth of information the microwave images provide on the Sun. Time series of such images capture the dynamic Sun and provide quantitative measurement of many physical parameters corresponding to the chromosphere and corona of the Sun. The prominence seen above the northeast limb in Figure 1 is eruptive as part of a coronal mass ejection (CME) also shown superposed. Hundreds of such eruptions have been documented on the NoRH web site (http://solar.nro.nao.ac.jp/norh/html/prominence/). Filament eruptions are similar to the "disparition brusques" observed in Hα. Both case studies (e.g., Hanaoka et al., 1994; Gopalswamy et al., 1996; 1999; Hanaoka and Shinkawa, 1999; Uralov et al., 2002; Kundu et al. 2004) and statistical investigations (Gopalswamy et al., 2003a; Hori, 2000; 2002) have been performed on these eruptions. This paper provides a summary of the important results on solar eruptions, especially in conjunction with data from the Solar and Heliospheric Observatory (SOHO) mission.

2. Case Studies of Solar Eruptions

2.1. Studies in the pre-SOHO Era

When routine NoRH observations of the Sun commenced in 1992, there was no spaceborne coronagraph available for comparing microwave eruptions with white light CMEs. Fortunately, the soft X-ray telescope (SXT) on board the Yohkoh satellite was observing solar eruptions, so most of the early studies involved coronal changes in X-rays in association with prominence eruptions (PEs). The X-ray and microwave signatures have been reviewed before (Gopalswamy, 1999; Cliver and Hudson, 2002).

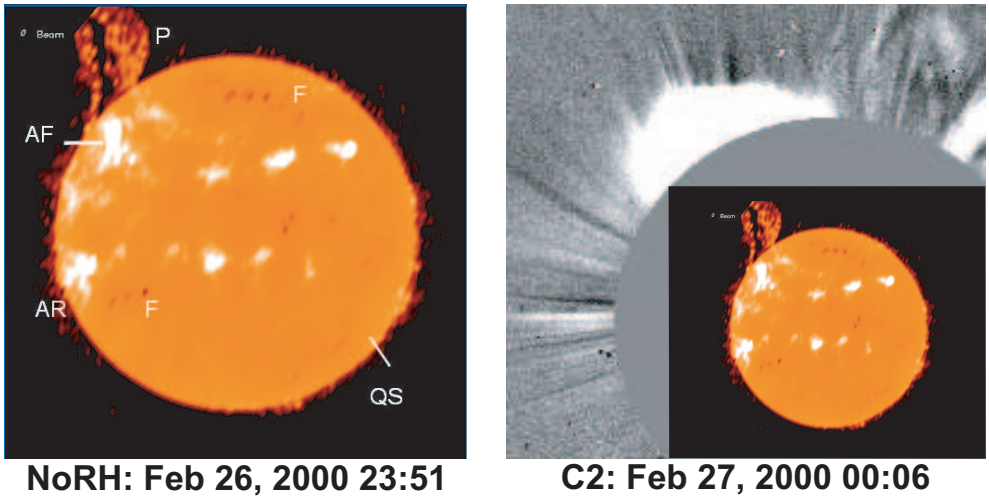

Fig. 1. *Left*: A NoRH image at 17 GHz obtained on 2000 February 26 at 23:51 UT with various observed features marked: QS - quiet Sun at 10,000 K, F - filament, AR - active region, AF - post-eruption arcade formation, and P - prominence. The beam size of NoRH is shown at the top left. *Right*: The image on the left superposed on a white light coronal image taken by SOHO's Large Angle and Spectrometric Coronagraph (LASCO) at 00:26 UT on 2000 February 27. Note the good position angle correspondence between the CME and the eruptive prominence.

The use of NoRH for the study of eruptive events started with the observation of a spectacular PE observed during 1992 July 30-31 (Hanaoka et al., 1994). This event displayed all the signatures of a major eruption: eruptive prominence followed by post-eruption arcade extending along the neutral line, and two-ribbon structure in Hα (see Fig.2). The prominence ascended with a speed of $\sim$100 km/s, and had an appearance very similar to what was observed in Hα, especially when the Hα images were degraded to the resolution of the microwave images. Unfortunately, there was no white light coronagraphic observation at that time, so the full picture of the eruption including the CME could not be obtained. However, a linear soft X-ray feature was observed moving away from the neutral line before the arcade formation (see Fig.2), which is likely to be part of the associated CME owing to its higher speed (160 km/s) and motion ahead of the prominence. The post-eruption arcade, normally observed in X-rays and EUV, was also detected in microwaves owing to the enhanced free-free emission from the hot dense loops making the arcade. The soft X-ray arcade had a temperature of $\sim$3.6 MK and a density of $\sim 2.4 \times 10^9$ cm^{-3}. This hot dense plasma produced a 17 GHz brightness temperature of $\sim$7500 K above the quiet Sun level ($\sim$10,000 K) via free-free emission. This event also demonstrated that it is possible to obtain quantitative information on various features in the eruption region. For example, the observed brightness temperature and the dimensions of the arcade can be used to infer the kinetic temperature of the post-eruption structure. The combined X-ray and microwave observations were found to be consistent with the Carmichael-Sturrock-Hirayama-Kopp-Pneuman (CSHKP) model (Svestka and Cliver, 1992) of prominence eruptions. A version of the model from Anzer and Pneuman (1982) is shown in Fig.2. The nested helices marked "prominence" may be taken to represent the cavity identified in CMEs as flux ropes.

Another very slow microwave prominence eruption (see Fig.3) was observed during 1993 July 10-11, which had an average speed of only 3.7 km/s over a period of $\sim$6 hours (Gopalswamy et al., 1996). Fortunately, the Yohkoh observations were extensive in this case and the frontal structure of the CME, which moved with a speed of 15 km/s, was observed in soft X-rays. A post-eruption arcade (AF) was also observed in Hα and microwaves (see Fig.3). The mass of the X-ray frontal structure was estimated to be $\sim 2.6 \times 10^{14}$ g, only slightly lower than the average mass of SOHO CMEs (Vourlidas et al., 2002). It must be pointed out that SOHO has observed many CMEs with mass of only $\sim 10^{13}$ g. The event also showed post eruption structure in X-rays, Hα and microwaves (Gopalswamy et al. 1997). Some of the important conclusions of this study were that a coronal volume much larger than that of the prominence was involved in the eruption and that the pre-eruption position of the leading edge was $\sim$0.3 R$_\odot$ above the solar surface. Another event with the opening of an X-ray structure 5 times as large as the microwave eruptive prominence was reported (Gopalswamy et al., 1998a). Thus the microwave observations have started contributing to the study of the early phase of CMEs, typically not observed by coronagraphs due to the occulting disk they employ.

Gopalswamy and Hanaoka (1998) tracked a long ($\sim$475,000 km) north-south filament during its disk passage for 2 weeks until it erupted above the west limb at a height of 175,000 km. At the start of the eruption, the prominence was massive ($\sim 6 \times 10^{16}$ g). The eruption was slow and the height-time measurements of the prominence could be fit to a second order polynomial (constant acceleration, $\sim$11 m/s^2). The final speed was only $\sim$70 km/s

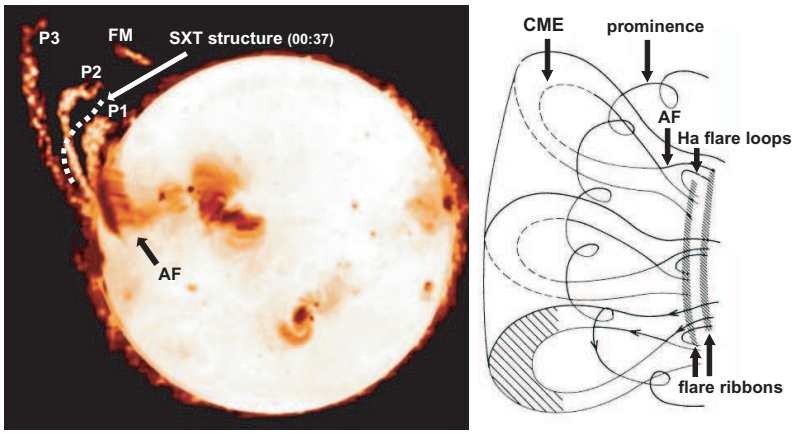

Fig. 2. The prominence eruption event of 1992 July 30-32 studied by Hanaoka et al. (1994). *Left*: Three stages of the prominence (P1 at ∼ 00:35, P2 at ∼00:45, and P3 at ∼01:25 UT) superposed on a Yohkoh SXT image showing the post eruption arcade (AF) under the eruptive prominence. A fragment of the falling prominence material (FM) is identified. The SXT structure at 00:37 is also shown, which was ahead of the prominence. *Right*: A version of the CSHKP model from Anzer and Pneuman (1982) that fits the observation. The helical structure may actually be more than just the eruptive prominence. It may represent the CME cavity. The Hα flare ribbons form the footpoints of the SXT post-eruption arcade (AF). Hα flare loops are the cooled form of the SXT loops in AF. There was no white light observation to provide information on the overlying CME.

when the prominence reached the edge of the NoRH field of view. There was no simultaneous white light observation, but the difference between white light images taken on consecutive days clearly indicated a major change in the streamer, confirming an associated coronal eruption. An extensive coronal dimming was observed in association with the prominence eruption (see Fig.4) with a long post-eruptive arcade formed close to the limb. From the dimming, the mass of the depleted coronal material was estimated to be $\sim 2 \times 10^{15}$ g, which is the typical mass of large CMEs. This is smaller than the initial prominence mass, but there was large down flow of material as the prominence rose. Thus even if only a small fraction of the prominence material escaped, it must have carried a mass comparable to the hot material ejected from the corona. Based on the extent of the dimming region and the north-south orientation of the pre-eruption filament, Gopalswamy and Hanaoka (1998) suggested that the cavity of the CME is not expected to be seen above the northwest limb in such a configuration and that an east-west filament would show the cavity. This was confirmed in a recent study involving a large number of CMEs (Cremades and Bothmer, 2004).

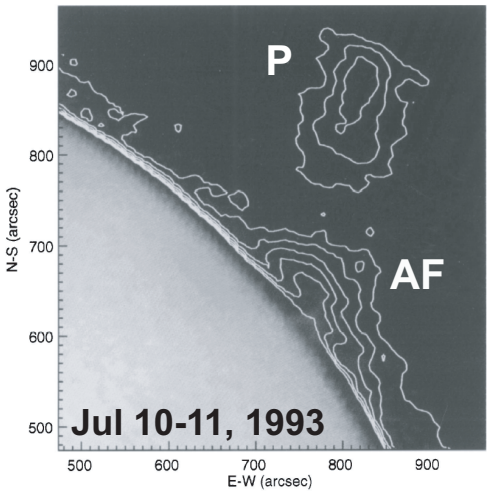

Fig. 3. Microwave eruptive prominence (P) and the post-eruption arcade (AF) presented as contours overlaid on an Hα picture. The Hα loop prominence (post-flare loops) can be seen faintly above the limb, partly coinciding with the AF contours (adapted from Gopalswamy et al. 1997).

Eruptions occurring close to the limb are easy to observe because of the weak coronal background at many wavelengths. This is usually not the case for disk eruptions. Hanaoka and Shinkawa (1999) studied two NoRH erupting filaments (1992 November 5 and 1994 February 20) at 17 GHz. Shortly after the apparent disappearance, a transient reduction occurred in the brightness of the nearby plage regions. The disappearance of the filament is due to the heating of the filaments at least to the temperature of the microwave disk, but to a temperature below that of the plage region. This is because the plages returned to their original brightness after the passage of the heated filament. It was also found that after the initial increase, the brightness temperature of the filaments was rather constant during their motion. Once heated, the filament disappears in Hα because of the spectroscopic nature of the observation. The microwave emission is via thermal free-free emission, which is a continuum emission, so the filament does not disappear. The lower limit of the energy supplied to the filament in the heating process was estimated to be $\sim 3.6 \times 10^{26}$ erg, a few orders of magnitude smaller than the kinetic energy of the filament or the energy of the associated flare. In some cases, the filament shows expansion but the average brightness temperature decreases due the increased area of the filament, but still remains optically thick (Gopalswamy, 1999).

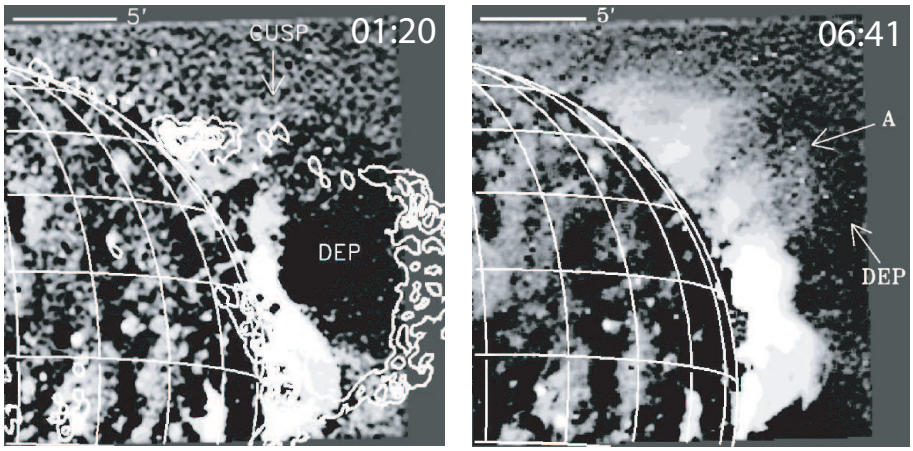

Fig. 4. The 1994 April 4-5 NoRH eruptive prominence (contour) overlaid on a soft X-ray difference image from Yohkoh showing the coronal depletion (DEP) and post-eruption arcade (A) at the limb at 1:20 UT (left) and the arcade late (6:41 UT) in the event (right) (adapted from Gopalswamy and Hanaoka, 1998).

2.2. Case Studies in the SOHO Era

2.2.1. Radio Prominence and White-Light CME

Direct comparison between NoRH prominence eruptions and white-light CMEs became possible when SOHO data became available in 1996. One of the well-observed events by various instruments was the 1997 February 6-7 CME, which consisted of all the standard features of an eruptive event. Several fragments of a filament located on a long neutral line erupted and became the core of a CME observed by SOHO/LASCO (Gopalswamy et al. 1998b). The location of the eruption on the southwest quadrant is evident from the spectacular soft X-ray post-eruption arcade (Fig.5) with the associated dimming (Gopalswamy, 1999). Figure 6 shows the CME at 03:30 UT with its familiar three-part structure. The leading edge had already crossed the LASCO FOV, but was clearly ahead of a bright blob with an extended component parallel to the limb. Superposed on this LASCO image is a 17 GHz NoRH image taken at 1:40 UT, showing that the microwave prominence was identical to the double structure in the bright core. The bright core was observed as a filament moving westward towards the limb for many hours before appearing as a prominence above the limb. The continuation of the radio prominence into the CME as its core is clear from the height-time plot of the frontal structure and the prominence core (see Fig.6). The radio and white light prominences fit to a constant acceleration curve. The frontal structure was accelerating ($\sim$17 m s^{-2}), resulting in a speed of $\sim$730 km/s at 25 R$_\odot$. The prominence had a smaller acceleration ($\sim$4 ms^{-2}) and had attained a speed of only 390 km/s at 25 R$_\odot$. The separation between the prominence and the frontal structure remained large all the way to 1 AU, as confirmed by in situ observations in the solar wind (Gopalswamy et al., 1998b).

2.2.2. Nonradial Motion of an Eruptive Prominence

A prominence core with nonradial motion on 1997 December 14 CME was studied by Gopalswamy et al. (2000). The prominence erupted from within a soft X-ray structure (ABC in Fig.7) above the southeast limb. As the eruption proceeded, the centroid of the prominence shifted equatorward with a speed of $\sim$27 km/s. The location of the prominence was at the southern foot of a helmet streamer observed by SOHO/LASCO at 00:30 UT. As the prominence erupted, the streamer showed a bulge roughly above the prominence, but the CME was fully formed with its leading edge at a CPA of 90 deg (see the LASCO image at 07:23 UT in Fig.7). Weak activity was also noted in the northern foot point of the streamer. The initial position angle of the 17 GHz prominence was $\sim$120 deg, while the white light observations placed the core at a position angle of $\sim$90 deg. That is, there was a 30 deg offset between the PE and CME position angles. The nonradial motion of the prominence suggests that the overlying streamer must have guided the eruptive prominence. Filippov et al. (2001) were able to model the eruption using a magnetic structure shown in Fig.8. They solved the equations of motion numerically to obtain the trajectory of the current carrying filament in the corona. The nonradial motion was also inferred in a statistical study by Plunkett et al. (2001) who found a bimodal distribution for the location of eruptions observed in EUV as compared to the equatorial position angle for the associated white light CMEs. It will be shown later that this bimodal distribution is confined to the solar minimum period.

2.3. A Microwave CME

A very fast eruption was detected by NoRH on 2001 April 18, originating from an active region behind the limb (9415 located about 30 deg behind the limb: S23W120). This active region had produced many energetic CMEs during its disk passage (Gopalswamy et al., 2002). The eruption in microwaves very much resembled a white light CME, with a diffuse frontal structure and a compact core.

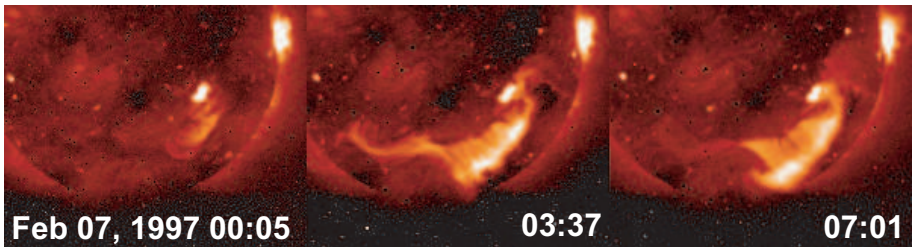

Fig. 5. Development of the post-eruption arcade during the 1997 February 07 CME as observed by Yohkoh's soft X-ray telescope.

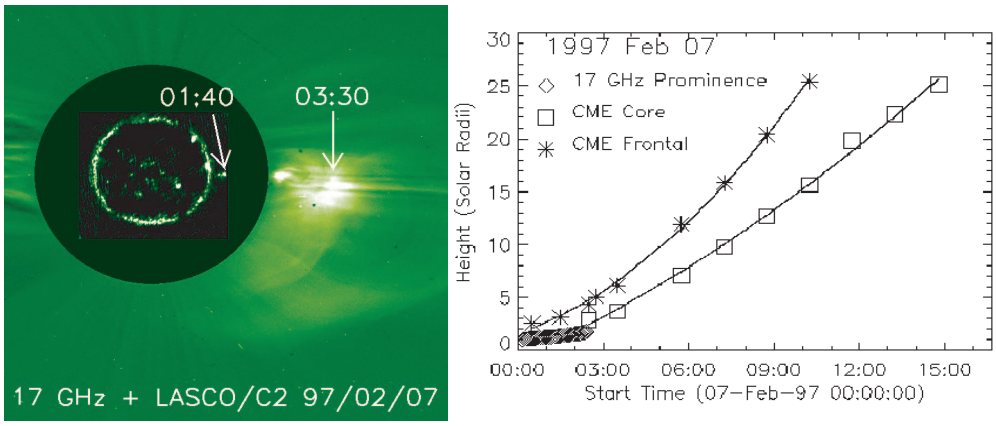

Fig. 6. *Left*: The NoRH 17 GHz eruptive prominence observed on 1997 February at 01:40 UT and its evolved form as the core of the CME observed by SOHO/LASCO/C2 at 3:30 UT. *Right*: Height-time plots of the leading edge of the CME (marked *), the NoRH prominence (diamonds) and the CME core in white light (squares).

Microwave emission appeared initially at 2:13 UT as a compact source and spread on either side of the location of initial appearance covering a position angle extent of ∼32 deg by 02:16 UT. The rapid expansion is evident in Fig.9 (left) where the loop-like appearance of the CME is the shell representing the expansion over just one minute (2:16 to 2:17 UT). When the CME first appeared in the LASCO/C2 FOV at 02:30 UT, it had an angular width of ∼70 deg at a distance of ∼5 $R_\odot$. Such early expansion is well known, and is also reflected in the mass increase up to a height of ∼8 $R_\odot$ before attaining a constant value (Vourlidas et al., 2002). The previous LASCO image at 02:06 UT had no sign of the CME. The CME had already left the C2 field of view by 02:54 UT, but appeared above the C3 occulting disk at 02:42 with the leading edge at a heliocentric distance of 7.7 $R_\odot$. Figure 9 (left) is a composite picture showing the microwave CME at 02:17 UT, becoming the white light CME at 02:30 UT (LASCO/C2) after the rapid expansion. In Fig.9 (middle), the 02:42 UT LASCO/C3 image is added, showing that the expansion has stabilized with very little increase in angular width between the C2 and C3 images. The images are 12-13 minutes apart and provide three snapshots of the rapid evolution of the CME. The microwave difference image at 02:17 UT clearly shows a core distinct from the main body of the CME. The thickness of the leading edge corresponds to the expansion in one minute. The leading edge of the microwave CME was not visible after 2:17 UT because it faded to the background level. However, the core was observed for the next 7 minutes (Fig.9 (right)). The speed of the core was ∼1635 km/s, while the average speed of the white light CME was ∼2500 km/s. It was also possible to track the core in white light. Both the core and the outer structure seem to be nonthermal microwave emission, probably due to accelerated electrons trapped in the CME magnetic structures. The core was also briefly observed in hard X-rays (Hudson et al. 2001) from lower energy electrons, while the microwave emission is from higher energy electrons.

Both the hard X-rays and microwave emission from the CME were observed because the main flare emission was occulted. Very high dynamic range would be needed to observe the diffuse CME for front side eruptions. Systematic search of such occulted fast events could provide additional information on the near surface evolution of very fast CMEs.

2.4. Evolution of a Complex CME

A filament eruption on 2001 November 17 with an unusually fast acceleration was reported by Kundu et al. (2004). NoRH was able to track the filament both on the disk and above the limb. The filament started moving outward from the southeast quadrant of the Sun around 3:30 UT with a constant acceleration (∼15 m/s^2) until about 04:45 UT, and then underwent a rapid acceleration from about 70 km/s to 425 km/s during the impulsive

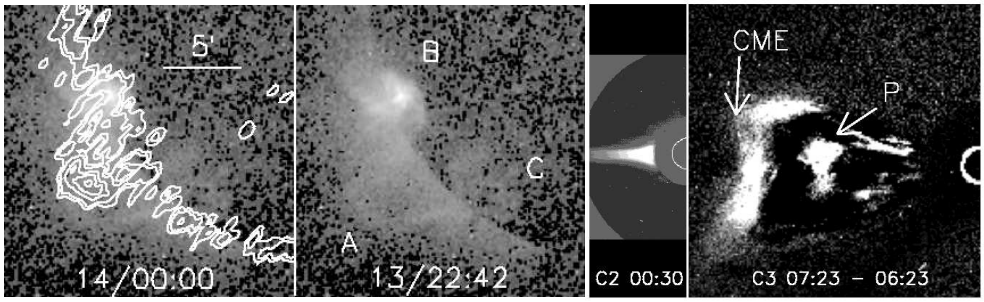

Fig. 7. The two panels on the left show the NoRH prominence (contour at 00 UT on 1997 December 14) within the soft X-ray structure (ABC at 22:42 UT on the previous day) above the southeast limb. The two panels on the right show the white light coronal streamer at 00:30 UT (December 14) and the CME with the prominence core (P) about 7 h later (07:23 UT, with the image at 06:23 UT subtracted).

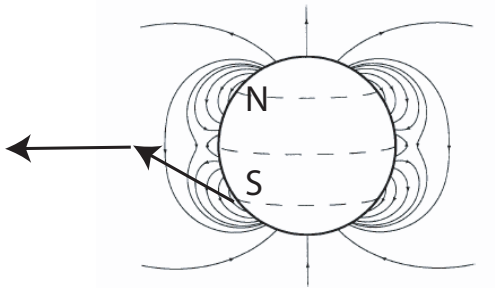

Fig. 8. The global magnetic field configuration considered by Filippov et al. (2001) to model the nonradial motion of the eruptive prominence from the location S towards the equatorial plane first and then in the equatorial plane (the trajectories shown by thick arrows). The X-ray structure ABC was located at S, while there was a dimming at N associated with the eruption. N and S were located at the northern and southern base, respectively of the streamer observed in white light.

phase of the associated flare (during 4:45 to 4:55 UT). Although the GOES X-ray flare onset was given as 4:49 UT, there was a slow rise around the time of the filament motion (see Fig.1 of Subramanian et al., 2003). The slow soft X-ray increase seems to be associated with a brightening below the filament, different from the post eruption loops in the associated active region. Kundu et al. (2004) also reported soft X-ray features moving in the direction of the filament and an X-ray dimming near the filament region around 4:31 UT. The CME first appeared in the SOHO/LASCO FOV at 3.8 $R_\odot$ at 5:30 UT and had a speed of ∼1380 km/s in the sky plane. Linear extrapolation of the height-time plot (see Fig.10) gives an onset time of 4:49 UT or slightly earlier when the projection effects are taken into account. Extrapolation of the constant speed part of the prominence trajectory yields an onset time just before 4:45 UT, coinciding with the white-light CME onset. Kundu et al. (2004) suggested that the rapid acceleration of the filament (and the associated CME) due to the flare process in the active region, similar to the scenario proposed by Zhang et al. (2001). Another possibility is that the filament might have undergone rapid acceleration due to the impact of the fast CME observed by LASCO (see Gopalswamy et al., 2001 for an example of a prominence core deflected by a fast CME). The onset of the filament eruption well before 04:00 UT and the soft X-ray loop motion followed by the dimming around 4:30 UT suggest a possible slow CME well before the observed fast CME. This would imply that the fast CME had overtaken the slow one within the occulting disk, so only a single CME was observed in LASCO field of view. Several examples of CME interaction below the occulting disk have been reported by Gopalswamy et al. (2004b).

3. Small-scale Ejecta

In addition to the CMEs and PEs, NoRH also observed other eruptive signatures such as coronal radio jets and blobs. These eruptions are generally of smaller spatial scale, some of which may be associated with PEs.

3.1. Jets

The motivation to the study of jets in microwaves came from the soft X-ray jets detected by Yohkoh (Shibata et al. 1992). Case studies of 17 GHz emission from X-ray jets were first performed by Kundu et al. (1997). The radio emission originated either from the base of the X-ray jets, or from the base and the lower part of jets. In a statistical study, Kundu et al. (1999) found an almost one-to-one correspondence between the X-ray and radio manifestations of the jets. There was also good correlation between the X-ray and microwave fluxes from the jets. The observed brightness temperature and polarization of the radio emission is generally consistent with free-free emission from the jet plasma. One of the jets showed motion in microwaves, amounting to a speed of ∼55 km/s, similar to the speeds of Hα surges. Jets are also known at other wavelengths: Wang and Sheeley (1998) found EIT counterparts of all 27 narrow (angular width 3-7 deg) CMEs observed by LASCO. Yashiro et al. (2003) identified a large number of narrow CMEs (up to 22% of all CMEs during solar maximum) when the angular width was increased to 20 deg. These narrow CMEs were similar to the normal CMEs in some respects and differed in others. Studies involving limb jets in X-rays, microwaves, EUV,

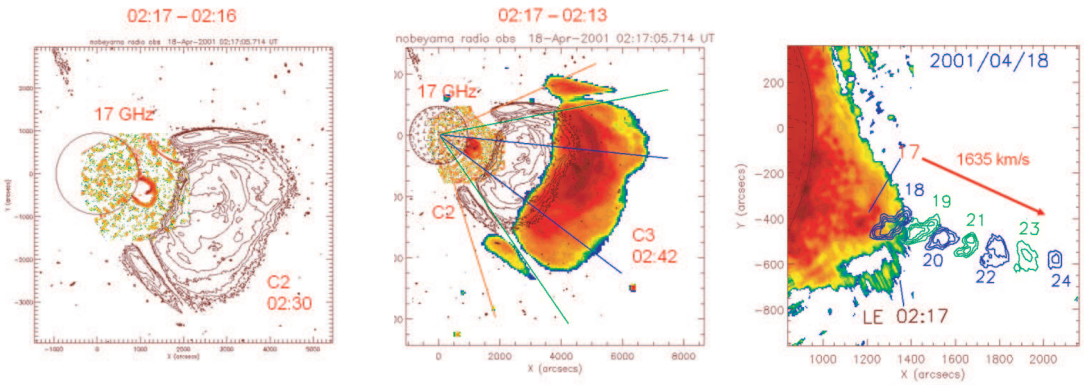

Fig. 9. *Left*: 17 GHz NoRH difference image at 2:17 UT (with the image at 2:16 UT subtracted) showing the expansion of the CME above the southwest limb. A contour image of the white light CME observed by SOHO/LASCO/C2 at 2:30 UT is superposed. The two linear features on either side of the CME are the displaced streamers. *Middle*: Same as in the left, but the NoRH image is a direct image and the LASCO/C3 image at 2:42 UT is also superposed. The position angle extent of the CME is shown by pairs of straight lines marking the edges of the CME in microwave, C2 and C3. *Right*: A small section of the corona above the southwest limb showing the microwave CME at 2:17 UT (the leading edge is marked as LE). The core at 2:17 UT is marked "17". The location of the core at subsequent times is superposed as contour images. The numbers near the contour images show the minutes after 2:00 UT. The speed (1635 km/s) and the direction of motion of the core are also indicated.

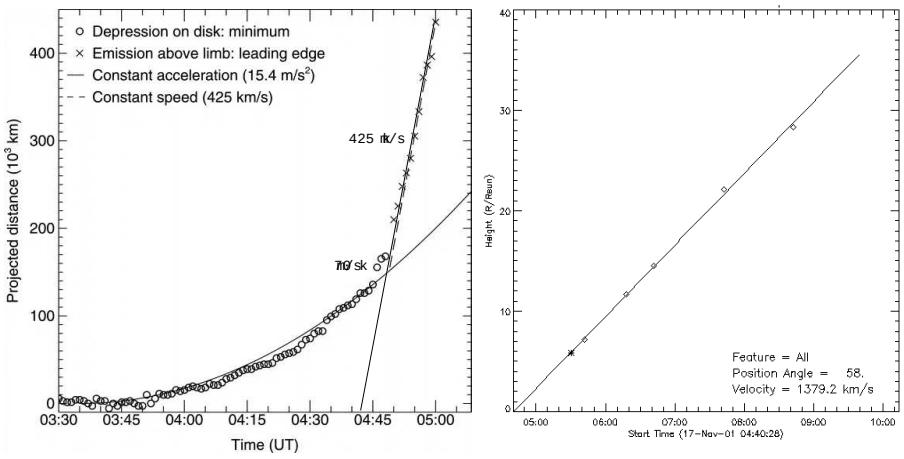

Fig. 10. *Left*: Height-time plot of the NoRH eruptive prominence on 2001 November 17 as it moved from the disk to above the limb (from Kundu et al., 2004). There was a sudden increase in speed around 4:45 UT. *Right*: Height-time plot of the LASCO CME.

and white light are needed to understand the connection between narrow CMEs and jets. The microwave data provide additional information to study the small-scale energy release, which may be similar to large eruptions, but observed with a lot of clarity.

3.2. Blobs

The appearance of compact microwave sources above a flaring loop was first reported by Shibasaki (1996) for the 1993 January 2 event. The blob was much smaller than the post flare loop in size and brightness. The blob appeared to grow out of a mound. Hori (2000) studied a few more blobs with sizes ranging from 90 to 320 arcsec. The brightness temperature was typically ∼20,000 K. Some blobs were flare remnants, while others were formed by chromospheric evaporation (or new activity). Unfortunately, some of these early events did not have CME observations to understand the overall event. Two of the events studied by Hori (2000) overlapped with SOHO observations. The 1998 May 19 event was clearly a prominence eruption and was associated with a fast CME at 1:27 UT (speed ∼600 km/s and width ∼100 deg). The CME association of this eruption was missed in the study of Gopalswamy et al. (2003a). The second event was a filament activation event with no clear ejection, and was not associated with a CME. Sometimes, blobs appeared to indicate magnetic connectivity between two mounds (Hori, 2000) and magnetic reconnection in the space between the mound and the blob. Most of the flare ejecta occur under the overall envelope of the CME, so the blob studies need to be performed again with the inclusion of CMEs to place them in the context of typical eruptions.

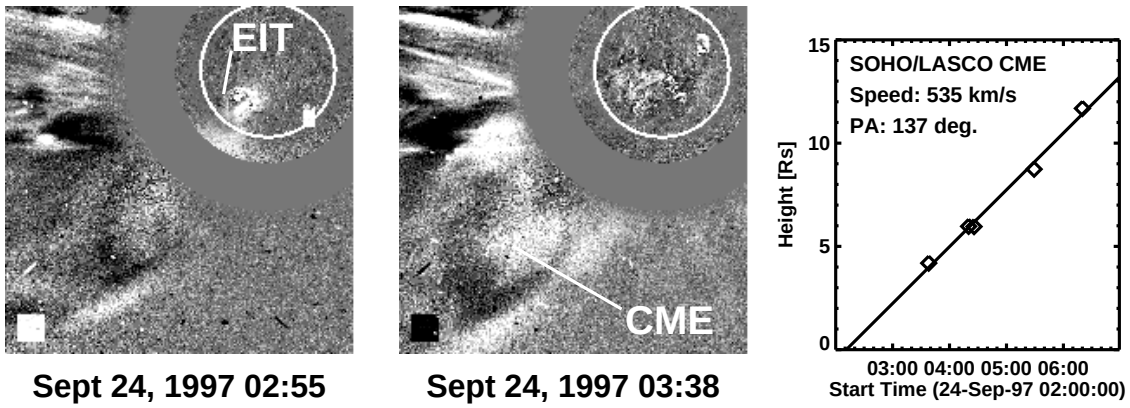

Fig. 11. The EIT brow wave of 1997 September 24 (marked EIT on the EIT difference image at 02:51 UT) with the associated white light corona from SOHO/LASCO at two times (02:55 and 03:38 UT). New material appears above the southeast limb only in the 3:38 UT LASCO frame. The height-time plot of the CME is shown on the right. The CME had an average speed of 535 km/s in the sky plane. The actual speed of the CME is likely to be much higher because of projection effects (location of the eruption at S31E19).

4. Microwave Manifestations of EIT Waves

Coronal waves in EUV, first detected by Neupert (1989), are now routinely observed by the Extreme-ultraviolet imaging telescope (EIT) on board SOHO (EIT waves - Thompson et al., 1999). The EIT waves are very helpful in identifying inner-coronal manifestations of CMEs in the spatial domain not accessible to coronagraphs. The EIT "brow waves" (so named because of their arc-like appearance in EIT images - see Gopalswamy, 2000; Gopalswamy and Thompson, 2000) are spatially and temporally coincident with metric type II radio bursts (Gopalswamy et al., 2000d). Biesecker et al. (2002) later classified the brow waves as "events with sharp brightenings" and found them to be associated with metric type II bursts, flares, and CMEs. They also found an unambiguous correlation between EIT waves and CMEs, but a significantly weaker correlation between EIT waves and flares. The brow waves are also highly likely to be associated with Moreton waves, which are chromospheric signatures. Recently, White and Thompson (2005) reported the microwave counterpart of the 1997 September 24 EIT wave using the NoRH data. They interpreted the microwave disturbance as the thermal free-free emission (optically thin) from material swept up or otherwise disturbed by the EIT wave. They also found a higher speed (835 km/s) for the microwave disturbance than for the EIT wave (500 km/s, Thompson et al., 2000).

The eruption occurred at S31E19, and the associated CME was accordingly moving in the SE direction. The sky plane speed of the CME was $\sim$ 530 km/s (see Fig.11), consistent with the EIT wave speed also measured in the sky plane. However, this speed is likely to be much smaller than the true speed due to projection effects. The true speed could exceed 1000 km/s. The CME onset has been estimated to be $\sim$02:33 UT, about 10 minutes before the onset of the EIT wave. The onset is likely to be earlier if initial acceleration and projection effects are taken into account. But the main point is the CME was expanding from the eruption site at least 10 minutes before the wave observed in EUV and microwave. At present there is no consensus on the driver of the EIT waves. Although EIT waves correlate better with CMEs than with flares, CMEs are either ignored or dismissed in some studies dealing with these waves (Hudson et al. 2003; Warmuth et al., 2004; White and Thompson, 2005). The assumption is that the EIT waves are flare blast waves. For example, White and Thompson (2005) argue that the radio emission from the EIT wave should increase if it is CME-driven, rather than the observed decrease. However, the CME is expanding and the CME brightness decreases even for accelerating CMEs. If an EIT wave surrounds the CME, the wave also expands and the radio brightness may not increase. The presence of the CME poses a problem for the blast wave scenario: since the CME is in progress when the flare starts beneath the CME, the blast wave has to move through the fast-moving CME material. This makes the shock formation difficult. Otherwise, one has to assume that the blast wave propagates only through coronal regions not occupied by the CME. Irrespective of the source of the EIT waves, their identification in microwaves is significant for further investigations (see also Aurass et al., 2002).

5. Statistical Studies of CME-PE Relationship

The case studies of solar eruptions reviewed above confirm the close relationship between CMEs and PEs. This relationship was already known from pre-SOHO observations of CMEs and Hα PEs (Webb et al., 1976; Munro et al, 1979; Webb and Hundhausen, 1987; St Cyr and Webb, 1991). However, doubts remained on this relationship until recently because some studies indicated only a minority of PEs from the disk and limb were associated with white light CMEs (Wang and Goode, 1998; Yang and Wang, 2002). Hori and Culhane (2002) and Gopalswamy et al.

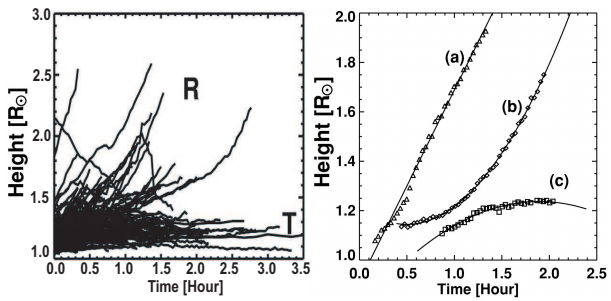

Fig. 12. *Left*: Observed trajectories of a large number of prominence eruptions (PEs). R and T represent the predominant motion in the radial and transverse directions, respectively. *Right*: The three primary types of trajectories (a) constant speed, (b) accelerating, and (c) decelerating. The heights were measured from the Sun center.

(2003a) revisited this issue using NoRH PEs. Hori and Culhane (2002) studied 50 NoRH PEs using simultaneous data available from SOHO and Yohkoh. Gopalswamy et al. (2003a) used all the 226 PEs detected automatically in NoRH images. Both confirmed the high degree of association between PEs and CMEs. These two studies used microwave PEs as the primary data set and searched for CME association, unlike most of the previous studies, which used CMEs as the primary data set. In addition to the PE-CME association, some global properties of PEs and CMEs were also investigated: latitude distribution of PEs and CMEs, position angle and onset correspondence, relation between CME cores and PEs, and solar cycle variation of PE and CME latitudes.

5.1. CME-PE Association Rate

Out of the 226 PEs were detected automatically from NoRH images between 1996 January and 2001 December, 186 overlapped with SOHO observations. The four years of NoRH data in the pre-SOHO era (before 1996) were not used due to lack of CME data. The leading edges of the PEs were tracked to the edge of the NoRH FOV (around 2.5 $R_\odot$ from the Sun center). The height-time trajectories of the PEs fell into two groups: radial (R) and transverse (T), as indicated in Fig.12. For the T events, the height remained roughly the same in time, but the prominence clearly moved horizontally from the initial location to a nearby location on the limb. It was possible to fit the trajectories either to first order or to second order polynomials (see curves marked (a), (b), (c) in Fig.12. The T events had trajectories of type (c). Linear fits were also made to all trajectories to get an average speed for statistical comparisons. The R and T events correspond to the classical "eruptive" and "active prominences", respectively (see e.g., Tandberg-Hanssen, 1995). There were 152 (or 82%) R events, while the remaining 34 (18%) were T events. The R events typically attained larger final heights or left the NoRH FOV, while the T events were confined to lower heights and never left the NoRH FOV.

Out of the 186 PEs, 144 (or 72%) were associated with SOHO/LASCO CMEs. If we consider the R events alone, the association rate increased to 83%. Clearly 52 (or 28%) events lacked white light CMEs. The CME-PE association rate is slightly lower than that (92%) obtained by Hori and Culhane (2002), but these authors used a smaller sample selected with a more restrictive criterion. The statistical results clearly confirm the close relationship originally found by Munro et al. (1979). A detailed investigation of the 52 PE events without CMEs revealed that 11 of them had changes taking place in the overlying coronal streamer (Gopalswamy et al. 2004a). The majority (7/11 or 64%) of the streamer-change PEs belonged to T events; in the R events, the PEs showed sudden stalling after traversing a small distance. The average speed and final height of the streamer-change PEs were 13 km/s and 1.19 $R_\odot$, respectively. These were intermediate between the R (65 km/s, 1.4 $R_\odot$) and T (10 km/s, 1.16 $R_\odot$) events.

5.2. PEs With and Without CMEs

The primary differences between PEs with and without associated CMEs are shown in Fig.13. On the average, PEs without CMEs attained a height of ∼1.2 $R_\odot$ compared to 1.4 $R_\odot$ for those associated with CMEs. Munro et al. (1979) had found 1.2 $R_\odot$ as the threshold height: virtually all prominences reaching this height had CME association. The CMEless PEs were also much slower (average speed ∼20 km/s) compared to the CME-associated PEs (average speed ∼70 km/s). There was also a good correlation between the final height attained and speed of PEs (correlation coefficient 0.62, see Gopalswamy et al., 2003a).

5.3. Spatial Comparison of PEs and CMEs

The NoRH images provide the exact locations of PEs, making it easy for spatial comparison between PEs and CMEs. Since the central position angle (CPA) is one of the basic attributes of CMEs, the heliographic coordinates of PEs were converted to CPAs. The CPAs of PEs and CMEs also give their respective latitudes. Since the projection effects are minimal for the limb events considered here, the latitudes derived from CPAs are expected to be accurate. Figure 14 shows that the latitude distributions of PEs and CMEs do not agree well. The latitude distribution of PEs is bimodal, whereas that of the CMEs is single peaked. This means a lack of position angle correspondence between PEs and CMEs. In order to investigate this further, the offset between the PE and CME latitudes was computed and is shown in Fig.14. The distribution of the offsets is clearly biased towards positive values suggesting that the PEs were typically located poleward of the CMEs (positive offset means the PE latitude is larger than the CME latitude). However, this offset did not occur always: it was mainly concentrated during solar minimum years, when the polar field strength is high and the global dipole of the sun is strong. It has been suggested that the strong dipolar field guides the inner coronal eruptions so that the CME observed in the coronagraphic FOV has its leading edge at lower latitude than the solar source latitude. In other words, the CMEs do not move radially away from the solar source region, as

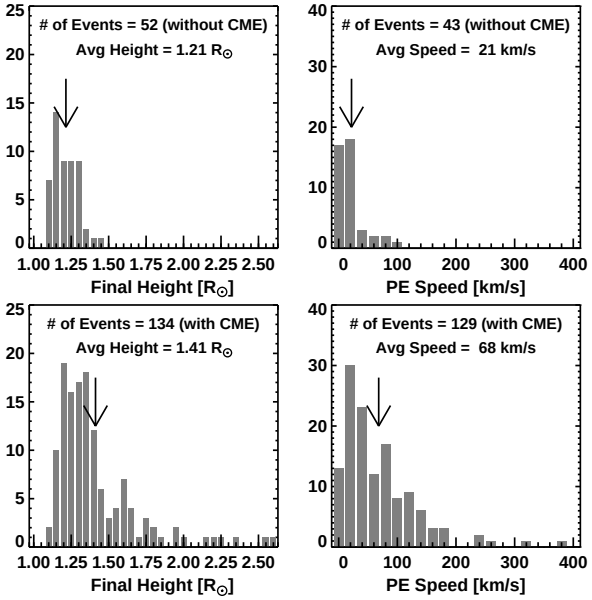

Fig. 13. Comparison of final heights (*left*) and speeds (*right*) of eruptive prominences without CMEs (top panels) with those with CMEs in the bottom panels. The average values of the distributions are marked. The final heights of prominences without CMEs never exceeded ∼0.5 $R_\odot$ from the surface, while those with CMEs reached larger heights. The CME-associated PEs were much faster than the PEs without CMEs. The speed could not be measured for all the PEs.

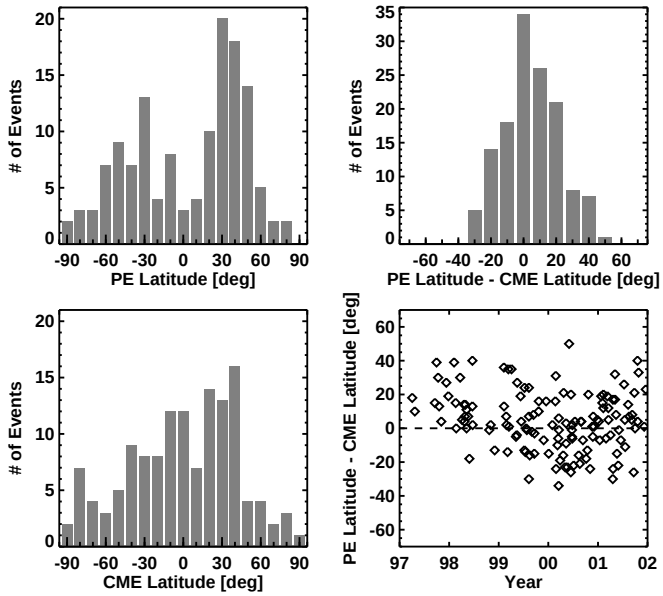

Fig. 14. *Left*: The latitude distribution of prominence eruptions compared with those of CMEs. *Right*: the offset between the central position angles of PEs and CMEs. Positive values indicate that the PEs were more poleward than were the CMEs. The offset was distinctly positive during the solar minimum phase compared to other times.

was demonstrated in a case study in section 2.2.2.

5.4. PEs and CME Core

Case studies presented here and elsewhere (Gopalswamy et al. 1998b; Hori, 2000; Srivastava et al., 2000) have clearly shown that eruptive prominences observed in the NoRH FOV become the core of the white light CMEs eventually observed at larger heights. Out of the 134 PE-associated CMEs, 98 (or 73%) had clear white-light cores (Gopalswamy et al., 2003a). This rate is slightly higher than the 65% reported by Hori and Culhane (2002) for a smaller sample. The white-light core speeds were always greater than those of the corresponding PE speeds. This is expected because of the continued acceleration (PEs generally have positive acceleration in the NoRH FOV). The average speed of PEs (∼81 km/s), white-light cores (348 km/s) and CME leading edges (609 km/s) had a definite order for all the events (Gopalswamy et al., 2003a). An exception to this was reported by Srivastava et al. (2000), in which the CME and prominence core had roughly the same speed. A scatter plot between NoRH PE speed and the speed of the corresponding white light cores showed a weak correlation: the faster the PEs the faster were their white light counterparts. As was pointed out by Hori (2000), a PE becomes a core when it remains dense enough during the transit from NoRH to LASCO FOV. PEs in streamer-change events and PEs with transverse trajectory are less likely to have cores in the LASCO FOV.

5.5. CMEs and Solar Polarity Reversal

During solar minima, most of the closed field regions (from which CMEs originate) are confined to the equatorial streamer belt. As the solar cycle progresses, closed field regions spread to all latitudes. This trend continues all the way to the solar maximum years. This pattern is clearly seen in the latitude distribution of PEs and the associated CMEs shown in Fig.15 (right). The spreading of PEs to higher latitudes is due to the "rush to the poles" of polar crown filaments (PCFs) starting in the rise phase of the solar cycle and ending somewhere during the maximum phase (see e.g. Cliver et al., 1994). The occurrence of PEs abruptly ended at high northern latitudes in October 2000 (indicated by the short vertical line between 60 and 90 deg latitudes in Fig.15 (right)). After this time, the PEs were located generally below 60 deg. In the southern hemisphere, the high-latitude PEs suddenly ended in May 2002 (indicated by the short vertical line). Clearly, there was an asymmetry in the number of PEs in the northern and southern hemispheres. The cessation of PEs at high latitudes coincided with the time of polarity reversal (Gopalswamy et al., 2003b). When all the CMEs (not just the PE-related) are grouped into high-latitude (HL, ≥60 deg) and low-latitude (LL, ≥40 deg) CMEs, the rates of HL and LL CMEs show different solar cycle variations (see Fig.15, top-left). The rate of HL CMEs is clearly related to the migration of PCFs to the poles, and the sharp decline in HL rate coincided with the polarity

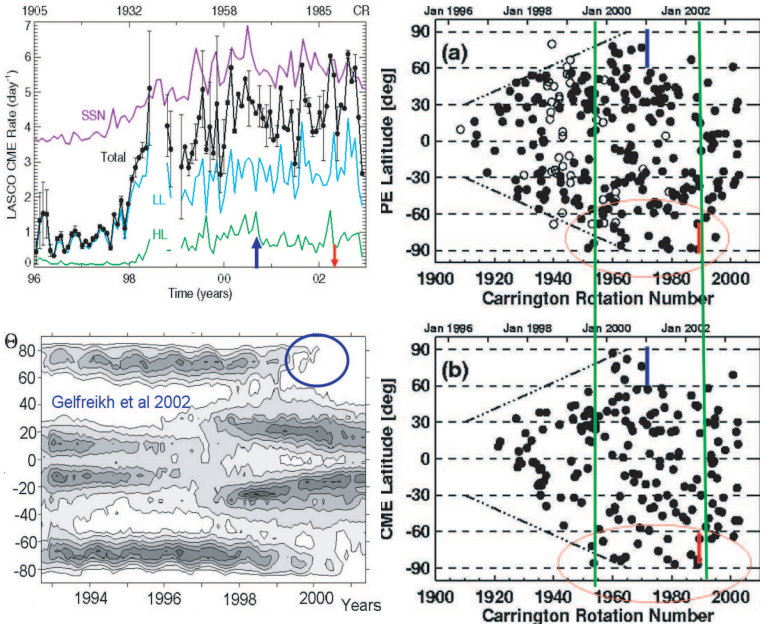

Fig. 15. Solar cycle variation of several quantities associated with solar eruptions: (top-left) The CME rates (total, high-latitude - HL, and low-latitude - LL) compared with the Sunspot number (SSN). The times of solar polarity reversal in the north (up arrow) and in the south (down arrow) Polar Regions of the Sun are shown. (bottom-left) Variation of microwave brightness as a function of time and latitude (θ) from Gelfreikh et al. 2002). The time when the northern hemispheric polar brightening disappeared is shown circled. (top-right) The latitudes of prominence eruptions (PE) and those of the associated CMEs (bottom-right) are compared. Both indicate high latitude activity up to the polarity reversal, and the sudden cessation at the time of the reversal. The short vertical lines mark the cessation of high-latitude activity. The duration of high-latitude activity is longer in the southern hemisphere (shown circled).

reversal in each pole. This close relationship between the cessation of high-latitude activity and the polarity reversal at the solar poles in cycle 23 was also found to hold for solar cycle 21 (Gopalswamy et al., 2003b). A precursor activity to the polarity reversal is the disappearance of the polar coronal holes (Harvey and Recely, 2002). In NoRH data, this precursor is seen as the cessation of polar brightenings (see the region circled in the bottom-left part of Fig.15). The microwave brightness enhancement in coronal holes is a distinct signature and may be indicative of conditions in the chromosphere favorable for solar wind acceleration (Shibasaki, 1999; Gopalswamy et al., 1999). The southern reversal occurred in 2002, beyond the data period considered by Gelfreikh et al. (2002). Thus, the high-latitude PEs and the associated CMEs provide a natural explanation for the disappearance of PCFs, which need to be removed before the poles can acquire open field structure of the opposite polarity. It must be pointed out that all the HL CMEs are PE-related, while the LL CMEs are mostly sunspot related. The LL CMEs follow the latitudinal variation of Sunspot number (SSN) because most of these CMEs originate in active regions, which contain the sunspots (confined to latitudes <45 deg). One can see that the LL CME rate is generally flat during solar maximum in contrast to the HL CME rate, which shows a sudden cessation at the time of polarity reversal in each pole. No sunspots are associated with the PCFs, so the PCF-related CMEs (or HL CMEs) are not expected to be correlated with sunspot activity.

5.6. High Latitude Eruptions and Modulation of Galactic Cosmic Rays

The increased high-latitude activity prior to the polarity reversal at solar poles has additional implications for the modulation of galactic cosmic rays (GCRs). Newkirk et al. (1981) identified CMEs as the solar origin of the low-frequency power in the interplanetary magnetic field fluctuations and suggested that the solar-cycle dependent modulation of GCRs can be explained by the presence of CME-related magnetic inhomogeneities in the heliosphere. However, the rate of CMEs known at that time (maximum rate ∼3 per day) and the minimum-to-maximum variability (by a factor of ∼6) were inadequate to cause significant GCR modulation (see the review by Wagner, 1984). Recent studies indicate that the maximum rate is as high as 6 per day and the minimum to maximum variability (by a factor of ∼10) is much higher (Gopalswamy, 2004; Lara et al., 2005). Furthermore, Newkirk et al. (1981) considered only LL CMEs (latitudes below 60 deg). As Fig.15 shows, the HL CME rate becomes almost comparable to the LL rate during solar maximum. When we consider the NoRH PEs alone, this is quite evident: The LL and HL PE rate is roughly the same during solar maximum, while the LL rate dominates during solar minimum (see Fig.16, where the NoRH PE rate is plotted since 1992). The HL CME rate may play an important role in modulating GCRs during the A>0 epochs (when the north-polar magnetic field of the Sun is

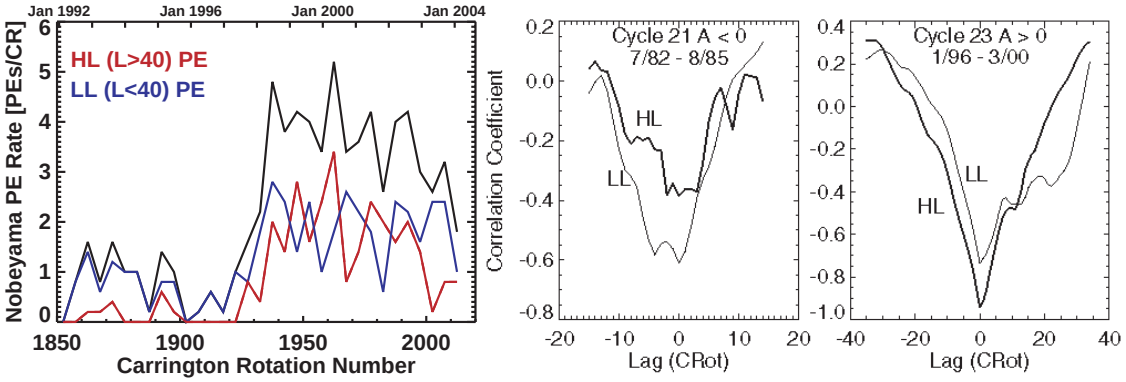

Fig. 16. *Left*: The rate of prominence eruptions (PEs) per Carrington rotation detected by NoRH. Note that the duty cycle of NoRH is only ∼8 h per day, so the actual number is expected to be much larger. The HL PEs have latitude L ≥40 deg while the LL PEs have L < 40 deg. This definition of HL PEs is slightly different from that in Fig.15. Note that the LL and HL PEs are roughly equal in number during solar maximum years compared to the solar minimum years. *right* The correlation coefficient between the CME rates (LL and HL) for the A<0 epoch cycle 21 and A>0 epoch of cycle 23. Note that the LL (HL) CME rate has a better correlation with GCR intensity in the A<0 (A>0) epoch.

northward) because the cosmic rays enter the heliosphere in the polar direction (Jokipii et al., 1977) thereby directly encountering the HL CMEs. On the other hand, the HL CMEs may not pay a role during the A < 0 epoch (when the north-polar magnetic field of the Sun is southward) because the cosmic rays enter the heliosphere along the equatorial current sheet (and hence mainly encountered by LL CMEs). The HL CME rate was found to be better (anti)correlated with the GCR intensity than the LL CMEs for the SOHO CMEs during the A>0 epoch of cycle 23 (see Fig.16). When the available CME data for the A <0 epoch in cycle 21 were examined, the relative importance was reversed: the LL CMEs were better (anti)correlated with the GCR intensity. While this work is preliminary, it certainly suggests the possibility of obtaining a better physical picture of the GCR modulation process. The continued operation of NoRH through the A ¡0 epoch will provide uniform PE data to confirm this important result. The role of CMEs is also bolstered by the recent result that global merged interaction regions (GMIRs) did not form (Richardson et al., 2005) during the intense eruptive activity during October November 2003 (Gopalswamy et al., 2005). When GMIRs do not form, the HL CMEs represent a major alternative for GCR modulation in the polar region.

6. Concluding Remarks

The NoRH observations have provided several key inputs to the ongoing study of CME initiation by observing one of the essential substructures of CMEs, viz., the prominence core. This is especially important because NoRH can observe both the per-eruptive and eruptive phases of prominences. Additional information simultaneously available on the post-eruption arcades has proved to be extremely useful in deriving physical conditions prevailing at the eruption site. The uniform and uninterrupted observation of NoRH for ∼8 h per day has enabled better comparison with data at other wavelengths (such as X-rays and EUV) obtained in overlapping fields of view. Although the spatial resolution of microwave images is not as high as that in Hα images, they can provide much better information on eruptive prominences because of the continuum nature of the radiation. Estimating the prominence mass from radio observations is a useful tool, which when compared with the CME core can provide early information on CMEs. A quantitative comparison between PEs and the associated white-light cores should help understand the fraction of prominence mass escaping the Sun and how it compares with the overlying frontal structure observed in white light. Although the microwave PEs and the white-light cores had little spatial overlap at present, future instruments such as the COR1 telescope on board the STEREO mission are expected to have a reasonable overlap with NoRH FOV. Thus, continued operation of NoRH during the STEREO mission will greatly enhance CME studies. For example, one should be able to observe the nonradial motion of CMEs overlying the nonradial PEs commonly observed by NoRH. Another important quantity will be the starting heights of CMEs. Combination of NoRH and Yohkoh data has shown that CMEs start typically from a height of ∼0.3 $R_\odot$ from the surface. This can be verified when CME observations become available from COR1, whose inner edge of the field of view is close to this (0.4 $R_\odot$ from the solar surface).

Continued operation of NoRH is also important for joint studies with the Solar-B data. One of the weaknesses of CME studies is the magnetic properties of CMEs at and before the eruption. Since Solar-B will provide such information, combining it with filament data from NoRH should be able to fill this gap. While the limb data from NoRH have been well utilized for CME studies, the disk data have not been fully exploited. With the aid of sophisticated imaging techniques, it may be possible to identify filament signatures indicative of potential eruptions. Such information will also be useful for space weather purposes because disk CMEs are the ones that impact Earth.

Quantitative information on the high-latitude PE rate became available for the first time during the A>0 epoch during cycle 23, which led to the discovery of the coincidence between solar polarity reversal and the cessation of high-latitude activity. In order to confirm this result, NoRH PE data are needed at least through the next solar maximum (around the year 2012), when the Sun will reverse its polarity and enter into the A>0 epoch. In addition, this will also provide an opportunity to verify the tandem influence of high and low-latitude activities on cosmic rays presented with noisy data in Fig.16.

The author would like to thank his long term collaborators Y. Hanaoka, M. Shimojo and K. Shibasaki. He is also grateful to the hospitality extended by S. Enome, T. Kosugi, and K. Shibasaki during his visits to the Nobeyama Radio Observatory. The author also thanks S. Yashiro and S. Akiyama for help in preparing some of the figures, and A. Asai for formatting the text.

References

Anzer, U., and Pneuman, G.W., Solar Phys. 79, 129, 1982
Aurass, H., Shibasaki, K., Reiner, M., & Karlicky, M., ApJ, 567, 610, 2002
Biesecker, D. A., Myers, D. C., Thompson, B. J., Hammer, D. A., ApJ, 569, 1009, 2002
Cliver, E. W., St. Cyr, O. C., Howard, R. A., and McIntosh, P. S., in Solar coronal structures, ed. V. Rusin, P. Heinzel & J.-C. Vial, VEDA Publishing House of the Slovak Academy of Sciences, p.83, 1994
Cliver, E. W. and Hudson, H. S., . Atmospheric Terrest. Phys., 64, 231, 2002
Cremades, H. and Bothmer, V., Astron. Astrophys., 422, 307, 2004
Filippov, B. P., Gopalswamy, N. and Lozhechkin, A. V., Solar Phys., 203, 119, 2001
Gelfreik, G., Makarov, V., Tlatov, A. G., Riehokainen, A., Shibasaki, K., Astron. Astrophys. 389, 618, 2002.
Gopalswamy, N., in 'Solar Physics with Radio Observations', ed. T. Bastian, N. Gopalswamy and K. Shibasaki, p. 141, 1999.
Gopalswamy, N., in Radio Astronomy at Long Wavelengths, Geophysical Monograph 119, AGU, Washington DC, p.123, 2000.
Gopalswamy, N., Adv. Space Res., 31 (4), 869, 2003
Gopalswamy, N. in "The Sun and the Heliosphere as an Integrated system", ASSL series, edited by G. Poletto and S. Suess, KLUWER/Boston, Chapter 8, p. 201, 2004
Gopalswamy, N. and Thompson, B. J., J. Atmospheric Terrest. Phys., 62, 1457, 2000.
Gopalswamy, N., Kundu, M. R., Hanaoka, Y., Enome, S., Lemen, J. R., and Akioka, M. New Astron., 1, 207, 1996
Gopalswamy, N., Hanaoka, Y., Kundu, M. R., Enome, S., Lemen, J. R., Akioka, M. and Lara, A., ApJ, 475, 348, 1997
Gopalswamy, N. and Hanaoka, Y., ApJ, 498, L179, 1998
Gopalswamy, N., Hanaoka, Y. and Lemen, J. R., in New Perspectives on Solar Prominences, edited by D. F. Webb, B. Schmieder, and D. M. Rust, p. 358, 1998a
Gopalswamy, N., et al., Geophys. Res. Lett., 25, 2485, 1998b
Gopalswamy, N.; Shibasaki, K.; Thompson, B. J.; Gurman, J.; DeForest, C., J. Geophys. Res., 104, 9767, 1999
Gopalswamy, N., Hanaoka, Y., and Hudson, H. S., Adv. Space Res. 25, 1851, 2000a
Gopalswamy, N., Kaiser, M. L., Sato, J., and Pick, M., in High Energy Solar Physics, Ed. R. Ramaty and N. Mandzhavidze, PASP Conf Ser., vol. 206, p. 355, 2000b.
Gopalswamy, N., Yashiro, S., Kaiser, M. L., Howard, Bougeret, J.-L., ApJ, 548, L91, 2001
Gopalswamy, N., Yashiro, S., Michalek, G., Kaiser, M. L., Howard, R. A., Reames,D. V., Leske, R. and Von Rosenvinge, T., ApJ, 572, L103, 2002.
Gopalswamy, N., Shimojo, M., Lu, W., Yashiro, S., Shibasaki, K., Howard, R. A., ApJ, 586, 562, 2003a
Gopalswamy, N., Lara, A., Yashiro, S., Howard, R. A., ApJ, 598, L63, 2003b
Gopalswamy, N., Shimojo, M., Lu, W., Yashiro, S., Shibasaki, K., Howard, R. A., Adv. Space Res., 33(5), 676, 2004a
Gopalswamy, N., Yashiro, S., Krucker, S., Stenborg, G.; Howard, R. A., J. Geophys. Res., 109, A12, CiteID A12105, 2004b
Gopalswamy, N., Yashiro, S., Liu, Y., Michalek, G., Vourlidas, A., Kaiser, M. L., and Howard, R. A., J. Geophys. Res., 110, A09S15, 2005
Hanaoka, Y. et al. PASJ, 46, 205, 1994
Hanaoka, Y. and Shinkawa, T., ApJ,510, 466, 1999.
Harvey, K., and Recely, F., Solar Phys., 211, 31, 2002
Hori, K, Adv. Space Res., 26(3), p. 481, 2000.
Hori, K., and Culhane, J. L., A&A, 382, 666, 2002
Hudson, H. S., Kosugi, T., Nitta, N., and Shimojo, M., ApJ, 561, L211, 2001
Hudson, H. S., Khan, J. I., Lemen, J. R., Nitta, N. V., & Uchida, Y., Solar Phys., 212, 121, 2003
Jokipii, J. R., Levy, E. H., and Hubbard, W. B., Astrophys. J., 213, 861, 1977
Kundu, M. R., Shibasaki, K., and Nitta, N., ApJ, 491, L121, 1997
Kundu, M. R. et al., ApJ, 520, 391, 1999
Kundu, M. R., White, S. M., Garaimov, V. I., Manoharan, P. K., Subramanian, P., Ananthakrishnan, S., Janardhan, P. ApJ, 607, 530, 2004.
Lara, A., Gopalswamy, N.,. Caballero-Lopez, R., Yashiro, S., and Valdes-Galicia, J., ApJ, 625, 441, 2005.
Munro, R. H., Gosling, J. T., Hildner, E., MacQueen, R. M., Poland, A. I., and Ross, C. L., Solar Phys., 61, 201, 1979
Nakajima, H. et al., Proc. EEE, 82, 705, 1994
Neupert, W. M., ApJ, 344, 504, 1989
Newkirk, G., Hundhausen, A. J. and Pizzo, V., J. Geophys. Res., 86, 5387, 1981
Plunkett, S. P., Thompson, B. J., St. Cyr, O. C., and Howard, R. A., J. Atmospheric Terrest. Phys., 63, 389, 2001.
Richardson, J. D., Wang, C. Kasper, J. C., and Liu, Y. Geophys. Res. Lett., 32, L03S03, 2005.
Shibasaki, K., in Magnetic reconnection in the Solar Atmosphere, ed, R.D. Bentley and J. Mariska, ASP conf., p. 176, 1996
Shibasaki, K., in Proceedings of the Nobeyama Symposium, held in Kiyosato, Japan, Oct. 27-30, 1998, Eds.: T. S. Bastian, Gopalswamy, N. and Shibasaki, K., NRO Report No. 479., p.1-9, 1999
Shibata, K., et al., PASJ, 44, L173, 1992
Srivastava, N., Schwenn, R., Inhester, B., Martin, S. F., and Y. Hanaoka, ApJ, 534, 468, 2000.

St. Cyr, O. C. and Webb, D. F., Solar Phys., 136, 379, 1991
Svestka, Z. and Cliver, E. W., in Proc. IAU Colloquium 133, edited by Z. Svestka, B. V. Jackson and M. Machado, M., Springer-Verlag, Berlin, p. 1, 1992.
Subramanian, P., Ananthakrishnan, S., Janardhan, P., Kundu, M. R., White, S. M., and Garaimov, V. I., Solar Phys., 218, 247, 2003.
Tandberg-Hanssen, E., The nature of solar prominences, Kluwer, Dordrecht, 1995.
Thompson, B. J., et al., ApJ, 517, L151, 1999
Thompson, B. J., et al., Solar Phys., 193, 161, 2000.
Uralov, A.M., Lesovoi, S. V., Zandanov, V. G., and Grechnev, V. V., Solar Phys., 208, 69, 2002
Vourlidas, A., Buzasi, D., Howard, R. A., & Esfandiari, E., Solar variability: from core to outer frontiers, Ed. A. Wilson. ESA SP-506, Vol. 1. Noordwijk: ESA Publications Division, p. 91, 2002.
Wagner, W. J., Ann. Rev. Astron. Astrophys., 22, 267, 1984
Wang, H., and Goode, P. R., ASP Conf. Ser. 140: Synoptic Solar Physics, 140, 497, 1998.
Wang, Y.-M. and Sheeley Jr., N. R., ApJ, 575, 542, 1998
Warmuth, A., Vrs nak, B., Magdalenic', J., Hanslmeier, A., and Otruba, W. Astron. Astrophys. 418, 1117, 2004
Webb, D. F., Krieger, A. S., and Rust, D. M., Solar Phys., 48, 159, 1976
Webb, D. F. and Hundhausen, A. J., Solar Phys., 108, 383, 1987
White, S. M. and Thompson, B. J., ApJ, 20, L63, 2005
Yang, G. and Wang, H., Solar-Terrestrial Magnetic Activity and Space Environment, 113, 2002
Yashiro, S., Gopalswamy, N. Michalek, G., and Howard, R. A., Adv. Space Res., 32(12), 2631, 2003
Zhang, J., Kundu, M. R., White, S. M., Dere, K. P., and Newmark, J. S., ApJ, 561, 396, 2001.

Global Development of the Solar Cycle as Found from the Nobeyama Radio Observations

G.B. Gelfreikh, A.G. Tlatov
Central astronomical observatory at Pulkovo of RAS, St.-Petersburg,196140, Russia
gbg@GG1623.spb.edu

Abstract

The interpretation of the nature of solar cycles needs its Hnalysis at all levels of the solar atmosphere. However today brilliant pictures of the solar corona obtained from space laboratories in EUV and X rays are available, no bank of such observations include data necessary for homogeneous analysis of 11-year cycle. The radio data, however, could be the solution of the problem. At present stage, only the Nobeyama radio heliograph is capable to present the necessary information in the form of high quality homogeneous 2D mapping of the whole sun with spatial resolution of about 10 arcsec. The radio maps of the sun at wavelength of 1.76 cm made with the NRH made it possible to investigate the following parameters of the progress of the cycles: - Development of the flocculae/faculae regions at all heliographic latitudes; - Sunspots with the high magnetic field strength at low corona levels; - Magnetic strength and structure of the active regions at the level of the upper chromosphere; - Development of differential rotation of the sun; - Filament and prominence development in the solar cycle; - Quasi-periodic oscillations of the plasma structures of the solar atmosphere; - Neutral line enhancements in ARs reflecting coronal arches structure. In this report the illustrations of the above method of investigation of the solar activity and its development are demonstrated and some samples of analysis of the 11-year solar cycles are shown.

Key words: $Sun : radioradiation_1$ — $Sun : magneticfields_2$ — $Sun : activity_3$ — $methods : data_4$ — $imageprocessing_5$

1. Introduction

The theory of physical nature of the solar activity and its cyclicity needs an analysis of different types of its appearance over the whole disk of the sun. For a long time, study of the 11-year cycles was based mainly on observations of the active regions at low heliographic latitudes. It is obvious, however, that the cycle is a global process and needs the knowledge at least of the magnetic field over the whole solar surface. More than that, it was found that oscillations of the faculae in the polar zone activity in some 5 or 6 years later are repeated in the main activities at lower latitudes of the next 11-year cycle. That implies that the real duration of a cycle in fact lasts about 17 years, and two successive cycles do overcome each other.Modern physics of the sun is still in the stage of developing the nature of the solar activity, including the problem of the solar cyclicity. This study is important for understanding the physical nature of such processes both at the sun and the stars, and also for the practical problems of forecasting the space weather and other forms of the influence of the sun on the human activity.

For effective study of solar physical processes we certainly need to observe and make diagnostics of the plasma parameters at all levels of the solar atmosphere. Though the observations from cosmos have made possible to register plasma structure in the corona, the radio observations did not loose their role in these problems. Complex studying of activity of the Sun allows us to restore fuller picture of excitation of magnetic field inside the Sun and to study properties of weak magnetic fields, especially in the corona. The basic properties of solar cyclicity in a radio range have allowed to establish use of regular observations of radio heliograph Nobeyama. So, presence of polar activity in a radio range, has been confirmed, speed of differential rotation is determined and torisional waves are revealed. The methods of studying magnetic fields of active areas based on the polarization measurements of radio emission have got further development. Regular observations of polarization on radio heliograph Nobeyama allow carrying out estimation of distribution of polarization of all disk of the Sun on different phases of solar activity. In this presentation we made a short overview of the results found from the Nobeyama radio heliograph with more attention to the latest attempt to study global polarization analysis, the latter reflecting developing of the solar magnetic cycle. The programs for future analysis of the solar cycle are discussed.

2. Methods of analysis

In analyzing development of the solar activity we refer to brightness and polarization maps obtained using NRH at the wavelength of $\lambda = 1.76cm$. The initial data for the analysis were the daily data on circular polarization (R-L) and intensity (R+L) of the radio heliograph Nobeyama, presented in fits format. The images received with 1 second accumulation of a signal were mostly used. Averaging the images received within day with periodicity of 10 minutes has been applied for each day of observation. Besides

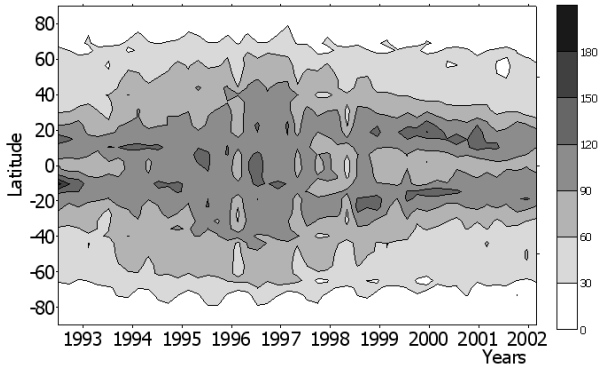

Fig. 1. Distribution of the number of the bright elements on polarization maps ($T_b > 200K$) with area exceeding 5000 m.hs (millionths of the hemisphere area) as function of helio latitude and time (years).

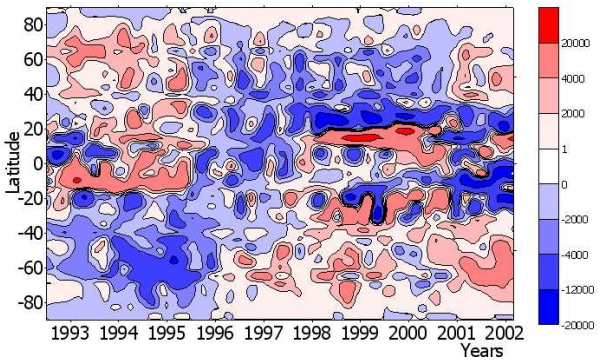

Fig. 2. Distribution of the area (millionths of the hemisphere area) of the bright elements for the two signs of the circular polarization as function of heliographic latitude and time (years).

the received row has been subjected to procedure of a filtration. For this purpose as criterion of level of noise it was calculated average polarization above a disk of the Sun. Images in which polarization in a corona at height of 1.1 solar radius exceeded some threshold size of 100 units of temperature were eliminated. Calculation of polarization was carried out at the disk of the Sun at distance from the central meridian no more than on 60°. Thus, matrixes of monthly average values of polarization in a latitude band ±80° have been generated. For the analysis of polarization of different kinds of activity procedure of definition of polarization also was applied to elements with various brightness temperatures. For this purpose the data of polarization were defined at joint processing images of polarization and intensity of radio emission. During th years 1992-2003 about 3900 days of observation have been processed.

3. Structure of active regions

The presence of the solar active regions is most effectively registered at polarization maps. To determine some conditional presentation of an active region we have chosen bright elements with brightness temperature exceeding $200K$ and the surface area exceeding 5000 millionths of the solar hemisphere. Monthly averaged values of the number of such ARs observed on the sun is shown in figure 1 as the function of the helio latitude and time (years 1992-2002).

At the picture one can easily see many forms of development of the solar cycle. In the years 1992-1994 we see the latest stage of the previous 22-d cycle with the two main heliogrphic regions of the highest activity. Near the minimum period of 1995-1998 we see the shift of activity higher latitudes. So, beginning the year of 1998 the drift of ARs to the lower latitudes began. Using this method we do not register high solar activity near the pole regions at the minimum phase of the cycle. This, however, become evident while using the other way of averaging observations (see figure 6), we will discuss later. On polarization picture of development of the ARs with illustration of the sign of polarization (figure 2) we can follow the development of the inversion of direction of the magnetic field structures. In this case more presentative form was based on the areas of polarized regions (instead of their numbers). The polarization of the discussed plasma structures is mostly that of the bremsstrahlung emission. The degree of polarization is determined by the formula

$$P = n\frac{f_B}{f}cos(\alpha),$$

where f_B is gyrofrequency of electrons and f – frequency of observations, α direction of the magnetic field in respect to the line of observation. The spectral index n represents the gradient of temperature in the region of formation of the radio emission. Generally one can expect that most of the active regions are bipolar structures. So, the two signs in polarized emission should be compensated. We may mention at least two important reason, why this is not the case. (1) The bipolar structures of the active regions are not symmetrical (different n and P parameters in the above formula). (2) The magnetic field of the ARs are partially connected with the global one. We need much more study to choose the correct conclusive answer to the problem.

The figure 2 presents a good illustration of development of the active magnetic structures at most latitudes (up to 70°). However, the inversion of the polar magnetic field connected with the global magnetic structure is not demonstrated by this method. We consider that later.

4. Differential rotation

It is well known that the law of differential rotation varies during the solar cycle resulting in so called torisional mode. The interpretation of its laws is an important problem while developing the theory of the solar cyclisity and the general nature of the solar activity. Figure 3 demonstrates the results of an analysis of the differential rotation of the sun found from observations at wavelength $\lambda = 1.76cm$ of the Nobeyama radio heliograph. To find ve-

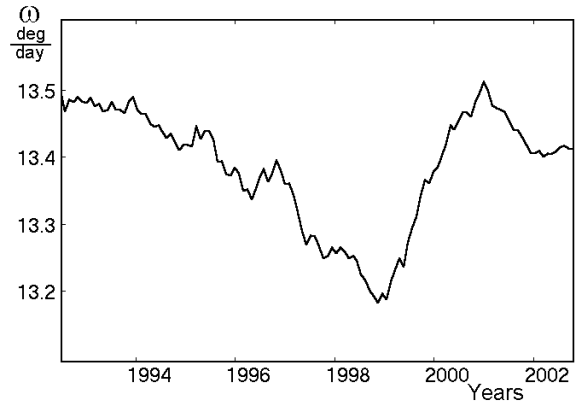

Fig. 3. Variation of the rotation velocity of the equatorial ($\pm 10 deg$) zone of the sun as function of time (years) as found from the Nobeyama heliograph observation.

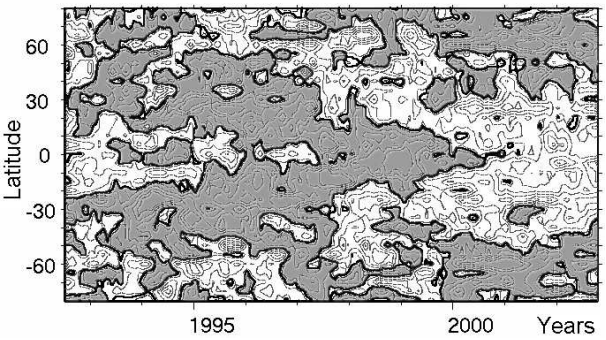

Fig. 4. Development of the differential solar rotation as the function of the time (years) according to Nobeyama heliographic observations. Darker regions belong to lower velocities.

locity the correlation method of the radio brightness was used. The figure shows the rotation velocity around the solar equator as function of time (years). The character of the curve shows a clear function dependence demonstrating the high accuracy of the radio method. Minimum of the velocity near the years of 1998-1999 is the epoch of the growth of the solar activity in the 23d cycle.

To study the appearance of torisional waves in radio wave range similar a analysis have been made for all heliographic latitudes. The result is shown in figure 4. Typical for torisional waves propagation of the deflections from mean velocity from higher latitudes to the lower ones is also demonstrated by the radio observations.

5. Prominences and filaments

In investigation of cycles of the solar activity prominences and filaments are used to find the lines separating the regions of different magnetic polarities. This refers even to weak global magnetic fields of the sun. In most studies they use the observations made in the chromosphere H_α line of the hydrogen. So, using this type of observations made in India, V.I.Makarov managed to restore development of the global magnetic field for the whole hundred years. In case of Nobeyama data (see figure 5) we deal with independent approach to this method of analysis. Important point here is that the cm radio waves may be more sensitive to the presence of the cold plasma in the solar corona than optical H_α maps and more directly represent parameters of the thermal plasma. However, the degree of correlating of the two methods still needs an analysis. From figure 6 one can see variations of the development of prominence activity during the solar cycles. The maximum of the number of the prominences obviously coincide with the maximum number of active regions at lower altitude. They are obviously belong to the neutral lines inside the the ARs. During the development of the cycle their position is shifting to the equator as do the ARs. At the same time we see the tendency to move the position of prominences to the pole regions (another branch). This reflects the motion of the neutral lines of the global magnetic fields at the proper phase of the 11-year cycle.

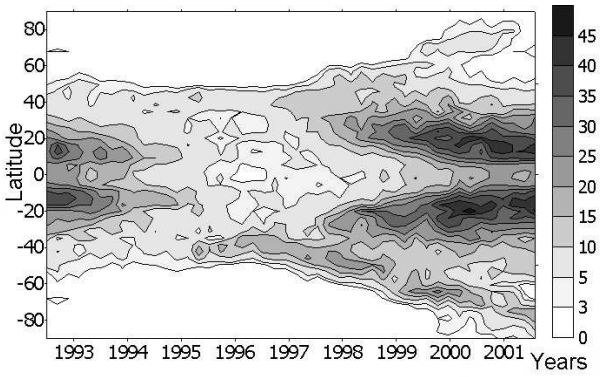

Fig. 5. (Top) Number of the prominences as function of the heliographic latitude and time (years).

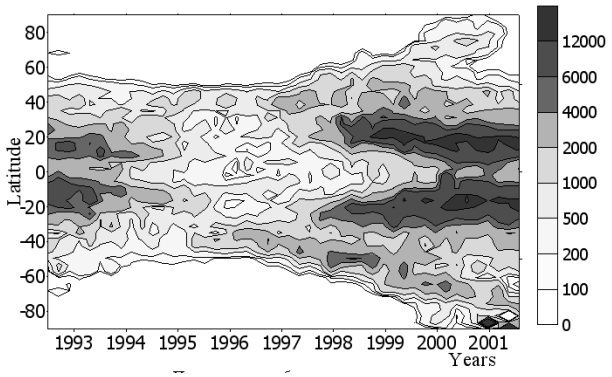

Fig. 6. Area of prominences as the helio latitude and time (years).

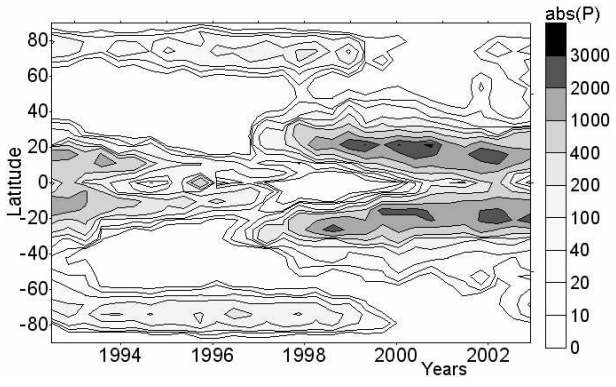

Fig. 7. Distribution of absolute value of polarization of a radio emission of 17 GHz, determined for the elements having brightness temperature higher $11000K$.

6. Global magnetic structure

Earlier in this presentation we analyzed the distribution of polarity of a radio emission considered as weak ARs. This time we analyze the polarization observed over the whole surface of the disk (inside $\pm 60°$ helio longitedes) with possible maximum averaging procedure. The latitude-time diagrams of distribution of circular polarization of a radio emission were constructed for the period of 1992-2003. Procedure of averaging has been applied for reduction of noise under several images for a day and a filtration of noisy images The analysis of distribution of polarization for structures of various brightness temperature has been carried out. The distribution of the amplitude of the polarized signal is shown on figure 6 as function of the time for the elements having brightness temperature not less $11000K$. It is possible to note, that he basic sources of polarization are sunspot. But also, bright polarized regions are present at high latitudes. The maximum of the solar activity at high altitudes is actually present near the period of minimum at lower helio latitudes. Also, one can notice that some variation of the polar activity is repeated in time some 5 or 6 years later at lower latitudes. The latter effect (known from optical observations) certainly needs a detailed analysis.

To estimate the contribution of various elements to polarization of background magnetic fields, we had carried out calculation of polarization above the areas having various brightness temperatures. On figure 9 distribution of polarization for areas with brightness in temperature above $11000K$ is presented. Most precisely, here zones of formation of spots are allocated. Wings of "butterfly" of polarization in the band of sunspots formation have an opposite sign. Probably, it occurs because polarization from leading spots in solar groups prevails.

The direction of a magnetic field will determine a sign of circular polarization. On figure 8 latitude-time distribution based on averaged polarization maps is presented. For the best allocation of background magnetic fields on these diagram areas with values above 200 K in terms of brightness temperature were not taken into account.

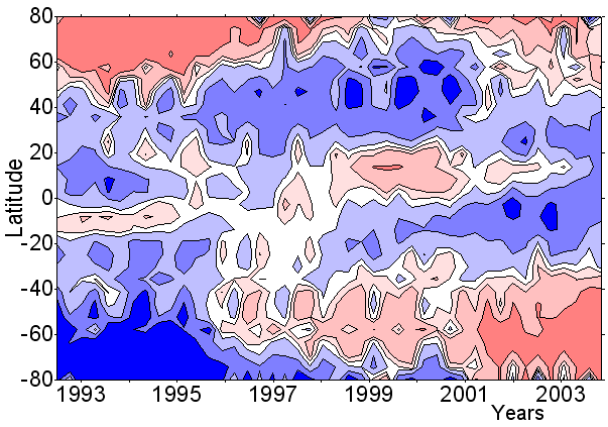

Fig. 8. The latitude-time diagram of distribution of polarization of the radio emission, received under the daily synthesized images, on the basis of 10 minute data Nobeyama. Areas with a level polarization are higher $200°T_b$ are excluded.

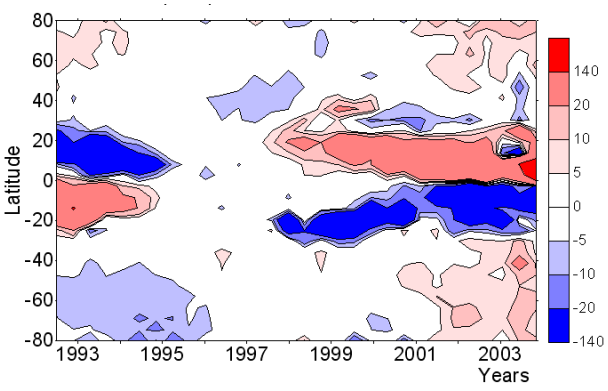

Fig. 9. The distribution of polarization received above areas with brightness temperature is higher $11000K$.

Various colors here present areas from prevailing polarity of the right or left polarization. It is possible to note, that distribution of polarization depends on a cycle of activity not only in the region of formation sunspots, but also in high-altitude areas. With the beginning of 23-rd cycle of activity during 1996-2000 drift of polarization of an opposite sign to poles is observed. The phase drift in polarization of a radio emission is close to drift of neutral lines during reversal of a large-scale magnetic field. To estimate the contribution of various elements to polarization of background magnetic fields, we had carried out also calculation of polarization above the areas having various brightness temperatures. On figure 7 distribution of polarization for areas with brightness temperature above $11000K$ is presented. In this case the zones of formation of spots are most obvious. Wings of "butterfly" of polarization in the band of sunspots formation have an opposite sign. Probably, it occurs because polarization from leading spots in solar groups prevails.

7. Future development

As we have illustrated above, the radio maps of the sun at wavelength 1.76 cm made with the NRH made it possible to investigate the following parameters of the progress of the solar cycles: - Development of the flocculi/faculae regions at all heliographic latitudes; - Sunspots with the high magnetic field strength at low corona levels; - Magnetic strength and structure of the active regions at the level of the upper chromosphere; - Development of differential rotation of the sun; - Filament and prominence development in the solar cycle, reflecting the development of the global magnetic field. In this report the illustrations of the above method of investigation of the solar activity and its development were demonstrated and some samples of analysis of the 11-year solar cycles shown. Important point of these studies is that the proper radio observations are capable to analyze most of the types of the solar activity, which were earlier found from observations in a number of different wavelength ranges. Analysis of the strength of the coronal magnetic fields is made mostly using radio observations. The Nobeyama radio heliograph is an effective instrument to solve these problems. The absence of detailed spectral analysis is certainly the weak point of the Nobeyama but the coordinate observational programs with the radio heliograph at Badary (SSRT) and the RATAN-600 observations significantly improve the situation. For study of the nature of the solar cycle is specially important point is the 12 year period of regular observations at Nobeyama. However, this period in fact is not enough for analyzing the nature of the solar periodicity. The point is that, however, the 11-year periodicity is clearly registered in solar observations, the real length of one section of the cycle is longer, probably about 17 years. So,for investigation of the nature of the solar cyclicity it is essential to look for the development of the present 23-d cycle till its end, somewhere in the year 2008. In spite of a lot of work to find the physical nature of the solar cyclicity we are far from satisfactory decision of the problem.

The work was carried out with support of grant of RFBR 02-02-16548,05-02-16749 programs of the RAS "Astronomy", "Integration" (I0208.1173).

References

Gelfreikh G.B.. 2004.Coronal magnetic field measurements through bremsstrahlung emission. In the book Solar and Space Weather Radiophysics, ed. D. Garry, Chr. Keller. Kluwer Academic Publishers, page 115.

Gelfreikh G.B. , and Shibasaki K. in Proc. 9th European Meeting on Solar Physics, Magnetic Fields and Solar Processes (ESA SP-448, December 1999), page139.

Gelfreikh G.B., Makarov V.I., and Tlatov A.G. 2000, Phys. Chem. Earth. v.25, No.5-6. page437.

Grebinskij A., Bogod V., Gelfreikh G., UrpoS., Pohjolainen S., and Shibasaki K. 2000 Astronomy and Astrophysics, Supplement Series. , V.144. page169.

Gelfreikh G.B., Makarov V.I, Tlatov A.G., 2002, in "Solar activity and Cosmic Rays after Inversion page of the Polar Magnetic Field, (GAO RAN, Pulkovo, Sanct-Petersburg), page133

G.B.Gelfreikh, V.I.Makarov, A.G.Tlatov, A.Richokainen, and K.Shibasaki. 2002,Astronomy and Astrophysics. page

Gelfreikh G.B., Makarov V.I., Tlatov A.G., Richokainen A., and Shibasaki K.. 2002, Astronomy and Astrophysics. page

Tlatov A.G. 2003, in Climate and Ecology Aspects of the Solar Activity (Central Astronomical (Pulkovo) Observatory,Sanct-Petersburg)page437

Tlatov A.G. 2003, in Climate and Ecology Aspects of the Solar Activity (Central Astronomical (Pulkovo) Observatory,Sanct-Petersburg)page443

Tlatov A.G., 2002, in "Solar activity and Cosmic Rays after Inversion of the Polar Magnetic Field, (GAO RAN, Pulkovo, Sanct-Petersburg) page559

Tlatov A.G., Shramko A.D. 2003, in Climate and Ecology Aspects of the Solar Activity (Central Astronomical (Pulkovo) Observatory,Sanct-Petersburg)page453

Observations of quiet solar features with the SSRT and NoRH

Victor V. Grechnev, Arcady M. Uralov, Vladimir P. Maksimov, Vasiliy G. Zandanov,
Gennady Ya. Smolkov, Alexander T. Altyntsev, Boris B. Krissinel,
Nadezhda N. Kardapolova, Sergey V. Lesovoi, Boris I. Lubyshev,
Dmitry V. Prosovetsky, and Georgy V. Rudenko
Institute of Solar-Terrestrial Physics, Lermontov Street 126, Irkutsk 664033, Russia
grechnev@iszf.irk.ru

Abstract

We demonstrate observations of such well-known relatively quiet solar features as filaments & prominences, coronal holes, bright points, and arcades with two radioheliographs, SSRT at 5.7 GHz and NoRH at 17 GHz. Simultaneous microwave observations with the two radioheliographs are promising and fruitful due to overlapping observational daytimes and three times different frequencies. Last circumstance determines significantly different coronal contribution at those frequencies, which governs dissimilar appearance of coronal features in images produced by the NoRH and SSRT. The emphasis is made on SSRT observations, which are not yet well known. We overview some results obtained with the two radioheliographs and discuss new opportunities of radioheliographic observations. Microwave observations are also compared with magnetograms. Only observations at several radio frequencies assure correct estimates of the magnetic field.

Key words: Sun: corona — Sun: radio radiation — Sun: magnetic fields

1. Introduction

The Sun is well known to be extremely variable. There hardly exist a feature on the Sun, which could be quiet absolutely; hence, it would be, probably, more correct to say that we will discuss *relatively* quiet solar features.

The Nobeyama Radioheliograph (NoRH, Nakajima et al. 1994) and the Siberian Solar Radio Telescope (Fig. 1; SSRT, Smolkov et al. 1986; the recent state and data of the SSRT were presented by Grechnev et al. 2003) are among the World's largest radio heliographs dedicated exclusively to solar observations. They have been operating simultaneously for the solar cycle. The SSRT (5.7 GHz) and NoRH (17 & 34 GHz) observe the Sun with a large overlapping of their observational daytimes (local noon at NoRH is at ∼02:45 UT, at the SSRT it is at about ∼05:15 UT), but at very different frequencies. Observations of the quiet Sun at 34 GHz with the NoRH are not straightforward because of the absence of the fundamental spacing at this frequency. Therefore, our discussion is related to NoRH observations at 17 GHz only. The data acquired at these frequencies supply information about coronal processes at different heights in the corona and give an opportunity to estimate contributions of various radio emission mechanisms.

Solar radio emissions in microwaves originate primarily in the solar corona, with some contribution from the transition region, both on the solar disk and above the limb. Thermal free-free emissions are well known to be the major contributor in microwaves. The magnetic field strengths in the corona overlying sunspots are such that gyroresonant absorption at low harmonics of the electron gyrofrequency leads to large optical thicknesses at frequencies below ∼5 GHz. Therefore, emission at the SSRT working frequency is characterized by a relatively large contribution of gyroresonance and thermal free-free emission with respect to the NoRH. A high contrast of radio sources relative to the quiet Sun is typical of the SSRT working frequency. The brightness temperature of steady radio sources in active regions sometimes exceeds 2 MK at 5.7 GHz.

Due to the directly-imaging operating principle of the SSRT, its beam pattern has a relatively low level of sidelobes ($\leq 22\%$ with an ideal field distribution). This allows using even "dirty" SSRT images when there are no very bright sources. However, under their presence, the input dynamic range of the SSRT receiver system becomes very high, unlike the NoRH; in this situation, "cleaning" SSRT images is also necessary. From spring 2000 on, the CLEAN routine has been introduced for SSRT images (Fig. 2). However, the cleaning SSRT images is still not perfect, because 1) the phase distribution over the aperture is not well known, and 2) some geometrical distortions are present, which make difficult cleaning the whole frame with a single beam pattern. For all those reasons, just the relatively quiet solar features of rather low contrast are the most favorable objects to observe with the SSRT.

The SSRT and NoRH observe the quiet Sun, filaments and prominences, coronal holes and bright points, features in active regions such as plages, sunspot-associated sources and neutral line-associated sources. High-sensitivity intensity and polarization observations of gyroresonance and free-free emissions with two-dimensional spatial resolution provide a powerful means by which the structure and dynamics of coronal magnetic fields can be

Fig. 1. View of the SSRT antenna array.

studied (Felli, Lang, Willson 1981; Kundu 1985; Gelfreikh, Pilyeva, Ryabov 1997).

2. Advantages of Observations with Two Radioheliographs

2.1. Two-frequency observations

Radio telescopes supply images of relatively poor spatial resolution with respect to spaceborne thermal imagers, especially those observing in single spectral lines (e.g., SOHO/EIT, TRACE). Besides instrumental limitations, there is a physical reason for that. For the major emission mechanism, thermal free-free emission, the optical thickness is determined by a well-know expression $\tau \propto n_e^2 L T^{-3/2} \nu^{-2}$, with ν being the observing frequency, n_e the electron density, L the depth of the emitting source, and T its temperature. In the optically thin case, this results in very weak temperature dependence $T_B \propto T^{-1/2}$ and, correspondingly, to smearing out the spatial structures observed due to multi-temperature plasmas localized along the line of sight.

However, in the optically thick case, the observed brightness temperature is almost equal to the kinetic temperature, which provides temperature measurements, if we are certain about $\tau \gg 1$. So, on the other hand, these circumstances determine good opportunities for plasma diagnostics, which is the first advantage of observations with two radioheliographs at distant frequencies, because the optical thickness for free-free emission recorded with the NoRH and SSRT differs by about one order of magnitude. Furthermore, the quiet coronal contribution is on the average about 6 000 K on the disk at 5.7 GHz, and it is one order of magnitude lower at 17 GHz, which determines different contrast of the features observed at the two frequencies.

2.2. Other opportunities

- When two-frequency observations are available, we can obtain hints on the presence of non-thermal emissions.
- Significant overlapping in observational daytimes of the SSRT and NoRH provides us with simultaneous observations, which allows realizing the above advantages.
- Finally, observations with two radioheliographs, whose operation principles are very different (synthesis for the NoRH and direct imaging for the SSRT), simplify detection of instrumental contributions, when the features of interest appear dissimilar in their images.

3. SSRT & NoRH Images Compared with Other Observations

Figure 3 shows an example of SSRT (a) and NoRH (c) observations in total intensity close to the previous solar minimum, on October 6, 1997 (from Grechnev et al. 2003), along with Hα images (Big Bear Solar Observatory, b) SOHO/EIT images at 304 Å (d) and 171 Å (e), and the *Yohkoh*/SXT image (f). The images produced with the SSRT, NoRH, and *Yohkoh*/SXT are averaged to enhance the sensitivity, and all the images are nonlinearly

Table 1. Some parameters of the NoRH and SSRT.

	NoRH	SSRT
Configuration	Non-equidistant T	Equidistant Cross
Number of antennas	84	256
Operating frequencies	17 & 34 GHz	5.7 GHz
Main modes	2D snapshots	2D imaging & 1D fast scanning
Angular resolution	10″ @ 17 GHz	21″ (2D mode)
	5″ @ 34 GHz	15″ (1D mode)
Time resolution	1s (steady)	∼ 2 min (2D, full disk)
	0.1 s (event)	∼ 10 s (2D, active region)
		14 ms (1D)
Sensitivity	400 K	1500 K
Imaging principle	Synthesis	Frequency scanning (112 MHz) + Earth rotation

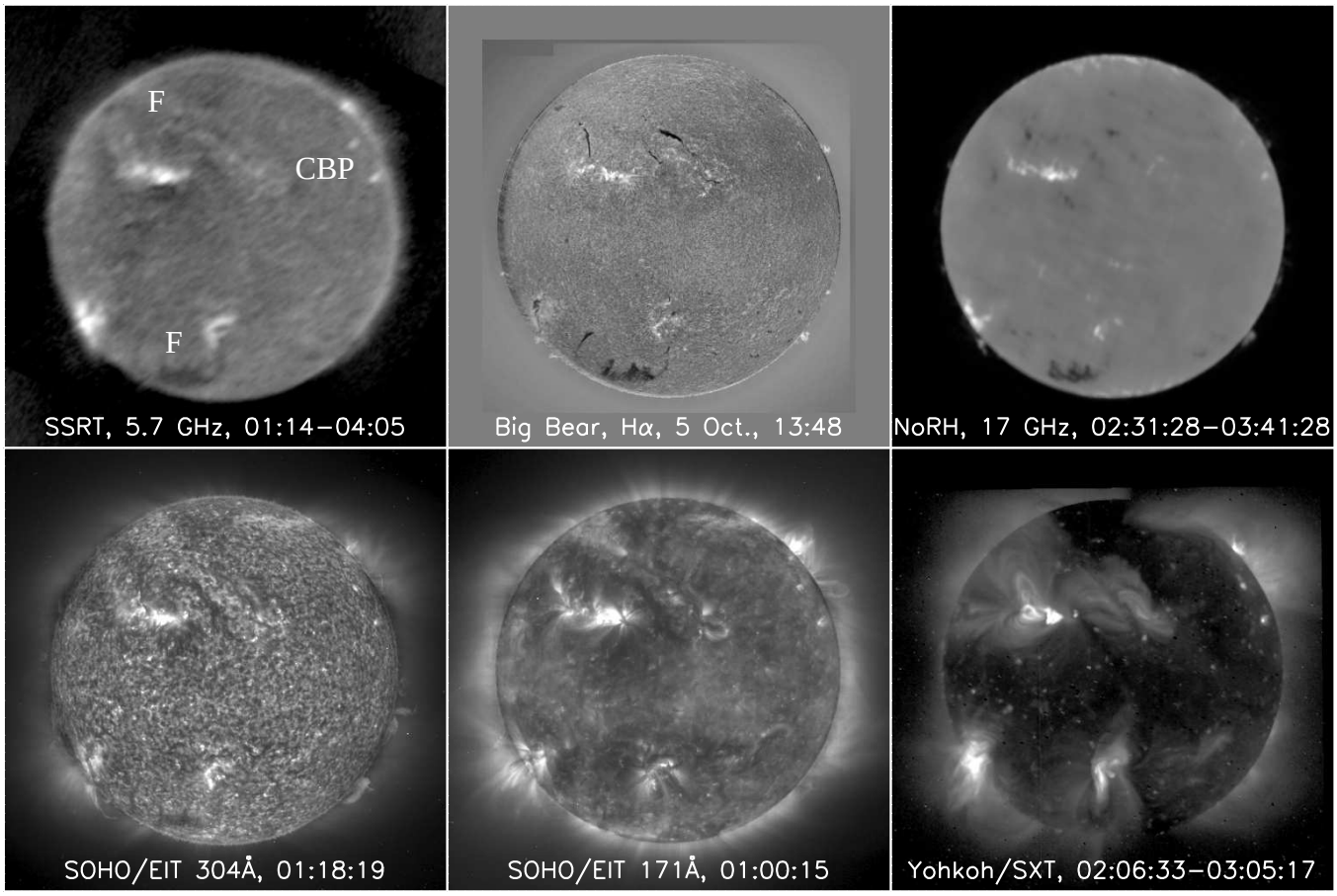

Fig. 3. Comparison of an SSRT Stokes *I* dirty map of 6 October 1997 with data from other spectral domains. All images are nonlinearly processed to make both bright sources and the quiet Sun pronounced. Solar North is up.

displayed to show both bright sources and the quiet Sun.

Optically thin bright features like emitting coronal loops above plages and coronal ("X-ray") bright points are visible in both SSRT and NoRH images. The SSRT map in Fig. 3 shows a wider range of brightness compared with the NoRH map at 17 GHz due to the greater contribution of coronal emissions at the lower frequency. The relation of brightness temperatures for such features is generally close to the frequency ratio squared, 8.8.

3.1. Filaments & Prominences

Filaments and prominences are pronounced in microwaves due to their low kinetic temperature and high density. Thus, they block brighter emission when observed on the solar disk, and produce well detectable own emission when observed against the sky.

Filaments and filament channels ("F" in Fig. 3) are supposed to be optically thick at both 5.7 and 17 GHz. Their brightness temperatures are usually close, which confirms

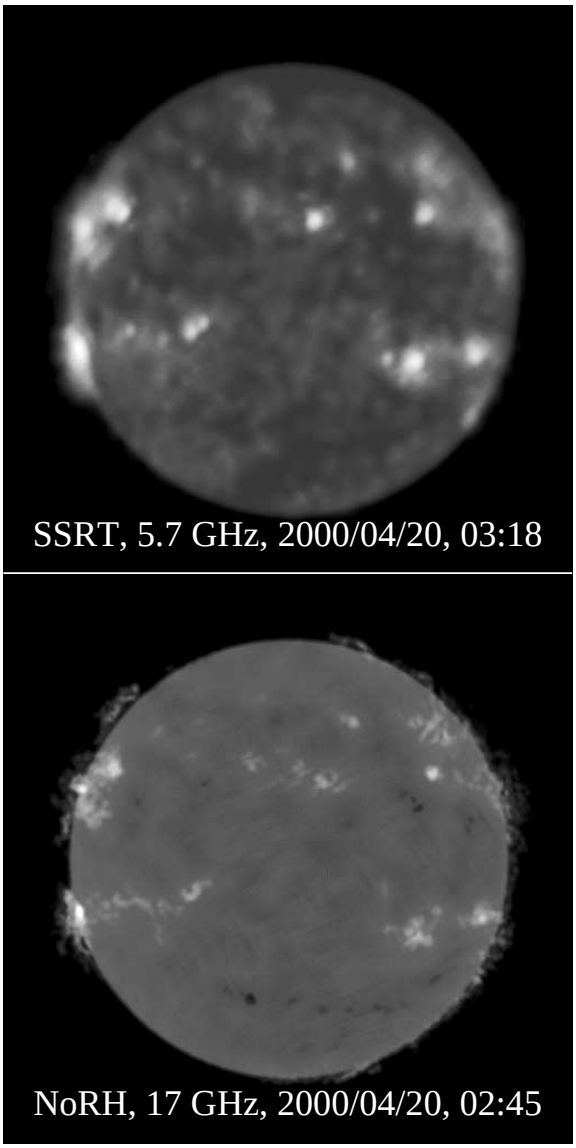

Fig. 2. SSRT clean image of April 20, 2000, and the corresponding NoRH image.

that. At 5.7 GHz, cool filaments and filament channels show higher contrast and more details. Some filaments not detectable with NoRH are nevertheless visible in SSRT maps (Zandanov and Lesovoi 1999). An apparent explanation of all these facts is the higher contrast with the quiet Sun ($T_{QS} = 16\,000$ K at 5.7 GHz and $T_{QS} = 10\,000$ K at 17 GHz). Filaments with higher kinetic temperature, about 10 000 K, are obviously not visible at 17 GHz, but still visible at 5.7 GHz.

Prominences are well observed with SSRT and NoRH, both quiescent and eruptive (Uralov et al. 2002, Grechnev et al. 2004a).

3.2. Coronal Bright Points

Coronal bright points (CBP), especially a pair localized close to the northwest limb in Fig. 3, are detectable in all images, and even in Hα filtergram. In SSRT images, they are usually well pronounced, and their brightness temperatures are typically some 10^4 K.

Analyses of simultaneous observations of CBPs at different frequencies does not show one-to-one correspondence between them. Besides coinciding CBPs, there are CBPs observed at one frequency, but absent at another one (Fig. 4). It is still not clear whether the differences are due to some physical properties of CBPs or the domains above which they are localized, or they are due to some observational aspects. Habbal et al. (1986) and Kundu et al. (1988) showed that properties of CBPs in the range of 1.5–5 GHz correspond to optically thin free-free emission. The same conclusion was made by Maksimov et al. (2001) for the observations with SSRT at 5.7 GHz and NoRH at 17 GHz. Thus, this emission mechanism is confirmed for CBPs in the frequency range of 1.5–17 GHz. Second, studying manifestations of CBPs at 5.7, 17 GHz, and in soft X-ray, Maksimov et al. (2001) concluded that some weak coronal bright points visible in other emissions are not pronounced in NoRH maps due to effects of the CLEAN routine. This also explains why the northern bright point of the pair is faint in NoRH image of Fig. 3 ($T_{B\,17} = 11\,900$ K).

3.3. Coronal Holes

Coronal holes are often visible in SSRT images. They are generally inhomogeneous, with brighter and darker portions (Krissinel et al. 2000). Due to this fragmentation, coronal holes are not as pronounced at 5.7 GHz as in soft X-ray images. Coronal holes are not distinct at 17 GHz, but sometimes they are manifest as fragmented bright features (Gopalswamy et al. 1998, Krissinel et al. 2000). To a first approximation, the more pronounced coronal contribution at 5.7 GHz (38% on the average, considering T_{QS}) is an apparent explanation of these facts. Detailed investigation of coronal holes at the two frequencies has revealed the following (Maksimov et al. 2004).

- Microwave observations confirm that coronal holes are inhomogeneous (cf., e.g., Chertok et al. 2002). The inhomogeneities have various sizes and shapes. Some of them are identified with features observed in other emissions, and some not.
- There are features within a hole and its vicinity whose brightness temperatures at both frequencies correlate: a) coronal bright points and diffuse brightenings, which are bright at both 5.7 and 17 GHz; b) filaments, which are dark at both 5.7 and 17 GHz.
- Maksimov et al. (2004) have found regions within coronal holes where, unlike features listed above, the brightness temperatures at 5.7 and 17 GHz anticorrelate. They are disposed radially. These regions are darkest at 5.7 GHz, but are not pronounced in either 195 Å, or Hα images. These regions dominate; hence, the image of a coronal hole resembles a negative of its image in extreme ultraviolet or in longer microwaves (Fig. 5).

For the enhanced brightness of coronal holes at 17 GHz

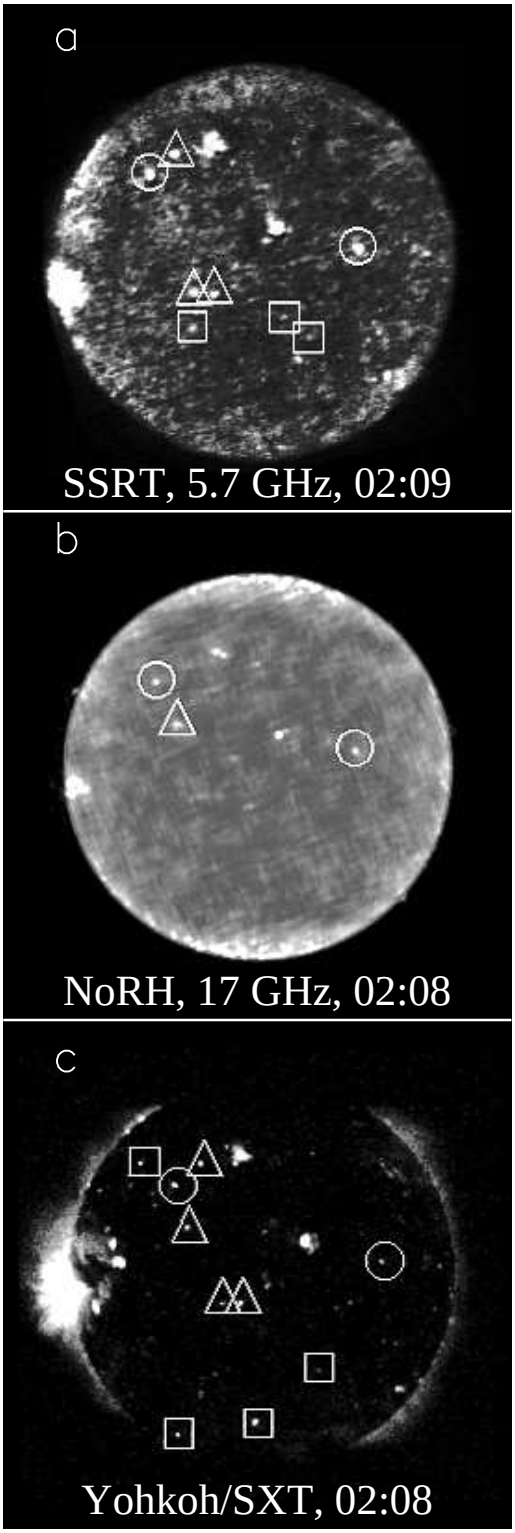

Fig. 4. Coronal bright points observed on June 3, 1996 with SSRT (a), NoRH (b), and *Yohkoh*/SXT (c). The selection criterion for CBPs is the excess of 3σ above the Sun's level. Circles mark CBPs observed in all images, triangles mark CBPs that have not all counterparts, squares mark CBPs with no counterparts.

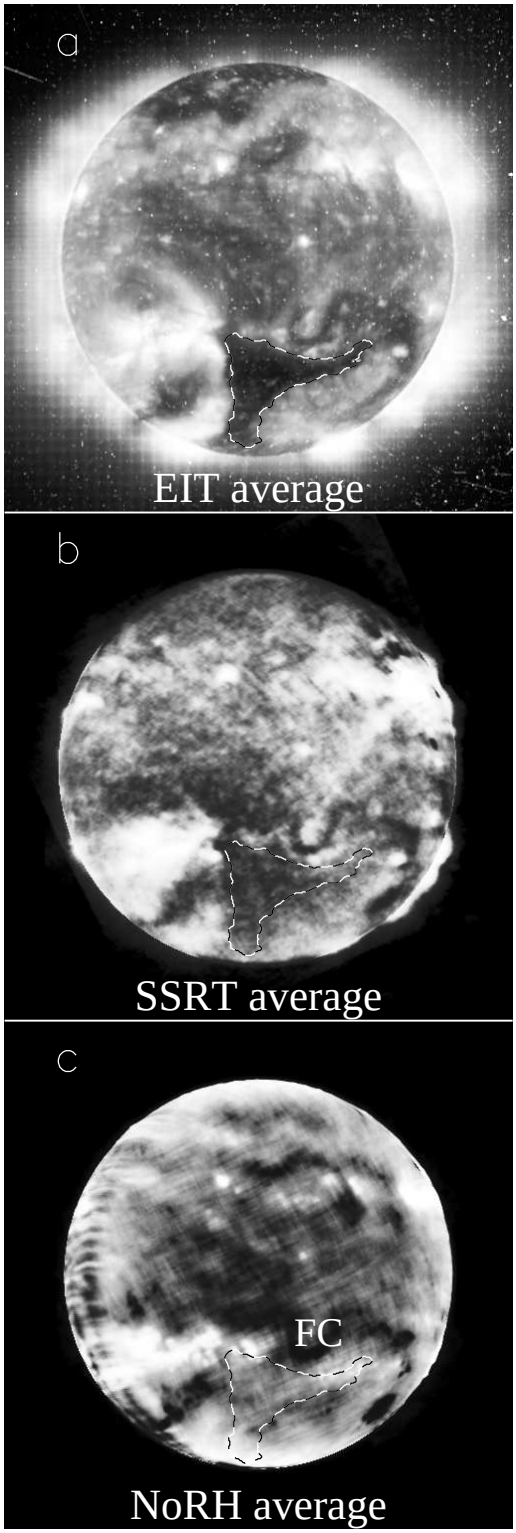

Fig. 5. A coronal hole observed during April 20–23, 1998: a) SOHO/EIT 195 Å, b) SSRT, c) NoRH images all averaged with their preliminary "derotation" to the same time of April 22, 06:00 UT. A dashed contour of the hole determined from the EIT image is superimposed on top of the SSRT and NoRH images. A filament channel is labeled "FC". Average brightness temperatures over the hole are $\langle T_{B\,5.7}\rangle = 15\,000$ K and $\langle T_{B\,17}\rangle = 11\,000$ K.

(at the chromospheric level), a mechanism can be responsible, which provides heating in the chromosphere (see, e.g., Gopalswamy et al. 1998), but simultaneously supplies cooling in the corona. The only known mechanism with such properties is dissipation of Alfvén waves. This mechanism requires further investigation, because there are some difficulties of their excitation and dissipation (see, e.g., Zirker 1993 and references therein).

The discussed radio observations at 5.7 and 17 GHz provide an identification criterion if a dark feature observed in radio images: if this feature is dark both at 5.7 and 17 GHz, it is a filament or a filament channel, not a coronal hole.

4. Studies of Magnetic Fields in the Corona

It was shown by Grechnev et al. (2003) that estimates of weak magnetic fields in the corona from SSRT polarization data for optically thin free-free emitting regions well correspond to a photospheric magnetogram (correlation of ≈ 0.95) even under very simple consideration (the magnetogram was convolved with the beam pattern of the SSRT). More rigorous approach permits to enhance significantly the correspondence of radio and magnetic measurements and to obtain new results, as shown further.

4.1. Coronal Arcades

Interesting and important bright features in SSRT and NoRH images are coronal arcades. Their studies promise diagnostics of thermal plasmas in coronal loops and disclosure of magnetic structures in the corona as well as estimates of the magnetic field strengths in them. Some of coronal arcades steadily persist for several days without conspicuous changes, and others, which form in the course of eruptions, gradually fade. The dominant emission mechanism of arcades is optically thin bremsstrahlung, but, especially in post-eruptive arcades, some non-thermal contribution can be present. It is important to identify the emission mechanism accurately, if we study the magnetic fields in the corona and try to estimate their strengths from polarization measurements. However, it can be impossible to do correctly from single-frequency observations. Two studies of coronal arcades carried out using NoRH and SSRT data along with observations in other spectral domains illustrate the above statements.

An arcade observed on November 23, 2000 in AR 9238 was analyzed by Grechnev et al. (2004b). The study has shown that the arcade formed in the course of an eruption, which occurred in an activity complex that included two active regions, AR 9231 and AR 9238. The eruptive event was triggered initially by a flux emergence in a remote site in AR 9231. Then the disturbance propagated along this active region, triggered activation and eruption of the filament, which was followed by a flare in AR 9238 and a CME. In that paper, the magnetic field in the arcade was studied, based on microwave data. The major emission mechanism in microwaves was assumed optically thin free-free emission.

However, some contribution of gyrosynchrotron emission from power-law electrons could significantly increase the degree of polarization. To evaluate its importance, Grechnev et al. (2004b) examined the flatness of the total intensity spectrum at lower frequencies using multi-frequency records from the RATAN-600 radio telescope.

The magnetic field strength in the arcade observed on November 23, 2000 was estimated from radio data to be $\sim$200 G at about 10 000 km, in accord with the extrapolation of the photospheric magnetic field into the corona.

Another arcade observed on October 22, 2001 (Fig. 6) formed also in the course of an eruption. Using multi-spectral data, Grechnev et al. (2004c) have estimated plasma parameters in the arcade several hours after the eruption at a height of ≈ 100 Mm: $N_e \sim 10^{10}$ cm^{-3} and $T_e \approx 6$ MK. Using deep averaging of NoRH data of 120 s for imaging, they have revealed a large-scale magnetic configuration surrounding the arcade high in the corona, in accord with the expected one from observations few days before as well as the potential-approximation extrapolation of the photospheric magnetic fields into the corona.

The arcade environment is negatively polarized both in NoRH and RATAN data at 17 GHz, thus delineating the magnetic configuration (x-mode, Fig. 7). A short-term appearance of the positive polarization in NoRH images southward of the arcade shows the presence there of a large-scale N-polarity magnetic field. The absence of the polarization in the brightest part of the arcade is due to the proximity of the opposite magnetic fields.

If the microwave emission mechanism would be optically thin bremsstrahlung exclusively, then the polarization measured of (10–12)% resulted in incomprehensible magnetic fields of $\sim$300 G at a height of $\sim$100 Mm. However, the total intensity spectrum of the microwave source measured with the RATAN-600 shows its non-thermal origin. Moreover, Fig. 6 shows that at 5.7 GHz, the arcade top is brighter with respect to the emitting source at its base than at 17 GHz, which could not be the case if the both sources were free-free emitting. Estimates show that an addition of 40%-polarized gyrosynchrotron emission with $T_B \sim$250 K can contribute the whole polarization observed. The extrapolation of the magnetic fields confirms the conclusions.

Grechnev et al. (2004c) also state a problem of long-term existence of the hot arcade high in the corona: either the magnetic field surrounding the arcade well exceeds 20 G at that height, or $\beta > 1$ both inside and outside the arcade. Note that a downflow observed in this case in soft X-rays, likely due to falling down remnants of the filament pre-ejected, can contribute to the balance of the arcade owing to the dynamic pressure of this downflow.

In summary, in those two papers, the importance was shown of the identification of the microwave emission mechanism from observations in a wide spectral range along with a technique to estimate contribution of non-thermal emissions to the polarization observed. Improper interpretation of the polarization measurements can result in well overestimated magnetic field strength in the corona due to non-thermal contributions.

It is worth to mention also coronal magnetography using

Fig. 6. A post-eruptive arcade observed on October 22, 2001 with the CORONAS-F/SPIRIT at 175 Å, NoRH, SSRT, and *Yohkoh*/SXT. The NoRH, SSRT, and *Yohkoh*/SXT images are averaged. The different ratio of the brightness in the top and at the base of the arcade at 5.7 and 17 GHz is due to non-thermal contribution at the arcade top.

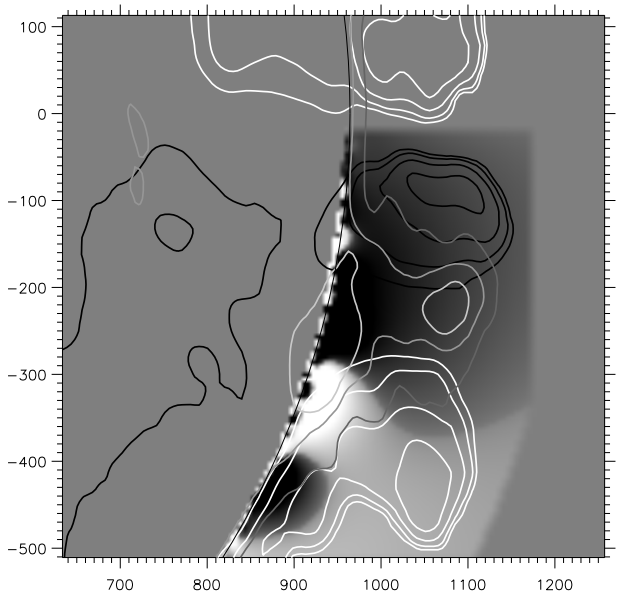

Fig. 7. A post-eruptive arcade observed on October 22, 2001: extrapolated in the potential approximation coronal magnetic fields (line-of-sight component) overlaid with gray contours of the NoRH total intensity and the degree of polarization (white contours positive). The axes show arc seconds from the solar disk center.

the polarization reversal effect in quasi-transverse magnetic field regions extensively addressed by Ryabov et al. (2003) and Ryabov (2004).

4.2. Identification of the type of a Radio Source

NoRH images of solar active regions (AR) show two types of quasi-stationary microwave sources. They are 1) compact sunspot-associated sources, and 2) neutral-line-associated sources (NLS), which are subdivided into weak, diffuse sources in simple bipolar regions, and rather bright, compact sources located in complex active regions in the vicinity of the inversion line of the radial component B_r of the coronal magnetic field. Uralov et al. (2000) first found compact NLS in NoRH images and classified them. SSRT observations of active regions containing NLS were studied earlier (e.g., Uralov et al. 1998), and those sources were regarded as predictors of powerful flares. Due to three times lower frequency, microwave sources in SSRT images are larger and usually cover sources visible in NoRH images.

It is rather difficult to recognize NLS in NoRH images. A direct comparison of microwave images of a solar active region with magnetograms of the longitudinal component of photospheric magnetic fields cannot correctly show *where* a microwave source is located within an active region. The main reason for that is the transformation of longitudinal magnetograms when we look at the solar surface non-radially. Due to the projection effect, magnetograms observed do not represent the true position of the magnetic field inversion line or the magnetic spot. Note also that NLS at 17 GHz are indistinguishable

from sunspot-associated gyroresonance sources in the degree of polarization, which can vary for sources of both types from small values up to 100%.

To avoid the projection effect and to detect NLS in NoRH maps, Uralov et al. (2004, 2005) propose a new procedure for the comparison of microwave images with the coronal magnetic field extrapolated from a single MDI magnetogram using the method by Rudenko (2001).

Figure 8 demonstrates results of this approach, representing 17 GHz intensity maps (background) along with extrapolated B_r magnetograms at a height of 2 000 km (contours) for AR 10486 on October 28–30, 2003. The magnetic inversion line is shown by thick solid line. The birth (solid arrows), displacement (dotted arrow), and persistence of compact neutral-line-associated sources along with development of the active region are seen. The birth and displacement of the NLS were accompanied by an X17.2 and X10 flares, correspondingly.

The investigation of the superactive period of October–November 2003 has shown that during that period, neutral-line-associated sources were not rare, but widespread at 17 GHz (Uralov et al. 2005).

5. Conclusion

Our overview emphasizes importance of observations with two radioheliographs. Putting additional constraints on physical conditions based on the observed quantities, microwave imaging data crucially enhance the reliability of results and consistency of interpretations. This is why microwave imaging data is a necessary constituent of observational data sets on solar phenomena.

Only observations at several radio frequencies assure identification of emission mechanisms and correct estimates of magnetic fields in the corona. In addition to traditional application of radio data, new research areas seem to appear: detection of flare-productive sites, coronal magnetography, non-local diagnostics of plasma parameters in height (in coronal holes), etc.

The results presented here have been possible due to the usage of microwave imaging data obtained with the solar dedicated radioheliographs NoRH and SSRT operating without interruption for over a decade.

Acknowledgments. We thank Pulkovo and Nobeyama Solar Groups and, especially, Prof. H. Nakajima and Prof. G. Gelfreikh for fruitful discussions and assistance. We are grateful to the Nobeyama Solar Group for the opportunity to participate this meeting and the hospitality. We thank the instrumental teams operating the Nobeyama Radioheliograph and the Siberian Solar Radio Telescope, SOHO/EIT & MDI, *Yohkoh*/SXT, and Big Bear Solar Observatory for data used here. This research was supported by the Russian Foundation for Basic Research (grants 03-02-16591 and 03-07-90087), the Russian Ministry of Education and Science (grant NSh-477.2003.2), the Russian Federal Program "Astronomy" and Lavrentiev's young scientist grant of SB RAS.

References

Chertok I.M., Obridko V.N., Mogilevsky E.I. et al. 2002, ApJ 567, 1225

Felli M., Lang K.R., Willson R.F. 1981, ApJ 247, 325

Gelfreikh G.B., Pilyeva N.A., Ryabov B.I. 1997, Sol. Phys. 170, 253

Gopalswamy N., Shibasaki K., DeForest C.E. et al. 1998, in Synoptic Solar Physics, ed. K.S. Balasubramanian, J.W. Harvey, D.M. Rabin, ASP Conf. Ser. 140, p363

Grechnev V.V., Lesovoi S.V., Smolkov G.Ya., Krissinel B.B., Zandanov V.G., Altyntsev A.T., Kardapolova N.N., Sergeev R.Y., Uralov A.M., Maksimov V.P., Lubyshev B.I. 2003, Sol. Phys. 216, 239

Grechnev V.V., Uralov A.M., Zandanov V.G., Baranov N.Y., Lesovoi S.V. 2004, Observations of Eruptive Events with Two Radioheliographs, SSRT and NoRH. Nobeyama Symp. 2004 "Solar Physics with the Nobeyama Radioheliograph", http://solar.nro.nao.ac.jp/meeting/nbym04/index.html; 2005, PASJ, in preparation

Grechnev V.V., Zandanov V.G., Uralov A.M., Maksimov V.P., Rudenko G.V., Borovik V.N., Gelfreikh G.B., Grigorieva I.Y., Medar V.G., Korzhavin A.N. 2004, Sol. Phys., in press

Grechnev V.V., Borovik V.N., Bugaenko O.I., Bogachev S.A., Grigorieva I.Y., Kuzin S.V., Lesovoi S.V., Livshits M.A., Pertsov A.A., Rudenko G.V., Slemzin V.A., Stepanov A.I., Shibasaki K., Uralov A.M., Zandanov V.G., Zhitnik I.A. Observations of a posteruptive arcade on October 22, 2001 with CORONAS-F, other spaceborne telescopes, and in microwaves. Nobeyama Symp. 2004 "Solar Physics with the Nobeyama Radioheliograph", http://solar.nro.nao.ac.jp/meeting/nbym04/index.html; 2005, PASJ, in preparation

Habbal S.R., Ronan R.S., Withbroe G.L., Shevgaonkar R.K., Kundu M.R. 1986, ApJ 306, 740

Krissinel B.B., Kuznetsova S.M., Maksimov V.P., Prosovetsky D.V., Grechnev V.V., Stepanov A.P., Shishko L.F. 2000, PASJ 52, 909

Kundu M.R. 1985, Sol. Phys. 100, 491

Kundu M.R., Schmahl E.J., Fu Q.-J. 1988, ApJ 325, 905

Maksimov V.P., Prosovetskii D.V., Krissinel B.B. 2001, Astron. Letters 27, 181

Maksimov V.P., Prosovetsky D.V., Grechnev V.V., Krissinel B.B., Shibasaki K. 2004, On the relation of brightness temperatures in coronal holes at 5.7 and 17 GHz. Nobeyama Symp. 2004 "Solar Physics with the Nobeyama Radioheliograph", http://solar.nro.nao.ac.jp/meeting/nbym04/index.html; 2005, PASJ, in preparation

Nakajima H., Nishio M., Enome S., Shibasaki K., Takano T., Hanaoka Y., Torii C., Sekiguchi H., Bushimata T., Kawashima S., Shinohara N., Irimajiri Y., Koshiishi H., Kosugi T., Shiomi Y., Sawa M., Kai K. 1994, Proc. IEEE 82(5), 705

Rudenko G.V. 2001, Sol. Phys. 198, 5

Ryabov B.I., Nindos A., Shibasaki K., Maksimov V.P., Lesovoi S.V., Pevtsov A.A. 2003, Fall Meeting AGU 2003, abst. #SH42B-0508

Ryabov B.I. Coronal magnetograms of solar active regions derived from polarization inversion in microwaves. 2004, Nobeyama Symp. 2004 "Solar Physics with the Nobeyama Radioheliograph", http://solar.nro.nao.ac.jp/meeting/nbym04/index.html;

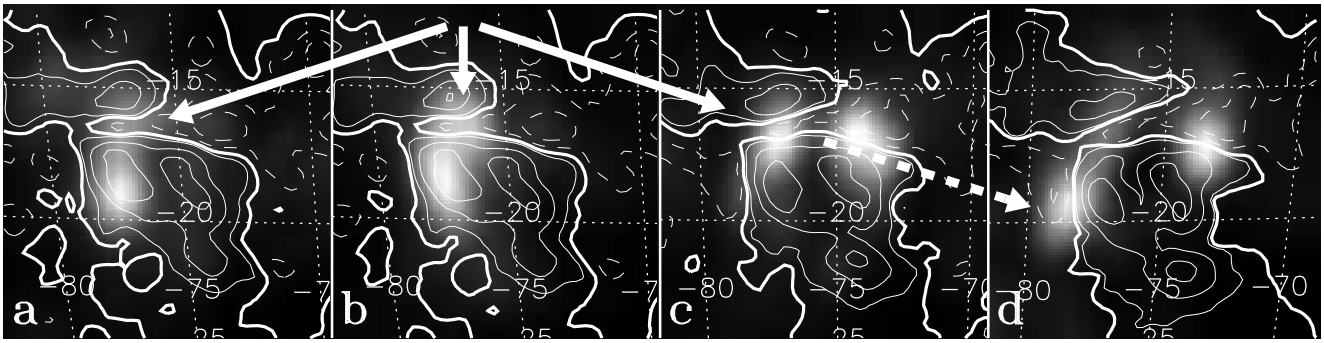

Fig. 8. 17 GHz intensity maps (background) and extrapolated B_r magnetograms (contours) of October 28, 03:10 (a) and 05:00 UT (b), October 29 (c), and 30 (d). Solid contours show positive polarity, dotted—negative. Magnetic inversion line is shown by thick solid line. One can see the birth (solid arrows) and persistence of compact neutral-line-associated sources. The arrows point out the birth site (solid) and the displacement (dashed) of the NLS.

this issue.
Smolkov G.Ia., Pistolkors A.A., Treskov T.A., Krissinel B.B., Putilov V.A. 1986, Ap&SS 119, 1
Uralov A.M., Sych R.A., Shchepkina V.L., Zubkova G.N., Smolkov G.Ya. 1998, Sol. Phys. 183, 359
Uralov A.M., Nakajima H., Zandanov V.G., Grechnev V.V. 2000, Sol. Phys. 197, 275
Uralov A.M., Lesovoi S.V., Zandanov V.G., Grechnev V.V. 2002, Sol. Phys. 208, 69
Uralov A.M., Rudenko G.V. 2004, Comparison of 5.7 and 17 GHz solar images with extrapolated magnetograms of coronal magnetic field. Active regions of the October/November 2003 period and forecast of powerful solar flares. Nobeyama Symp. 2004 "Solar Physics with the Nobeyama Radioheliograph", http://solar.nro.nao.ac.jp/meeting/nbym04/index.html; PASJ, 2005, in preparation
Uralov A.M., Rudenko G.V., Rudenko I.G. 2005, J. Geophys. Res., submitted
Zandanov V.G., Lesovoi S.V. 1999, Proc. Nobeyama Symp., Kiyosato, Japan, Oct. 27–30, 1998, ed. T. S. Bastian, N. Gopalswamy, K. Shibasaki, NRO Report 479, p37
Zirker J.B. 1993, Sol. Phys. 148, 43

Coronal Magnetograms of Solar Active Regions

Boris RYABOV
Institute of Astronomy, Latvian University, Riga LV-1586, Latvia
ryabov@latnet.lv

Abstract

The state of the art in the coronal magnetography through quasi- transverse (QT-) propagation of microwaves is discussed. The measurements are based on the fact that the circular polarization modification depends on the intensity of the magnetic field in the QT-region, where microwaves pass through the magnetic field lines at the right angle. The obtained coronal megnetograms are a series of 2D partial magnetograms, covering on each day a part of the active region. The Nobeyama Radioheliograph provides the coronal magnetograms of 110 - 50 G and the Siberian Solar Radio Telescope those of 30 - 10 G. The first results are encouraging in the sense that the features of the measured coronal magnetograms are consistent with the geometry of the QT-region. Two problems of the coronal magnetography are outlined: (1) the correct identification of QT effects and (2) the determination of the only unknown coordinate, i.e., the QTR height.

Key words: Sun: radio emission - low corona - magnetic fields

1. Introduction

This paper discusses some recent results concerning the coronal magnetography through the quasi-transverse (QT-) propagation of microwaves. The other types of coronal magnetography in microwaves make use of (1) the polarization of gyro-resonance emission (e.g. Alissandrakis et al., 1980) and (2) the polarization of free-free emission proposed by Gelfreikh (1999) (see also White 2004; Gelfreikh 2004; Ryabov 2004 for comprehensive reviews of all the types of coronal magnetography).

The observable effect of QT-propagation is the change of the circular polarization in the microwave source "screened" by the region of QT-propagation (QTR). The effect is coronal magnetic field and wavelength- dependent and is most pronounced as the inverted sense of circular polarization.

There is some transformation of circular polarization in the site where the coronal magnetic field is perpendicular to the line of sight. The theory of the QT-propagation (Cohen 1960; Zheleznyakov 1970; Bandiera 1982) predicts that the circular polarization sign reverses if the

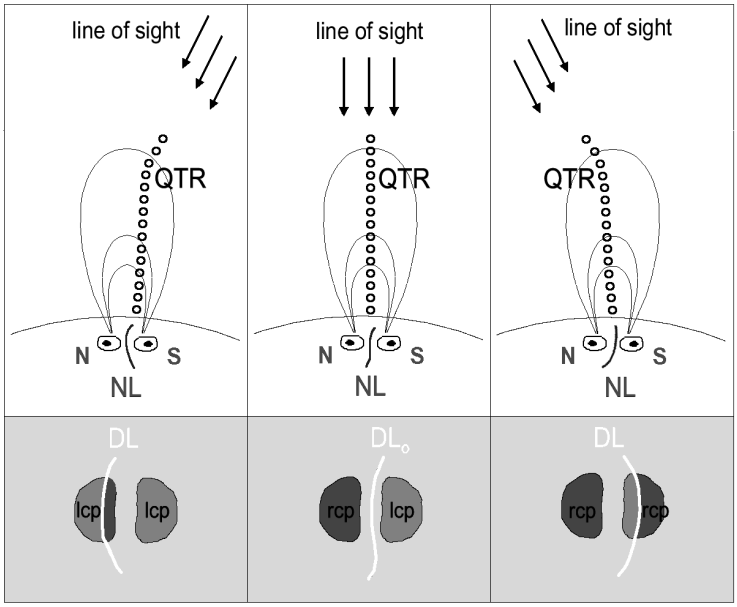

Fig. 1. Sketch of polarization changes in two microwave sources with time (lower row) associated with a bipolar active region (upper row) during its transit on the solar disc. The coronal QT-region (circles) is the site of polarization changes observed in either limbward microwave source.

ray path of microwaves crosses, almost perpendicularly, strong enough magnetic fields (Figure 1). The polarization is only slightly modified in case of weak coronal fields. A moderate field in the coronal QT-region appears as a zero circular polarization line (depolarization line, DL). The sense of the original circular polarization corresponds to the sign of longitudinal component of magnetic fields in a source of microwave emission. The polarization of a sunspot-associated source can be related with the sign of sunspot magnetic fields. Right hand circular polarization (r.c.p.) corresponds to N (positive) magnetic fields; left hand circular polarization (l.c.p.) corresponds to S (negative) magnetic fields, provided the extraordinary mode prevails in the emission of a microwave source.

Polarization changes and inversions have been detected in some microwave sources both as continuing phenomena at a fixed observational wavelength (Piddington and Minnett 1960; Peterova and Akhmedov 1974) and through the cm wavelength range (Peterova and Akhmedov 1974; Gelfreikh et al. 1987). No corresponding changes of magnetic polarity in the photosphere have been observed. It appears that the polarization is strongly affected by propagation conditions on the way through the solar corona to the observer.

The first problem a solar physicist encounters is the correct identification of the observed polarization inversion. Some other effects, distinct from QT-propagation, can give rise to polarization inversion in microwaves. A persistent problem here is the determination of the accurate distance between the microwave source and the QTR. The distance or the height of the QTR above the photosphere is the only unknown coordinate of the measured magnetic

field.

The features of the previously measured coronal magnetograms and some possible ways for solving problems mentioned above are discussed in this paper.

2. On the Technique of Coronal Magnetography

If the original degree of circular polarization ρ_0 is undergoes the QT effect, the coronal magnetic field $B(G)$ to be measured in the QTR reads:

$$B \approx 2.05 \times 10^2 \lambda^{-4/3} \left[-ln \left(\frac{\rho + \rho_0}{2\rho_0} \right) \right]^{1/3}, \tag{1}$$

where ρ is the observed polarization degree affected by QT- propagation and λ(cm) is the observational wavelength. Equation (1) is inferred from Equations (2), and (3), given by Zheleznyakov and Zlotnik (1964), under the assumption $NL_d = 10^{18} cm^{-2}$, where N is the electron density and L_d is the scale of the ambient magnetic filed divergence.

$$\rho = \rho_0 \left[2 \exp(-2\delta_0) - 1 \right], \tag{2}$$

where

$$2\delta_0 \approx 1.15 \times 10^{-25} B^3 N L_d \lambda^4. \tag{3}$$

According to a simple active region model, N decreases with height whereas L_d increases with height. Therefore, the product of these two quantities tends to be constant. Segre and Zanza (2001) found NL_d in the range of $(1.04 - 2.08) \times 10^{18} cm^{-2}$ on the base of the WSRT observations analyzed by Alissandrakis and Chiuderi Drago (1994). We suppose that the constant value of $NL_d = 10^{18} cm^{-2}$ is a good approximation.

The procedure starts with the selection of an unaffected by QTR radio map with the circular polarization degree $\rho_0(x, y) = V_0(x, y)/I_0(x, y)$. A microwave source associated with a bipolar active region can be considered unaffected if it looks like a bipolar microwave source, with the sense of circular polarization corresponding to that of the extraordinary mode (Figure 2e). This map ρ_0 is used for the normalization of a set of active region polarization maps $\rho(x, y) = V(x, y)/I(x, y)$.

The next step is to shift all normalized ρ/ρ_0 maps to the position of the normalizing map ρ_0. And finally, the normalized maps ρ/ρ_0 are converted into coronal magnetograms using Equation (1). The borders of the coronal magnetograms are derived from the reasonable limitation of $|\rho/\rho_0| < 1 - \sigma$, where σ represents the relative accuracy of these ρ maps.

3. Inspection of Results

3.1. Coronal Magnetography Using Different Microwave Sources: Time and Space Coverage

A bright sunspot-associated source is the most appropriate microwave source to reveal the QT-propagation effect. In this case the emission with strong polarization originates from the

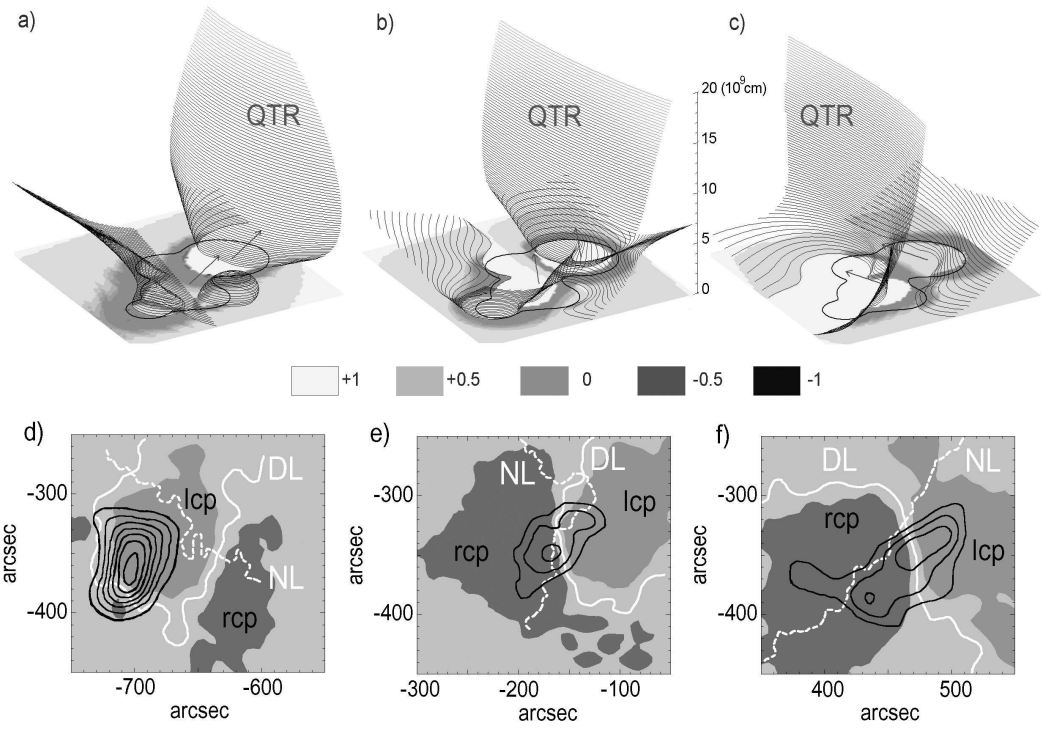

Fig. 2. Simulated QT-surfaces are presented in the top panels as the loci where microwaves cross the coronal magnetic vectors at the right angle. Grayscale images show the modification of circular polarization in the QTR according Eq.(2). The NoRH I (black contours) and V radio maps (greyscale) of the active region 9068 at 1.76 cm are coaligned with neutral line from the KPNO magnetograms on (d) July 3, (e) July 6 (near the central solar meridian), and (f) Jyly 9, 2000.

low-lying gyroresonance layers. The weaker magnetic fields higher up in the coronal QT-region make themselves evident in the changed sense of circular polarization. Since the QTR can lie on the way from the source to the observer, its effect is detectable. A coronal magnetogram as narrow as 30" - 40" was calculated from the Nobeyama Radio Heliograph radio maps of the active region NOAA 7260 with a bright sunspot-associated source at 1.76 cm (Ryabov et al. 1999).

A few coronal magnetograms 60" x 60" of a wide microwave source were determined using the Nobeyama Radio Heliograph (NoRH) and the Siberian Solar Radio Telescope (SSRT) maps at 1.76 cm and 5.2 cm correspondingly (Ryabov et al. 2004). The authors did not analyze the radiation mechanism of the microwave source with the circular polarization degree of 25%. The coronal magnetogram of 50 - 110 G at 1.76 cm and that of 30 - 10 G at 5.2 cm found to be complementary and spread over the heights of $(1.5 - 9) \times 10^9$ cm. The magnetograms were calculated for the day of the polarization inversion (Figure 3).

Recently, Bezrukov et al. (2004) have attempted to determine a long series of coronal magnetograms of the loop-associated sources undergoing polarization inversions in both solar hemispheres. The polarization inversion characteristics are assumed to be of the same origin,

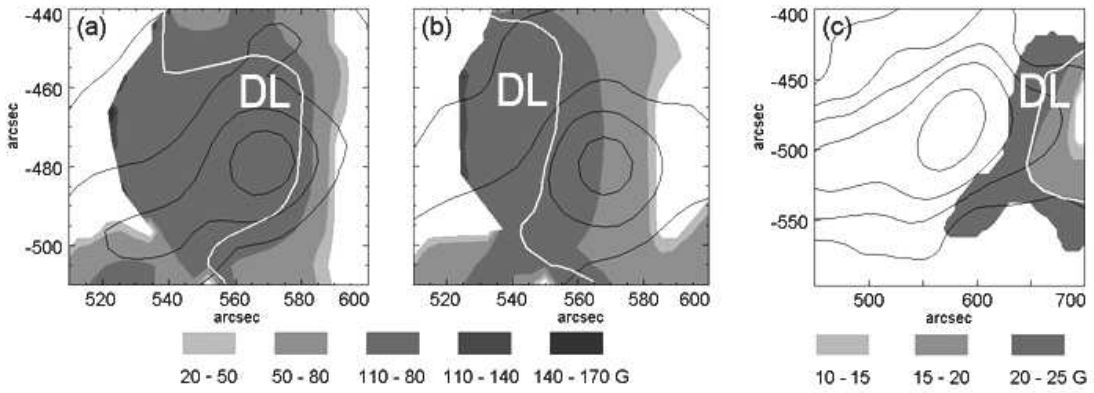

Fig. 3. Coronal magnetograms of solar active region NOAA 8365 on October 23, 1998 (a) and (b) are overlaid on the contours of total intensity I at 1.76 cm (NoRH) in the image plane. A coronal magnetogram (c) is overlaid on the contours of total intensity I at 5.2 cm (SSRT). (From Ryabov et al. 2004).

i.e. the QT-propagation, as those of the sunspot- associated sources (Figure 4).

3.2. Characteristic Lines and Features

An obtainable coronal magnetogram can be defined as the measured strength distribution of the magnetic vectors in the QTR as seen in the plane of view. The QT coronal magnetography is applicable to rather limited portion of the active region, which is effected by the QT-propagation and where the normalized degree of circular polarization ranges from $+1-\sigma$ to $-1+\sigma$. According to Equation (1), the measurable range is 28 -150 G at the wavelength 1.76 cm of the NoRH and 6.7 - 35 G at 5.2 cm of the SSRT, provided the radio map accuracy $\sigma = 0.05$. Stronger fields of each coronal magnetogram correspond to the circular polarization with the inverted sense, while weaker coronal fields correspond to only depressed original polarization. The intermediate strength of the measured coronal field is delineated by the zero circular polarization line (so called depolarization line; Bandiera 1982).

We can conveniently analyze the obtained coronal magnetograms using three characteristic lines:

- The depolarization line DL is the line where V = 0 on the sampled V radio map. At a given wavelength λ (cm) it delineates nearly the most precise magnetic field that can be measured by this technique (Ryabov 2004): $B_0 = 182\lambda^{-4/3}$. When normalizing the sampled maps, the position of DL remains unchanged.
- The depolarization line DL_0 is the line where $V_0 = 0$ on the normalizing map. This line has no direct correspondence in the coronal magnetograms. However, it is responsible for the position and shape of the strongest measurable field: $B_{max} = 318\lambda^{-4/3}$, provided $NL = 10^{18} cm^{-2}$ and $\sigma = 0.05$.
- The magnetic neutral line NL is the line where $B_l = 0$ on the photospheric magnetogram . It

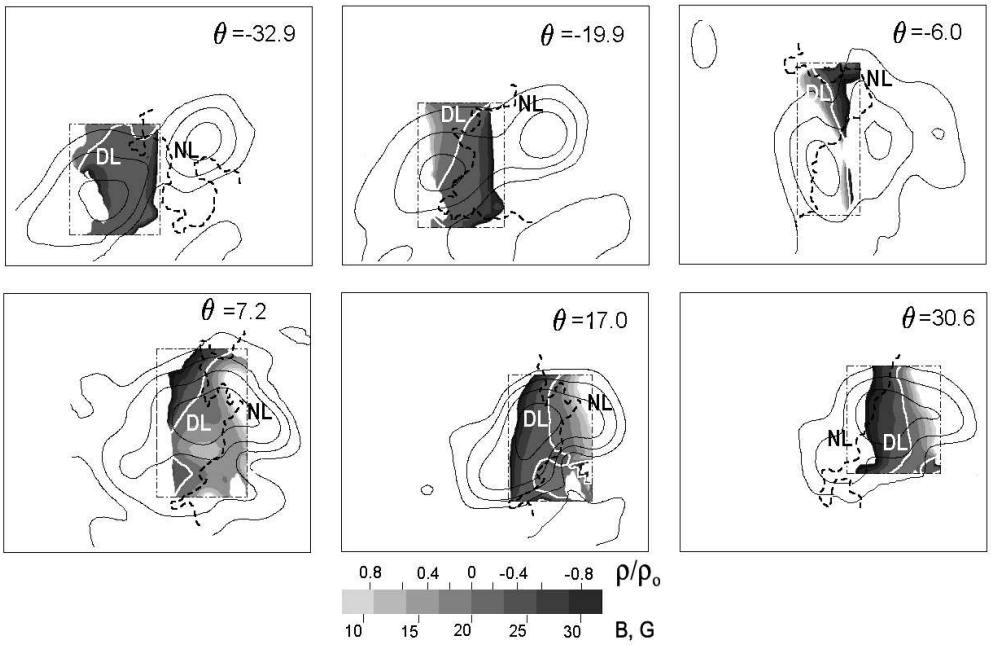

Fig. 4. A series of daily coronal magnetograms (greyscale) of the NOAA 9068 at several longitudinal displacements θ from the central solar meridian are overlaid on the contours of total intensity I at 5.2 cm (SSRT). (Fragment of Figure 4 from Bezrukov et al. 2004).

is also the lower border of the QT-surface, where the propagation angle strictly equals 90^o. The line provides one of the best means o determine the unknown height (Bandiera 1982; Kundu and Alissandrakis 1984), as well as the share and the inclination (Lee et al. 1998) of the QT-surface which "screens" the microwave source.

Bezrukov et al. (2004) have applied the above technique of coronal magnetography to the bipolar active region NOAA 9068 (Figure 4), observed with the SSRT from July 3 to July 10, 2000. During its transit on the solar disk the loop-associated microwave source inverted its polarization sense in each solar hemisphere, thus providing two sequences of coronal magnetograms. Some center-to-limb circular polarization variations in the loop legs have been noticed. Therefore, this technique can be applied as long as those variations do not significantly affect ρ/ρ_0, the quantity assumed to be due to the QT effects only.

Bezrukov et al. (2004) noted the westward movement of the DL due to the projection effect. The gradient of the measured coronal fields is directed east - west in the eastern hemisphere and west - east in the western hemisphere with the characteristic value of $8 \times 10^{-9} Gcm^{-1}$ in the plane of view. The gradient direction is assumed to be the result of two factors: the opposite inclination of the QT-surface in the eastern and the western hemispheres and the general tendency of the coronal magnetic fields to decrease with height. The relative positions of NL and DL indicate the QT-surface inclination, while smoother shapes of DL as compared with those of NL show the simplification of large-scale coronal magnetic fields with height.

Depolarization lines at two wavelengths together with neutral line outline the QTR with height. Ryabov et al. (2004) have compared the DLs, as they observed at 1.76 cm of the NoRH and at 5.2 cm of the SSRT, with the photospheric magnetic fields and their force-free field extrapolations. The DL is found to be closer to the NL at shorter wavelength in accordance with the Eq.(1) and the general tendency of coronal fields to diminish with height. The spatial location of each point in the QTR was restored and the two-dimensional coronal magnetograms were presented in three-dimensional space. The magnetic field extrapolations and the simulations of the QTR are found to be of great help since it is difficult to ascertain the foldness and correct position in the QTR even for simple active regions (see Lee et al. 1998).

4. Difficulties of Coronal Magnetography

Some radiation and propagation conditions for the polarization changes (polarization inversions) similar to those caused by the QT-propagation have been reported (Zlotnik 1999; Bogod et al. 2003). Bogod et al. (2003) found some rapid non-QT polarization inversions together with the QT polarization inversion in the flare-productive active regions. Recently Uralov and Rudenko (2005) revealed the near loop-top position of a lot of circularly polarized sources at 5.2 cm. This kind of sources may show a polarization inversion, where the radiation and propagation effects are combined (Alissandrakis and Preka-Papadema 1984). Thus, we need to elaborate more stringent requirements on the radio map sampling to avoid confusion with non-QT effects.

Difficulties emerge when one evaluates the only unknown coordinate, that is, the height in the QTR. The QTR height involved in coronal magnetography can be determined either from the displacement of the DL with respect to the NL (Kundu and Alissandrakis 1984; Alissandrakis 1999), or from the averaged rate of polarization inversion (Peterova 1975; Gelfreikh et al. 1987). The height can be calculated using the photosphere magnetic field extrapolation at coronal levels (Alissandrakis et al. 1996; Lee et al. 1998; Ryabov et al. 2004). A lot of uncertainty up to about a factor 2 of various estimates is another problem.

We propose the following improvements of the coronal magnetography technique in an effort to achieve more stable and correct results:

- Although this coronal magnetography is radiation independent, the radiation conditions, especially the position and the directivity $V(\theta)$ of the microwave source, should be analyzed to avoid confusion with non-QT effects.
- To eliminate the polarization changes of fluctuating microwave sources the V maps should be averaged. In case of the NoRH observations at 1.76 cm, we propose averaging over the time interval of 30 - 60 min. Doing so we can improve the estimates of the polarization inversion rate and the QTR height, but miss some possible oscillations of coronal fields. (Gelfreikh et al. (2005) have observed such active regions with an oscillating DL and

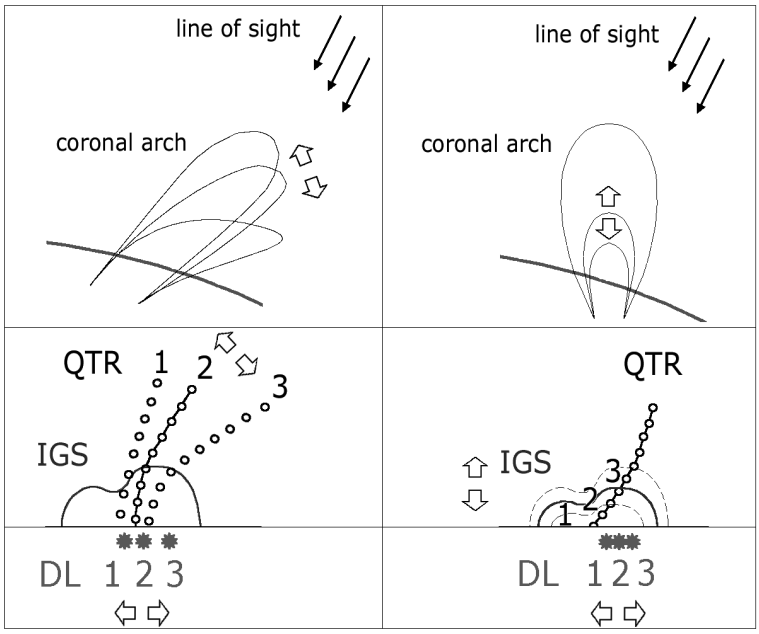

Fig. 5. Sketch of depolarization line (DL) oscillations give evidence of the oscillations of QTR (left column) and/or the oscillations of iso-gauss surface (IGS; right column).

a stable microwave source. The alternative ways to treat the microwave obsevations of oscillating DL are presented in Figure 5.)

5. Concluding Remarks

Radio mapping of the Sun with the NoRH at 1.76 cm and with the SSRT at 5.2 cm has provided data for two-dimensional coronal magnetograms in the range of 50 - 110 G and 10 - 30 G respectively (Ryabov 2004). Each magnetogram covers a QT-propagation affected part of the active region and is consistent with the presumed QTR geometry. For this reason we conclude that the first results of the coronal magnetography through QT-propagation are encouraging. Despite the radiation mechanism independence of this coronal magnetography, we propose an analysis of radiation conditions in microwave sources. This will help to reveal some non-QT polarization changes in a source, including center-to-limb variations during the solar disk transit.

An attempt (Bezrukov et al. 2004) to calculate a series of coronal magnetograms of a few bipolar regions shows that the evolutional changes of microwave sources do not completely distort the expected feature of the coronal magnetograms. For stable and correct coronal magnetograms we propose to sample the normalization map as close to the onset of polarization inversion as possible and average the sampled V maps over the 30 - 60 min intervals.

References

Alissandrakis C.E. 1999, in Proceedings of the Nobeyama Symposium, Kiyosato, Japan, Oct. 27-30, 1998, ed T. Bastian & N. Gopalswamy & K. Shibasaki, NRO Report No.479, 53

Alissandrakis C.E., Borgioli F., Chiuderi Drago F., Hagyard M., Shibasaki K. 1996, Sol. Phys., 167, 167

Alissandrakis C.E. and Chiuderi Drago F. 1994, ApJ, 428, L73

Alissandrakis C. E., Kundu M. R., Lantos P. 1980, A&A, 82, 30

Alissandrakis C.E. and Preka-Papadema P. 1984, A&A, 139, 507

Bandiera R. 1982, A&A, 112, 52

Bezrukov D.A., Ryabov B.I., Bogod V.M., Gelfreikh G.B., Maksimov V.P., Drago F., Lubyshev B.I., Peterova N.G., Borisevich T.P. 2004, Baltic Astronomy, submitted

Bogod V.M., Gelfreikh G.B., Drago F.Ch., Maksimov V.P., Nindos A., Kaltman T.I., Ryabov B.I., Tokhchukova S.Kh. 2003, ASTROPAGE astro-ph/03009444, http://lanl.arxiv.org/abs/astro-ph/?astro-ph

Cohen M.H. 1960, ApJ, 131, 664

Gelfreikh G. B. 1999, in Proceedings of the Nobeyama Symposium, Kiyosato, Japan, Oct. 27-30, 1998, ed T. Bastian & N. Gopalswamy & K. Shibasaki, NRO Report No.479, 41

Gelfreikh G.B. 2004, Solar and Space Weather Radiophysics, ed D. E. Gary & C. O. Keller, Kluwer ASSL volume 314, Chapter 6

Gelfreikh G.B., Peterova N.G., Ryabov B.I. 1987, Sol. Phys., 108, 89

Gelfreikh G.B., Ryabov B.I., Agalakov B.V., Nindos A., Borisevich T.P., Peterova N.G. 2004, Baltic Astronome, submitted

Kundu M.R. and Alissandrakis C.E. 1984, Sol. Phys., 94, 249

Lee J., White S.M., Kundu M.R., Mikic Z., Mc Clymont A.N. 1964, Sol. Phys., 180, 193

Peterova N.G. 1975, Soln.Dann.Bull., 3, 96 (in Russian)

Peterova N.G. and Akhmedov Sh.B. 1974, Soviet Astron., 17, 768

Piddington J.H. and Minnnett H.C. 1951, Austral. J. Sci. Res., A4, 131

Ryabov B.I. 2004, Solar and Space Weather Radiophysics, ed D. E. Gary & C. O. Keller, Kluwer ASSL volume 314, Chapter 7

Ryabov B.I., Maksimov V.P., Lesovoi S.V., Shibasaki K., Nindos A., Pevtsov A.A. 2004, Sol. Phys., in press

Ryabov B.I., Pilyeva N.A., Alissandrakis C.E., Shibasaki K., Bogod V.M., Garaimov V.I., Gelfreikh G.B. 1999, Sol. Phys., 185, 157

Segre S.E. and Zanza V. 2001, ApJ, 554, 408

Uralov A.M. and Rudenko G.V. 2005, this issue

White S.M. 2004, Solar and Space Weather Radiophysics, ed D. E. Gary & C. O. Keller, Kluwer ASSL volume 314, Chapter 5

Zheleznyakov V.V. 1970, Radio Emission of the Sun and Planets, Pergamon Press, Oxford

Zheleznyakov V.V. and Zlotnik E.Ya. 1964, Soviet Astron., 7, 485

Zlotnik E.Ya. 1999, in Proc. 9th European Meeting on Solar Physics, Florence, ESA, SP-448, 1239

FASR Flare Science: Lessons from the Nobeyama Radioheliograph

Dale E. Gary
Center for Solar-Terrestrial Research, New Jersey Institute of Technology
323 M L King Blvd, Newark, NJ 07102
dgary@njit.edu

Abstract

We compare and contrast the instrumental parameters of the Nobeyama Radioheliograph (NoRH) and the future Frequency Agile Solar Radiotelescope (FASR) with an emphasis on flare research. The primary results and discoveries of NoRH in the realm of flare science are presented and used to motivate many of the choices for design parameters and science goals for FASR. Key parameters of NoRH for flare science are its dual-frequency, dual-polarization, excellent image quality, solar-dedicated and solar-optimized design, and high time resolution. Its main limitations are spatial resolution, frequency coverage, and frequency resolution. FASR's design makes use of the strengths of NoRH, and adds these three missing elements: a factor of 10 improvement in spatial resolution, broad frequency coverage and high frequency resolution. We discuss the manner in which these improvements extend the legacy of NoRH for flare science.

Key words: Sun:flares Sun:corona radio:instrumentation

1. Introduction

The Nobeyama Radioheliograph (NoRH, Nakajima et al. 1994) has now operated over more than a solar activity cycle, and has amassed the largest database to date of solar flare radio imaging data. This paper reviews some of the major discoveries and lessons learned from this large database, and the studies done by an international community of researchers over the 13 years from 1992-2004, in order to apply them as we plan for a new radio facility, the Frequency Agile Solar Radiotelescope (FASR).

Radio studies of the Sun are well known to provide unique information unavailable by any other means. Chief among the unique aspects is (1) sensitivity to magnetic field strength, but also important are (2) direct information on the coronal component of the high energy electron population, (3) simultaneous sensitivity to the thermal and nonthermal electron populations, (4) the fact that the emission may be both optically thick and optically thin in different parts of the radio spectrum, and (5) the sensitivity to coherent emission, which renders even a relatively small number of electrons visible.

These advantages, when combined with observations at other wavelengths, help to provide a full picture of the solar atmosphere and activity therein. For flare research, radio emission is most complementary with soft and hard X-ray observations, which are sensitive to the same electrons, but with different weighting. The hard X-rays are generally from loop footpoints, where the electrons meet the chromosphere, while the radio emission provides information about the coronal population. The soft X-rays provide mostly thermal plasma diagnostics, and are entirely optically thin, whereas the radio emission provides both thermal and nonthermal diagnostics and may be both optically thick and thin at different radio frequencies. The radio emission is complementary to Hα, EUV and white-light coronagraph observations in the case of wave and eruptive phenomena (filaments, prominences, CMEs). For non-flare research, the radio observations are highly complementary to magnetographs, chromospheric and coronal observations in the optical, UV, EUV and soft X-rays.

The two NoRH frequencies, 17 and 34 GHz, are often optically thin and well above frequencies where the coronal plasma typically supports coherent emission. Therefore, the results from Nobeyama mainly involve advantages 1–3 from the list above, although advantage 4 is sometimes made use of. To make full use of the entire list, however, requires broad frequency coverage, which is what FASR is designed to do. As we will see, FASR takes many design parameters from Nobeyama, such as the use of many small antennas for excellent imaging with full-Sun coverage, high time resolution, solar-dedicated and solor-optimized design, and pipelined data processing to remove the burden of image reconstruction from the typical user.

In § 2 we list the basic parameters and main science goals of FASR. In § 3 we first list the instrumental parameters of NoRH that are important for flare research, and then examine some of the main discoveries and results of NoRH for flare science. In § 4 we compare and constrast the instrumental parameters of FASR and NoRH, and discuss how FASR can be expected to extend the NoRH legacy for flare science. Finally, we conclude in § 5.

2. The Frequency Agile Solar Radiotelescope

The broad outlines of the FASR instrument have been described in numerous publications (e.g. Bastian 2003*ab*; Gary 2003; Gary & Keller 2003; White et al. 2003), while much of the science is presented in Gary & Keller (2004). Here we briefly describe the FASR instrument concept in order to examine the similarities and differences with the

Fig. 1. Artist's conception of the FASR-A and FASR-B arrays on the Plains of San Augustine.

NoRH. The nominal frequency range of FASR covers three orders of magnitude, from roughly 30 MHz to 30 GHz. No single antenna and feed system can cover so great a range in frequency, so the design calls for three separate systems, which we designate FASR-A (covering 2-30 GHz), FASR-B (covering 200-3000 MHz), and FASR-C (covering 30-300 MHz). Each array will have a maximum baseline of 6 km, providing spatial resolution of $20''/f_{\rm GHz}$ at 30° elevation, where $f_{\rm GHz}$ is the frequency in GHz. Table 1 gives some general characteristics of the three arrays. An artist's conception of the FASR-A,B arrays is shown in Figure 1. In order to accomplish the broad range of science envisioned, the FASR receivers and digital signal processing requires the capabilities listed in Table 2.

Table 1. Characteristics of FASR's Three Arrays

Array Designation	Number Antennas	Frequency Range	Antenna Size/Type
FASR-A high ν array	~ 100	2-30 GHz	2 m
FASR-B low ν array	~ 60	0.2-3 GHz	6 m
FASR-C dipole array	~ 40	30-300 MHz	log dipoles

Table 2. FASR Receiver Specifications

Quantity	Spec
Frequency Resolution	0.1% (FASR-C)
	1% (FASR-A,B
Time Resolution	10 ms (FASR-B,C)
	100 ms (FASR-A
Polarization	Stokes IV (QU)
Instantaneous Bandwidth	~ 1 GHz

FASR will have to calibrate for instrumental/environmental changes such as temperature and other secular changes, as well as external variations such as the troposphere (weather) above ~ 1 GHz and the ionosphere below that frequency. The design will emphasize instrumental stability and monitoring of secular changes (including a front-end noise cal source and phase monitoring), so that cosmic sources may be used only before sunrise and after sunset for absolute amplitude and phase calibration. During solar observations, self-calibration methods will be used for the FASR-A,B arrays, and monitoring of ionospheric tip-tilt will be done, perhaps through the use of GPS measurements of total electron content, for the FASR-B,C array.

FASR will be designed to be the world's premier solar radio facility for at least two decades after completion. The science goals include:

- Directly measure coronal magnetic fields
- Image coronal mass ejections (CMEs)
- Obtain radio spectral diagnostics of particle acceleration and energy release, with excellent spatial and temporal resolution
- Image radio emission from shocks (type II), electron beams (type III), and other bursts over heights 1-2.5 $R_\odot$
- Construct 3D solar atmospheric structure (T, B, n_e) over a wide range of heights

The science to be addressed in each of these areas, and some of the challenges for FASR, were raised at an international science workshop held 2002 May in Green Bank, WV, and at a special session of the American Astronomical Society in 2002 June. The topics presented at these two meetings were expanded and collected in a book in the Kluwer *Astronomy and Astrophysics Library* series (Gary & Keller 2004). For the purposes of this paper, we emphasize flare science (energy release, particle acceleration, and related activity), and the legacy of NoRH for our current understanding of these phenomena.

3. Nobeyama Legacy for Flare Science

The instrumental parameters of NoRH that are relevant to flare science are:

- dual frequency operation at 17 and 34 GHz, both of which are typically optically thin and provide sensitivity to both thermal and nonthermal emission
- full Sun field of view, which insures that no event or phenomenon on the visible disk is missed
- solar-dedicated operation and solar-optimized performance, which provides coverage and optimal data quality on every event or phenomenon
- dual circular polarization, which is critical to the interpretation of the emission for physical diagnostics
- spatial resolution of $15''$ (17 GHz) and $8''$ (34 GHz)
- uses the Sun itself for calibration, based on redundant baselines and the fact that the solar disk brightness at 17 and 34 GHz is relatively constant
- 84 antennas (providing > 1500 independent baselines) for excellent imaging properties

- pipeline processing scheme for quick look and permanent archiving of images
- 50 ms time resolution, with 1 s resolution for non-flare data

The strengths and limitations contained in the above list of properties color the results that we will examine in this section. The results detailed below make it clear which properties should be emulated by FASR and which should be improved upon. Thus, the results from NoRH are a treasure to be exploited fully in the design of FASR. Of course, many new results are still to come from the NoRH, both from new observations and from new studies of the events already contained in the NoRH database. It is important that the NoRH continue to operate, and the FASR design continue to be examined in the light of these continued new discoveries.

3.1. Source Morphology

The NoRH spatial resolution is often not sufficient to fully resolve individual burst sources, but Hanaoka (1997) was able to deduce the morphology of small loops, with closely spaced footpoints, by examining their polarization signature. Figure 2 illustrates this. What appears to be two well-separated sources in Stokes I (Fig. 2*e*) is revealed from the polarization (V/I) image (Fig. 2*f*) to be three separate footpoints as shown schematically in Fig. 2*i*. This conclusion can be checked by referring to such other data as the Yohkoh SXT image in Fig. 2*h*.

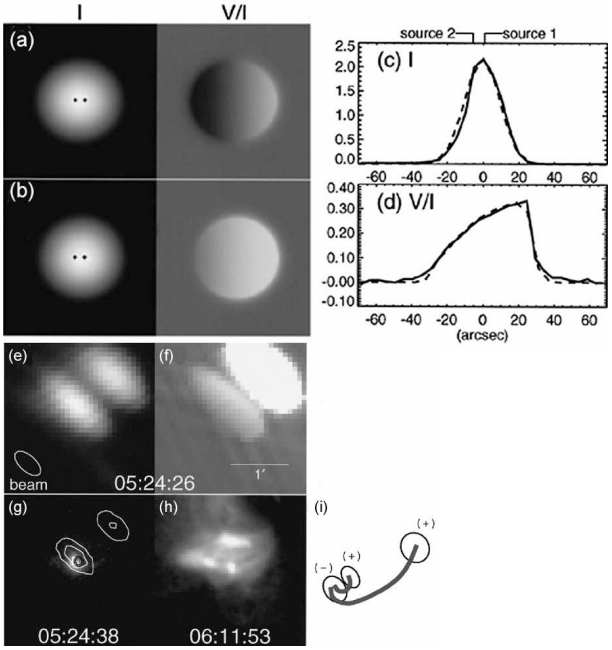

Fig. 2. Using polarization as a guide to morphology (from Hanaoka 1997).

Using similar methods, Nishio et al. (1997; 2000) studied 25 events at 17 GHz, selected for relatively simple time profiles (single, or multiple but well separated, spikes

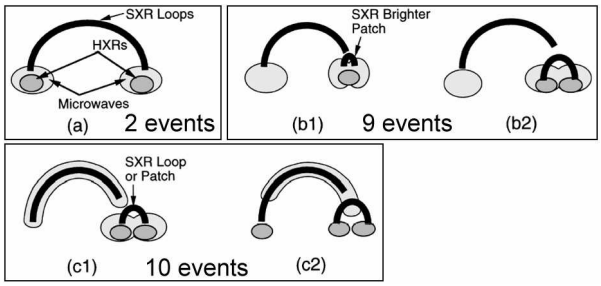

Fig. 3. Schematic diagram of flare morphological types based on 17 GHz microwave (NoRH), and HXR (HXT) observations (from Nishio et al. 1997).

with durations of order 10 s), to obtain statistics of occurrence for different morphological classes. The descriptive types included not only the radio morphology but also the accompanying soft X-ray (SXR) and hard X-ray (HXR) morphology seen with Yohkoh SXT and HXT. The results are summarized in Figure 3, from Nishio et al. (1997) who defined 3 basic types, two of which are divided into two subclasses each. The types are stated as follows:

- cospatial microwave/HXR double sources (type *a*)
- double microwave source with a single HXR source on one side (type *b*1)
- double microwave source with a double HXR source on one side (type *b*2)
- single, elongated microwave source with a double HXR source on one side (type *c*1)
- single, elongated microwave source with three HXR sources (double on one side, and a remote one connected by the loop on the other side) (type *c*2)

Among the list of 25 events described by Nishio et al. (2000), Fig. 3 indicates the number of events of type *a* (2 events), *b* (9 events), and *c* (10 events). A minority of bursts (4) were denoted unclassified (type *u*) because their morphology fit none of the above descriptions. From this study and others (e.g. Kundu et al. 1995; Hanaoka 1997), we can conclude that most bursts show some asymmetry at 17 GHz. The microwave emission may come from either the looptop, or the footpoints, or both. Missing from this list are events showing almost no spatial structure (even with super-resolution using a 5″ restoring beam), such as the 5 events reported by Kundu et al. (2001*c*).

It is clear from the NoRH morphological studies that FASR's factor of 10 higher spatial resolution will be needed.

3.2. Dual Frequency Loop Observations

A subset of the type *c* events are those for which the microwave source is not only elongated, but shows a clear loop shape. Those that have been studied at both 17 and 34 GHz are especially useful for comparison with theoretical expectations. In this section we discuss some of these observations and some important implications for the accelerated electron energy and pitch angle distributions. It should be kept in mind, however, that the events discussed

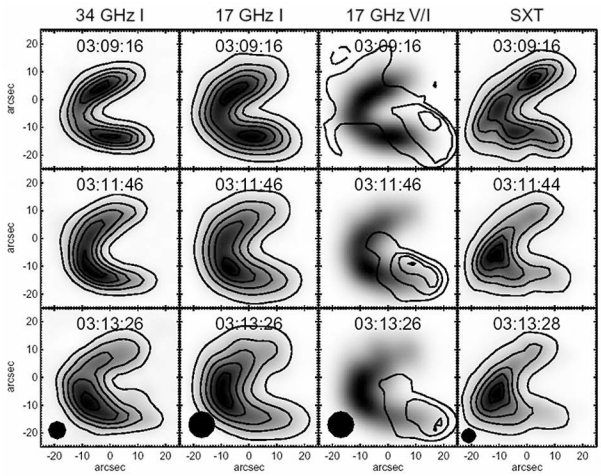

Fig. 4. Dual-frequency loop observations at different times for the event of 1999 May 29, near 03:10 UT. Shown are images at 34 GHz (left column), 17 GHz Stokes I (second column), 17 GHz Stokes V (third column), and soft X-rays (right column). (From White et al. 2002).

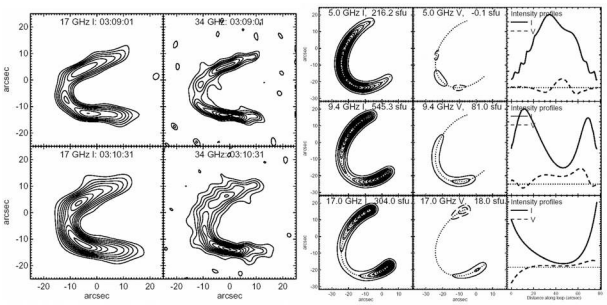

Fig. 5. 17 and 34 GHz NoRH images at two selected times deconvolved using 0.5″ pixels and a maximum entropy algorithm. These are the model brightness distributions resulting from the deconvolution; i.e., they have not been smoothed with a Gaussian in the way that the images in Fig. 4 were.

here are rather rare, being large (40-80″ long), and loop-shaped (i.e. not footpoint) sources. Higher resolution is needed to determine whether the conclusions drawn from these events also pertain to the more typical small loops discussed above.

A rather complete study of such a loop event was done by White et al. (2002), as shown in Figure 4. The appearance of the loop at 34 and 17 GHz are shown in the first two columns at various times during its development. The source is also loop-like as seen in soft X-rays (last column, from SXT), while the HXT sources (not shown) were footpoint sources in M1, M2 and H channels (i.e. > 23 keV energies). Note that the radio emission early on (at 03:09 UT) is concentrated near the footpoints, but part way up the loop legs. Later the source peaks more or less at the loop top.

The left four panels of Figure 5 show the same observations at two times, reconstructed with a maximum entropy algorithm but not convolved with a gaussian restoring beam. The panels on the right show a typical flaring loop model, for electrons with isotropic pitch angles, for comparison with images at three microwave frequencies and brightness and polarization profiles (far right column) along the loop axes. There is a clear tendency for the high-frequency (> 17 GHz) emission in the model to be concentrated at the footpoints, in clear disagreement with the observations. White et al. (2002) point out the need for a mechanism to keep the electrons concentrated near the loop top.

Melnikov et al. (2002*a*) did a comparative analysis of four such loop sources, for which the brightness profiles along the loop axes at the time of peak flux density are shown in Figure 6. In each case, the 17 and 34 GHz emission is concentrated at or near the loop tops, again in violation of expectations from simple loop models.

Melnikov et al. (2002*a*) examined the range of param-

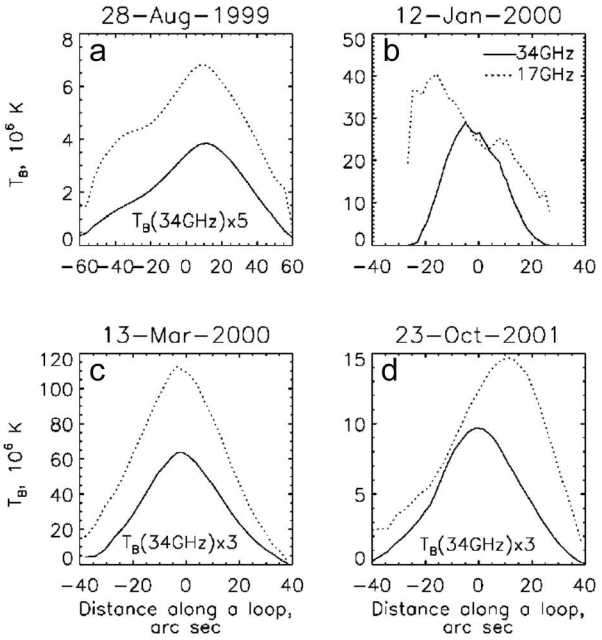

Fig. 6. Spatial distribution of radio brightness temperatures at 34 GHz (solid line) and 17 GHz (dotted line) along a flaring loop for the four events under study. (From Melnikov et al. 2002*a*).

eter values that would be necessary to form a loop-top source, as shown in Figure 7, for a model loop with modest mirror ratio $B_{\rm tr}/B_0 = 2$, where $B_{\rm tr}$ is the magnetic field strength in the transition region (the base of the loop), and B_0 is the field strength at the loop top. They found that a significant pitch angle anisotropy is needed. An isotropic pitch angle distribution (panel b) concentrates the electrons near the loop top, but when the emission is calculated (panel e) the dependence of emissivity on magnetic field strength causes the emission to peak near the footpoints of the loop. Among the models considered by Melnikov et al. (2002a), the emission is concentrated near the loop top only for a pancake pitch angle distribution:

$$\phi(\mu_0) = \exp[-(1-\mu_0)^2/\mu_1^2],$$

where $\mu_0 = \cos\alpha$ (α is the pitch angle), and μ_1 is a constant parameter describing the width of the distribution (Fig. 7f). For Fig. 7c, f, the electrons are quite well constrained to pitch angles perpendicular to the magnetic field ($\mu_1 = 0.4$), which says something important about the acceleration mechanism. Other evidence by Lee, Gary & Shibasaki (2000), described in §3.3, agrees with the idea that electrons are accelerated at least initially with pitch angles in a pancake distribution.

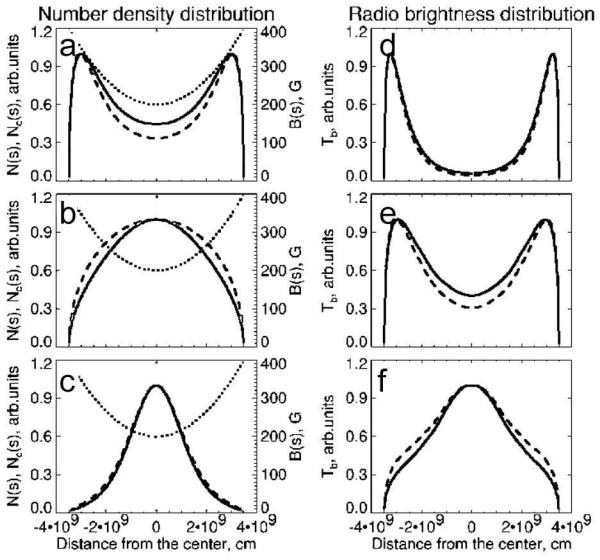

Fig. 7. Normalized spatial distributions along a loop. *Left panels:* Number density (dashed line) and column number density (solid line) for the (a) beamlike, (b) isotropic, and (c) pancake electron pitch-angle distributions; the magnetic field distribution is shown as a dotted line, the mirror ratio $B_{\rm tr}/B_0 = 2$, and the loss-cone pitch angle $\alpha_l = 45°$. *Right panels:* Corresponding gyrosynchrotron intensity in the optically thin regime (at 34 GHz). (From Melnikov et al. 2002a).

Some general conclusions can be deduced from dual-frequency loop observations and models:

- About half of the "large" loop events observed at 17 and 34 GHz are brighter near the footpoints, as expected from earlier models.

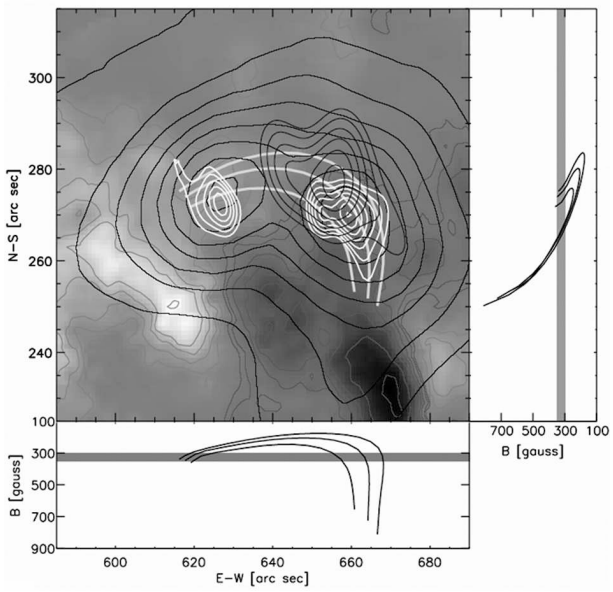

Fig. 8. Radio morphology and magnetic fields at the impulsive phase of a flare. The center frame shows 5 GHz (thick black contours), 10.6 GHz (white contours) and 17 GHz (thin black contours) on top of the longitudinal magnetogram. The thick white curves are selected field lines from the field extrapolation to represent the loop involved with the flare. Two boxes at the right and bottom give the field strength of the three field lines as function of distance along east-west and north-south, respectively. The gray strips in the boxes are to locate the magnetic trap (from Lee et al. 2000).

- However, a significant number have looptop sources, an observation that appears to require anisotropic pitch angles for the injected electrons.
- We must be more sophisticated in our models to account for even the grossest of characteristics for some events, i.e. the concentration of radio brightness at the top of loops.

The higher spatial resolution and much greater frequency coverage of FASR will give more complete loop diagnostics, as well as allowing smaller loops to be studied. We are sure to find that the simple models that assume isotropic pitch angle distributions will have to be thrown out. However, we can expect to discover new clues to the nature of the energy release and particle acceleration through studying the pitch angle distribution.

3.3. Electron Dynamics

In addition to the spatial morphology of radio sources, NoRH has provided excellent data of the dynamical development of the radio emission (e.g. Melnikov et al. 2002b). Lee et al. (2000) used the morphology of the bursts at several frequencies (17 GHz from NoRH, and 5.0 and 10.6 GHz using OVSA) to identify the magnetic topology of the flaring loop. This was compared to magnetic field extrapolations to estimate the magnetic field strength in the radio sources, to identify mirror points of the electrons, as shown in Figure 8.

The specific geometry obtained from Fig. 8 allowed a

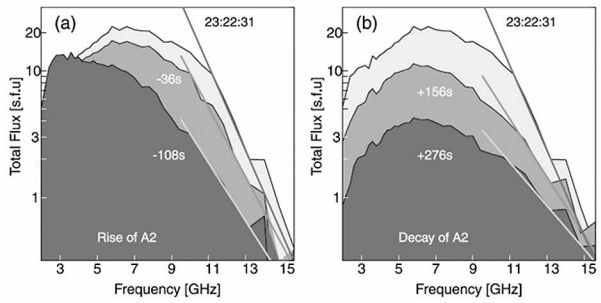

Fig. 9. Spectral variation of the event in Fig. 8: (*a*) and (*b*) show total power spectra in the rise and decay phase, respectively, at five selected times relative to the time of the maximum flux. The straight lines are guide lines for spectral slope at the corresponding times (from Lee et al. 2000).

rather complete magnetic loop model to be developed, in which accelerated electrons of different energy and pitch angles were introduced in an attempt to match the spectral dynamics shown in Figure 9. In order to match the changes in spectral slope, and at the same time the relative flux densities on the optically thin side of the spectrum, the pitch angle distribution had to be restricted to a pancake distribution that was initially narrow (small μ_1 in the notation above) but broadened over time due to collisions.

As a result of the flare morphologies mentioned in § 3.1, the footpoint source at the remote end of the longer loop may show "time-of-flight" (TOF) delays in radio and/or hard X-rays (e.g. Bastian 1999). Hanaoka (1999) studied three such events, using the high time resolution (50 ms) capability of NoRH. Results for one of the events are shown in Figure 10. There is a clear indication that the radio emission from the remote source is delayed about 500 ms relative to the emissions from the main source. The delay in this and the other two flares indicates a velocity for the exciter of about $0.5c$, suggesting that the exciter is high-energy electrons that are accelerated first in the vicinity of the main source and then arrive in the remote source.

It should be mentioned that other exciters and propagation speeds have been seen in other events. Yokoyama et al. (2002), again using the high-time-resolution NoRH data, imaged a traveling disturbance in a radio loop moving with a speed of 6×10^3 km s^{-1}, consistent with the Alfven velocity in the loop. We note that FASR will likewise be able to follow such fast dynamics, but will have the advantage of images at many frequencies. This will allow the electrons to be followed along the loop as their emitting frequency shifts due to the changing magnetic field. Such observations will yield a more complete picture of the transport of electrons, and will also allow deduction of the magnetic field strength within the loop along which the electrons are propagating.

3.4. Long Duration Events

In addition to the rather short-lived impulsive events described in the foregoing, NoRH has provided detailed

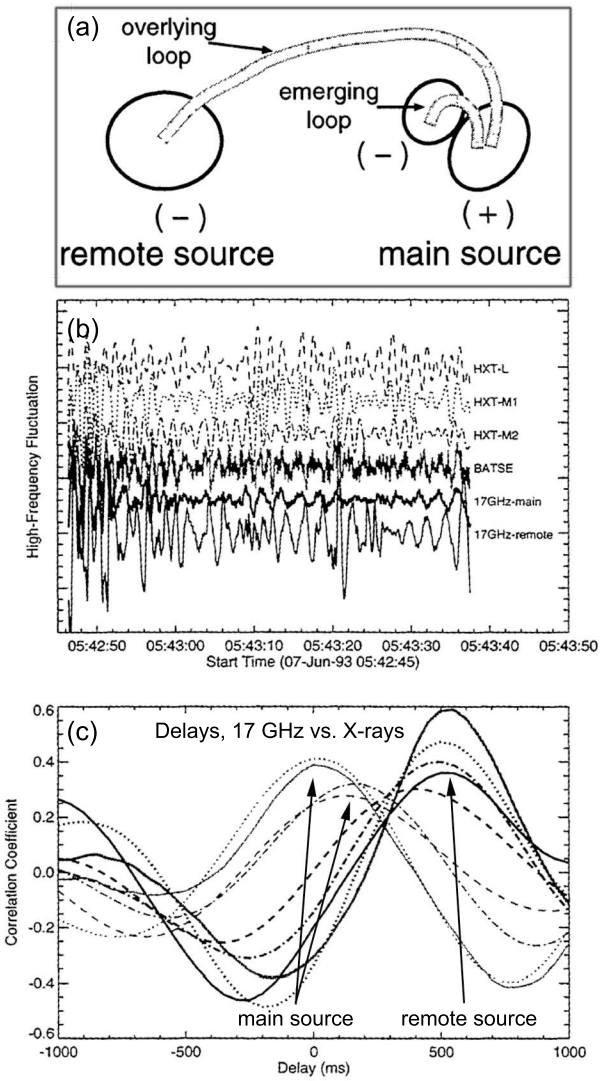

Fig. 10. *a*) Schematic drawing of the loop geometry of the event of 1993 June 07. *b*) Rapidly fluctuating components filtered from the HXR and NoRH spatially resolved light curves. *c*) cross-correlations between time profiles in *b*. Curves representing the main component all occur within 200 ms of each other, while the HXR curves and the 17 GHz main source occur more than 500 ms before the 17 GHz remote source (adapted from Hanaoka 1999).

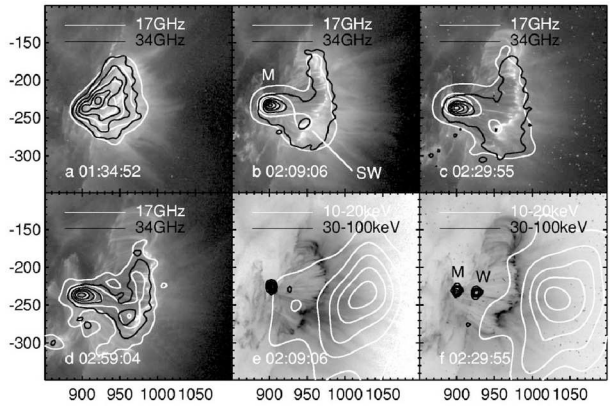

Fig. 11. Evolution of the radio and hard X-ray sources later in the flare of 2002 Apr 21. The first four images show a sequence of overlays of 17 (white contours) and 34 (black contours) GHz images on TRACE 195 Å Fe XII images during the extended phase of the flare when the loop system is expanding above the west limb. The last two images show contours of the RHESSI 1020 keV (white) and 30 100 keV (black) emission overlaid on the TRACE 195 Å Fe XII images at 02:09:56 and 02:29:55 (displayed with inverted color table) (from Kundu et al. 2004).

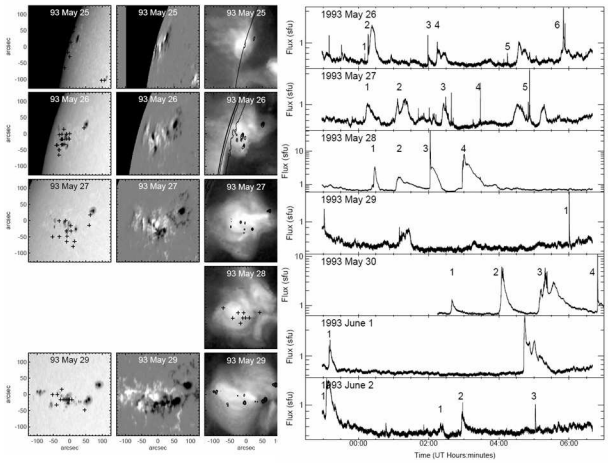

Fig. 12. *Left Side:* Sequence of white-light images (left), KPNO magnetograms (second column), and Yohkoh SXT images (third column) for the period 1993 May 25 to May 29 (there are no KPNO data for May 28). The plus signs on the white-light images represent the locations of optical flares, while contours of the white-light images are overplotted on the soft X-ray images to show the locations of sunspots. *Right Side:* Time profiles of the bursts observed by NoRH at 17 GHz during the period 1993 May 26 to June 3. (From Kundu et al. 2001*b*).

observations of the morphology and evolution of long duration events, which are typically associated with two-ribbon flares and the development of post-flare loop systems.

An example of a well-observed event is the one studied by Kundu et al. (2004), which also happens to be the first large (X-class) flare that RHESSI observed. Images from later in the event are shown in Figure 11, and clearly show the correspondence of the radio emission with the post-flare loops seen in TRACE. Kundu et al. (2004) conclude that this flare is striking in the complex and numerous ways that radio emission could be generated within multiple acceleration sites over a long period of time. Another example of a long-duration event observed with NoRH is that reported by Altyntsev et al. (1999). Again, this event showed a close correspondence with post-flare loops being formed at the closing of once open fields in the classic two-ribbon flare scenario. FASR will improve on these results due to its higher spatial resolution, but also due to its broad frequency coverage, which will allow more complete diagnostics of the conditions both in the flaring loops and in the region above the loops. We come back to this in § 4.3.

3.5. Flare Productivity and Space Weather

Because of the large database of radio bursts available from the NoRH, and its solar-dedicated operation, statistical studies of flare productivity are possible (Kundu et al. 2001*b*). In addition, although high-frequency radio emission at 17 and 34 GHz is not optimum for studies of space weather (that is, studies of the influence of solar activity on the Earth and near-Earth environment), NoRH data have proven useful for such space-weather-related phenomena as coronal heating (White et al. 1995), eruptive events (Hori et al. 2000), and connecting near-surface phenomena to metric burst (type II and III) activity (Nakajima & Yokoyama 2002; Aurass et al. 2002).

Kundu et al. (2001*b*) examined dozens of bursts that occurred at 17 GHz in a single active region over 9 days in May/June 1993, to study the evolution in spatial structure of the region in relation to flare activity. Despite its being a rather complex active region, the region had only weak, but repetitive flaring at 17 GHz (see Figure 12), leading the authors to suggest that many small events in a "typical" active region may be a sign of relaxation of energy buildup, avoiding major flares.

Figure 13, also from Kundu et al. (2001*b*), compares the spatial structure for 16 weak bursts (gray scale background) with the quiet active region emission (contours). No clear pattern is discernible, but more information is needed than is provided by images at a single radio frequency. Through its spectral diagnostics, FASR will provide magnetic field and temperature maps of the active region, along with full spectroscopic imaging of the events (and at 10 times higher spatial resolution). Radio diagnostics should allow us to track energy release and conversion to heating.

In related work, White et al. (1995) investigated the 17 GHz radio counterparts of small brightenings seen in soft X-rays, which at that time were referred to as active region transient brightenings, but have since been identified (Gary, Hartl & Shimizu 1997) with the microflares first reported by Lin et al. (1984). White et al. (1995) could not distinguish the bursts at 17 GHz from thermal heating events, but Gary, Hartl & Shimizu (1997), using OVSA observations ranging from 1–18 GHz in frequency,

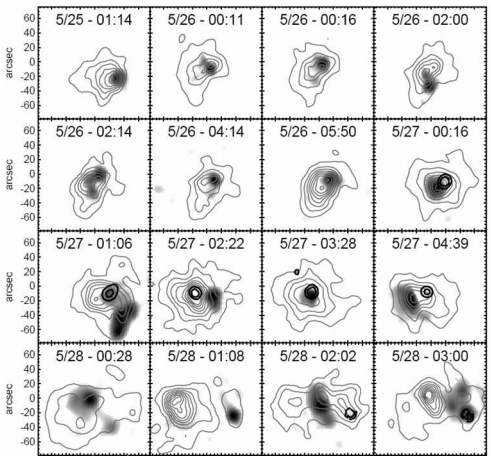

Fig. 13. Preflare active region emission contours (gray) from 15,000–120,000 K overlaid on a gray-scale representation of the subsequent burst emission for 16 flares. Black contours show strong circular polarization in the preflare maps (from Kundu et al. 2001*b*).

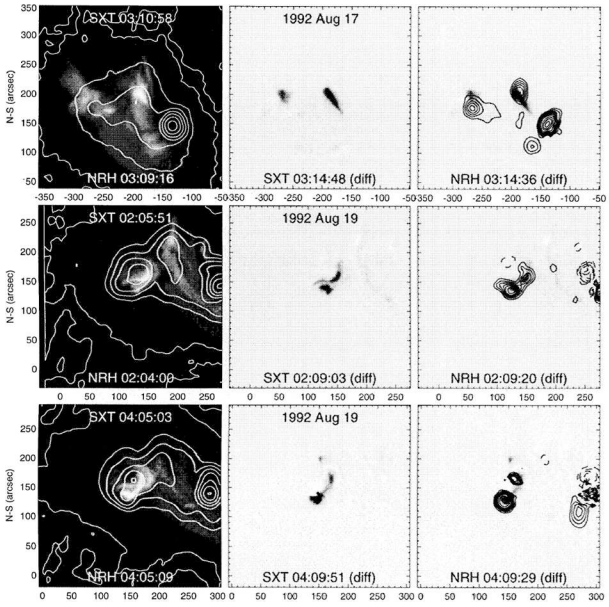

Fig. 14. Four active region transient brightenings (from White et al. 1995). *Left Column:* quiet active region emission just before the outburst, *Middle:* SXT difference image showing the soft X-ray transient, *Right:* NoRH 17 GHz difference image (contours) overlaid on the SXT difference image.

were able to identify copious nonthermal emission, with all of the characteristics of ordinary flares, only with energy output of order $< 10^{29}$ ergs. Since then, even smaller radio events have been seen (Krucker et al. 1997), both in and out of active regions. FASR should be extremely sensitive to small events, primarily due to its wide spectral coverage. The OVSA results showed that the spectral characteristics can vary widely, and FASR's excellent imaging will pick up a burst no matter what its peak frequency may be.

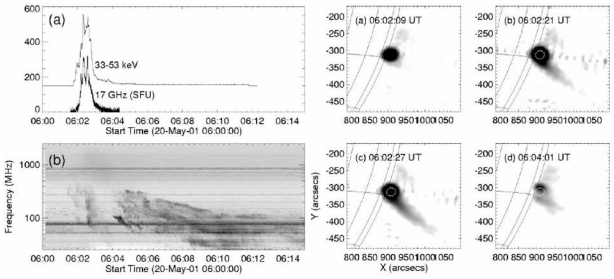

Fig. 15. *a*) Time profile of a burst at 17 GHz and 33–53 keV hard X-rays. *b*) Associated Hiraiso dynamic spectrum showing a type II and type III burst. *Right panels:* NoRH 17 GHz radio images showing the development of a collimated ejector during the burst. (From Nakajima & Yokoyama 2002).

Despite the fact that NoRH operates at high microwave frequencies for which typically only near-surface phenomena are visible, in many events there is a hint of a connection with much larger-scale phenomena. The event shown in Figure 15, for example, seems to show a connection between the main phase of the flare and large scale loops extending upward from it, and possibly a connection with the associated type III burst. Likewise, Aurass et al. (2002) studied two events seen with NoRH that had accompanying type II bursts, and were able to relate moving features at 17 GHz (which they referred to as "type II burst-exciting disturbances") with EIT waves and, temporally, with features seen in the dynamic spectrum from Potsdam. We discuss in the next section FASR's expected performance in relating the low-atmosphere phenomena with large-scale features.

4. Lessons Learned

In this section we discuss specific lessons from NoRH and other existing instruments that have gone into our current design for FASR. We also outline the ways in which FASR can be expected to extend the flare science of NoRH.

4.1. FASR Instrumental Parameters and the NoRH Legacy

Refering to § 2, we can see how the FASR design makes use of the lessons learned from the NoRH results of § 4. Like NoRH, the FASR design incorporates full-Sun coverage to as high a frequency as possible (17 GHz for 2 m antennas), solar-dedicated operation and solar-optimized design. This will allow FASR to observe every solar burst that occurs during its observing day, with instrumental characteristics that are optimized for the spatial, spectral, and temporal variability (and dynamic range) presented by the Sun. Taking another lesson from NoRH, FASR also employs a large number of antennas, and hence a large number of baselines (~ 5000) for excellent imaging and dynamic range.

FASR also incorporates NoRH's high time resolution (10-100 ms in the case of FASR) in order to follow the

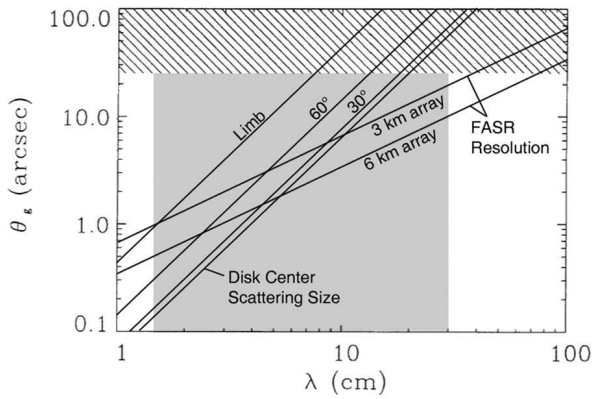

Fig. 16. Spatial resolution as a function of wavelength, showing coronal scattering limits (steep diagonal lines) for different distances from disk center—Limb, 60°, 30° and Disk Center—and the FASR resolution for arrays both 3 and 6 km maximum baseline. The FASR frequency range is shown as the gray rectangle. (Adapted from Bastian 1994).

dynamical behavior inherent in impulsive solar bursts, including delays due to time of flight. A challenge for FASR will be to cover a large range of frequency at the relevant timescales. With an instantaneous bandwidth of 1 GHz, FASR will require many sample times to cover the ~ 30 GHz total bandwidth. Therefore, observing modes will have to be developed that allow the instrument to follow the most "interesting" spectral range of the burst at high time resolution while providing wider spectral coverage at lower time resolution.

The NoRH instrumental limitations, too, inform the design of FASR. For example, the spatial resolution of NoRH is clearly insufficient to provide the detail needed resolve most sources and to follow spectral and spatial evolution. Therefore, the 6 km maximum baselines of FASR, about 10 times longer than those of NoRH, are chosen to give FASR a spatial resolution of at least $20''/\nu_{\rm GHz}$ for Sun elevations of greater than 30°. This spatial resolution compares well with the fundamental limitation on source size given by typical coronal scattering (Bastian 1994), as shown in Figure 16. FASR resolution is better than the scattering limit at wavelengths longer than 5 cm (6 GHz) over the entire disk, and over 3/4 of the disk to 2.3 cm (13 GHz).

Likewise, the dual-frequency operation of NoRH is often too restrictive to provide adequate, unambiguous diagnostics of the source and electron parameters, and the relatively high frequencies (17 and 34 GHz) restrict sources to relatively low heights, high densities (for thermal emission) and high magnetic field strength (for gyroemission). FASR's three decades of frequency coverage are chosen to enable it to observe phenomena throughout the Sun's atmosphere from the low chromosphere to a height of roughly $2.5R_\odot$, and will make it sensitive to radio emission from virtually any solar radiation mechanism. Meanwhile, its frequency resolution will enable spectral diagnostics (e.g. Gary & Hurford 2004) for measuring coronal magnetic fields, densities and temperatures, as well as a variety of high-energy electron parameters.

4.2. The Challenge of High Spatial Resolution

The combination of high spatial resolution and full-Sun coverage is a significant challenge for FASR at the higher end of its frequency range (at > 10 GHz). A comparison with NoRH is enlightening. Consider the number of independent measurements by NoRH (1500 baselines of amplitude and phase, i.e. 3000 independent measurements) and the number of resolution elements on the full disk of the Sun at 17 GHz (about $[d_\odot/d_{\rm beam}]^2 = [1920''/15'']^2 \approx 16000$). A reasonable figure of merit for imaging performance would be the ratio of these, or $3000/16000 \approx 0.19$. FASR will have a somewhat larger number of baselines, providing ~ 10000 independent measurements, but a far smaller beam ($1.17''$ at 17 GHz), giving a value for this figure of merit $10000/2.7 \times 10^6 \approx 0.0037$—more than 1400 times worse. However, there are several problems with this naive argument that make the situation for FASR far less dire than it may appear.

First, one does not need to fully characterize every resolution element on the Sun, only those containing the bulk of the flux density. Put another way, if we consider the chromosphere to be a uniform brightness temperature on which is superimposed a finite number of sources of higher and lower brightness temperature, then in a single-frequency snapshot image FASR will be able to characterize some 1700 sources (assuming "characterize" means to determine 2D position (x, y), major and minor axes (a, b), orientation, and brightness). By the same argument, NoRH can characterize 500 such sources. Although we cannot be sure at present how many sources are "enough" to characterize the entire flux distribution (and the necessary number will depend greatly on solar cycle and the presence of flares and active regions), it is highly unlikely that the number of sources will increase with resolution as rapidly as the number of resolution elements.

Second, under most circumstances FASR can make use of modest frequency synthesis (combining spatial information at neighboring frequencies over a limited band) to increase the number of independent measurements in a snapshot image. It remains to be seen over what frequency range such frequency synthesis is useful, since it depends on the spectral characteristics of the emission, but it will certainly be helpful in many situations.

Third, it is always possible to spatially average (i.e. taper the beam) to reduce the resolution and decrease the number of resolution elements. So long as the number of baselines does not decrease too rapidly as the long baselines are tapered out (and indeed, the FASR array will be highly centrally condensed), FASR will retain most of its independent measurements under such tapering, and hence the image quality will improve. Thus, FASR will certainly be at least as good as NoRH, and even when heavily tapered the data will yield far more powerful diagnostics due to FASR's multi-frequency coverage.

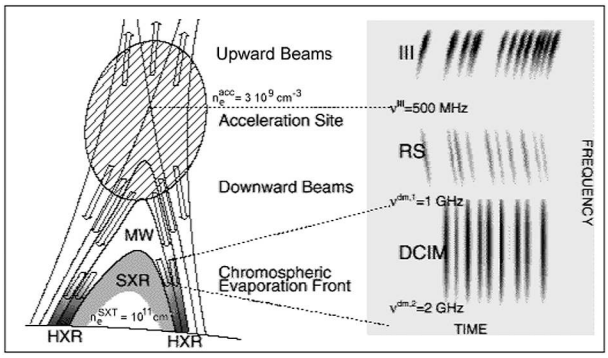

Fig. 17. Aschwanden cartoon (from Achwanden 1996).

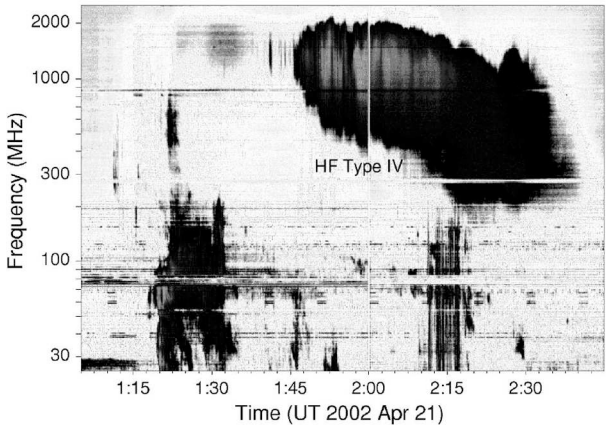

Fig. 18. Hiraiso spectrograph record showing decimetric emissions from the flare of Fig. 11 (from Kundu et al. 2004).

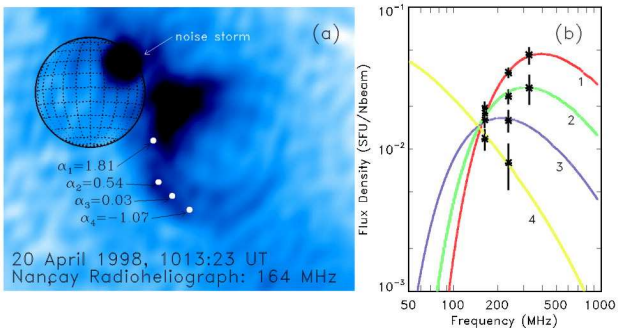

Fig. 19. CME (from Bastian et al. 2001).

4.3. How FASR Will Extend the Flare Science of NoRH

FASR's increased spatial resolution, broad spectral coverage, and improved dynamic range will yield a panoramic view of solar flares that will greatly extend the flare science that has been done to date with NoRH. In this regard, FASR is a transformative instrument—one that will transform our understanding of solar flares and many other solar phenomena through its complete coverage of solar radio emission.

As a simple example of the importance of frequency coverage, the NoRH images given in Fig. 11 (Kundu et al. 2004) were used in conjunction with RHESSI hard X-ray images to understand the initiation and subsequent development of post-flare loops of this long-duration event. However, the standard model for such long-duration events (the CSHKP model; Carmichael 1964; Sturrock 1966; Hirayama 1974; Kopp & Pneuman 1976) involves a 3D structure that is much more extended than that seen at 17 and 34 GHz. Figure 17 schematically shows some of this extended structure, emphasizing that the acceleration may take place above the newly closed loops that make up the main microwave (MW) loop (although other models such as interacting loops may apply to some bursts). Direct signatures of this acceleration may take the form of type III-like forward and reverse slope (RS) bursts as seen on a spectrograph record (right side of Fig. 17). If one wishes to have a complete picture of the relevant structure, one must obtain images in the relevant frequency range, which typically is the decimetric range (roughly 0.3-1 GHz).

That such signatures are present in the flare of Fig. 11 is amply shown in the Hiraiso spectrograph record for this event (Figure 18), as presented by Kundu et al. (2004). All of this complex radio emission is completely missed by NoRH, yet certainly can be expected to contain important clues about the extent and course of development of the 3D structure of the event.

For the first time, FASR will routinely image both the high-frequency part of the flare that NoRH sees, and the decimetric part of the event pertaining to the upper part of the 3D structure where, if the models are correct, all of the real action is. In fact, FASR will image virtually the entire range of heights shown in Fig. 17 relevant to the early stage of the events, and provide spectral diagnostics that will allow the physical parameters to be deduced throughout the region.

In at least some events, such as the one shown in Figure 19 by Bastian et al. (2001), even the accompanying coronal mass ejection (CME) may be imaged by FASR. The event in Fig. 19*a* was imaged at three frequencies by the Nançay Radioheliograph, allowing some crude spectral diagnostics (Fig. 19*b*) to be performed. The emission in this case is gyrosynchrotron emission produced by a relatively small number of energetic electrons, so constraints on the magnetic field strength and number of particles were obtained. FASR's better image quality, dynamic range, and spectral coverage will provide far better diagnostics of CMEs in their nascent stages.

5. Conclusions

The foregoing has only touched on the many discoveries made by a large number of researchers using NoRH flare data, together with supporting data from spacecraft and other groundbased observatories. The power of NoRH for flare research lies in large part on its solar-dedicated, solar-specific design, its full-Sun coverage, its imaging characteristics, and its pipelined data processing. The NoRH results, which are still being added to as more research

continues, form a legacy for flare science that is of great importance in design choices that future instruments will make, FASR in particular.

NoRH flare research has amply demonstrated that flare models need more sophistication, especially in our understanding of the importance of non-isotropic pitch-angle distributions of the accelerated particles. We can expect that the more complete frequency coverage and higher spatial resolution of FASR will clarify the fundamental relationships between the small-scale, lower-atmosphere phenomena and the large-scale phenomena of importance to space weather, which the NoRH observations have hinted at.

With FASR, solar radio physics is poised for the next great step, a transformative leap to a new understanding for all of solar and space weather physics. FASR will succeed only when we fully heed the legacy of the NoRH.

Acknowledgments: This work was supported by NSF grant AST-0307670 to New Jersey Institute of Technology. The author gratefully acknowledges financial support from the organizers of the Nobeyama symposium to attend the meeting.

References

Altyntsev, A. T., Grechnev, V. V., Nakajima, H., Fujiki, K., Nishio, M. & Prosovetsky, D. V. 1999, A&AS, 135, 415

Asai, A., Shimojo, M., Isobe, H., Morimoto, T., Yokoyama, T., Shibasaki, K. & Nakajima, H. 2001, ApJL, 562, L103

Aschwanden, M. J. 1996, American Institute of Physics Conference Series, 374, 300

Aurass, H., Shibasaki, K., Reiner, M. & Karlický, M. 2002, ApJ, 567, 610

Bastian, T. S. 1994, ApJ, 426, 774

Bastian, T. S. 1999, Proceedings of the Nobeyama Symposium, held in Kiyosato, Japan, Oct. 27-30, 1998, Eds.: T. S. Bastian, N. Gopalswamy and K. Shibasaki, NRO Report No. 479., 211

Bastian, T. S., Pick, M., Kerdraon, A., Maia, D., & Vourlidas, A. 2001, ApJL, 558, L65

Bastian, T. S. 2003*a*, Proc. SPIE, 4853, 98

Bastian, T. S. 2003*b*, Adv. in Space Res., 32, 2705

Carmichael, H. 1964, in Proc. NASA Symp. on the Physics of Solar Flares, ed. W. N. Hess (NASA SP-50), 451

Gary, D. E. 2003, J. Korean Astr. Soc., 36, 135

Gary, D. E., Hartl, M. D., Shimizu, T. 1997, ApJ477, 958

Gary, D. E. & Keller, C. U. 2003, Proc. SPIE, 4853, 523

Gary, D. E., & Keller, C. U. 2004, Solar and Space Weather Radiophysics—Current Status and Future Developments. Edited by Dale E. Gary & Christoph U. Keller, ASTROPHYSICS AND SPACE SCIENCE LIBRARY Volume 314 Kluwer Academic Publishers, Dordrecht, 400pp

Grechnev, V. V. White, S. M. & Kundu, M. R. 2003, ApJ, 588, 1163

Hanaoka, Y. 1997, Sol. Phys., 173, 319

Hanaoka, Y. 1999, PASJ, 51, 483

Hirayama, T. 1974, Sol. Phys., 34, 323

Hori, K., Kosugi, T., Fujiki, K., Koshiishi, H., & Shibasaki, K. 2000, ApJ, 533, 557

Kopp, R. A., & Pneuman, G. W. 1976, Sol. Phys., 50, 85

Kundu, M. R., Nitta, N., White, S. M., Shibasaki, K., Enome, S., Sakao, T., Kosugi, T., & Sakurai, T. 1995, ApJ, 454, 522

Kundu, M. R., White, S. M., Shibasaki, K., & Sakurai, T. 2000, ApJ, 545, 1084

Kundu, M. R., White, S. M., Shibasaki, K., Sakurai, T., & Grechnev, V. V. 2001*a*, ApJ, 547, 1090

Kundu, M. R., White, S. M., Shibasaki, K., & Raulin, J.-P. 2001*b*, ApJS, 133, 467

Kundu, M. R., Nindos, A., White, S. M., & Grechnev, V. V. 2001*c*, ApJ, 557, 880

Kundu, M. R., Garaimov, V. I., White, S. M., & Krucker, S. 2004, ApJ, 600, 1052

Lee, J., Gary, D. E., & Shibasaki, K. 2000, ApJ, 531, 1109

Lin, R. P., Schwartz, R. A., Kane, S. R., Peling, R. M. & Hurley, K. C. 1984, ApJ, 283, 421

Melnikov, V. F., Shibasaki, K., & Reznikova, V. E. 2002*a*, ApJL, 580, L185

Melnikov, V. F., Reznikova, V. E., Yokoyama, T., & Shibasaki, K. 2002*b*, ESA SP-506: Solar Variability: From Core to Outer Frontiers, 339

Nakajima, H., et al. 1994, Proc. IEEE, 82, 705

Nakajima, H., & Yokoyama, T. 2002, ApJL, 570, L41

Nishio, M., Yaji, K., Kosugi, T., Nakajima, H., & Sakurai, T. 1997, ApJ, 489, 976

Nishio, M., Kosugi, T., Yaji, K., Nakajima, H., & Sakurai, T. 2000, Advances in Space Research, 25, 1791

Raulin, J.-P., White, S. M., Kundu, M. R., Silva, A. V. R., & Shibasaki, K. 1999, ApJ, 522, 547

Shibasaki, K., et al. 1994, Space Science Reviews, 68, 217

Shibasaki, K. 2002, ApJL, 567, L85

Sturrock, P. A. 1966, Nature, 211, 695

White, S. M., Kundu, M. R., Shimizu, T., Shibasaki, K., & Enome, S. 1995, ApJ, 450, 435

White, S. M., Kundu, M. R., Garaimov, V. I., Yokoyama, T., & Sato, J. 2002, ApJ, 576, 505

White, S. M., Lee, J., Aschwanden, M. A. & Bastian, T. S. 2003, Proc. SPIE, 4853, 531

Yokoyama, T., Nakajima, H., Shibasaki, K., Melnikov, V. F., & Stepanov, A. V. 2002, ApJL, 576, L87

Yokoyama, T., Nakajima, H., Shibasaki, K., Melnikov, V. F., & Stepanov, A. V. 2003, Advances in Space Research, 32, 2517